

Visualizing fluidized beds with X-rays

by

Nathan Paul Franka

A thesis submitted to the graduate faculty
in partial fulfillment of the requirements for the degree of
MASTER OF SCIENCE

Major: Mechanical Engineering

Program of Study Committee:
Theodore J. Heindel, Major Professor
Robert C. Brown
Hui Hu

Iowa State University

Ames, Iowa

2008

Copyright © Nathan Paul Franka, 2008. All rights reserved.

UMI Number: 1453162

INFORMATION TO USERS

The quality of this reproduction is dependent upon the quality of the copy submitted. Broken or indistinct print, colored or poor quality illustrations and photographs, print bleed-through, substandard margins, and improper alignment can adversely affect reproduction.

In the unlikely event that the author did not send a complete manuscript and there are missing pages, these will be noted. Also, if unauthorized copyright material had to be removed, a note will indicate the deletion.



UMI Microform 1453162
Copyright 2008 by ProQuest LLC
All rights reserved. This microform edition is protected against
unauthorized copying under Title 17, United States Code.

ProQuest LLC
789 East Eisenhower Parkway
P.O. Box 1346
Ann Arbor, MI 48106-1346

Table of Contents

Table of Contents	ii
List of Figures.....	v
List of Tables	xiv
Nomenclature	xv
Acknowledgements	xviii
Abstract.....	xix
Chapter 1: Introduction	1
1.1 Motivation.....	1
1.2 Objectives	3
Chapter 2: Literature Review.....	6
2.1 Fluidization	6
2.1.1 Fluidization and Fluidized Beds	7
2.1.2 Fluidization Regimes	9
2.1.3 Types of Gas-Solid Reactions.....	10
2.1.4 Material Classification, Size Distribution, and Elutriation.....	11
2.1.5 Bubbling and Gas Holdup.....	14
2.1.6 Minimum Fluidization Velocity	15
2.1.7 Static Electricity Buildup.....	17
2.2 Biomass and Thermochemical Conversion	18
2.2.1 Biomass and Biomass Fluidization.....	19
2.2.2 Thermochemical Conversion of Biomass Fuels	22
2.2.2.1 Combustion	22
2.2.2.2 Fast Pyrolysis.....	23
2.2.2.3 Gasification	24
2.3 Noninvasive Multiphase Flow Visualization.....	26
2.3.1 Noninvasive Techniques.....	26
2.3.2 X-Ray Techniques	30
2.3.2.1 X-Ray Computed Tomography.....	31
2.3.2.2 X-Ray Radiography	34
2.3.2.3 X-Ray Stereography/Particle Tracking Velocimetry.....	36
2.4 Relating CFD to Multiphase Flows	38
2.4.1 CFD and Multiphase Flows	38
2.4.2 CFD and Fluidized Beds.....	39
2.5 Summary	41
Chapter 3: Experimental Setup.....	43

3.1 System Design	43
3.1.1 Fluidized Bed Reactor.....	44
3.1.2 Particle Injection System	48
3.1.2.1 Tracer Particles	48
3.1.2.2 Injection System.....	50
3.1.3 Air Flow System	54
3.1.4 Pressure and Flow Measurement	56
3.2 Bed selection.....	58
3.2.1 Material Selection Criteria	58
3.2.2 Bed Preparation and Measurement	60
3.3 Determining Minimum Fluidization Velocity	63
3.3.1 Method	63
3.3.2 Test Conditions	65
3.4 XFloViz Facility	66
3.4.1 X-ray Equipment.....	66
3.4.2 X-ray Parameters	69
3.5 XCT.....	70
3.5.1 Procedure	71
3.5.2 Calibrations	74
3.5.2.1 Pixel Normalization	74
3.5.2.2 Beam Hardening	75
3.5.2.3 Volumetric Image Stretching.....	78
3.5.3 Finding Gas Holdup from CT Data	79
3.5.3.1 Gas Holdup Derivation	79
3.5.3.2 Gas Holdup from CT Data	80
3.5.3.3 Validating Gas Holdup	82
3.5.3.4 Gas Holdup Summary.....	83
3.6 Radiography/Stereography/Particle Tracking.....	84
3.6.1 Procedure	85
3.6.2 Calibrations	86
3.6.2.1 12-bit to 16-bit Conversion (Lightening).....	87
3.6.2.2 Pixel Normalization	87
3.6.2.3 Unwarping.....	87
3.6.3 Colorizing Images.....	88
3.6.4 Particle Tracking.....	89
Chapter 4: Results and Discussion	91
4.1 Minimum Fluidization Velocity	91
4.1.1 Minimum Fluidization with No Side Air Injection.....	92
4.1.2 Minimum Fluidization with Side Air Injection	94
4.2 Gas Holdup	97
4.2.1 Effect of Various Flow Conditions on Local Gas Holdup.....	98
4.2.1.1 Glass Beads.....	99
4.2.1.2 Walnut Shell.....	118
4.2.1.3 Corncob.....	127

4.2.2 Effects of Bed Material on Local Gas Holdup.....	129
4.3 Stereography	137
4.3.1 Effects of Various Flow Conditions	138
4.3.1.1 Glass Beads.....	138
4.3.1.2 Walnut Shell.....	145
4.3.1.3 Corncob.....	149
4.3.2 Effects of Bed Material.....	153
4.4 XPTV	154
Chapter 5: Conclusions and Recommendations	161
5.1 Conclusions.....	161
5.2 Recommendations.....	168
References.....	170
Appendix A: Experimental Setup.....	177
Appendix B: Minimum Fluidization Velocity Results.....	189
Appendix C: CT and Gas Holdup Results.....	201
Appendix D: Particle Tracking Results	234
Appendix E: 10.2 cm Fluidized Bed Reactor Drawings	239

List of Figures

Figure 2.1:	Fluidized bed reactor example.....	8
Figure 2.2:	Geldart's classification (Geldart, 1973).....	12
Figure 2.3:	U_{mf} schematic.....	16
Figure 3.1:	Schematic of the fluidized bed reactor.....	45
Figure 3.2:	Photograph of the distributor plate.	46
Figure 3.3:	Photograph of the cold-flow fluidized bed reactor (without the expansion column).	48
Figure 3.4:	Polypropylene tracer particles.....	50
Figure 3.5:	Schematic of particle injection system.	51
Figure 3.6:	Single particle injection system.	53
Figure 3.7:	Schematic of the air flow control system.....	54
Figure 3.8:	Air flow control board.	56
Figure 3.9:	Material selection based on Geldart's classification (Geldart, 1973).....	60
Figure 3.10:	Bed materials used in this fluidization study (a) glass beads, (b) ground walnut shell, and (c) ground corncob.	61
Figure 3.11:	Static electricity buildup after 1 hour for (a) glass, (b) walnut shell, and (c) corncob.	63
Figure 3.12:	Determining U_{mf} from a pressure-flow plot for glass beads.	65
Figure 3.13:	XFloViz imaging room.	68
Figure 3.14:	ISU XFloViz facility.....	69
Figure 3.15:	CT imaging planes.	73
Figure 3.16:	CT slices for bulk glass bead bed: (a) x-slice and (b) z-slice without corrections for beam hardening, (c) x-slice and (d) z-slice with corrections for beam hardening.	76
Figure 3.17:	CT x-slice for glass bead bed: (a) original image, and (b) corrected for stretching.	79
Figure 3.18:	Flowchart for calculating local gas holdup from XCT data.	84

Figure 3.19:	Radiographs of glass bead fluidized bed: (a) original warped image, and (b) resulting image after unwarping.....	88
Figure 3.20:	Radiographs of glass bead fluidized bed: (a) original image, and (b) the same image after colorizing.....	89
Figure 4.1:	Sample $U_{mf,0}$ experimental curves for glass beads, walnut shell, and corncob with no side air injection.....	93
Figure 4.2:	Fluidization curves for glass beads, walnut shell, and corncob with $Q_s = 0.20Q_{mf}$	95
Figure 4.3:	Fluidization curves for glass beads with five side air flow rates.....	96
Figure 4.4:	U_{mf} for various side air flow rates in beds of glass beads, walnut shell, and corncob.....	97
Figure 4.5:	Gas holdup y- and z-slices for glass bead fluidization: $U_g = 1.25U_{mf}$, varying Q_s	100
Figure 4.6:	X-slice gas holdup for glass bead fluidization at four heights: $U_g = 1.25U_{mf}$, $Q_s = 0Q_{mf}$	101
Figure 4.7:	Y-slice gas holdup for glass bead fluidization at four heights: $U_g = 1.25U_{mf}$, $Q_s = 0Q_{mf}$	101
Figure 4.8:	Average gas holdup by height for glass bead fluidization: $U_g = 1.25U_{mf}$, $Q_s = 0Q_{mf}$	103
Figure 4.9:	Y-slice gas holdup for glass bead fluidization at four heights: $U_g = 1.25U_{mf}$, $Q_s = 0.10Q_{mf}$	104
Figure 4.10:	Y-slice gas holdup for glass bead fluidization at $z = 3.2$ cm: $U_g = 1.25U_{mf}$, varying Q_s	106
Figure 4.11:	Y-slice gas holdup for glass bead fluidization at $z = 9.0$ cm: $U_g = 1.25U_{mf}$, varying Q_s	106
Figure 4.12:	Average gas holdup by height for glass bead fluidization: $U_g = 1.25U_{mf}$, varying Q_s	107
Figure 4.13:	Gas holdup y- and z-slices for glass bead fluidization: $U_g = 1.5U_{mf}$, varying Q_s	108
Figure 4.14:	Gas holdup y- and z-slices for glass bead fluidization: $U_g = 1.75U_{mf}$, varying Q_s	109
Figure 4.15:	Gas holdup y- and z-slices for glass bead fluidization: $U_g = 2U_{mf}$, varying Q_s	110
Figure 4.16:	Gas holdup y- and z-slices for glass bead fluidization: $U_g = 3U_{mf}$, varying Q_s	111

Figure 4.17:	Average gas holdup by height for glass bead fluidization: $Q_s = 0.10Q_{mf}$, varying U_g .	114
Figure 4.18:	Y-slice gas holdup for glass bead fluidization at $z = 3.2$ cm: $Q_s = 0.10Q_{mf}$, varying U_g .	115
Figure 4.19:	Y-slice gas holdup for glass bead fluidization at $z = 9.0$ cm: $Q_s = 0.10Q_{mf}$, varying U_g .	116
Figure 4.20:	Gas holdup y- and z-slices for walnut shell fluidization: $U_g = 1.5U_{mf}$, varying Q_s .	119
Figure 4.21:	Gas holdup y- and z-slices for walnut shell fluidization: $U_g = 3U_{mf}$, varying Q_s .	120
Figure 4.22:	X-slice gas holdup for walnut shell fluidization at four heights: $U_g = 1.5U_{mf}$, $Q_s = 0Q_{mf}$.	121
Figure 4.23:	Y-slice gas holdup for walnut shell fluidization at four heights: $U_g = 1.5U_{mf}$, $Q_s = 0Q_{mf}$.	122
Figure 4.24:	Y-slice gas holdup for walnut shell fluidization at four heights: $U_g = 1.5U_{mf}$, $Q_s = 0Q_{mf}$.	123
Figure 4.25:	Y-slice gas holdup for walnut shell fluidization at $z = 3.2$ cm: $U_g = 1.5U_{mf}$, varying Q_s .	124
Figure 4.26:	Y-slice gas holdup for walnut shell fluidization at $z = 9.0$ cm: $U_g = 1.5U_{mf}$, varying Q_s .	124
Figure 4.27:	Y-slice gas holdup for walnut shell fluidization at $z = 3.2$ cm: $Q_s = 0.10Q_{mf}$, varying U_g .	126
Figure 4.28:	Y-slice gas holdup for walnut shell fluidization at $z = 9.0$ cm: $Q_s = 0.10Q_{mf}$, varying U_g .	126
Figure 4.29:	Gas holdup y- and z-slices for corncob fluidization: $U_g = 1.5U_{mf}$, varying Q_s .	127
Figure 4.30:	Gas holdup y- and z-slices for corncob fluidization: $U_g = 3U_{mf}$, varying Q_s .	128
Figure 4.31:	Gas holdup y-slices for all materials: $U_g = 1.5U_{mf}$, varying Q_s .	130
Figure 4.32:	Gas holdup y-slices for all materials: $U_g = 3U_{mf}$, varying Q_s .	131
Figure 4.33:	Average gas holdup by height for all materials: $Q_s = 0Q_{mf}$, $U_g = 1.5U_{mf}$.	132
Figure 4.34:	Average gas holdup by height for all materials: $Q_s = 0.10Q_{mf}$, $U_g = 1.5U_{mf}$.	134

Figure 4.35:	Average gas holdup by height for all materials: $Q_s = 0Q_{mf}$, $U_g = 3U_{mf}$	137
Figure 4.36:	Stereographic images of glass bead fluidization: $U_g = 1.25U_{mf}$, $Q_s = 0Q_{mf}$	139
Figure 4.37:	Stereographic images of glass bead fluidization: $U_g = 1.25U_{mf}$, $Q_s = 0.05Q_{mf}$	140
Figure 4.38:	Stereographic images of glass bead fluidization: $U_g = 1.25U_{mf}$, $Q_s = 0.10Q_{mf}$	140
Figure 4.39:	Stereographic images of glass bead fluidization: $U_g = 1.25U_{mf}$, $Q_s = 0.15Q_{mf}$	141
Figure 4.40:	Stereographic images of glass bead fluidization: $U_g = 1.25U_{mf}$, $Q_s = 0.20Q_{mf}$	141
Figure 4.41:	Stereographic images of glass bead fluidization: $U_g = 1.5U_{mf}$, $Q_s = 0Q_{mf}$	143
Figure 4.42:	Stereographic images of glass bead fluidization: $U_g = 1.5U_{mf}$, $Q_s = 0.10Q_{mf}$	143
Figure 4.43:	Stereographic images of glass bead fluidization: $U_g = 3U_{mf}$, $Q_s = 0Q_{mf}$	144
Figure 4.44:	Stereographic images of glass bead fluidization: $U_g = 3U_{mf}$, $Q_s = 0.10Q_{mf}$	144
Figure 4.45:	Stereographic images of walnut shell fluidization: $U_g = 1.5U_{mf}$, $Q_s = 0Q_{mf}$	146
Figure 4.46:	Stereographic images of walnut shell fluidization: $U_g = 1.5U_{mf}$, $Q_s = 0.10Q_{mf}$	147
Figure 4.47:	Stereographic images of walnut shell fluidization: $U_g = 3U_{mf}$, $Q_s = 0Q_{mf}$	148
Figure 4.48:	Stereographic images of walnut shell fluidization: $U_g = 3U_{mf}$, $Q_s = 0.10Q_{mf}$	149
Figure 4.49:	Stereographic images of corncob fluidization: $U_g = 1.5U_{mf}$, $Q_s = 0Q_{mf}$	150
Figure 4.50:	Stereographic images of corncob fluidization: $U_g = 1.5U_{mf}$, $Q_s = 0.10Q_{mf}$	151
Figure 4.51:	Stereographic images of corncob fluidization: $U_g = 3U_{mf}$, $Q_s = 0Q_{mf}$	152

Figure 4.52:	Stereographic images of corncob fluidization: $U_g = 3U_{mf}$, $Q_s = 0.10Q_{mf}$	153
Figure 4.53:	Particle tracking in glass bead fluidization: $U_g = 1.5U_{mf}$, $Q_s = 0.05Q_{mf}$	155
Figure 4.54:	Injected tracer particle trajectory in x-z plane (each data point represents a time interval of 0.05 sec).	156
Figure 4.55:	Injected tracer particle trajectory in y-z plane (each data point represents a time interval of 0.05 sec).	157
Figure 4.56:	Injected tracer particle trajectory in x-y plane (each data point represents a time interval of 0.05 sec).	157
Figure 4.57:	Injected tracer particle velocity in x-, y-, and z-directions.	158
Figure 4.58:	Tracer particle x-z location superimposed on gas holdup y-slice for glass bead fluidization: $U_g = 1.50U_{mf}$, $Q_s = 0.05Q_{mf}$ (each data point represents a time interval of 0.05 sec).	160
Figure A.1:	Four tracer particles developed in this research (measurements in cm).	178
Figure A.2:	Wiring schematic for solenoids.	178
Figure A.3:	Sifting glass beads: (a) pouring glass in sieve, (b) cleaning sieve, and (c) shaking sieve with shaker.	179
Figure A.4:	Glass bead preparation: (a) washing, (b) initial fan drying, and (c) drying in fluidized bed.	179
Figure A.5:	Weighing glass beads.....	180
Figure A.6:	Static electricity test for glass bead fluidization for one hour.	180
Figure A.7:	Static electricity test for walnut shell fluidization for one hour.....	180
Figure A.8:	Static electricity test for corncob fluidization for one hour.	181
Figure A.9:	Fluidized bed setup in X-ray vault.....	181
Figure A.10:	DAQ equipment.....	182
Figure A.11:	LabView 8.0 DAQ GUI.....	183
Figure A.12:	Flow meter calibration drum.....	183
Figure A.13:	Calibration curves for (a) 30 Lpm, (b) 100 Lpm, (c) 200 Lpm, and (d) 500 Lpm flow meters.	184
Figure A.14:	Pressure transducer calibration.	185

Figure A.15:	Pressure transducer calibration curve.	185
Figure A.16:	Glass wedge for beam hardening calibrations: (a) radiographic image, and (b) digital photo.	186
Figure A.17:	Intensity vs glass wedge thickness for beam hardening calibration (P(T) and S(T)).	187
Figure A.18:	Beam hardening correction factor vs intensity (F(T)).	187
Figure B.1:	U_{mf} curves for walnut shell and $Q_s = 0Q_{mf,0}$ with two methods: linear interpolation of empty bed data and curve-fit of empty bed data.	190
Figure B.2:	Example minimum fluidization curve for glass beads with $Q_s = 0Q_{mf,0}$ (corresponding to Table B.1)	192
Figure B.3:	Sample U_{mf} curves for all materials with $Q_s = 0.05Q_{mf,0}$	193
Figure B.4:	Sample U_{mf} curves for all materials with $Q_s = 0.10Q_{mf,0}$	194
Figure B.5:	Sample U_{mf} curves for all materials with $Q_s = 0.15Q_{mf,0}$	194
Figure B.6:	U_{mf} for walnut shell at all five Q_s conditions.	200
Figure B.7:	U_{mf} for corncob at all five Q_s conditions.	200
Figure C.1:	Gas holdup y-slice images in bulk glass beads ($Q_s = U_g = 0$) for six calculation methods: a) average, b) average (smoothed after), c) local, d) local (smooth before), e) local (smooth after), and f) local (smooth before and after).	203
Figure C.2:	Average gas holdup by height for bulk glass beads using various calculation methods.	204
Figure C.3:	Local y-slice gas holdup for bulk glass beads at $z = 7.0$ cm using various calculation methods.	204
Figure C.4:	Gas holdup y-slice images for glass bead fluidization with $U_g = 1.50U_{mf}$ and no side air injection for six calculation methods: a) average, b) average (smoothed after), c) local, d) local (smooth before), e) local (smooth after), and f) local (smooth before and after).	205
Figure C.5:	Average gas holdup by height for glass bead fluidization using various calculation methods: $U_g = 1.50U_{mf}$, $Q_s = 0Q_{mf}$	206
Figure C.6:	Local y-slice gas holdup for glass bead fluidization at $z = 7.0$ cm using various calculation methods: $U_g = 1.50U_{mf}$, $Q_s = 0Q_{mf}$	206
Figure C.7:	Gas holdup x-slices for glass bead fluidization: varying U_g and Q_s	207

Figure C.8:	X-slice gas holdup for glass bead fluidization at four heights: $U_g = 1.25U_{mf}$, $Q_s = 0.10Q_{mf}$	208
Figure C.9:	X-slice gas holdup for glass bead fluidization at $z = 3.2$ cm: $U_g = 1.25U_{mf}$, varying Q_s	208
Figure C.10:	X-slice gas holdup for glass bead fluidization at $z = 9.0$ cm: $U_g = 1.25U_{mf}$, varying Q_s	209
Figure C.11:	X-slice gas holdup for glass bead fluidization at $z = 3.2$ cm: $Q_s = 0.10Q_{mf}$, varying U_g	209
Figure C.12:	X-slice gas holdup for glass bead fluidization at $z = 9.0$ cm: $Q_s = 0.10Q_{mf}$, varying U_g	210
Figure C.13:	Average gas holdup by height for glass bead fluidization: $U_g = 3U_{mf}$, varying Q_s	210
Figure C.14:	Y-slice gas holdup for glass bead fluidization at $z = 3.2$ cm: $U_g = 3U_{mf}$, varying Q_s	211
Figure C.15:	Y-slice gas holdup for glass bead fluidization at $z = 9.0$ cm: $U_g = 3U_{mf}$, varying Q_s	211
Figure C.16:	X-slice gas holdup for glass bead fluidization at $z = 3.2$ cm: $U_g = 3U_{mf}$, varying Q_s	212
Figure C.17:	X-slice gas holdup for glass bead fluidization at $z = 9.0$ cm: $U_g = 3U_{mf}$, varying Q_s	212
Figure C.18:	Average gas holdup by height for glass bead fluidization: $Q_s = 0Q_{mf}$, varying U_g	213
Figure C.19:	Y-slice gas holdup for glass bead fluidization at $z = 3.2$ cm: $Q_s = 0Q_{mf}$, varying U_g	213
Figure C.20:	Y-slice gas holdup for glass bead fluidization at $z = 9.0$ cm: $Q_s = 0Q_{mf}$, varying U_g	214
Figure C.21:	X-slice gas holdup for glass bead fluidization at $z = 3.2$ cm: $Q_s = 0Q_{mf}$, varying U_g	214
Figure C.22:	X-slice gas holdup for glass bead fluidization at $z = 9.0$ cm: $Q_s = 0Q_{mf}$, varying U_g	215
Figure C.23:	Gas holdup x-slices for walnut shell fluidization: varying U_g and Q_s	216
Figure C.24:	Gas holdup y- and z-slices for walnut shell fluidization: $U_g = 1.25U_{mf}$, varying Q_s	217

Figure C.25:	Gas holdup y- and z-slices for walnut shell fluidization: $U_g = 1.75U_{mf}$, varying Q_s	218
Figure C.26:	Gas holdup y- and z-slices for walnut shell fluidization: $U_g = 2U_{mf}$, varying Q_s	219
Figure C.27:	X-slice gas holdup for walnut shell fluidization at four heights: $U_g = 1.5U_{mf}$, $Q_s = 0.10Q_{mf}$	219
Figure C.28:	Average gas holdup by height for walnut shell fluidization: $U_g = 1.5U_{mf}$, varying Q_s	220
Figure C.29:	X-slice gas holdup for walnut shell fluidization at $z = 3.2$ cm: $U_g = 1.5U_{mf}$, varying Q_s	220
Figure C.30:	X-slice gas holdup for walnut shell fluidization at $z = 9.0$ cm: $U_g = 1.5U_{mf}$, varying Q_s	221
Figure C.31:	Average gas holdup by height for walnut shell fluidization: $Q_s = 0.10Q_{mf}$, varying U_g	221
Figure C.32:	X-slice gas holdup for walnut shell fluidization at $z = 3.2$ cm: $Q_s = 0.10Q_{mf}$, varying U_g	222
Figure C.33:	X-slice gas holdup for walnut shell fluidization at $z = 9.0$ cm: $Q_s = 0.10Q_{mf}$, varying U_g	222
Figure C.34:	Gas holdup x-slices for corncob fluidization: varying U_g and Q_s	223
Figure C.35:	Gas holdup y- and z-slices for corncob fluidization: $U_g = 1.25U_{mf}$, varying Q_s	224
Figure C.36:	Gas holdup y- and z-slices for corncob fluidization: $U_g = 1.75U_{mf}$, varying Q_s	225
Figure C.37:	Gas holdup y- and z-slices for corncob fluidization: $U_g = 2U_{mf}$, varying Q_s	226
Figure C.38:	Y-slice gas holdup for corncob fluidization at four heights: $U_g = 1.5U_{mf}$, $Q_s = 0Q_{mf}$	226
Figure C.39:	X-slice gas holdup for corncob fluidization at four heights: $U_g = 1.5U_{mf}$, $Q_s = 0Q_{mf}$	227
Figure C.40:	Y-slice gas holdup for corncob fluidization at four heights: $U_g = 1.5U_{mf}$, $Q_s = 0.10Q_{mf}$	227
Figure C.41:	X-slice gas holdup for corncob fluidization at four heights: $U_g = 1.5U_{mf}$, $Q_s = 0.10Q_{mf}$	228
Figure C.42:	Average gas holdup by height for corncob fluidization: $U_g = 1.50U_{mf}$, varying Q_s	228

Figure C.43:	Y-slice gas holdup for corncob fluidization at $z = 3.2$ cm: $U_g = 1.5U_{mf}$, varying Q_s	229
Figure C.44:	Y-slice gas holdup for corncob fluidization at $z = 9.0$ cm: $U_g = 1.5U_{mf}$, varying Q_s	229
Figure C.45:	X-slice gas holdup for corncob fluidization at $z = 3.2$ cm: $U_g = 1.5U_{mf}$, varying Q_s	230
Figure C.46:	X-slice gas holdup for corncob fluidization at $z = 9.0$ cm: $U_g = 1.5U_{mf}$, varying Q_s	230
Figure C.47:	Average gas holdup by height for corncob fluidization: $Q_s = 0.10Q_{mf}$, varying U_g	231
Figure C.48:	Y-slice gas holdup for corncob fluidization at $z = 3.2$ cm: $Q_s = 0.10Q_{mf}$, varying U_g	231
Figure C.49:	Y-slice gas holdup for corncob fluidization at $z = 9.0$ cm: $Q_s = 0.10Q_{mf}$, varying U_g	232
Figure C.50:	X-slice gas holdup for corncob fluidization at $z = 3.2$ cm: $Q_s = 0.10Q_{mf}$, varying U_g	232
Figure C.51:	X-slice gas holdup for corncob fluidization at $z = 9.0$ cm: $Q_s = 0.10Q_{mf}$, varying U_g	233
Figure C.52:	Average gas holdup by height for all materials: $U_g = 3U_{mf}$, $Q_s = 0.10Q_{mf}$	233
Figure D.1:	Supplemental particle tracking images in glass bead bed from $t = 0.45$ to 1.00 s: $U_g = 1.5U_{mf}$, $Q_s = 0.05Q_{mf}$	235
Figure D.2:	Injected particle speed as a function of time in glass bead bed: $U_g = 1.5U_{mf}$ and $Q_s = 0.05Q_{mf}$	236

List of Tables

Table 3.1:	Bed material summary.	62
Table 4.1:	Minimum fluidization velocity with no side air injection for glass beads, walnut shell, and corncob.	92
Table 4.2:	Superficial gas velocity test conditions for glass beads, walnut shell, and corncob.	94
Table 4.3:	Side air injection flow rate test conditions for glass beads, walnut shell, and corncob.	94
Table 4.4:	U_{mf} for various side air flow rates in beds of glass beads, walnut shell, and corncob.	96
Table A.1:	Glass wedge specifications.	186
Table A.2:	Beam hardening calibration raw data.	188
Table B.1:	Example minimum fluidization test data for glass beads with $Q_s = 0Q_{mf,0}$	191
Table B.2:	All $U_{mf,0}$ results for all materials with no side air.	192
Table B.3:	Experimental flow conditions for U_{mf} , CT, stereography, and particle tracking.	193
Table B.4:	Sample U_{mf} data for all materials with $Q_s = 0Q_{mf,0}$	195
Table B.5:	Sample U_{mf} data for all materials with $Q_s = 0.05Q_{mf,0}$	196
Table B.6:	Sample U_{mf} data for all materials with $Q_s = 0.10Q_{mf,0}$	197
Table B.7:	Sample U_{mf} data for all materials with $Q_s = 0.15Q_{mf,0}$	198
Table B.8:	Sample U_{mf} data for all materials with $Q_s = 0.20Q_{mf,0}$	199
Table C.1:	Local y-slice gas holdup average and standard deviation at $z = 7.0$ cm for bulk glass beads using various calculation methods.	203
Table C.2:	Local y-slice gas holdup average and standard deviation at $z = 7.0$ cm for bulk glass beads using various calculation methods.	205
Table D.1:	Tracer particle locations at 0.05 s increments.	237
Table D.2:	Tracer particle velocities at 0.05 s increments.	238

Nomenclature

Abbreviations

CAD	Computer-Aided Design
CARPT	Computer Automated Radioactive Particle Tracking
CCD	Charge Coupled Device
CFB	Circulating Fluidized Bed
CFD	Computational Fluid Dynamics
CNDE	Center for Nondestructive Evaluation (Iowa State University)
CT	Computed Tomography
DAQ	Data Acquisition
EALR	External Airlift Loop Reactor
ECT	Electrical Capacitance Tomography
EIT	Electrical Impedance Tomography
ESD	Electrostatic Discharge
FCC	Fluidized Cracking Catalyst
GDT	Gamma Densitometry Tomography
LDA	Laser Doppler Anemometry
MRI	Magnetic Resonance Imaging
NMRI	Nuclear Magnetic Resonance Imaging
PEPT	Positron Emission Particle Tracking
PET	Positron Emission Tomography
PIV	Particle Imaging Velocimetry
PTV	Particle Tracking Velocimetry
PSD	Particle Size Distribution
RDF	Refuse Derived Fuel
ROI	Region of Interest

RPT	Radioactive Particle Tracking
XCT	X-Ray Computed Tomography
XDT	X-Ray Diffraction Tomography
XFloViz	X-ray Flow Visualization facility (Iowa State University)
XPTV	X-Ray Particle Tracking Velocimetry
XRIP	X-ray Image Processor program

Roman Symbols

D	Bed diameter (internal diameter)	(cm)
H	Bed height	(cm)
I	X-ray CT intensity of fluidized bed	(-)
I	X-ray intensity incident on a detector	(-)
I_0	X-ray intensity incident on an object	(-)
I_{avg}	Average of local image intensities in dark and flat frames	(-)
I_b	X-ray CT intensity of bulk material	(-)
I_{dark}	Local image intensity of dark frame	(-)
I_{flat}	Local image intensity of flat frame	(-)
I_g	X-ray CT intensity of gas	(-)
I_{image}	Local raw image intensity of raw image	(-)
I_{new}	Local image intensity of pixel normalized image	(-)
I_p	X-ray CT intensity of particle	(-)
ID	Internal diameter	(cm)
OD	Outer diameter	(cm)
Q_{mf}	Minimum fluidization flow rate	(Lpm)
$Q_{mf,0}$	Minimum fluidization flow rate with no side air	(Lpm)
Q_s	Side air injection flow rate	(Lpm)
t	Time	(s)

T	Imaging object thickness	(cm)
U_c	Critical gas velocity	(cm/s)
U_g	Superficial gas velocity	(cm/s)
U_{mb}	Minimum bubbling velocity	(cm/s)
U_{mf}	Minimum fluidization velocity	(cm/s)
$U_{mf,0}$	Minimum fluidization velocity with no side air	(cm/s)
U_{trans}	Transition velocity	(cm/s)
V_{bed}	Bed volume	(cm)
W_{bed}	Bed weight	(g)

Greek Symbols

ϵ_g	Local gas holdup (void fraction)	(-)
$\epsilon_{g,b}$	Bulk material gas holdup (void fraction)	(-)
μ	Linear X-ray attenuation coefficient	(cm ⁻¹)
μ_g	Linear X-ray attenuation coefficient of gas	(cm ⁻¹)
μ_p	Linear X-ray attenuation coefficient of particle	(cm ⁻¹)
ρ_b	Bulk density of bed material	(g/cm ³)
ρ_{gas}	Gas density	(g/cm ³)
ρ_p	Particle density	(g/cm ³)
ρ_{solid}	Solid density (particle density)	(g/cm ³)

Acknowledgements

I would especially like to thank Dr. Ted Heindel for being my major professor and for providing me with this research opportunity. He has continually given valuable advice, support, patience and friendship and this thesis would not be possible without him.

Thank you to Dr. Hui Hu and Dr. Robert Brown for being on my committee and reviewing this thesis.

Thank you to my collaborators on this project; Dr. Francine Battaglia, Mirka Deza, and Frontline Bioenergy, LLC. Their valuable insight helped to guide this research.

Thanks to Joshua Drake and Tim Morgan for assisting this research and for patiently working with me to develop the X-ray imaging software used for data analysis. Also thanks to Joshua Drake, Sam Jones, and Terry Jensen for troubleshooting various research problems and for brainstorming research ideas. Thanks to the freshmen honors students that assisted with this research.

Thank you Dr. Brown and Dr. Battaglia for introducing me to fluidized beds as an undergraduate research assistant and for getting me involved with experimental research. I also want to thank Dr. Heindel, Dr. Battaglia, and Dr. Gloria Starns for encouraging me to go to graduate school and for assisting me in the application process.

I also want to thank my family for their continuing support, love, and encouragement and for demonstrating the value of education. Finally, I would like to thank my fiancé, Adrian, for the incredible support, patience, love and encouragement she has constantly given. I could not have finished without her.

The X-ray facility used in this research was funded by the National Science Foundation under award number CTS-0216367. Partial support for the work described in this thesis is provided by the Grow Iowa Values Fund and is also appreciated.

Abstract

Fluidized beds are central components in thermochemical conversion processes, like gasification, which can convert biomass into usable forms of energy. Due to the high availability of biomass, biomass gasification has gained popularity as a renewable energy source; however, gasification efficiency still requires improvement. Currently, little is known about the behavior of biomass as it is injected into a gasifier, or how air injection with the biomass affects fluidization behavior. Computational fluid dynamic (CFD) models are being designed to provide insight into fluidization hydrodynamics and to improve process efficiency; however, CFD simulations require high-quality, reliable experimental data for simulation validation. Since fluidized beds are opaque in nature, noninvasive X-ray techniques provide a method of visualizing internal fluidization features, and can generate the necessary high-quality experimental data for CFD validation.

This study applies X-ray computed tomography (CT) and radiography/stereography to fluidized beds of glass beads, ground walnut shell, and ground corncob operating with a variety of flow combinations. 3-D local, time-averaged gas holdup is calculated from CT data, while dynamic features are captured by X-ray stereography. The effects of bed material, superficial gas velocity (U_g), and side air injection on fluidization behavior are subsequently described. Internal flow features are identified from the gas holdup and stereography data. A method of tracking tracer particles upon injection into the fluidized beds is also presented as a proof-of-concept. Additionally, the minimum fluidization velocity, an important parameter for CFD modeling and for describing fluidization regimes, is determined for the three bed materials with and without injection of side air.

The results show that CT is most effective on glass bead fluidized beds. Due to high X-ray attenuation, glass bead CT data has higher resolution than walnut shell and corncob beds. Glass bead gas holdup data also feature the lowest noise due to the high homogeneity of the

beads. Conversely, stereography is most effective in corncob and walnut shell fluidized beds. High X-ray penetration in these beds allows clear observation of internal flow features.

It is also determined that increasing the superficial gas velocity in the bed decreases the effects of side air injection. From gas holdup data, a clearly defined flow path is shown to extend from the side air injection port to the surface of the bed with low U_g . This flow path becomes much less distinguishable as U_g increases. Consequentially, with higher superficial gas velocity, fluidization occurs more uniformly.

Chapter 1: Introduction

1.1 Motivation

In fluidization, a fluid passes through a collection of solid particles, or fluidized bed, and causes the particles to achieve hydrodynamic behavior which is similar to a fluid. Fluidized beds are commonly utilized in industrial processes and feature many advantages; they exhibit low pressure drops, approximately uniform temperature distributions, high heat and mass transfer rates, and the ability to fluidize many particle types of varying sizes (Cui et al., 2007; Grace et al., 2006; Utikar et al., 2007). As a result, fluidized beds are often central components in thermochemical conversion processes, such as in biomass gasification. In gasification, biomass is typically injected into a heated bed of an inert catalyst, such as sand, and undergoes a thermochemical reaction to create a flammable hydrocarbon gas, called producer gas. Gasification is becoming an important process due to the large amount of waste biomass available and the limited production of greenhouse gases in the producer gas combustion cycle (Cui et al., 2007). In addition, gasification may be directly applied to electricity generation, or coupled to an ethanol plant to provide the distillation energy necessary for ethanol production. This is beneficial because quality requirements do not restrict usage of producer gas in combustion, and fossil fuels are not necessary for energy production (Bridgwater, 2003). While gasification has recently gained popularity, its efficiency requires improvement, and consequently, the process must be researched in greater detail.

To aid in the understanding of gasification, fluidized bed computational models are being developed to simulate the injection of biomass particles into fluidized beds. By experimentally tracking biomass particles, these computational fluid dynamics (CFD) simulations can be validated; the validated models can then be used to potentially enhance gasification efficiency. However, the capabilities to experimentally track biomass particles

are limited and there is currently a need for high quality experimental data for validation of these simulations.

Limited experimental data is available on biomass injection in gasification systems due to the difficulty in monitoring biomass as it is injected into a fluidized bed. Problems arise with biomass reacting and being destroyed after injection into the bed. Also, since bed materials are typically opaque, efforts to optically visualize internal flow and track injected biomass particles are difficult. Additionally, the effects of gas injection through the biomass injector port, common in many gasifiers, have not been studied in detail.

Noninvasive monitoring techniques are ideal for providing high quality quantitative data about fluidization hydrodynamics since they do not influence the internal flow and have high reliability. X-ray techniques, such as X-ray computed tomography and X-ray radiography/stereography, have been applied to fluidized beds in the literature but have not been utilized to visualize effects of side gas/particle injection.

One of the most important fundamental parameters for designing, analyzing, and simulating fluidized beds is the minimum fluidization velocity, U_{mf} . It sets the lower boundary for fluidization and is necessary when modeling the hydrodynamics using CFD (Hilal et al., 2001). U_{mf} is a complex function of particle properties/geometry, fluid properties, and bed geometry, and is generally determined experimentally since many of the parameters used in theoretical calculations can only be estimated (Davidson, 1963). Currently, no studies have been performed to show the effects of side gas injection on minimum fluidization velocity.

Another important factor in fluidization behavior is the bed material. In gasification, fluidized beds are commonly composed of sand due to its uniform fluidization and heat transfer properties; however, beds made solely of biomass can also fluidize. Fluidized bed models, or cold-flow beds, are generally comprised of uniform diameter and density glass beads, which represent uniformly fluidizing bed material. Glass beads are useful in achieving

uniform fluidization because of their high sphericity, uniform density, and resistance to breakage. However, due to difficulties in penetrating glass beads with X-rays, beds composed of low density biomass are of interest to improve X-ray penetration and quantify fluidized bed hydrodynamics.

1.2 Objectives

The goals of this research are to use X-ray computed tomography (CT) and radiographic/stereographic imaging to understand the effects of bed material, superficial gas flow, and side air injection on fluidization hydrodynamics. X-ray particle tracking of simulated biomass injection is also desired to better understand biomass injection in gasifiers. Additionally, the study will provide experimental data for use in CFD model validation by other investigators. The CFD model will ultimately improve the efficiency of biomass injection into a fluidized bed gasifier.

To accomplish these goals, this study will complete the following specific objectives.

1. Review current literature to better understand fluidization, biomass and its relationship to thermochemical conversion, nonintrusive testing methods that can be used to visualize internal fluidization features, and current needs in CFD simulation.
2. Compare the effects of bed material on the minimum fluidization velocity to better understand the relationship between fluidization of the inert catalyst bed material and biomass fluidization.
3. Evaluate the effects of side gas injection, typical of biomass feed systems in gasifiers, on the minimum fluidization velocity.
4. Apply X-ray CT imaging to calculate time-averaged local gas holdup for fluidized beds in order to visualize time-averaged internal flow features.

5. Compare the effects of side gas injection on fluidization using local gas holdup data.
6. Assess the effects of varying superficial gas velocity on fluidization using local gas holdup information.
7. Distinguish the effects of bed material on fluidization, with and without side air injection, through gas holdup information.
8. Demonstrate the application of X-ray stereographic imaging towards understanding dynamic fluidization features.
9. Evaluate the effects of side gas injection on fluidization hydrodynamics using stereographic imaging.
10. Compare the effects of varying superficial gas velocity on fluidization hydrodynamics through stereographic imaging.
11. Contrast the effects of bed material on fluidization hydrodynamics and on stereographic imaging.
12. Present a proof-of-concept technique for tracking a particle upon injection into a fluidized bed through a side injection port.

The following thesis describes the research performed to meet these objectives. Chapter 2 presents a review of selected literature pertaining to fluidized beds and fluidization, biomass and thermochemical conversion processes, the application of noninvasive techniques to multiphase flow visualization, and CFD simulation of multiphase flows. Next, Chapter 3 describes the fluidization equipment and the methods used in this research to collect data relating to the fluidization hydrodynamics. Minimum fluidization velocity tests and X-ray techniques are described in detail. Chapter 4 presents selected minimum fluidization velocity, local time-averaged gas holdup, stereographic imaging, and particle tracking results and describes observed trends. In Chapter 5, a review of important results from Chapter 4 is

provided as well as recommendations for future work. Next is a list of literature references followed by appendices of selected reference materials.

Chapter 2: Literature Review

This Chapter intends to give a brief overview of four topics useful in understanding the subsequent research. Section 2.1 will explain fluidization with an emphasis on fluidization regimes, types of gas-solid reactions, bubbling in fluidized beds, minimum fluidization velocity, bed material classification, bed material size distribution, elutriation, and static electricity buildup. Section 2.2 will then provide an introduction to biomass, biomass fluidization, and its relation to thermochemical conversion. The three most common thermochemical conversion methods using fluidized bed technology will also be examined; combustion, fast pyrolysis, and gasification. In section 2.3, multiphase flow visualization will be summarized. First, a brief introduction will provide basics of noninvasive visualization techniques, followed by a description of X-ray techniques with an emphasis on three common visualization methods; X-ray computed tomography, X-ray radiography, and X-ray stereography/particle tracking velocimetry. Section 2.4 will briefly explain the importance of computational fluid dynamics as related to modeling fluidized bed reactors. Finally, section 2.5 will provide a brief summary of this review and explain its applicability towards the current research.

2.1 Fluidization

The goal of section 2.1 is to relate fundamental fluidization principles and fluidization characteristics to important parameters, as supported by the literature. This section is divided into seven subsections. The first provides an overview of fluidization and fluidized beds, noting important features. The next subsection characterizes fluidization regimes and outlines the similarities between gas-solid and gas-liquid systems. The third subsection explains the four main types of gas-solid reactions found in fluidized beds. In the next subsection, Geldart's particle classification, particle size distributions (PSD), and elutriation of fines is

described. Bubbling, bubble coalescence, and gas holdup is then briefly explained in subsection five, followed by a discussion on minimum fluidization velocity in subsection six. The final subsection examines static electricity buildup in fluidization of granular material and outlines methods of reducing its effect. It should be noted that since fluidization is such a large field, this section only touches the surface of fluidization behavior.

2.1.1 Fluidization and Fluidized Beds

Fluidization refers to the process by which a fluid passes vertically through a collection of solid particles, or fluidized bed, causing the particles to achieve hydrodynamic conditions similar to a fluid. As fluid passes through the bed, the drag force overcomes the gravitational force and reduces the frictional force between particles, allowing relative motion between particles. Fluidized bed reactors are vessels in which this fluidization of granular material occurs. Many different reactor geometries and setups have been researched; however, all contain key features of a plenum, a distributor, a bed region, and a riser. Figure 2.1 shows an example of a 9.5 cm (3.75 in) diameter fluidized bed reactor with 500-600 μm diameter glass beads in the bed region.

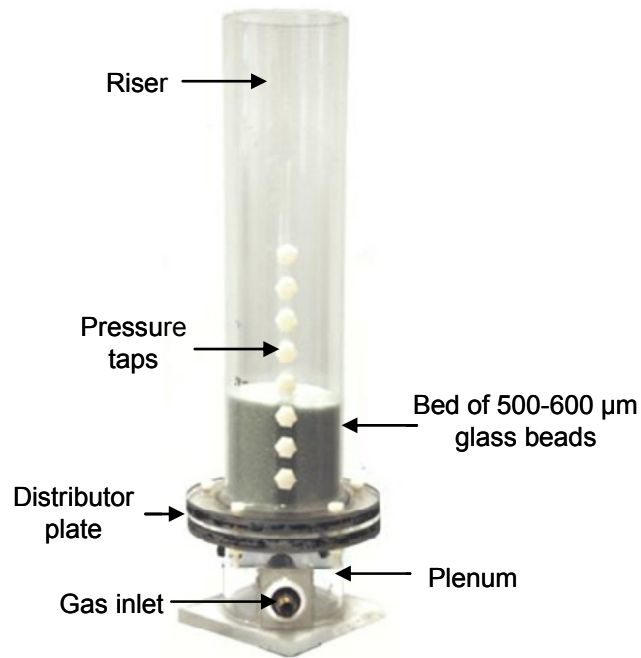


Figure 2.1: Fluidized bed reactor example.

The plenum, or windbox, is the location where fluid enters the bed. Fluid next passes through a distributor which uniformly distributes the fluid at the base of the bed. Distributors (aerators) include porous plates, pipe grid distributors, straight-hole distributor plates, and nozzle or bubble cap distributors (Brown, 1997). Granular material is located above the fluid distribution system in a bed region. Located above the bed is the riser, or freeboard, which contains particles that have been ejected from the bed. Fluid passing through the fluidized bed can be a liquid, gas, or liquid-gas combination. Gas-liquid and gas-liquid-solid systems are typically found in fuel, biochemistry, mineral processing, pharmaceutical, and food industries. Reese et al. (1999) gives a thorough overview of gas-liquid-solid, three-phase fluidization systems which are beneficial because of high macromixing and high reactant conversions. Despite the importance of three-phase and liquid-solid fluidization, this research will primarily focus on the more common gas-solid fluidized beds.

2.1.2 Fluidization Regimes

Various fluidization regimes have been described for gas-solid fluidized beds, and depend on characteristics of the specific system. Grace et al. (2006) provide an overview of common regimes, as well as their defining characteristics, and is summarized here. As gas begins to pass through the bed, a minimum fluidization velocity, U_{mf} , is reached, at which point the bed expands because the drag force from the flowing gas overcomes the gravitational force of the particles. As the gas flow rate is further increased, the bed expands uniformly until bubbles start to form at the minimum bubbling velocity, U_{mb} (also called the transition velocity U_{trans}) (Krishna et al., 1993). The regime between minimum fluidization and minimum bubbling velocities is called particulate, or homogeneous fluidization and usually only occurs over a small range of flow rates in gas-solid systems with fine particles (Singh et al., 2005). Geldart type A particles (to be discussed in section 2.1.4) typically exhibit a significant difference between U_{mf} and U_{mb} ; however, most commercial beds bubble as soon as U_{mf} is reached and therefore $U_{mf} \approx U_{mb}$. Transition to heterogeneous flow corresponds with the onset of the bubbling bed regime. In some beds, the ratio of bed height to bed diameter may allow a special form of bubbling called slugging. This occurs when bubbles have sufficient time to coalesce before reaching approximately 50% of the column's diameter. Constantineau et al. (2007) investigated this transition between bubbling and slugging regimes and developed a generalized bubbling-slugging model to improve scale-up of fluidized bed reactors. The model, which is a function of bed height, bed diameter, gas velocity, and gas/bed material properties, employed probabilistic averaging to identify the transition between regimes.

As the gas flow rate further increases, bubbles and slugs deteriorate and turbulent fluidization takes over after the critical gas velocity, U_c , is passed. This critical gas velocity, which is a function of bed height, generally occurs when the standard deviation of the

pressure fluctuations is at a maximum. At even higher superficial gas velocities, fast fluidization begins once the transition velocity, U_{trans} (not to be confused with minimum bubbling), is reached. Particles are carried outside of the bed and the definable boundary of the bed surface becomes indistinguishable. Finally, at extremely high superficial gas velocities, dense suspension upflow begins followed by dilute pneumatic conveying. The fast fluidization, dense suspension upflow and dilute pneumatic conveying fluidization regimes are characteristic of circulating fluidized beds (CFB) and transport reactors. Conventional fluidized beds typically operate in the bubbling, slugging, and/or turbulent fluidization regimes, also known as the aggregative fluidization regimes (Krishna et al., 1993; Grace et al., 2006). This research will focus on the bubbling regime in conventional fluidized beds since different bed materials, reactor designs, and flow conditions affect each regime independently.

Gas-solid fluidized bed systems have often been related to bubble columns in the literature. Krishna et al. (1993) and Ellenberger et al. (1995) described the development of a unified approach to the hydrodynamics of bubble columns and fluidized beds. They concluded that both bubble columns and fluidized beds are hydrodynamically similar and exhibit comparable flow regimes. Both may be described with a generalized dense and dilute phase model, where the dilute phase corresponds to large bubbles and the dense phase corresponds to bulk material (or liquid with small bubbles in bubble columns). In the dense phase, the void fraction is nearly independent of bed diameter but increases with increasing gas density, while the dilute phase void fraction can be modeled (Ellenberger et al., 1995).

2.1.3 Types of Gas-Solid Reactions

Gas-solid fluidized beds are common to many industries and are classified by four different processes, as outlined by Grace et al. (2006). In gas catalytic reactions, products and reactants are gaseous; however, they react on the surface of a solid catalyst. Gas catalytic

reactions are the most commonly encountered form of gas-solid fluidization and the basis for fluid catalytic cracking (FCC) processes in the refining industry. In FCC fluidization, a solid catalyst breaks down long gaseous hydrocarbon chains from crude oil into smaller, more useful chains like gasoline, diesel, and kerosene. The second gas-phase reaction type, useful for highly exothermic and endothermic processes, occurs when both products and reactants are gaseous but reactions occur because of heat stored in a solid material. An example of this reaction is in coking, which is similar to FCC in that large hydrocarbons are broken into smaller chains. A third gas-solid reaction takes place when the reactants are in solid and gas phases but the products are gases or a combination of gas and solids. This reaction type is common to combustion and gasification. A final classification, called physical processing, has no chemical reactions and is used in drying or in particle separation (Grace et al., 2006). Drying in fluidized beds is highly efficient due to high air-solid contact area, rapid heat transfer rates, and short drying times (Wang et al., 2008). Of the four fluidization categories, the gas-solid reaction is most important to biorenewable energy.

2.1.4 Material Classification, Size Distribution, and Elutriation

One of the most important factors in fluidization hydrodynamics is the classification of the bed material. Geldart (1973) provided the standard particle classification scheme for beds fluidized by gas, which is presented as a plot in Figure 2.2. Essentially, all particles may be categorized according to the density difference between the solid and gas phases ($\rho_{\text{solid}} - \rho_{\text{gas}}$) and the mean particle size (diameter). The first classification, type A, contains particles with a small mean size and low particle density. The defining characteristic of type A powders is the significant bed expansion before bubbling and the slow bed collapse when gas is suddenly removed. Group A powders also mix rapidly, even without bubbles. Group B particles generally have mean diameters between 40-500 μm with densities between 1.4-4 g/cm^3 . The formation of bubbles immediately after gas has reached minimum fluidization

velocity is characteristic of type B powders. There is usually no particle movement without bubbles. Powders in Geldart's C classification exhibit strong cohesive forces and are therefore difficult to fluidize. Because particle mixing and heat transfer between the surface and the bed is poor, these powders are typically not used in fluidized bed applications without mechanical stirrers or vibrators. Group D particles are very large and/or very dense. Mixing in type D powders is poor because bubbles rise more slowly than the flowing gas and spouting is a common occurrence; however, this group of particles shows slight fluidization behavior (Geldart, 1973).

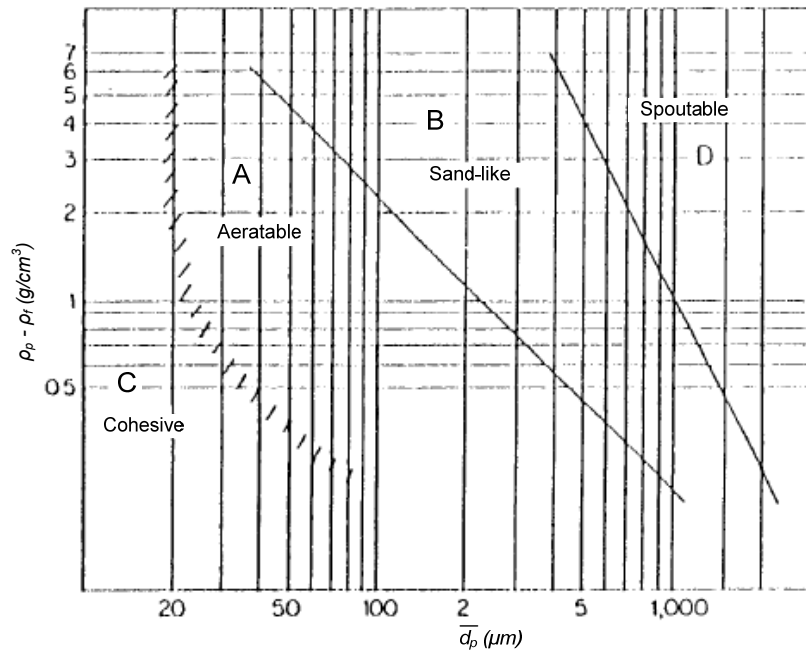


Figure 2.2: Geldart's classification (Geldart, 1973).

In addition to bed material, bed geometry affects fluidization hydrodynamics. Singh et al. (2005) investigated the fluidization quality and minimum bubbling velocities of various Geldart type A particles in the particulate fluidization regime using various column geometries. It was found that beds in a semi-cylindrical or hexagonal conduit have better fluidization characteristics than those in a square conduit.

It is common to fluidize mixtures of Geldart particles. Gauthier et al. (1999) studied the effect of particle size distributions (PSDs) on fluidization using Geldart types B and D river sand with four PSDs: a reference (narrow) PSD, a Gaussian distribution, a binary mixture, and a wide PSD powder. The Gaussian type powder and reference powder were found to have similar behavior with a clearly definable minimum fluidization velocity. The binary mixture and wide PSD powders were found to segregate during fluidization, causing some particles to fluidize at one velocity and others to fluidize at a completely different velocity. Similarly, Sahoo et al. (2005) examined mixing of Geldart B and D particles in a fluidized bed and created a correlation for the mixing index, or the degree of mixing. A bed was fluidized and particles were injected through side-ports in the reactor located every 2 cm vertically. It was found that the mixing index decreased with the height of the particle injection location.

An inherent difficulty in the fluidization of mixtures is the elutriation of fines from the bed material. When the local gas velocity is greater than the particle's terminal velocity, the particle will be ejected from the bed and carried upward with the fluid flow. Elutriation can be detrimental in industrial applications since most elutriated particles are unused fuel or char. Typically, elutriated fines are caught in a cyclone trap after exiting the gas flow. Callen et al. (2007) successfully reduced elutriation by installing inclined parallel plates over the bed. Xie et al. (2007) used computational fluid dynamics to predict elutriation of fines from a coarse bed media, and the results were verified with experimental data. The study found that elutriation rate constants (governing elutriation phenomena) increased with increasing superficial gas velocity and with decreasing particle diameters. While elutriation is an important effect in fluidized bed reactors, it is not a major concern in this research.

2.1.5 Bubbling and Gas Holdup

While there are many factors responsible for the hydrodynamics of fluidization, bubbles, bubble coalescence, and gas holdup (volumetric gas fraction or void fraction) are often studied for various particle classifications. These factors are important for homogeneous mixing, fluidization quality, and process efficiency. They are also useful in finding the interfacial area between the dense and dilute phases that are used in heat and mass transfer calculations (Kumar et al., 1997). Zhu et al. (2007) used an optical probe method to measure solids concentration (the inverse of gas holdup) in bubbling and turbulent fluidized beds. The study found that in a turbulent fluidized bed, the solids holdup was approximately radially symmetric with a dilute center and a dense annulus. It was also determined that by increasing superficial gas velocity, the local solids concentration underwent three evolution stages, suggesting a gradual transition regime. In addition, both upflowing and descending of particles occurred at all measurement locations.

Lim et al. (2007) investigated bubble distribution and the effects upon fluidization. By using a planar fluidized bed and capturing images with a video camera, it was found that bubble distribution and interactions were strongly affected by the inlet flow conditions. The study also found the bubble profile had concentration zones near the distributor by the walls but gradually migrated inwards until coalescing at a critical height. The profile also revealed a strong correlation between bed height and geometry.

The formation of bubbles in a fluidized bed of Geldart type B particles was studied by Kant Pandit et al. (2007). Using a discrete element method, a simulation was created which allowed estimation of interaction forces between multiple particle contacts. It was concluded that bubble shape and growth were a function of superficial air velocity, air jet velocity, and the degree of particle-particle interaction. Additionally, the formation of a continuous stream of bubbles required a higher gas velocity than that required for the formation of a single

bubble to form. Finally, interparticle forces caused bubbles to form at higher gas velocities and influenced bubble size and shape. Gas holdup data acquisition in fluidized beds has been improved using tomographic methods, and is described in a later section.

2.1.6 Minimum Fluidization Velocity

Despite the many transitional flow velocities, the onset of fluidization at the minimum fluidization velocity, U_{mf} , is the most important fundamental parameter for analyzing and designing fluidized beds. It sets the lower boundary for fluidization and is necessary when modeling the hydrodynamics using CFD (Hilal et al., 2001). The minimum fluidization velocity is a complex function of particle properties/geometry, fluid properties, and bed geometry and may be calculated using correlations from the literature (Grace et al., 2006). U_{mf} is usually determined experimentally since many of the parameters used in theoretical calculations can only be estimated (Davidson et al., 1963). To find U_{mf} , pressure drop across the bed is typically measured as gas flow rate is decreased from a high flow rate, where the bed is fully fluidized, to no gas flow. A noted hysteresis effect exists when increasing and decreasing gas flow rate in the bed and is caused by packing effects of the bed; consequentially, U_{mf} experiments generally begin with a fully fluidized bed and decrease gas flow in order to reduce these effects (Davidson et al., 1963; Felipe et al., 2007; Hilal et al., 2001). U_{mf} is identified at the intersection of the constant pressure drop line and the fixed bed pressure drop line (the linearly increasing pressure-velocity curve) (Felipe et al., 2007). Figure 2.3 shows the location of U_{mf} on the pressure curve for a typical minimum fluidization test.

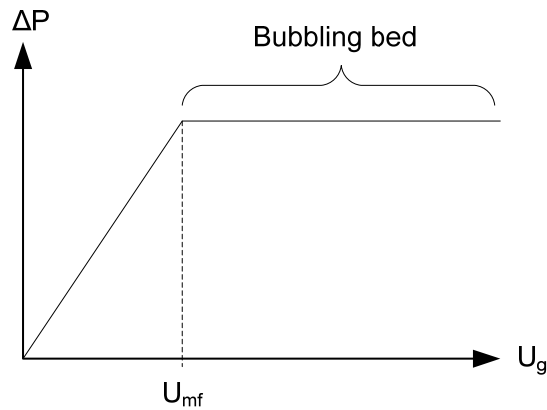


Figure 2.3: U_{mf} schematic.

Hilal et al. (2001) used this methodology to analyze the effects of bed diameter, distributor design, and inserts on minimum fluidization velocity. It was shown that U_{mf} decreased with increasing bed diameter, increased with decreasing distributor plate hole pitch, and decreased with increasing number of vertical inserts. Wu et al. (2007) used the same technique to find U_{mf} of polyethylene resins in 3 different fluidized beds. While the study was not focused on minimum fluidization research, it was again observed that U_{mf} decreased with increasing bed diameter. The study hypothesized that higher friction forces in small-scale beds caused an increase in the velocity. An alternate method of finding minimum fluidization velocity, using the standard deviation of pressure fluctuations, was investigated by Felipe et al. (2007). Geldart A and B type beds were fluidized and pressure fluctuations were recorded at various locations in the bed. The study showed that the pressure fluctuation measurement technique was accurate for both type A and B bed materials when compared with the standard measuring technique. It was also found that pressure measurements taken in the plenum chamber gave the most reliable data since particles did not interfere with the probes, and dynamic phenomena in both the bed and plenum could be seen.

2.1.7 Static Electricity Buildup

One feature arising from the fluidization of powders and granular material is static electricity buildup. The electrical charging of particles in a fluidized bed, called triboelectrification, occurs in the movement of solid particles. Essentially, the contact of two objects transfers electrons from one to another. If these objects are then suddenly separated, the electrons cannot be neutralized and the two objects become charged, but the total system charge remains unchanged. When one of the objects is grounded, a net charge is created in the system, which is called static electricity (Guardiola et al., 1996). This static charge is typically generated with dielectric materials and can be detrimental to fluidization. Additionally, during fluidization of some materials, static charge accumulates until reaching a threshold value at which point the buildup discharges violently, called electrostatic discharge (ESD), and can potentially cause explosions or fire. This is of particular concern in the transportation and filtration of fuels since fuel is often dielectric and generates charge when passing through fuel pipes (Park et al., 2007). Static buildup is also unfavorable to polymer production in slurry reactors because of agglomeration. In addition to being dangerous, electrostatic buildup negatively impacts the hydrodynamics of fluidization as particles may adhere to the column (Revel et al., 2003). Since charge generation is also difficult to reproduce and is not constant, modeling fluidization hydrodynamics with CFD is difficult if charge generation is present. Some industries take advantage of static electrification, however, such as in the separation of binary mixtures and in dust removal (Guardiola et al., 1996).

Static charge buildup in the fluidization of insulating materials has been researched extensively and is related to the hydrodynamics of the bed. Boland et al. (1971) described this static buildup as being caused by gas bubbles and gas bubble velocity. As bubble size increases, the degree of electrification also increases because large bubbles rise more rapidly

than small bubbles (Boland et al., 1971). Key bed parameters that affect fluidization are the particle size and superficial gas velocity; increasing either will also increase the electrification in the bed (Guardiola et al., 1996).

Many different methods of reducing static electricity on fluidizing particles have been studied. Park et al. (2007) described two attempts to reduce charge generation; adding 15 wt% fine particles and adding 0.5 wt% of a liquid anti-static agent to a gas-solid-liquid fluidized bed. Fine particles increase the surface area of the bed and neutralize charges. Both methods were found to reduce the electrostatic charge; however the anti-static agent was more effective. The addition of an anti-static agent, Larostat (Quaternary ammonium compound) powder, was also successfully used in a study by Shen et al. (2007). Another common method to reduce electrostatic buildup is to increase the relative humidity in the fluidize bed. This technique was studied by Guardiola et al. (1996) and five distinct electrification zones were identified. Generally, the higher the relative humidity, the less electrostatic buildup; however, static buildup seems to be unaffected at very low or high levels of relative humidity. Additionally, at very high relative humidity levels, fluidization becomes impossible because water surrounds the hydrophilic particles, causing cohesion (Guardiola et al., 1996). In order to reduce the risk of affecting fluidization hydrodynamics by adding fines or humidifying the bed, Revel et al. (2003) used a supersonic ion injector to create an ionic cloud in the bed. This technique was found to have no significant effect in the bulk particles and was only effective on surface particles. Another common method to reduce static electricity buildup is to ground the fluidized bed. For example, Utikar et al. (2007) reduced static electricity by grounding a square reactor with a thick copper strip.

2.2 Biomass and Thermochemical Conversion

This section refers to biomass and thermochemical conversion of biomass into useful products such as fuel, chemicals, and polymers, or disposal of waste materials. In the first

subsection, a review of biomass is provided with a discussion regarding the advantages of biomass as a fuel. Fluidization of biomass is also explained and recent studies on biomass fluidization are described. The second subsection describes the three main thermochemical conversion processes that use biomass in gas-solid fluidized beds. Basics of combustion, fast pyrolysis, and gasification are explained and experimental examples and relevant statistics are cited. The goal of this section is to show the importance of biomass as a fuel with worldwide potential.

2.2.1 Biomass and Biomass Fluidization

Biomass typically refers to the material that comes from animal waste or from plant growth and is the basis for biorenewable energy production. Most biorenewable energy is produced from wood and wood waste (64%), however municipal solid waste (24%), agricultural waste (5%), and landfill gases (5%) are also significant sources of biomass fuel (Demirbas, 2007). Energy from biomass accounts for about 14% percent of the worldwide energy consumption; a significant portion is consumed in developing countries (35%), while only a minor portion is consumed in industrialized countries (3%) (Demirbas, 2007). Recently, biomass, especially switchgrass and corn, has gained public interest in the United States in hopes of reducing the reliance on fossil fuels for energy production, which represents over half of the oil used annually in the US (Mohan et al., 2006). Renewable energy from biomass is currently the most feasible form of renewable energy, recently surpassing hydropower (Mohan et al., 2006).

As a renewable resource, biomass may be continually grown to be used as fuel. Unlike fossil fuels, there is no limited reservoir to be depleted. In addition, planting biomass can reduce CO₂ in the atmosphere since organic matter consumes carbon dioxide and generates breathable oxygen. Alternatively, waste products can be effectively used to create energy instead of being thrown into a landfill. In rural areas, especially in developing countries,

planting biomass may stimulate the local economy. As a fuel, biomass has been shown to burn with fewer greenhouse gases than fossil fuels and is essentially CO₂ neutral (Demirbas, 2007; Gera et al., 2002; Asadullah et al., 2003). Highly volatile biomass also has potential to significantly reduce harmful NO_x to neutral N₂ when used for reburning in coal-fired boilers (McIlveen-Wright et al., 2006; Gera et al., 2002). Additionally, when compared against other renewable energies, biomass has a reasonable cost level. (Gera et al., 2002). As a fuel, biomass may be used in biological conversion, physical conversion, or thermal (thermochemical) conversion processes. Thermal conversion of biomass is of particular interest to this research because of its relationship to fluidized beds and relative simplicity. Biomass fluidization can be applied to most forms of thermal conversion and is beneficial since fluidized beds feature high heat transfer rates, uniform and controllable temperatures, and large surface areas; they can also accept a wide variety of particle shapes (Cui et al., 2007).

Before biomass is utilized in a fluidized bed, it typically goes through size reduction steps, such as grinding, to allow for proper material feed. Because grinding does not produce a homogenous size distribution with a uniform shape, there are considerable difficulties in fluidizing biomass independently. Therefore a fluidized bed of an inert material (sometimes called a catalyst), like sand or another insulating material, is used to improve fluidization and to act as a heat transfer medium (Cui et al., 2007; Rao et al., 2001). Rasul (1998) studied the fluidization of a sugar cane by-product, bagasse, in an FCC fluidized bed. Since bagasse has low density, high moisture content, and is very fibrous, it does not independently fluidize. It was determined that with an inert fluidizing FCC bed, bagasse can successfully fluidize and may be used for energy generation (Rasul, 1998). Since most biomass contains a wide variety of particle shapes, it is difficult to understand the fluidization hydrodynamics. Limited research, however, has been devoted to biomass fluidization (Cui et al., 2007).

Rao et al. (2001) studied fluidization of rice husk, sawdust, and groundnut shell powder in different sizes of sand and was able to generate correlations to satisfactorily predict U_{mf} based on the particle densities and sizes (Rao et al., 2001). Gera et al. (2002) used CFD to model the effects of biomass aspect ratio on cofiring coal and switchgrass. It was found that cylindrical shaped bio-particles were more suitable than spherical biomass because of higher combustion efficiency and less bottom ash (Gera et al., 2002). Sawdust, coal bottom ash, coconut shell, rice husk, and palm fiber were also fluidized in a study by Abdullah et al. (2003). The study showed that sawdust, coal ash, and coconut shell (Geldart B classification) have better fluidization than rice husk (Geldart D classification) or palm fiber (Geldart A classification). The main factors that contribute to fluidizing quality were found to be bulk density and voidage; larger bulk density and smaller void fraction enhances fluidization quality (Abdullah et al., 2003).

To improve process efficiency it is important to understand the mixing and segregation behavior of biomass injection into a fluidized bed. Shen et al. (2007) simulated a biomass/sand system by injecting red wooden balls into a fluidizing bed of glass beads. By using a digital image-processing-based technique, it was found that the simulated biomass particles tend to move faster vertically than laterally; consequently, the vertical convection was much higher than the lateral convection. Also, as superficial gas velocity increased, the surface biomass concentration increased and the time required to reach steady state decreased. In their study, it was assumed that the probes used for measurements and the injection system had no effect on biomass mixing patterns (Shen et al. 2007). Glicksman et al. (2008) also studied the mixing characteristics of particle injection in a fluidized bed. A thermal tracing technique monitored cryogenically cooled balls as they were injected into a one-quarter scale pressurized bubbling fluidized bed combustor. The study found that the high initial jet momentum caused particles to travel large horizontal distances and some

particles were drawn upwards due to bubble wakes. It was concluded that further research needs to investigate the injector geometry.

2.2.2 Thermochemical Conversion of Biomass Fuels

Three main gas-solid fluidization reactions exist to convert biomass to usable forms of energy in three different phases; combustion uses biomass as a solid fuel, fast pyrolysis creates a liquid fuel, and gasification creates a gaseous fuel. Each process is described in the following three subsections.

2.2.2.1 Combustion

Combustion is one of the oldest forms of energy generation. Biomass undergoes a reaction in which carbon oxidizes into carbon dioxide, hydrogen oxidizes into water, and energy is produced in the form of heat. Generally this energy is used to heat homes, cook food, or boil water to run turbines for electricity production. It is estimated that combustion accounts for over 97% of all bio-energy production (Demirbas, 2007). Many developing countries rely almost exclusively on the combustion of biomass for their energy needs since it is the most readily available energy form. Combustion is also the least efficient method of converting biomass to energy; however, it still produces fewer greenhouse gasses than fossil fuel combustion (McIlveen-Wright et al., 2006). Combustion of biomass can be performed in fluidized beds to improve combustion efficiency by 96-98% and improve the heat transfer rate by 60-80 times (Abdullah et al., 2003). Also, due to lower operating temperatures, fluidized combustors reduce greenhouse gas emissions; both NO and SO₂ emissions are significantly reduced (Glicksman et al., 2008). Additionally, waste incineration in fluidized beds is an environmentally friendly alternative to landfills, while producing useful energy. Hernandez-Atonal et al. (2007) studied the combustion of three types of refuse-derived fuel (RDF) in two different atmospheric fluidized bed reactors. High calorific RDF pellets were

produced from municipal waste and incinerated. It was found that only 2.6% to 4.3% of the fuel's nitrogen was converted to NO_x which was lower than expected (Hernandez-Atonal et al., 2007).

2.2.2.2 Fast Pyrolysis

Unlike conventional pyrolysis which usually produces charcoal, fast pyrolysis has recently become a feasible method of converting biomass into a liquid fuel, and is extensively outlined by Bridgwater et al. (2000) and Mohan et al. (2006). Fast pyrolysis occurs under high temperatures when biomass is quickly heated without air and vaporizes through pyrolysis (Bridgwater et al., 2000). Matter undergoes six general changes in pyrolytic reactions; (i) fuel is heated by a heat source, (ii) primary pyrolysis occurs which releases volatiles and forms char, (iii) hot volatiles flow towards cooler solids and heat is transferred between volatiles and the unpyrolyzed fuel, (iv) some volatiles condense and undergo a secondary reaction to produce tars, (v) secondary and primary pyrolytic reactions compete simultaneously, and (vi) the products may reform to produce water gas reactions or radical recombination (Mohan et al., 2006). In fast pyrolysis, pyrolyzed vapor is rapidly cooled via a quenching process and a liquid fuel condensate forms. According to Bridgwater (2003), there are four essential features required for fast pyrolysis; (i) high heat transfer rates requiring fine biomass particles, (ii) controlled temperatures around 500°C , (iii) short gas time of less than 2 seconds, and (iv) rapid cooling of the gases to produce liquid fuel. The liquid fuel, called bio-oil, may be extracted and transported or burned for heat (Bridgwater et al., 2000).

Typical fast pyrolysis systems include feed driers to reduce biomass moisture, grinders to decrease particle size, a fluidized bed reactor where biomass is injected, a cyclone to capture char and ash, and a cooling chamber or condenser which is responsible for converting hot pyrolysis vapors into bio-oil. Waste heat from the process can be reused for the feed dryer,

preheating fluids, and for pyrolysis. Cooling time is of particular interest to system design; if cooling is not performed correctly, bio-oil becomes unstable and inefficient. Generally, cooling consists of quenching the gas with a cooled liquid and then filtering the liquid to produce fuel. Bio-oil (17 MJ/kg) has less than half the heating value as conventional fossil fuel oil (42-44 MJ/kg) and is not economically viable for upgrade into transportation fuels. However, this oil can be directly combusted as a fuel source or can be used as fuel in specially modified engines or gas turbines. Bio-oil is also used in the production of chemicals like food flavoring (liquid smoke), fertilizers, resins, and agricultural chemicals. The main advantage fast pyrolysis has over gasification and combustion is that liquid fuel simplifies transportation and storage, especially in locations far from the production unit (Bridgwater et al., 2000).

2.2.2.3 Gasification

Despite advances in combustion and fast pyrolysis, interest in thermochemical conversion of biofuels has focused on gasification because of its high efficiency compared to combustion, and because fast pyrolysis is still in preliminary stages of development (Bridgwater, 2003). In gasification, biomass is converted into a gaseous hydrocarbon fuel containing CO, CO₂, hydrogen and methane through three different methods: steam gasification, pyrolytic gasification, or partial oxidation (Bridgwater, 2003). In each case biomass is injected into the high temperature gasifier where moisture is evaporated, and then undergoes pyrolysis to produce vapors, tars and oils, and a solid substance called char. The pyrolysis reaction (not to be confused with the fast pyrolysis thermochemical conversion process) is the rate controlling step in the reaction and occurs before gasification. Next, gasification or oxidation occurs on the pyrolyzed tars, char, and gases to create gaseous fuel (Bridgwater, 2003; Grace et al., 2006). The gaseous fuel is called producer gas or, upon contaminant removal, synthesis gas (syngas), and can be used directly as fuel or to create

substances like methanol, dimethyl ether, Fischer-Tropsch oils or other chemicals (Rao et al., 2001; Asadullah et al., 2003).

The main difficulty in gasification is the production of tars and char, which are detrimental to power systems and to catalytic conversion processes (Asadullah et al., 2003). To break down tars and speed up the reaction, a catalyst (catalytic cracking) or oxidation (thermal cracking) method can be employed. Asadullah et al. (2003) examined the effects of adding a Rh/CeO₂/SiO₂ (60) catalyst to cedar wood gasification. Using this catalyst, about 98 to 99% of the carbon in the biomass was converted to biofuel gas.

Because biofuel gas is expensive to transport and store, gasifiers are commonly connected directly to power cycles which can have efficiencies up to 97% (hot gas) or 85% (cold gas) (Bridgwater, 2003). Overall system efficiencies can reach 50% for large units, decreasing to 35% for small units (Bridgwater, 2003). Wu et al. (2002) performed an economic analysis on a gasifier in China and found gasification to be an economically viable means of power production with current biomass prices and plant capacity. The 1 MW scale CFB biomass gasifier was found to have only 60-70% of the capital cost and a much lower operational cost than a similar capacity coal plant. It was also found that gasification is only attractive when the plant produces at least 160 kW and biomass costs less than 200 Yuan RMB/ton (Wu et al., 2002). Gasifiers can also be directly coupled to ethanol plants to provide the distillation energy necessary for ethanol production. This technique can produce biorenewable fuel capable of direct implementation into the transportation industry, without the use of fossil fuel sources.

In addition to gasifying 100% biomass, it is possible to gasify a combination of biomass and other fuels. McIlveen-Wright et al. (2006) describe the cofiring of coal, biomass, and waste plastics in a gasifier. Using a 20% biomass and 80% coal mixture, it was found that the gasification efficiency, CO₂ emissions, and capital costs were not significantly affected. The study concluded that co-firing with biomass or plastic is a valuable method of obtaining

useful energy out of waste products without major modifications to the power production system (McIlveen-Wright et al., 2006).

2.3 Noninvasive Multiphase Flow Visualization

This section describes methods in visualizing opaque multiphase flows with an emphasis on noninvasive X-ray techniques including computed tomography, radiography, stereography, and particle tracking velocimetry (PTV). The first subsection contains information about common noninvasive techniques used for monitoring various multiphase flows. Examples of these methods relating to fluidized beds are provided. The second subsection explains basic X-ray techniques including, X-ray computed tomography, X-ray radiography, and X-ray stereography/particle tracking velocimetry. The basics of each method are explained and examples are provided with an emphasis on fluidized bed visualization. The section aims to show the importance of X-ray techniques in visualizing fluidized beds.

2.3.1 Noninvasive Techniques

Because of the difficulty in visualizing opaque fluid flows such as in fluidized beds and bubble columns, noninvasive methods have been established that attempt to gather all information within a flow field without disturbing the system hydrodynamics (Kumar et al., 1997; Boyer et al., 2002; Bhusarapu et al., 2006). Invasive methods, such as the optical probe method described by Zhu et al. (2007), have also been applied to multiphase flows; however, these methods can potentially affect fluidization hydrodynamics and will not be discussed here. Chaouki et al. (1997) and Boyer et al. (2002) give extensive overviews of commonly used noninvasive techniques as well as recent advances in visualizing multiphase flows. Noninvasive techniques are generally categorized as either tomography/radiography, which provides the concentration, holdup or density distributions through a multiphase flow, or as

velocimetry which provides dynamic features like the flow pattern and velocity field. Tomographic and radiographic techniques include nuclear based techniques like gamma computed (densitometry) tomography (GDT), X-ray computed (transmission) tomography (XCT), X-ray radiography/stereography, neutron transmission tomography and radiography, positron emission tomography (PET), and X-ray diffraction tomography (XDT), nuclear magnetic resonance imaging (MRI or NMRI), and non-nuclear based techniques like electrical capacitance tomography (ECT), optical tomography, and ultrasonic tomography. Conversely, positron emission particle tracking (PEPT), radioactive particle tracking (CARPT or RPT), cinematography, laser Doppler anemometry (LDA), and particle image velocimetry (PIV or PTV) are forms of velocimetry (Chaouki et al., 1997; Boyer et al., 2002).

Despite the variety of visualization techniques, only a few are suitable for fluidized bed systems. Halow (1997) provides a thorough overview of electrical capacitance tomography (ECT), a form of electrical impedance tomography (EIT), applied to fluidized bed systems. In ECT, probes are placed around an object and voltage is applied to energize the system. Charge accumulates and an electric current, which is affected by the bed hydrodynamics, can be measured between the probes. In fluidized beds, if there is adequate contrast between material (phase) impedances, the local material distribution can be calculated using a mixture model (Tortora et al., 2006). Even though ECT has limited resolution compared with other visualization techniques, it is beneficial in high-speed applications since over 200 frames per second can be collected. ECT is also advantageous over other noninvasive methods because the hardware is relatively inexpensive, and is suitable for both small and large systems (Du et al., 2005). In addition, since no nuclear radiation is employed, electrical methods are much safer than X-ray or gamma ray techniques. A drawback to ECT is that image reconstruction accuracy is critical and involves complicated algorithms. Halow (1997) shows how ECT has been effectively used in fluidized beds to visualize features such as bubble coalescence, gas

holdup, bubble diameter and length, rise velocity, voids occurring near U_{mf} , and emulsion phase expansion.

Du et al. (2005) successfully used ECT to investigate three FCC fluidized beds, with 0.05 m, 0.1 m, and 0.3 m diameters. The ECT system had temporal resolution of 100 frames per second and spatial resolution up to 3% of the cross-sectional area. The study found that the two largest beds showed spiral bubble motion in the bubbling regime and did not exhibit slugging behavior as in the smallest bed. ECT showed the average solids concentration in the turbulent regime to be radially symmetrical. ECT also found that the standard deviation of solids concentration fluctuations peaked at U_c in the largest bed. The ECT data was verified with an intrusive optical probe technique (Du et al., 2005).

Gamma densitometry tomography (GDT) is another powerful noninvasive visualization method and is considered mature and reliable compared with other techniques (Bhusarapu et al., 2006). GDT is nearly identical to XCT with the exception that ionizing energy is generated by gamma-rays instead of X-rays. An advantage of GDT over XCT is its ability to penetrate dense flows as well as flow system pipes and containers; however, X-ray energy is much easier to control than gamma-rays and can provide better spatial resolution (Bhusarapu et al., 2006). XCT will be explained in depth in section 2.3.2.1. GDT in fluidized beds has been compared to less reliable techniques like EIT, notably in the study by Tortora et al. (2006). The study employed a GDT system consisting of 8 NaI(Tl) detectors and a Cs-137 gamma radiation source to find local solids distributions in a 0.14 m diameter CFB of FCC. Similarly, a 16 electrode EIT system generated impedance profiles which were converted into solids distributions using a Rayleigh mixture model. The resulting EIT and GDT solids distributions were found to correspond well; however, EIT slightly over-predicted the solids volume fractions by up to 0.03. Tortora et al. (2006) concluded that when possible, EIT can be used instead of GDT since it is safer, faster, and less costly.

GDT has also been compared to computer automated radioactive particle tracking (CARPT) by Bhusarapu et al. (2006). The study applied both techniques to glass bead fluidization in a 15.2 cm (6 in) diameter CFB. The purpose of the study was to generate relevant data for improved phenomenological models and to examine the effectiveness of GDT and CARPT in calculating solids holdup. In CARPT, the motion of a single radioactive tracer particle marking the solid phase is tracked, and a complete Lagrangian description of the solids flow is generated. This technique is beneficial since almost no data is available that shows 3-D particle trajectories and velocities. Additionally, CARPT allows tracer particles to be identical in diameter and density to the fluidizing particles. This study used tracer particles made of radioactive ^{46}Sc coated polymers with similar size and density to the fluidizing glass beads. Twenty NaI(Tl) scintillation detectors were positioned around the CFB to monitor the tracer location. The resulting data tracked the tracer particles with less than 5 mm error. The GDT system had a spatial resolution of 2 mm and consisted of a gamma-ray emitting source and 7 detectors spanning the fan beam. The study found that through the use of GDT and CARPT, a large amount of empirical information was collected. CARPT identified occasional down flow of solids in the core region in the fast fluidization regime. The solids flow was found to be nearly axis-symmetric for the CFB. Additionally, the holdup profiles generated by CARPT and GDT were found to match well (Bhusarapu et al., 2006).

Other particle tracking methods have also been applied to fluidized beds. Stein et al. (1997) reported experiments using positron emission particle tracking (PEPT) in fluidized beds of Geldart type D sand with 2 mm diameter ^{18}F -silica tracers. PEPT tracks single radioactive tracer particles that constantly emit gamma rays, providing information about solids mixing and bubble interactions. The technique may also be useful for investigating particle attrition, scale-up laws, defluidization, and segregation. Stein et al. (1997) concluded that while PEPT is a fast and effective measurement technique, improvements must be made in finding the tracer particles in order to apply PEPT to CFBs.

Müller et al. (2007) applied ultra-fast magnetic resonance imaging to a fluidizing bed of Geldart type B and D seeds in order to study the rise velocities of bubbles and slugs. MRI was successful in calculating rise velocities of axis-symmetric and square-nosed slugs, determining zones of fluidization, evaluating bubble acceleration, and observing bubble coalescence. The study concluded that because of its excellent temporal and spatial resolution, MRI is a powerful noninvasive technique for studying 3-D features of fluidized beds (Müller et al., 2007).

2.3.2 X-Ray Techniques

X-rays are commonly employed in noninvasive techniques because they are safer than other nuclear based techniques which cannot be turned on and off at will, have high resolution, and can be controlled by varying voltage or current to improve penetration or contrast (Chaouki et al., 1997). X-rays are forms of ionizing electromagnetic radiation created by the rapid deceleration of high speed electrons. A large voltage is maintained across X-ray tube electrodes to accelerate electrons towards a target material; upon impact of the electrons, the target ejects additional electrons and is simultaneously ionized. Most of the generated energy is in the form of heat, but a small portion of the collisions produce X-rays. The X-ray spectrum consists of a continuous portion (bremsstrahlung) created by electrons losing energy when passing an atom's nucleus, and a characteristic section, created by high-speed electrons ejecting inner shell electrons from an atom to produce give off distinct energy wavelengths (Pederson, 2005; Hokel 1996). Common X-ray source target materials are tungsten or molybdenum and have relatively low characteristic energy; consequently these may not be suitable for imaging through materials requiring higher penetration (Chaouki et al., 1997).

X-ray attenuation by a material is due to photoelectric absorption, Compton scattering, and pair production. In photoelectric absorption, all energy from an incident X-ray photon is

transmitted to an atom's internal electrons, which are subsequently ejected. Compton scattering occurs with higher energy X-rays when incident photons interact with outer shell electrons. Like photoelectric absorption, the electrons are ejected; however, photons are also deflected in different directions with a reduction in energy. Pair production takes place as photons interact with a nucleus to create a positron-electron coupled pair with increased kinetic energy (Ketcham et al., 2001; Grassler et al., 2000). Since X-ray absorption is inversely proportion to one-third the X-ray energy, it is important to modify the energy for each system according to that system's characteristics (Chaouki et al., 1997). High energy X-rays penetrate farther than low energy X-rays but reduce the ability to distinguish changes in density and composition. Other variables determining the source effectiveness include the focal spot size which influences spatial resolution, the energy spectrum which affects X-ray penetration power, and the X-ray intensity which affects the signal-to-noise ratio and image clarity (Ketcham et al., 2001).

2.3.2.1 X-Ray Computed Tomography

X-ray transmission tomography involves the transmission of X-rays through a medium at several angular projections to create a 2-D or 3-D "map" of the reconstructed absorption coefficients. This type of tomography, usually referred to as X-ray computed tomography (XCT or CT), is typically automated and reconstructed by a computer. In computed tomography, a theoretically monoenergetic beam of radiation following a linear path is attenuated by an object via absorption and scattering. The attenuation of radiation is controlled by the Beer-Lambert law which is an exponential function of the incident radiation, linear attenuation coefficient, and path length. A detector captures the projected attenuation information which is an integral sum of the local attenuation coefficients along the beam path. Because these attenuation coefficients vary along the radiation path, multiple scans at different angles must be performed in order to find local attenuation information in

the 3-D object. Multiple scans necessarily cause data to be time-averaged with the effect that XCT images have poor temporal resolution; however, more data is obtained with multiple scans contributing to the high spatial resolution of XCT (Kumar et al., 1997). Since density is directly related to attenuation, XCT data can be converted into a material distribution, most often in the form of gas or solids holdup (Tortora et al., 2006). Hence, XCT is an effective tool in finding the time-averaged local gas holdup distribution within a multiphase flow.

Computed tomography requires two main components; X-ray emitting sources and camera/detector pairs to capture attenuation information. Ionization chamber and scintillation type detectors are the two main categories of detectors. In ionization chamber detectors, sensors react to the ionization produced by X-rays. Scintillator detectors are most common in XCT and rely on excitation of scintillation crystals to produce a voltage which is amplified by a photocathode and photomultiplier. Scintillation screens are often made of thallium activated sodium iodide crystals because of its high conversion efficiency and slow decay time (Kumar et al., 1997).

Four source-detector configurations have been described in the literature. First generation scanning uses a pencil-sized radiation beam to penetrate an object and is the slowest form of tomography. A coupled detector-source pair travel across an object in various steps to obtain one “view”, and then are rotated to obtain another view at a different orientation. In second generation scanning, an array of detectors is placed opposite the radiation source and multiple views can be obtained simultaneously. Third generation scanning employs a collimated fan beam to capture an entire 2-D attenuation map of an object. The source-detector combination rotates around the imaging region after each projection is captured. Fourth generation scanning requires a fixed ring of detectors with a fan beam source that rotates around the imaging region. Once attenuation data has been collected it must be reconstructed into a 2-D or 3-D image. Typically, reconstruction is done through a filtered

back projection or convolution back projection algorithm (Chaouki et al., 1997; Ketcham et al., 2001).

XCT is particularly useful in visualizing fluidized beds, and can provide a three dimensional time-averaged density map of the flow structure. As discussed earlier, it is possible to calculate time-averaged local gas holdup data (or inversely the solids holdup) from CT data. This method has been applied to fluidized beds in the literature but the technology is still under development. Grassler et al. (2000) developed a third generation XCT system to measure local solids concentration in a 0.19 m diameter CFB of 50-70 μm diameter glass beads. It was determined that XCT has many advantages over capacitance probes, optical probes, and EIT because it does not affect the flow structure, is applicable at high temperatures, and can tolerate static electricity buildup. The study also showed that the solids concentration was accurately calculated within 5% error for concentrations up to 20 vol% with a minimum resolution of 0.2 mm (Grassler et al., 2000).

Kantzas et al. (1997) used computed tomography to quantify channeling in a fluidized bed of polyethylene resin at various heights and superficial gas velocities. The study illustrated the usefulness of XCT as a tool in determining gas holdup, especially in high-voidage channels. XCT showed that channeling occurred in the fluidized resin bed and exhibited a variety of characteristics with only slight differences in operating conditions. The study noted the importance of bed uniformity in fluidization modeling, which may not exist experimentally (Kantzas et al., 1997).

Similarly, Wu et al. (2007) employed XCT to characterize the fluidization of polyethylene resins in three fluidized beds, with diameters of 10 cm, 20 cm, and 30 cm. Both gas holdup and bubble properties were extracted from the CT data. The study found that the average voidage in the 10 cm column was larger than in the other columns, potentially because of a strong slugging effect. The CTs allowed calculation of time-averaged voidage distributions, bubble area fractions, average bubble diameters, and bubble number at given

heights throughout the beds. Bubble information was time-averaged due to the 2 second measurement time, and was validated with pressure fluctuation measurements. The study also illustrated that fluidization hydrodynamics can be significantly affected by bed scale.

Franka et al. (2007) used CT capabilities in Iowa State University's XFloViz facility to image fluidized beds of glass beads, ground walnut shell, ground corncob, and melamine plastic with various flow conditions. While the local gas holdup was not calculated for the beds, time-averaged flow structures were captured for each bed at three flow conditions and qualitative comparisons were made. The CT imaging showed glass bead beds fluidized uniformly; however, channeling was observed in the lower density materials. CTs revealed that increasing superficial gas velocity increased the fluidization uniformity. In addition, CTs showed that the bottom edges of the corncob beds did not fluidize at low superficial gas velocities, but instead remained stagnant.

Other multiphase experiments have utilized XCT to examine gas holdup, such as in the research done by Toye et al. (1998). This study successfully used a third generation CT scanner to determine gas holdup in a packed column of polypropylene rings filled with water. The calculated global void fraction was within $\pm 0.2\%$ of the specifications given by the manufacturer (Toye et al., 1998).

2.3.2.2 X-Ray Radiography

X-ray radiography, also known as fluoroscopy, records the integral X-ray attenuation through an object to create two dimensional images of a three dimensional object (Hubers et al., 2005). Radiography is similar to XCT with the exception of detector type (Chaouki et al., 1997). Instead of using scintillating screens to capture data, detectors consist of sheets of film or an image intensifier coupled to a camera. Individual images can be recorded using a cine camera or video recorder or, more recently, can be directly digitized and sent to a computer (Chaouki et al., 1997; Heindel et al., 2008). The improvement of computer aided acquisition

has increased the popularity of radiography since large amounts of data can be captured and compiled with little effort (Heindel et al., 2005). Since multi-directional scanning is unnecessary, data may be collected as quickly as the information can be digitized and stored. Consequently, radiography has good temporal resolution while maintaining average spatial resolution compared to XCT (Heindel et al., 2008).

X-ray radiography has been widely used for imaging fluidized beds in the literature. Van Dijk et al. (1998) studied the effects of baffles on fluidization bubbles with X-ray radiography. The X-ray system included a conical X-ray source, an image intensifier with a phosphor photographic screen, a CCD camera with up to 25 fps, and an S-VHS video camera to capture the radiographic movies. For single bubble experiments, soda-lime glass beads were placed above higher X-ray attenuating lead-glass ballotini in order to isolate individual bubbles. By studying the radiographic movies, it was found that baffles did not significantly affect mean bubble size or bubble rise velocity (Van Dijk et al., 1998).

Similarly, Hulme et al. (2004) tracked individual bubbles with X-ray fluoroscopy to investigate bubble diameters and velocities in fluidized beds of polyethylene and glass. Images were captured at 30 fps for 2 minutes and stored in a computer where image processing was performed. In-house software applied image corrections and determined bubble boundaries. It was found that bubble properties observed on the radiographs matched those provided by correlations from the literature. The study also noted that the radiographic technique provided good resolution ($0.1 \text{ mm} \times 0.1 \text{ mm}$) but improved contrast is necessary between the bubbles and bed material in order to more accurately view internal hydrodynamics (Hulme et al., 2004). Newton et al. (2001) described X-ray radiography, performed by BP (British Petroleum), to visualize large scale fluidized beds for gas phase polyethylene fluid-bed processes, FCC technology, and acrylonitrile and vinyl acetate processes. The study concluded that X-ray imaging of large scale fluidization units is a

reliable technique for accessing equipment design and scale-up of literature correlations should be used with care (Newton et al., 2001).

In addition to utilizing CT, the previously mentioned study by Franka et al. (2007) used radiographic imaging to visualize fluidized beds of four different materials with various flow conditions. A 30 second movie was subsequently created at 20 fps to show the dynamic features of each bed. The radiographic movies validated the CT results that glass beads fluidized most uniformly while channeling occurred in the less-dense melamine, walnut shell, and corncob beds. Additionally, the radiographs showed the difficulties in resolving internal features of the glass bead fluidization without saturating the edges of the image.

2.3.2.3 X-Ray Stereography/Particle Tracking Velocimetry

Multiple third generation source-detector pairs can be configured to allow imaging in multiple projections, creating stereographic images. If images are acquired simultaneously, stereography allows the location of dynamic 3-D features to be calculated from 2-D projections (Heindel et al., 2005; Heindel et al., 2008). To improve accuracy, markers can be implemented for a reference coordinate system (Heindel et al., 2005). X-ray stereography has also given rise to X-ray particle tracking velocimetry (XPTV), a type of particle image velocimetry (PIV). In XPTV, the fluid is seeded with X-ray absorbing particles with similar density to the fluid. Stereographic images are recorded and fluid velocity is calculated by monitoring the movement of the tracer particles (Seeger et al., 2001). Since two projections are imaged simultaneously, three dimensional velocity profiles can be generated. Velocity profiles are calculated using an algorithm consisting of three steps; particle recognition, particle tracking in two dimensions, and three-dimensional reconstruction (Kertzscher et al., 2004). XPTV has several advantages over other methods like CARPT and optically based particle tracking methods; no light reflection or refraction occurs at the phase boundaries, a complete three dimensional velocity profile is generated, opaque flows may be visualized,

intrusive probes are unnecessary, and multiple locations can be monitored independently (Seeger et al., 2001; Kertzscher et al., 2004).

Seeger et al. (2001) developed XPTV equipment and particle tracking algorithms for use in a bubble column. The equipment included image intensifiers, CCD-cameras, and 8-bit frame grabbers which captured 512×512 pixel images at 25 fps. The neutrally buoyant tracer particles were cubes of polyurethane foam with cylindrical lead inserts. In the tracking portion of the algorithm, pixel intensity values were compared with an average surrounding intensity value. If the pixel intensity was significantly larger than the surroundings, it was compared to successive pixel values. When successive pixel intensities were larger than a certain threshold value, between 10 and 45 pixels², the region was identified as a particle. Once particles were recognized, the motion of each was tracked. By investigating the location of a particle in two preceding frames, and by assuming the travel of the particle was approximately linear within the small time frame, a search area was generated to determine the new particle location. 3-D velocity profiles were calculated using the data from tracking the same particle in two projections. The study successfully tracked 96-98% of the particles; however, some limitations were found including the difficulty in tracking particles which approached other particles and insufficient time resolution (Seeger et al., 2001). The algorithms developed by Seeger et al. (2001) were later updated by Kertzscher et al. (2004) because the original software was later found to accurately reconstruct only 48-62% of the seeded particles. Improvements in the 3-D reconstruction and an isocenter correction increased the particle tracking accuracy to 69-76%. The study also concluded that large amounts of particles with high image acquisition frequency must be used to improve the accuracy of XPTV (Kertzscher et al., 2004).

Particle tracking also has implications in tracking materials of different density than the bulk media, such as biomass or biomass-like particles. Bruni et al. (2002) used a particle tracking method to monitor biomass particles injected into a fluidized bed reactor. Individual

particles of ligneous biomass, doped with lead nitrate by impregnation, were injected into a bed of sand or FCC, fluidized with nitrogen gas, and monitored with a radiographic X-ray system. The reactor was heated with ceramic heaters to devolatilize the biomass particles. The study noted difficulties in doping the biomass; doped particles were significantly heavier than the raw material, and the lead nitrate decomposed at 470°C, which affected attenuation characteristics. Using X-ray tracking techniques, the study found that 4 mm diameter biomass particles self-segregate in the bed quickly (less than 1 second) but the behavior was difficult to reproduce.

2.4 Relating CFD to Multiphase Flows

Section 2.4 briefly explains fluidized bed simulation using computational fluid dynamics (CFD) models, and the importance of generating high-quality, reliable experimental data for validation. The first subsection explains the benefits of simulating multiphase flows with CFD. It also lists issues that must be overcome to improve the viability of CFD simulations. The next subsection describes specific examples of fluidized bed CFD modeling. This section attempts to tie together previous sections by explaining the importance of noninvasive techniques on the fluidization of biomass/catalyst beds to validate CFD simulations.

2.4.1 CFD and Multiphase Flows

Many studies have explained the importance of modeling multiphase flow systems in order to improve process efficiencies and to better understand fluidization hydrodynamics (Boyer et al., 2002; Cui et al., 2007; Dudukovic, 2002; Kantzas et al., 1997; Kertzscher et al., 2004; Hulme et al., 2004; Toye et al., 1998; Wu et al., 2007). Computational fluid dynamics has become one of the most important tools for flow modeling, and is almost always coupled with an experiment for model validation. For example, Wang et al. (2008) applied ECT

imaging to a fluidized bed drying process and used the results to validate a FLUENT CFD simulation and a mathematical model. Both the simulation and the mathematical model were found to adequately describe the heat and mass transfer within the dryer. It was also noted that CFD simulations are extremely complex and are only effectively used in process optimization.

Joshi et al. (2003) provides an overview of the current status of CFD, some examples of CFD multiphase flow models, and improvements that still must be made. According to the study, Eulerian CFD models have been applied to various multiphase systems to aid in system design (i.e., distributor design), and to simulate flow regimes, minimum fluidization velocity, system sensitivity to hardware change, distribution of dispersed phase and interfacial area, mass and heat transfer, continuous phase entrainment, and model scale-up. Some problems that must be addressed include difficulties with grid independent solutions, obstacles in creating system-specific codes, lack of experimental data to validate simulations, and limitations due to phase changes, agglomeration/coalescence, and turbulence generated by dispersed particles. At present it is impractical to create an all-encompassing CFD model for complex process equipment (Joshi et al., 2003).

2.4.2 CFD and Fluidized Beds

CFD relating to fluidized beds has recently been the subject for numerous studies. Scale-up is one of the main difficulties in simulating fluidized beds since wall effects become more pronounced with decreased bed diameter, and because initial predictions of the complex hydrodynamics are difficult and are not completely accurate (Bhusarapu et al., 2006; Van Ommen et al., 2006; Wu et al., 2007). Van Ommen et al. (2006) applied CFD simulations to 15 and 30 cm diameter fluidized beds to investigate scaling problems associated with fluidized beds. Three sets of dimensionless parameters were applied to the simulation and are outlined in the paper; a simplified set, a full set, and an extended full set. The study showed

that scaling of average bubble size as a function of height was consistent regardless of the parameter sets used. It was also found that the extended set more accurately scaled voidage, especially at low velocities. Interestingly, the simplified parameter set simulated fluidization more accurately than the full parameter set. Despite the successes of the simulation, it was concluded that scaling laws remained insufficient to describe scale-up of fluidized beds (Van Ommen et al., 2006).

A CFD model was developed by Bradnani et al. (2006) in an attempt to predict transition between homogeneous and bubbling fluidized beds. The simulation results successfully predicted minimum bubbling velocity when compared to experimental fluidized beds of Geldart type A alumina powder and Geldart type B sand (Bradnani et al., 2006). Peirano et al. (2002) examined effects of the air inlet on a fluidized bed using a CFD model. Since bubble pressure fluctuations at the bottom of the bed gave rise to nonuniform spatial effects at the distributor, the plenum was included in the computational domain and the inlet air boundary conditions occurred at the entrance to the plenum. It was discovered that for high pressure drops across the distributor, the CFD simulation correlated well with the experiments. For low pressure drops across the distributor, results were mostly qualitative and not reproducible. The study concluded that with low pressure drops across the distributor, both distributor and plenum should be included in the model as a coupled effect.

Deza et al. (2007) modeled the fluidized beds described by Franka et al. (2007) using MFIX CFD software. The CFD simulations were generated for beds of glass beads and ground walnut shell, with inlet air velocities of $U_g = 1.3U_{mf}$. The glass bead bed was considered as a benchmark case since fluidization characteristics of glass beads were well-known. A parametric study was subsequently performed on the walnut shell bed to find unknown input parameters such as the coefficient of restitution and particle sphericity. The CFD simulations were successfully validated by the experimental CT and radiography data; gas holdup maps were qualitatively compared to CT data while the dynamic responses of the

bed were compared to radiographic movies. The simulation was found to accurately predict bed height expansion and bubbling hydrodynamics.

2.5 Summary

This Chapter discussed four major topics related to the following work. In section 2.1, fluidization was examined and related to current research. The section described fluidized beds, fluidization regimes, the four types of gas-solid reactions, bubbling, the importance of the minimum fluidization velocity, bed material parameters like Geldart's classification and PSDs, and static electricity buildup. Section 2.2 considered biomass and thermochemical conversion. First, biomass was described with details on its fluidization, followed by the three key methods of converting biomass into useful energy using fluidization technology; (i) combustion, (ii) fast pyrolysis, and (iii) gasification. Next, section 2.3 described the problems in visualizing multiphase flows and explained the importance of noninvasive measurement techniques. Current research on various noninvasive methods relating to fluidized beds was examined. The remainder of the section focused on the X-ray techniques used in this study, XCT, radiography, and stereography/particle tracking velocimetry. Finally, section 2.4 described the importance of CFD in improving the efficiency and scale-up of multiphase flows with an emphasis on fluidized beds. This background is helpful in understanding the following work.

The literature has shown that while there has been much research done on fluidization and fluidization behavior, the hydrodynamics are extremely complex and not well understood. A deficiency described in the literature is the limited knowledge on biomass fluidization; most studies concentrate on fluidization of highly idealized glass or sand particles. CFD simulations can be used as a tool to better understand fluidization hydrodynamics and can improve process efficiency and yields. Additionally, work is being done to improve CFD scale-up of fluidized beds, allowing smaller, less expensive bed

models to be created as prototypes. Unfortunately, many CFD input parameters are empirical and the literature has described a need for relevant, high-quality experimental data for use in validation. Additionally, little is known about the effects of air injection with biomass in gasification systems. Experimental data is difficult to obtain in fluidized beds since the flow is generally opaque. Nonintrusive methods provide the best opportunity for monitoring multiphase flows, since invasive monitoring methods can influence the internal flow, thereby reducing measurement reliability. X-ray techniques are particularly useful since X-ray energy can be controlled, and because high temporal and spatial resolutions are possible; however, X-ray techniques are not often applied towards fluidized beds.

The goal of this research is to generate high quality experimental data through noninvasive X-ray techniques, in order to evaluate the effects of bed material, side air injection, and superficial gas velocity on fluidization behavior. It is also desired to understand the behavior of biomass as it is injection into a fluidized bed. The results from this research will assist in validating a concurrently developed CFD model that accounts for bed material and flow conditions, and will be used to improve the efficiency of biomass gasification.

Chapter 3: Experimental Setup

The purpose of Chapter 3 is to provide a basic understanding of the experimental equipment, setup, and methods used in the subsequent research. Section 3.1 describes the design and development of the fluidized bed equipment including the fluidized bed reactor, the tracer particles and tracer particle injection system, the compressed air system, and the pressure and flow instrumentation. Next, section 3.2 describes the method of selecting the bed materials with an emphasis on the bed selection criteria and the bed preparation method. Next, section 3.3 explains the method of calculating the minimum fluidization velocity for various bed materials, and the flow conditions used for the main experiments in this research. Iowa State University's XFloViz facility is described in section 3.4 with details about the X-ray equipment and important X-ray parameters. Section 3.5 presents the CT data collection method, required CT calibrations, and how gas holdup is calculated from CT volumetric images. Finally, section 3.6 examines the radiographic/stereographic data collection method, explains the important calibrations that are needed for the radiographic/stereographic images, and describes a coloring technique used on some radiographic/stereographic images to enhance internal features. In addition, section 3.6 outlines the particle tracking method employed in the study.

3.1 System Design

Section 3.1 describes the main fluidization equipment developed for this research including the fluidized bed reactor, the particle injection system, the air flow system, and the instrumentation used to measure pressure and flow rates. The first subsection explains the cold-flow fluidized bed reactor designed and built for this research. The next subsection describes the tracer particles used in this study and the development of the tracer particle injection system used to inject the tracers into the fluidized bed. Since compressed air is the

fluidizing media and controls particle injection, a discussion of the air flow system is presented in the third subsection. The last subsection contains information about the pressure and flow sensors and the data acquisition system.

3.1.1 Fluidized Bed Reactor

For this research, a cold-flow fluidized bed reactor is developed to study fluidization behavior with additional particle and air injection. Material consideration is an important factor in the reactor design. The reactor requires strength to withstand the maximum pressure of the flow system (up to 620 kPa (90 psi)), while still allowing X-ray penetration necessary for X-ray imaging. Therefore, nearly all components are fabricated from either acrylic or nylon. The fitting thread type is another important design consideration. Since acrylic is a brittle material, all holes on the reactor are tapped to accept fittings with straight threads with the exception of a pressure tap at the base. Unlike NPT pipe threads, straight threads do not taper and can therefore be tightened without risking a crack in the brittle acrylic. To maintain geometric compatibility with the external airlift loop reactor (EALR) described in Jones (2007), the fluidized bed reactor is constructed of 10.2 cm internal diameter (ID) acrylic tubing with a 0.64 cm (0.25 in) wall thickness, and dimensioned accordingly. Future studies may compare fluidization behavior to bubbling behavior in these two reactors. Figure 3.1 shows a schematic of the fluidized bed reactor used in this research.

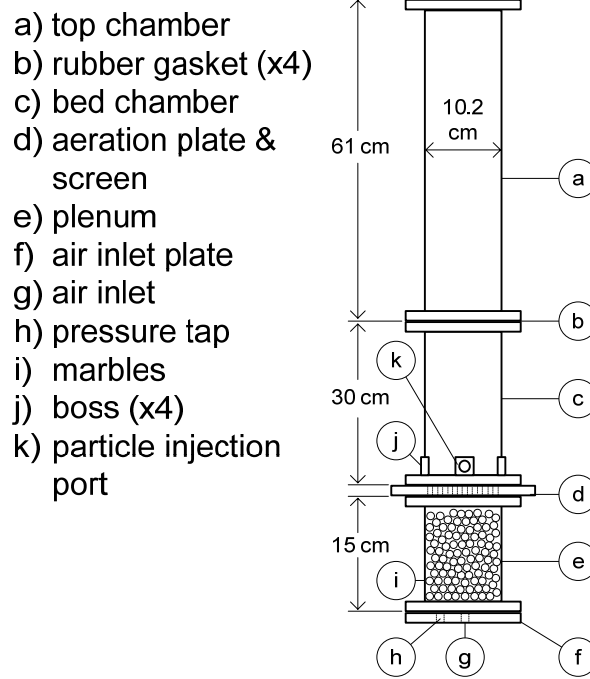


Figure 3.1: Schematic of the fluidized bed reactor.

The reactor consists of three main chambers: a top chamber (a), a bed chamber (c), and a plenum (e). Bed material is fluidized in the 30.5 cm (12 in) tall, 10.2 cm (4 in) ID bed chamber. Two 16.5×16.5 cm (6.5×6.5 in) square flanges are located on the top and bottom of the bed chamber and are used to connect sections together. Each flange contains eight 0.83 cm (0.33 in) ID holes spaced evenly around a radius of 7.32 cm (2.88 in) from the center of the flange. Four 3.18×3.18×1.27 cm (1.25×1.25×0.50 in) bosses (j) are located on the side-wall of the bed chamber, spaced in 90° increments, to allow fitting installation on the side of the reactor without compromising the column's structural integrity. The bed chamber includes one injection port (k) located in one of the four bosses, 1.27 cm (0.5 in) above the bottom of the bed chamber. This port allows particle and gas injection during fluidization. When the port is not in use, it is plugged with a 1.91 cm UNF (0.75 in-16) nylon plug fitting with an O-ring (to ensure a seal) which is custom designed and fabricated. During injection experiments, a 1.91 cm UNF (0.75 in-16) nylon Swagelok fitting with an O-ring is used as an entry port fitting. The three remaining bosses are not used for this research.

Below the bed chamber rests the distributor (aeration) plate (d). It was initially desired to develop a distributor plate system which featured adjustable flow controls for each individual orifice like the system designed by Hartevelde et al. (2003) and Hartevelde (2005). This approach was abandoned since fluidization hydrodynamics depend more on the average superficial gas flow than the individual orifice flow. Consequently, a traditional distributor plate is used in this research. The distributor plate was originally built for a 10.2 cm (4 in) ID bubble column described by Su et al. (2006), but has been modified to fit the cold-flow fluidized bed reactor. The 1.27 cm (0.5 in) thick acrylic plate has 62, 1 mm diameter holes spaced approximately 1.27 cm (0.5 in) apart in a circular grid for a total open area of 0.62 %. To eliminate bed particles from lodging inside the distributor plate orifices, a 45 mesh screen with openings of 0.04 cm is attached to the plate using silicone adhesive. Silicone prevents gas from escaping through the sides of the screen. It should be noted that the screen is made of metal but does not affect the X-ray data since no imaging is done on the distributor plate. The distributor plate, screen, and rubber gasket are shown in Figure 3.2.

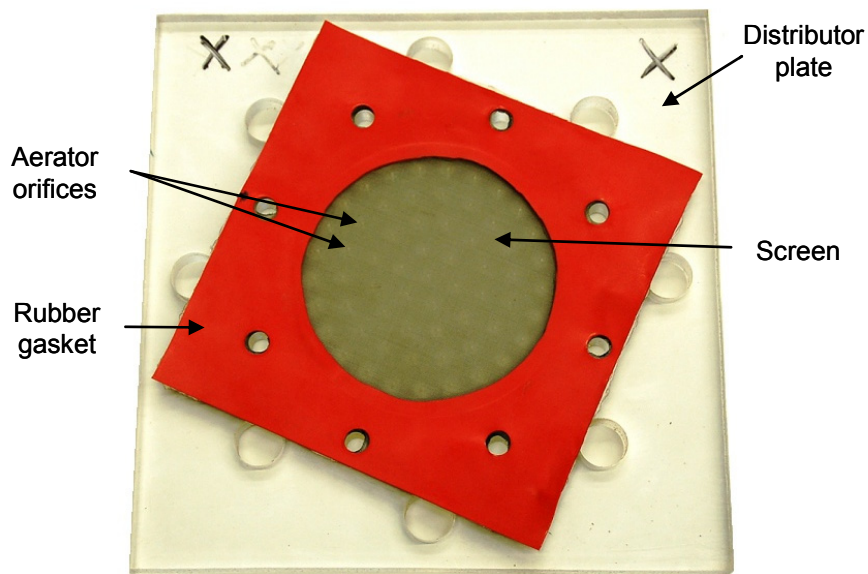


Figure 3.2: Photograph of the distributor plate.

The 15.2 cm (6 in) tall, 10.2 cm diameter plenum, or windbox, is located directly under the distributor plate and is filled with 1.27 cm (0.5 in) diameter glass marbles (i). The marbles allow uniform distribution of the fluidizing gas throughout the plenum before reaching the distributor plate. The plenum has two flanges that are identical to those used on the bed chamber. Gas enters the reactor through a 1.91 cm UNF (0.75 in-16) threaded fitting in the air inlet hole (g), which is located in the center of the 16.5×16.5 cm (6.5×6.5 in) air inlet plate (f). A section of screen with openings of 0.127 cm (0.05 in) is located above the air inlet hole to keep marbles from lodging inside the inlet hole. A 0.64 cm (0.25 in) NPT threaded pressure tap (h) is located off-center on the air inlet plate. The pressure tap in the plenum allows reliable pressure measurements, capturing both bed and plenum dynamics, as described by Felipe et al. (2007).

Above the bed chamber is an optional top chamber which contains ejected particles from the bed. This column is only necessary under high gas velocity conditions. The top chamber is 61 cm (24 in) tall and 10.2 cm (4 in) in diameter. Like the bed chamber and plenum, two identical flanges are placed on the top and bottom of the column. To seal the reactor from gas leakage, four rubber gaskets (b) are placed between each section's flanges. The reactor is assembled by bolting the flanges in each section with eight, 5.1 cm (2 in) long, 1.27 cm (0.5 in) diameter nylon bolts and 16 nylon washers. Nylon bolts are durable enough to assemble the reactor, but still allow X-ray penetration. A photograph of the assembled reactor is shown in Figure 3.3 without the top chamber. The CAD drawings used to fabricate the reactor may be found in Appendix E.

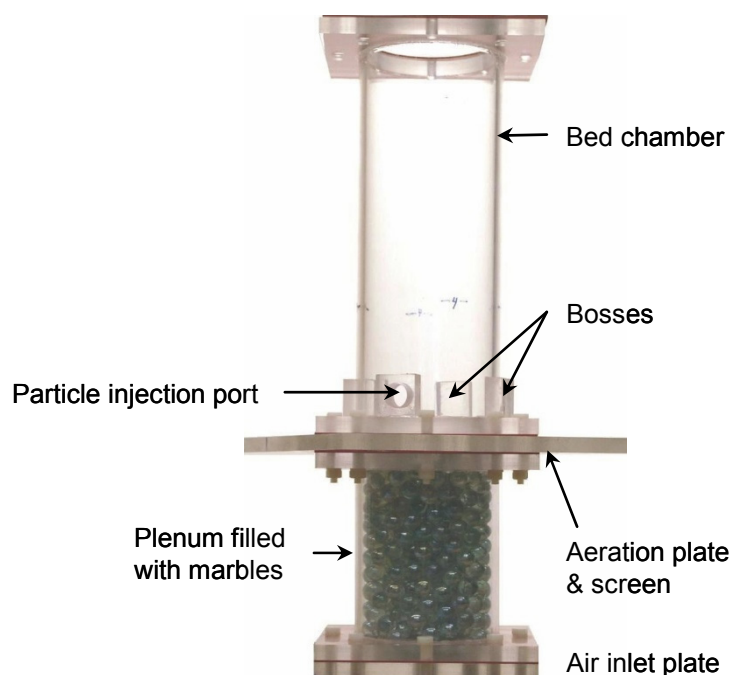


Figure 3.3: Photograph of the cold-flow fluidized bed reactor (without the expansion column).

3.1.2 Particle Injection System

In thermochemical conversion processes, biomass is injected into a heated fluidized bed where it undergoes combustion, pyrolysis, or gasification to produce a flammable hydrocarbon byproduct. In order to better understand the hydrodynamics of biomass injection, tracer particles have been developed which attenuate X-ray energy more than the surrounding material. These tracer particles are subsequently injected into the cold-flow bed through the side port, and tracked using X-ray techniques. To remotely inject tracer particles, a single particle injection system has been developed.

3.1.2.1 Tracer Particles

Tracer particles are designed for fluidized beds to have higher X-ray attenuation than the surrounding material, with densities similar to those in typical biomass particles. Several types of particles have been developed for glass bead beds in this study. In one tracer particle

type, dried corn and sections of dried corncob are soaked in a saturated solution of X-ray attenuating KI and allowed to dry. This produces doped biomass particles which are identical to types of biomass used in actual conversion processes. Unfortunately, these tracer particles are difficult to simulate using CFD due to their irregular shapes and densities. In addition, the doped KI particles are difficult to visualize in glass-bead fluidized beds. As a result, the KI doped tracer particles are not used in this study, however future work may utilize these particles.

A second method of creating tracer particles involves painting sections of corncob with silver paint to attenuate X-rays. This approach also produces a true biomass tracer particle; however, fluidization is found to remove some paint from the tracer surfaces. Also, the irregular shape and density causes difficulties in simulating this type of tracer particle. As with the KI doped particles, the silver painted tracers are not used in this research.

The most reliable tracer was developed in previous experiments for bubble columns, and consists of a 0.95 cm diameter polypropylene sphere. Inside the sphere, a 0.635 cm long, 0.159 cm diameter slug of 95% tin-5% antimony solder is inserted. The resulting density is $\sim 1.0 \text{ kg/m}^3$, approximately the same as water. Since the solder attenuates X-rays more than KI or silver, these particles are more distinguishable than the other tracers. The symmetrical shape and well-known density also makes simulating the particle less complex. Figure 3.4 shows the tracer particles used in this research. These tracers are successful for glass bead beds; however, they are found to sink in walnut shell and corncob beds. Since particle tracking in this research is only presented as a proof-of-concept, particle injection is only performed with glass bead fluidized beds. Four tracers developed in this research for glass bead beds are shown in Appendix A.

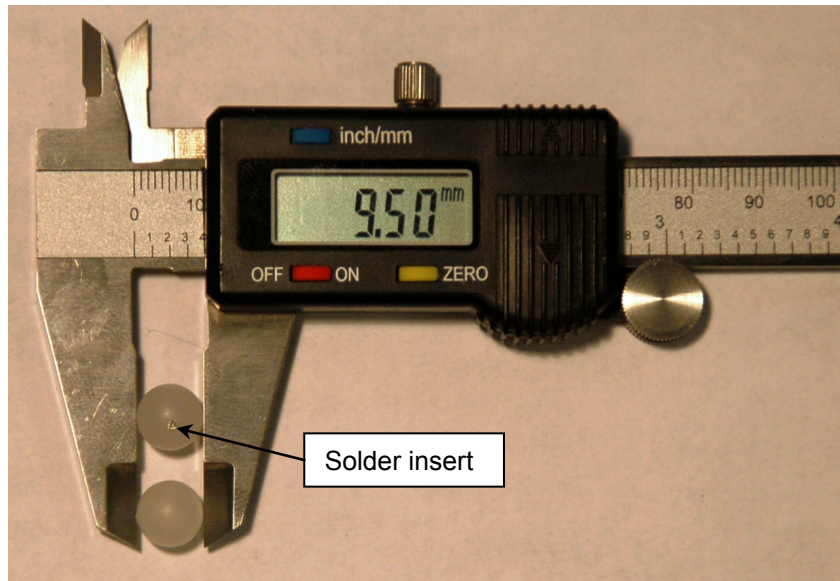


Figure 3.4: Polypropylene tracer particles.

3.1.2.2 Injection System

The particle injection system is designed to inject a single particle into a fluidized bed at a desired time. It is similar to the design presented by Bruni et al. (2002) which involves a pneumatic actuator that pushes tracer particles directly into the bed. In the current study it is desired to directly inject the particle into the bed using compressed gas to represent air injection systems common in actual gasifiers. The gas injection also simulates the vaporization of biomass as it is injected into the fluidized bed. Pneumatic systems are preferred over hydraulic and electromechanical systems since compressed air is readily available in the laboratory. Also, since the injector must be in close proximity to the reactor, and the fluidized beds are imaged with harmful ionizing X-rays, remote activation of the injector is required. In addition, the system is desired to maintain constant pressure to reduce the chance of backflow. To allow for varying sizes of particles, the system is designed for tracers up to 10 mm in diameter, the size of the polypropylene tracer particles mentioned earlier. It is assumed that 10 mm is approximately the size of large biomass particles and

injection of particles larger than this is unnecessary for this research. Figure 3.5 shows a schematic of the single particle injection system.

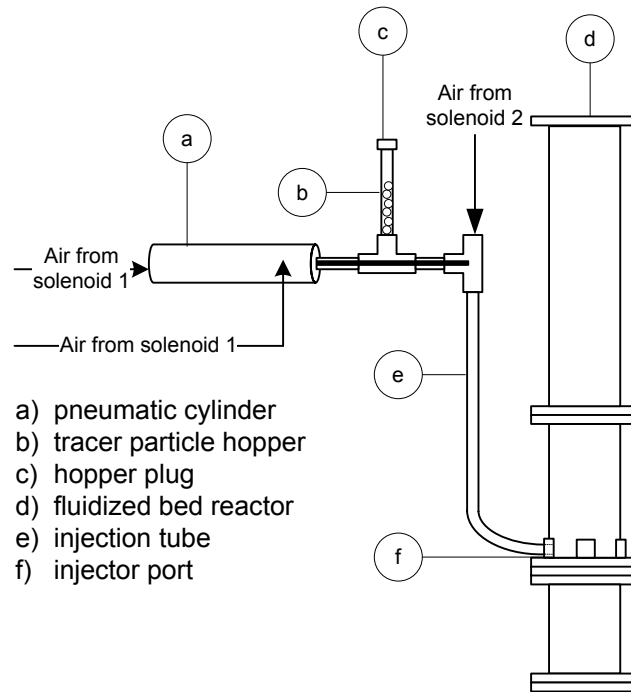


Figure 3.5: Schematic of particle injection system.

Tracer particles are stacked in a single vertical column in the hopper (b) which is connected to the upright section of a female 1.27 cm (0.5 in) Swagelok tube tee. The 15.2 cm (6 in) tall hopper is made of 1.04 cm (0.41 in) ID copper pipe for rigidity and strength. Gravity is used to feed particles to the tee. The top of the hopper is plugged with a 1.27 cm (0.5 in) Swagelok tube plug fitting (c) in order to maintain pressure in the injection system. For easier particle loading, the hopper is angled approximately 20° from vertical. A double-acting pneumatic cylinder (a) with a stroke length of 15.2 cm (6 in), bore size of 3.18 cm (1.25 in) and a shaft diameter of 0.97 cm (0.38 in) provides the initial motion for injecting particles. Since the cylinder is double-acting, it relies on compressed air to extend and retract the shaft. Compressed air is supplied to two ports with 0.318 cm (0.125 in) NPT threads, directly on the cylinder; one in the rear and one near the nose. Two sections of 0.64 cm (0.25

in) outer diameter (OD) polypropylene tubing supply the compressed air to the cylinder ports through two Swagelok tube fittings.

The nose-mounted cylinder is connected to a 5.72 cm (2.25 in) long steel nut with female 1.91 cm UNF (0.75 in-16) threads. A custom built rubber gasket is placed between the nut and the cylinder to prevent pressure leakage. The nut is also attached to a Swagelok tube fitting with male 1.91 cm UNF (0.75 in-16) threads, which is subsequently connected to a 3.18 cm (1.25 in) section of 1.04 cm (0.41 in) ID copper pipe. This section of pipe is connected to one of the straight legs of the Swagelok tee. An 8.4 cm (3.31 in) long, 0.97 cm (0.38 in) diameter rod is welded to the end of the cylinder's shaft to extend the stroke length to 23.6 cm (9.31 in). The first Swagelok tee is connected to another female 1.27 cm (0.5 in) Swagelok tube tee through a 12.1 cm (4.75 in) section of 1.04 cm (0.41 in) ID copper pipe. One branch of the second tee is connected to a section of 1.27 cm (0.5 in) OD polypropylene tubing. An 89 cm (35 in) long, 1.10 cm (0.43 in) ID injection tube (e) connects the second Swagelok tee to the injector port located on the fluidized bed reactor.

To inject a particle, the cylinder extends through the first tee where it contacts a particle and pushes it from the hopper to the center of the second tee. Compressed gas is supplied to the second tee which forces the tracer particle to travel into the injection tube. A combination of pressurized gas and gravitational force accelerates the tracer particle through the injection tube until it emerges in the fluidized bed (d) by way of the injector port (f) mentioned earlier. After particle injection, the cylinder is retracted and the process begins again. Because of the tight 0.07 cm tolerance between the cylinder rod and the copper tubing, additional tracer particles do not leave the hopper until the cylinder is retracted. Consequently, only one particle is injected by the cylinder at a time. The entire system is fastened to plywood and hung in the X-ray vault above the imaging region. A photograph of the injector system is shown in Figure 3.6. The setup of the injector system and the fluidized bed reactor is shown in Appendix A.

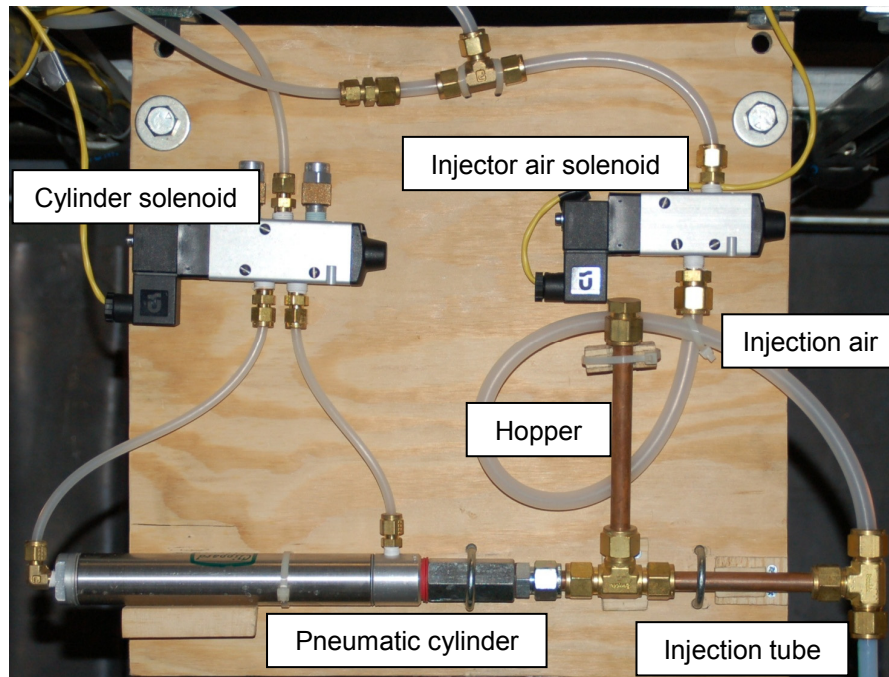


Figure 3.6: Single particle injection system.

The compressed air lines running to the two ports on the pneumatic cylinder are controlled by a 4-way, 2-position body-ported solenoid control valve with 5 ports. When the solenoid is in the closed position, compressed air flows to the front port, retracting the shaft. When the solenoid is in the open position, compressed air flows to the back port which extends the cylinder shaft. Adjustable quick-exhaust flow control valves are located on two of the exit ports to control the speed of the cylinder shaft's extension and retraction.

A 3-way, 2-position body-ported solenoid control valve with 3 ports controls the gas flow in the injection tube. The exit port on this solenoid is plugged to keep the system pressurized when there is no injection gas flow. The tubing connecting the injection air solenoid to the Swagelok tee is twisted 360° to prevent tracers from travelling upwards to the solenoid. All ports on both solenoids have 0.64 cm (0.25 in) NPT threads for pipe fittings. Both solenoids are controlled by two-way toggle switches which allow for remote control of the injection system; this is necessary since the injector board is located in the X-ray vault and is

inaccessible during X-ray experiments. The toggle switches are located on the flow control board discussed later. The solenoids are enabled by a 24 vdc power supply from an AC/DC converter. Supply voltage to the AC/DC converter is 120 vac from the building supply. The electrical diagram is shown in Appendix A.

3.1.3 Air Flow System

Due to availability, the fluidizing gas used in this research is compressed air from the laboratory's built-in compressed air supply. The compressed air enters the facility at a regulated 620 kPa (90 psi). Since the air flow rates used in fluidization and side injection vary depending on the experimental conditions, a flow control board has been designed to individually control four separate air lines. The air flow control system is represented schematically in Figure 3.7.

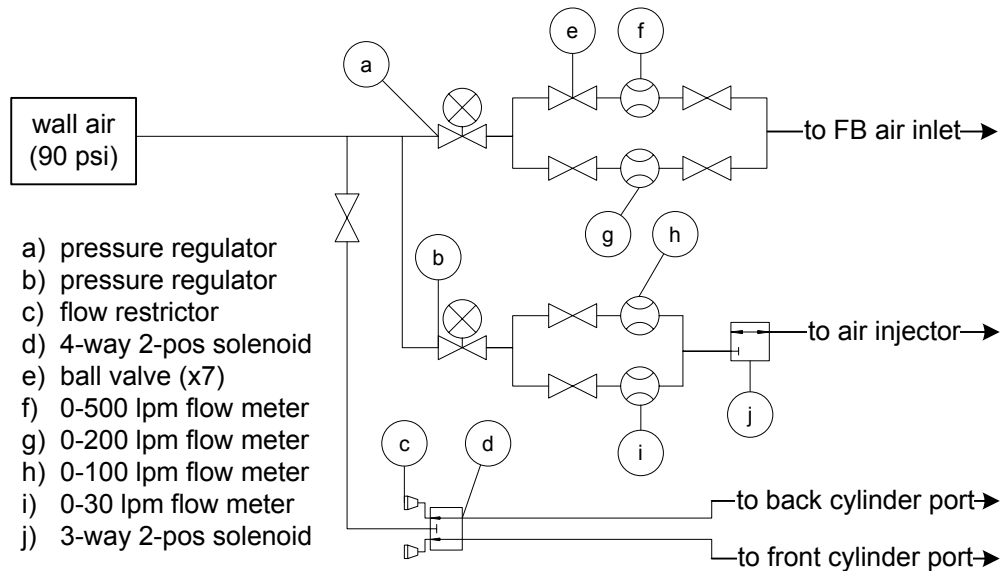


Figure 3.7: Schematic of the air flow control system.

Three paths branch from the laboratory air supply system and control the bed superficial gas velocity, side injection air flow rate, and the injector cylinder independently. In the first

path, air flow is supplied to the air inlet of the fluidized bed reactor and serves to fluidize the bed. Air is regulated with a stainless steel pressure regulator and attached filter (a) with a regulating pressure range of 0-862 kPa (0-125 psi) and maximum inlet pressure of 2.07 MPa (300 psi). The regulator accepts 1.27 cm (0.5 in) NPT fittings and pressure is measured by a 0-1.1 MPa (0-160 psi) pressure gauge. The regulator controls air flow through one of two mass flow meters; a 0-500 Lpm stainless steel Aalborg GFM671S flow meter (f) is used in high gas velocity applications, and a 0-200 Lpm Aalborg GFM571 flow meter (g) is used in lower gas velocity applications to improve measurement resolution. The flow meters are enabled and disabled using a series of ball valves (e). The outlets of the 500 Lpm and 200 Lpm flow meters are connected to the fluidized bed air inlet.

The second path branching from the air supply is used to control the injection air flow rate. Air is regulated by a 0-862 kPa (0-125 psi) stainless steel pressure regulator and filter (b) which accepts 0.64 cm (0.25 in) NPT fittings. Pressure is measured with a 0-1.1 MPa (0-160 psi) pressure gauge. From this regulator, flow passes through one of two flow meters; an Aalborg GFM471 0-100 Lpm flow meter (h) is used for high side air flow conditions and a stainless steel Aalborg GFM371S 0-30 Lpm flow meter (i) is used for lower flow applications to improve measurement resolution. The flow meter outlets are connected to the 3-way, 2-position solenoid (j) in the injection system. As before, the flow meters are enabled and disabled using ball valves. By adjusting the regulator control, flow rates are controlled through the air injector. All flow meters in this study are reported to have an error of $\pm 2\%$ of the full scale reading.

The third branch off the laboratory air supply is directly connected to the 4-way, 2-position solenoid valve (d) which controls cylinder movement in the injection system. Since pneumatic cylinders require high pressure to operate correctly, this flow is not restricted with a pressure regulator; however, a ball valve is in place to shut off the flow when the injector is not in use. The three flow branches from the air supply use a combination of 1.27 cm (0.5 in),

0.95 cm (0.38 in), and 0.64 cm (0.25 in) OD tubing, depending on the air flow rate passing through the tubing. The four flow meters are individually powered by 12 vdc power supplies. The flow controls, power sources, and solenoid toggles are mounted on plywood. A photograph of the flow control board is shown in Figure 3.8.

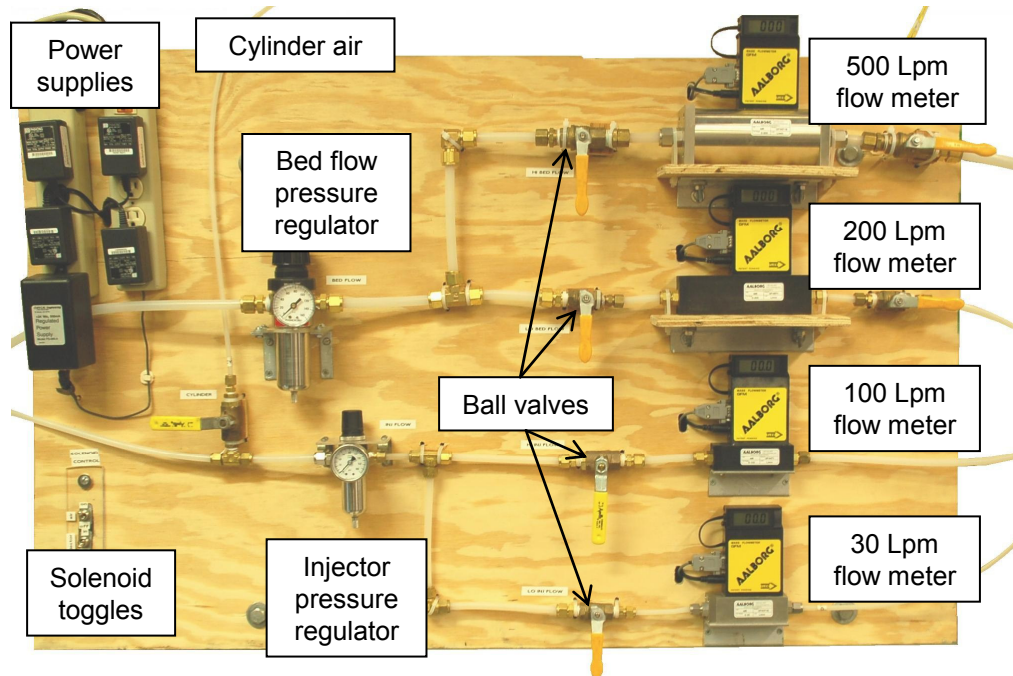


Figure 3.8: Air flow control board.

3.1.4 Pressure and Flow Measurement

Two important parameters measured throughout this study are pressure and air flow rate. Pressure is measured by a Dwyer 0-34.5 kPa (0-5 psig), 4-20 mA output pressure transducer attached to the pressure tap on the fluidized bed air inlet plate. Error on the pressure transducer is reported as $\pm 0.25\%$ of the full scale reading, or ± 86 Pa. The pressure transducer is connected to the plenum since measurements in the plenum are the most representative of overall bed hydrodynamics. The four flow meters on the flow control board are also equipped with 0-10 vdc outputs to measure air flow rate. The outputs of the pressure

transducer and flow meters are connected to a data acquisition system (DAQ) on a personal computer. The DAQ system, described by Jones (2007), is composed of a National Instruments 6030 E-series multifunction data acquisition card, a National Instruments SCB-68 shielded connector block, a 24 vdc Cole-Parmer PS2-24-15-007 instrument power supply, and National Instruments LabView 8.0 acquisition software. DAQ equipment is shown in Appendix A.

LabView 8.0 VIs (Virtual Instruments) developed in this study, record real-time measurements of pressure and flow rate for a given measurement period, defined by the user, and then calculates the average pressure and flow rate during the measurement time. Averaging measurements is necessary due to the highly variable pressure signal caused by fluidized bed bubbling. The measuring technique is repeated on an additional time interval, also set by the user. Data collection occurs at a rate of 1000 samples per second for each instrument (channel). Time interval, pressure, and flow rate measurements are subsequently written to a data file. The LabView graphical user interface (GUI) is shown in Appendix A.

To ensure accurate measurements, the pressure transducer and the four flow meters are calibrated against known standards. The pressure transducer is calibrated by measuring the output voltage of the transducer as a function of pressure. Various hydrostatic pressures are generated by filling a vertical section of 0.79 cm (0.31 in) ID Tygon tubing with water to specific heights above the transducer. A linear curve fit is applied to the data and the coefficients are applied as a scaling function directly in the LabView VI. The flow meters are calibrated by measuring voltage as a function of flow passing through a calibration drum. By measuring the time required to move the drum a given number of revolutions, an accurate flow rate is calculated. As with the pressure transducer, a linear curve fit is applied to the calibration data for each flow meter and the coefficients are applied as a scaling function in the VI. Calibration images and calibration curves are shown in Appendix A.

3.2 Bed selection

A major component in this study is the comparison of fluidization behavior between different materials. In most fluidized bed applications, inert materials like sand or glass beads compose the bed due to uniform properties and uniform fluidization hydrodynamics. While some research has focused on the independent fluidization of biomass, described in Chapter 2, there has been little work in using noninvasive measurement techniques on biomass fluidization. Section 3.2 describes the bed selection process in two subsections. The first subsection describes how three materials are chosen based on four main criteria. The second subsection describes how the three bed materials are prepared for use in the cold-flow reactor.

3.2.1 Material Selection Criteria

Three materials are chosen for comparison in this study based on four main criteria: (i) fluidization behavior, (ii) size range, (iii) density, and (iv) aspect ratio. To establish similar fluidization hydrodynamics, only Geldart type B particles are desired. This group fluidizes most like conventional fluidized bed systems used in gasification and pyrolysis. Also, to directly compare different beds, the particles are desired to have normally distributed diameters between 500–600 μm . This size range is chosen because of its availability and its representation of real-life fluidized beds. Materials with low densities are also desirable since X-ray attenuation is more pronounced in high density materials. Finally, each particle is required to have an aspect ratio close to unity. Uniformly shaped particles simplify modeling, thus decreasing the complexity and calculation time for CFD simulations.

Glass beads between 500–600 μm in diameter are studied as a benchmark since the fluidization of glass is well characterized and because glass has similar properties to inert sand used in gasification. Additionally, modeling glass bead fluidization is ideal due to its

high sphericity, uniform density, narrow particle size distribution, and resistance to breaking. One disadvantage of glass bead fluidization is the difficulty in the bed with X-rays without saturating regions of the image. As a result, it is desirable to visualize materials with lower densities than glass beads using the X-ray techniques described in this study. Ground walnut shell and ground corncob, typically used in blasting applications, are both found to have lower densities than glass while maintaining a similar size distribution of 500-600 μm . Additionally, upon visual observations, the corncob and walnut shell aspect ratios appear to be near unity. An added advantage is that both corncob and walnut shell are forms of biomass so the fluidization of biomass may be compared to the inert bed material. Since the fluidizing gas is compressed air, and it is assumed the air has constant density, all three materials fall within Geldart's type B classification. Figure 3.9 shows that glass beads, walnut shell, and corncob are all type B particles. Also, it should be noted that the density for glass beads is well-known while walnut shell and corncob have a range of particle densities. Preliminary testing has also performed using granular melamine resin in a 9.5 cm (3.75 in) ID fluidized bed reactor; however this material is not studied in this research since it is not likely to be used in fluidization applications (Franka et al., 2007).

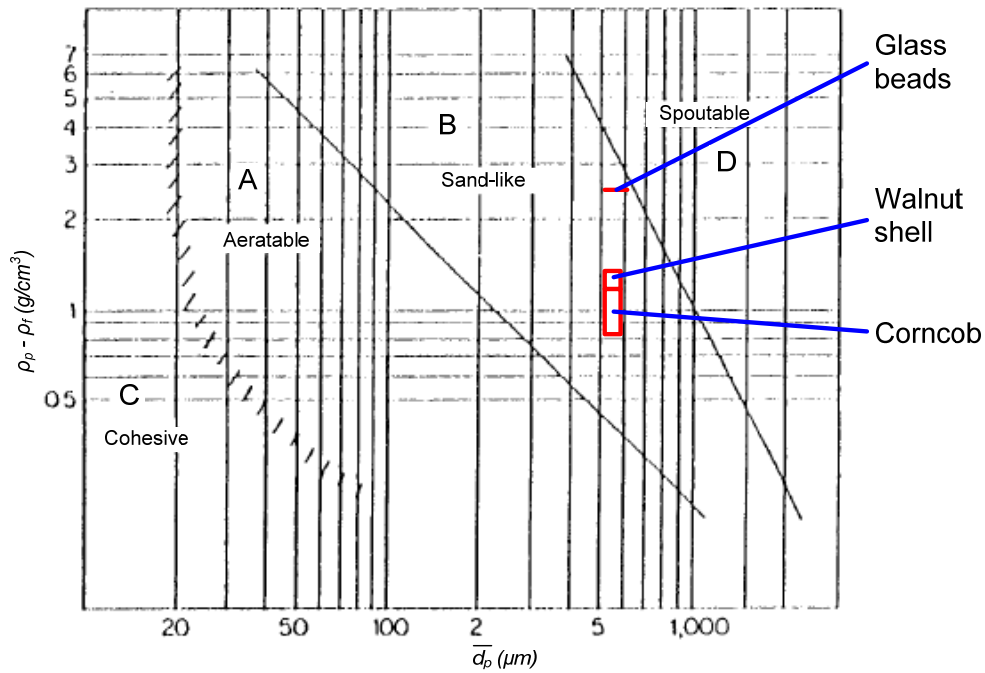


Figure 3.9: Material selection based on Geldart's classification (Geldart, 1973).

3.2.2 Bed Preparation and Measurement

Figure 3.10 shows the glass beads, walnut shell, and corncob that are fluidized in this research, with a penny shown for a reference size. Before fluidizing, each material is first prepared and important quantities are measured. A sieve shaker is used to reduce the size range from the initial particle size distribution of about 400-800 μm to the desired 500-600 μm range. Each material is sifted multiple times between a 500 μm and a 600 μm metal screen sieve set, and it is assumed that the particle size follows a Gaussian distribution within the sieved range. Particles are removed from the sieves with a stiff paintbrush and sifting is performed over a plastic storage tub to contain the particles. Photographs of the sifting method are shown in Appendix A.

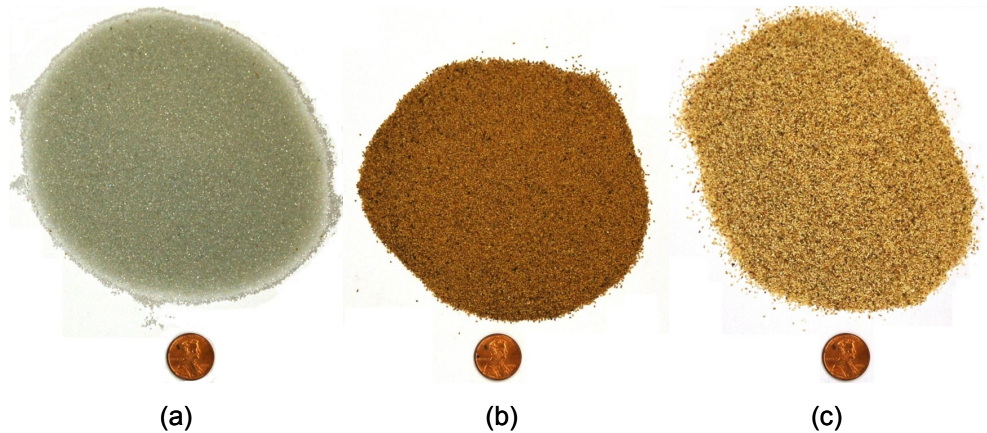


Figure 3.10: Bed materials used in this fluidization study (a) glass beads, (b) ground walnut shell, and (c) ground corncob.

Once particles are sifted, it is observed that fines and dirt are present in the materials. To remove undesirable fines and dirt from the bed materials, two methods are employed. The glass beads are placed in a 200 μm sieve screen (which is smaller than the mean particle diameter) and cleaned with running water. The wet glass is next dried with a box fan until most of the water has evaporated. The damp glass is further dried in a 15.2 cm cold-flow fluidized bed reactor. The cleaning and drying method for glass is shown in Appendix A. Since corncob and walnut shell absorb water, these materials are cleaned by rapidly fluidizing in the 10.2 cm diameter reactor in order to elutriate the fines. Both methods are found to work reasonably well.

After material preparation, three important parameters are measured and calculated for each bed. Each material is placed in the 10.2 cm reactor and a bed height of 10.2 cm ($H/D = 1.0$) is established using an iterative process. The bed is slightly fluidized to remove initial packing effects in order to get an accurate height measurement. Bed height is measured with a ruler. The bed is next weighed using a Fisher XL-3000 scale with 0.01 g resolution and a capacity of 3000 g. A photograph of the measurement technique is available in Appendix A. By calculating the bed volume from the measured bed weight and height, the bulk density (ρ_b) for each bed is calculated by

$$\rho_b = \frac{W_{bed}}{V_{bed}} \quad (3.1)$$

where W_{bed} is the bed mass and V_{bed} is the bed volume. The particle density for each material is provided by the manufacturers. The bulk void fraction (gas holdup) of each material is also calculated using the approach outlined in subsection 3.5.3. Table 3.1 presents a summary of the bed properties.

Table 3.1: Bed material summary.

	Glass Beads	Walnut Shell	Corncob
Diameter (μm)	500-600	500-600	500-600
Bed height (cm)	10.2	10.2	10.2
Bed weight (g)	1220	477	323
Bulk density (kg/m^3)	1481	579	392
Particle density (kg/m^3)	2600	1200-1400	800-1200
Bulk void fraction (-)	0.43	0.55	0.68

Static electricity buildup of each material is also qualitatively assessed for its affect on fluidization measurements. A 10.2 cm tall bed is rapidly fluidized for one hour in a 9.5 cm (3.75 in) ID fluidized bed (used in previous work), while digital images are captured. Figure 3.11 shows that glass beads exhibit the highest level of static electricity buildup, followed closely by corncob. In contrast, the walnut shell bed shows almost no signs of static charge buildup. While charge buildup is observed for the glass beads and corncob, it is assumed that the impact on bubbling bed hydrodynamics is not significant since the mass of particles adhering to the reactor walls is much less than the mass of particles in the bed. Additional images of static electricity testing are available in Appendix A.

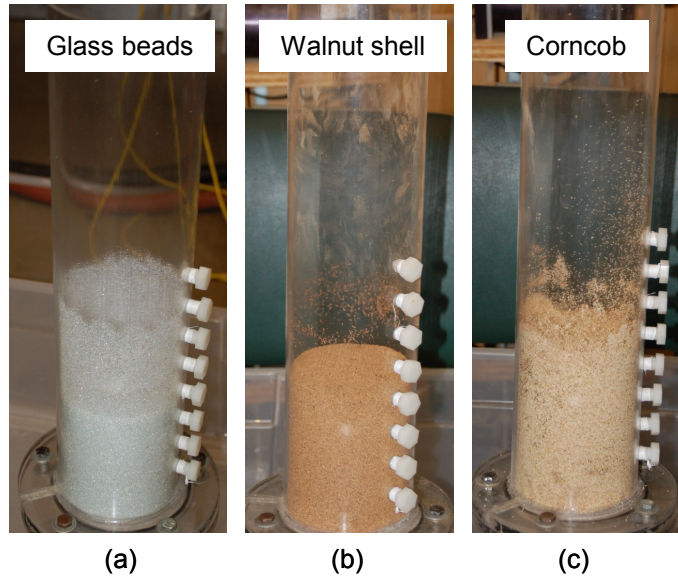


Figure 3.11: Static electricity buildup after 1 hour for (a) glass, (b) walnut shell, and (c) corncob.

3.3 Determining Minimum Fluidization Velocity

The minimum fluidization velocity is one of the most important fundamental parameters in modeling fluidization hydrodynamics and is used as the basis for flow conditions in this study. The first subsection in section 3.3 explains the method used to determine U_{mf} for various bed materials and various side air flow conditions. The next subsection describes the relationship between U_{mf} and the flow conditions used in the experiments.

3.3.1 Method

The minimum fluidization velocity for each material is determined experimentally using the pressure measurement procedure summarized in Chapter 2. To find U_{mf} for a given bed, each material is fluidized with air at 200 Lpm, measured by the 0-200 Lpm flow meter. Upon reaching a steady-state bubbling bed condition, pressure and flow rate data are acquired with the DAQ system, averaged over a 5 second interval, and output to a file. Next, the air flow rate in the bed is decreased 5 Lpm by manually closing the pressure regulator. After waiting

for 15 seconds, pressure and flow rate data are again averaged over a 5 second period and the process is repeated. While the setup allows for varying measurement intervals, it is found that 15 seconds between 5 second testing times gives the bed adequate time to reach quasi steady-state while minimizing data collection time. The air flow rate in the bed is decreased in 5 Lpm intervals until reaching 0 Lpm, at which point the test is completed. When U_{mf} is determined with side air injection, the side air flow rate remains constant throughout data collection.

Once the fluidized bed data are collected, the process is repeated without material in the reactor to determine the pressure drop caused solely by the reactor; the reactor exhibits a pressure drop due to the plenum marbles and the distributor plate. The empty reactor pressure data is then subtracted from the fluidized bed data for each 5 Lpm flow rate interval. To find U_{mf} , the pressure drop across the bed is plotted against the superficial gas velocity in the bed (U_g), which is derived from the flow rate. Since the flow rates between the empty reactor and fluidized bed tests do not match exactly, a linear interpolation method is employed to calculate the empty bed pressures corresponding to the fluidizing bed flow rates. Initially it was believed that the empty bed pressure-flow curve followed a simple second order polynomial curve-fit; however, this introduced large amounts of noise which obscured the location of U_{mf} on the pressure-flow plot. A comparison of the two methods is shown in Appendix B for a walnut shell bed. U_{mf} is defined as the location where the pressure drop across the bed ceases to increase linearly with U_g and instead remains constant. Figure 3.12 shows U_{mf} is approximately 22.2 cm/s for a glass bead U_{mf} experiment with no side air injection.

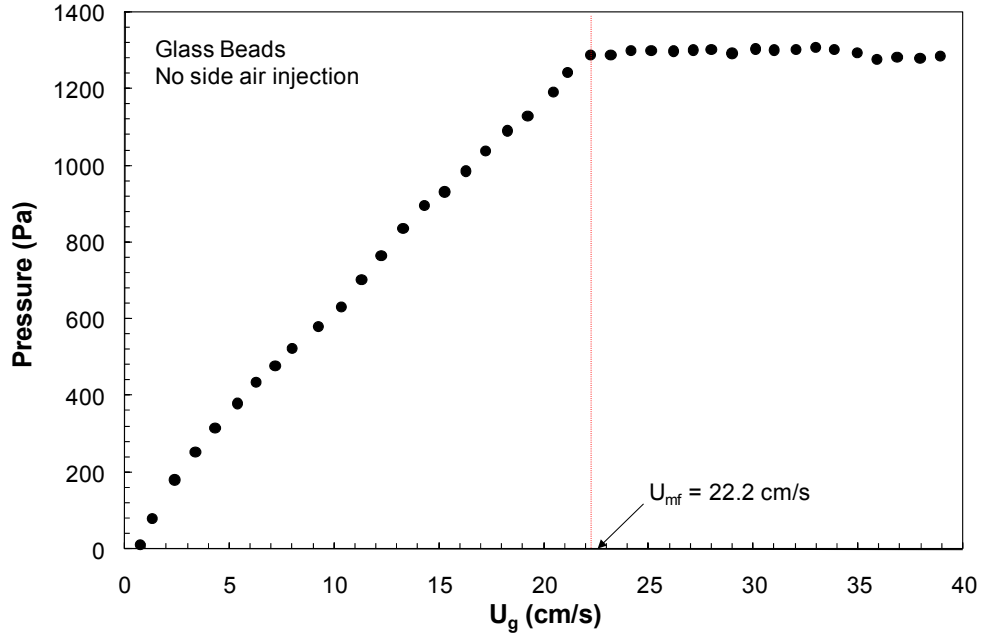


Figure 3.12: Determining U_{mf} from a pressure-flow plot for glass beads.

3.3.2 Test Conditions

Not only is the minimum fluidization velocity an important parameter for modeling, it is also the basis for flow conditions used in this study. Without side air flow, the minimum fluidization air velocity ($U_{mf,0}$) and minimum fluidization air flow rate ($Q_{mf,0}$) are experimentally measured for each material. This provides a method of normalizing both bed and side air flow conditions by the fundamental parameter $U_{mf,0}$ (or $Q_{mf,0}$). Each bed is fluidized with five different superficial air velocities (U_g) which are based on typical superficial gas velocities in gasifiers: $U_g = 1.25, 1.50, 1.75, 2.00$, and $3.00 \times U_{mf,0}$. Similarly, five side air flow rates (Q_s) including the no side air condition, are tested to encompass a range of biomass injection flow rates in gasifiers: $Q_s = 0, 0.05, 0.10, 0.15$, and $0.20 \times Q_{mf,0}$. Since the introduction of side air affects the total flow rate through the bed, U_{mf} is also determined for each bed while Q_s remains constant at $Q_s = 0, 0.05, 0.10, 0.15$, and $0.20 \times Q_{mf,0}$.

3.4 XFloViz Facility

Iowa State University developed the X-ray Flow Visualization (XFloViz) facility in the Experimental Multiphase Flow Laboratory to study multiphase flows using noninvasive X-ray techniques. This facility and its development have been thoroughly explained in the literature (Ford 2006; Ford et al., 2007; Heindel et al., 2005; Heindel et al., 2008; Hubers et al., 2005; Striegel, 2005), and only a summary is provided in section 3.4. The X-ray equipment is described in the first subsection, followed by a discussion of important X-ray parameters in the second subsection.

3.4.1 X-ray Equipment

Two LORAD LPX200 portable X-ray systems (sources) produce X-ray energy. X-rays are emitted from the beryllium window on the tubehead in a 60° horizontal, 40° vertical conical beam. The beam spot size of each source is 1.5 mm. Current and voltage can be adjusted from 0.1 to 10.0 mA and 10 to 200 kV, respectively, with a maximum total power of 900 W. The X-ray tubes are liquid-cooled with two LORAD pump systems. X-ray energy is limited by a collimator surrounding the source. Copper and aluminum filters may be placed in front of the source to reduce the low energy radiation. Filters are used according to the attenuation characteristics of the object being visualized.

Located opposite each X-ray source is an X-ray detector/CCD camera pair. The XFloViz facility has two image intensifier/CCD camera detectors which are used primarily for radiographic and stereographic imaging due to their high temporal resolution and good spatial resolution. The image intensifier acts to strengthen incident X-ray signals, similar to intensifying light with a magnifying glass. Each image intensifier consists of a 40.6 cm diameter Precise Optics PS164X screen detector with a 35.0 mm output image diameter. A DVC-1412 monochrome digital camera with 1388×1024 active pixels captures the image

from the intensifier. In previous work, these detectors were also used for CT imaging (Streigel, 2005); however, this feature is now obsolete with the addition of a scintillator-type detector. Images are transferred to a 12-bit EDT PCI DV C-Link frame grabber and downloaded to a computer. The image intensifier detectors have temporal resolution ranging from 10 frames per second (fps) to 60 fps, depending on binning options.

A second detector/camera pair is primarily used for CT imaging because of its high spatial resolution. In addition, individual radiographs may be captured. Incident X-ray energy is transformed into visible light by a square 44×44 cm cesium-iodide (CsI) scintillator screen. A 50 mm Nikon lens captures images which are digitized by an Apogee Alta U9 system. This system has 3072×2048 active pixels and is thermoelectrically cooled to allow long exposure times with low noise conditions. One difficulty in using the CsI scintillator screen is in the response of the scintillation crystals at the beginning of an X-ray test. If the detector is used without previously exciting the crystals, the detector's response will change throughout a test, causing inaccurate data. To overcome this problem, the scintillator is excited with X-rays for approximately 20 minutes before data collection. Additionally, the scintillator requires about 5 minutes without incident X-rays to completely return to an unexcited state. This is important when collecting normalization images.

The XFloViz facility allows two detectors to image an object simultaneously; therefore, all three detectors are removable to allow for different visualization techniques. The detectors and sources are located on a 1.0 m ID rotation ring that can rotate 360° around the fluidized bed. The rotation ring is controlled by a stepper motor to allow for different visualization orientations. Figure 3.13 shows the XFloViz imaging room with the empty fluidized bed reactor in the imaging region.

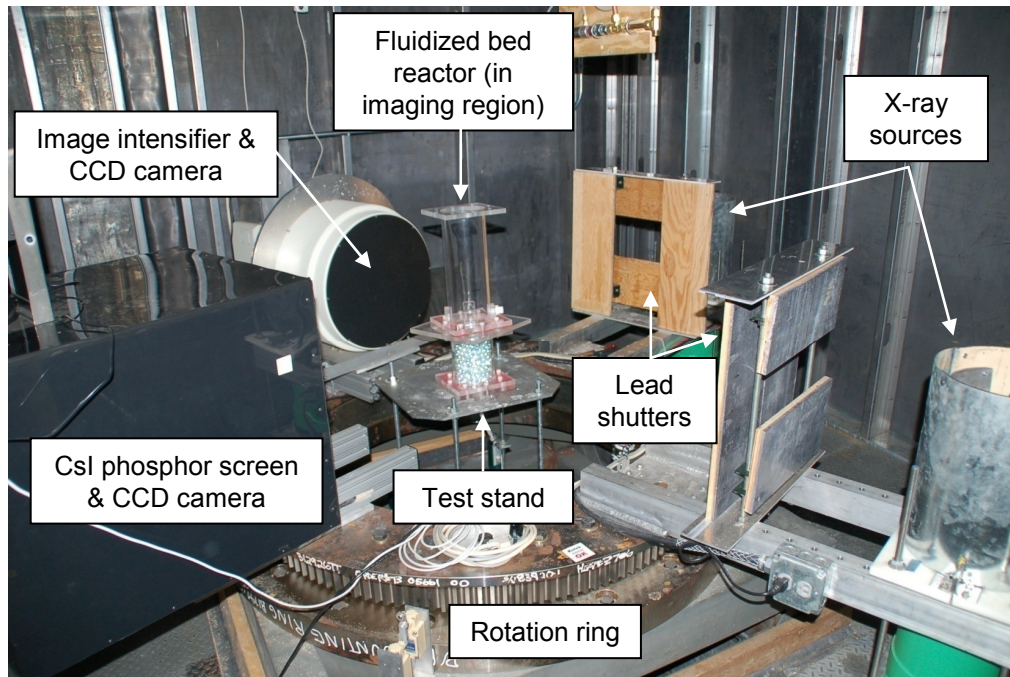


Figure 3.13: XFloViz imaging room.

The facility also features a vertical lift which is located under the imaging region to adjust the vertical location of an object. The lift is controlled by a 910 kg winch to provide 2.75 m of vertical travel, giving an overall span of 4 m. The lift is not used in the current study due to the small height of the fluidization region. Data acquisition is accomplished using software developed by Iowa State University's Center for Nondestructive Evaluation (CNDE) and a personal computer with 4 GB of RAM. The software allows control of both detectors and provides motion control for the rotation ring.

The XFloViz equipment is located 3.7 m above the lab floor in a 2.4 m tall lead-lined imaging room. The imaging room is accessible through a series of catwalks, stairs, and a lead-lined sliding door. The vertical lift system is located under the imaging room and is also enclosed within lead-lined walls. A system of interlocks and emergency shutoff controls is in place for safety considerations. Additionally, the facility is regularly tested for radiation leaks. Figure 3.14 shows the exterior of the XFloViz facility.

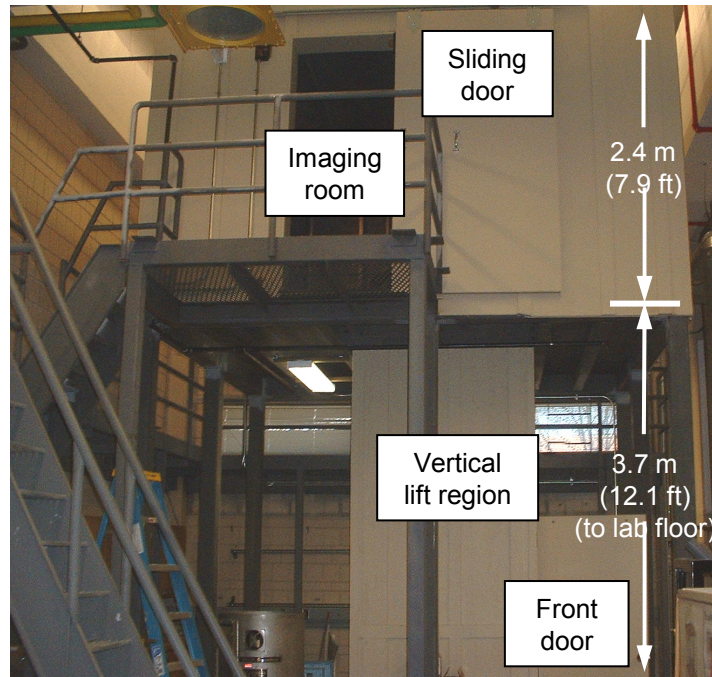


Figure 3.14: ISU XFloViz facility.

3.4.2 X-ray Parameters

In the XFloViz facility, a few basic X-ray parameters may be adjusted to improve contrast, X-ray penetration, resolution, and noise reduction. These parameters are modified according to the object being visualized and the visualization method (CT verses radiography). The parameters are adjusted through two imaging programs developed by CNDE, and by the X-ray control box. X-ray voltage generally controls the image contrast while X-ray current significantly affects X-ray penetration. To find the power settings for an X-ray experiment, the power is first increased by increasing current and voltage until the resulting image is nearly saturated. The two imaging programs allow a user to see the resulting image intensity values which have specific ranges depending on binning levels. Binning is a method of combining pixels together into clusters of “effective pixels” and affects the resolution, image acquisition speed, and image size. Four binning options are available for the image intensifier CCD cameras: 1×1 (1388×1024 pixels), 2×2 (640×512

pixels), 4×4 (320×256 pixels), and 8×8 (160×128 pixels). The CsI scintillator screen CCD camera has binning options of 1×1 , 1×2 , 1×3 , 2×2 , 2×3 , 2×4 , 3×3 , 4×4 , 5×5 , 6×6 , 7×7 , and 8×8 . Low binning levels such as 1×1 , have high spatial resolution but long acquisition times and require large amounts of memory. Conversely, high binning levels like 8×8 have lower spatial resolution but much faster acquisition times requiring less memory. As a result, for radiographic or stereographic imaging, high binning levels for the image intensifier CCD cameras have better temporal resolution.

When capturing radiographic or stereographic images it is also possible to average a specified number of frames using various averaging methods. This feature decreases noise in the data but increases acquisition time. Averaging frames is typically only used in calibrating the system since radiographic movies require high frame rates. Similarly, the CT software allows for camera exposure times from 0.1 to 100 s which reduces the noise in the data. Also, the thermoelectric cooler on the CsI CCD camera can be set to various temperatures to reduce noise. In this study, 2×2 binning (640×512 active pixels) at 20 fps is used for radiographic movies in order to maximize picture quality while maintaining good temporal resolution. An exposure time of 1 second with 4×4 binning and camera temperature of 0°C is chosen for CT imaging to minimize acquisition time while maintaining the signal strength. The X-ray power settings for each test are dependent upon the materials being fluidized and the type of test (CT or radiograph).

3.5 XCT

In this study, CT scans are captured for fluidized beds of all three materials at the flow conditions mentioned earlier. Manipulation of CT data can produce quantitative time-averaged local gas holdup information to show effects of various flowrates and materials in the fluidized beds. CTs are acquired in the XFloViz facility with the equipment described earlier, and three-dimensional images are reconstructed using CNDE and in-house software.

Each CT also undergoes a series of calibrations to remove artifacts. Once reconstructed, the time-averaged local gas holdup for each of the 3-D CT images is calculated. Section 3.5 begins with a subsection on the method of capturing CT data. Three important calibrations are described in the second subsection: normalization, beam hardening, and stretching of the volumetric image. The last subsection explains the method of calculating gas holdup from CT data by developing the fundamental equations, and then describing various calculation techniques. The final subsection also gives an overview of the entire process of generating gas holdup data, beginning with the CT acquisition.

3.5.1 Procedure

A similar procedure is followed for each CT test to maintain consistency between scans. The X-ray source opposite the CT detector initially undergoes a warm-up process. The thermoelectric cooler on the camera is simultaneously cooled to 0°C to reduce noise and allow for long CT scans. A program called PS_CT, developed by CNDE, is used to capture CT information, display real-time X-ray images, control camera settings, and control the rotation ring motion. After warm-up, the X-ray power, exposure time, and binning are adjusted based on the bed material in the imaging region. Both current and voltage are manually adjusted to produce good contrast and penetration without saturating the detector. For the CsI scintillator detector at 4×4 binning, saturation occurs when the pixel intensity on the resulting image reaches 65535. It is important to keep the image intensity values below the saturation level since information within a saturated region is essentially lost. In this study, the X-ray power settings are held constant for each fluidizing material, regardless of the testing flow rate. However, X-ray power is individually adjusted for beds of glass beads, walnut shell, and corncob. This allows for direct comparison between CT scans for a given material. For this research, CTs of glass bead beds are acquired with an X-ray voltage of 150 kV and current of 3.5 mA. An X-ray voltage of 130 kV and current of 3.2 mA is used for

both walnut shell and corncob beds. Because the walnut shell and corncob beds have similar densities, the CT X-ray power settings were identical for the two materials. For each test the fluidized bed reactor is placed in the same location to maintain consistency. It should also be noted that the side injection port is plugged for walnut shell and corncob beds with no side air injection conditions, while the port remains open for the glass bead beds. This is due to slight changes in experimental setup between the materials. Results make note of this effect.

Once the X-ray power settings are determined, a dark and light radiographic image are captured without an object in the imaging region; the dark image is captured without incident X-ray energy and the light image is captured with incident X-ray energy at the power settings used in the fluidization CT test condition. These two images are used for a linear normalization calibration discussed in the following section. Next, the fluidized bed is placed in the imaging region and the scintillation crystals in the detector are excited with X-rays for 20 minutes. The CT scan settings, including the number of vertical slices (horizontal cross-sections), slice interval, and slice start location, are also specified and the scan is initiated. Each CT scan in this research is completed in approximately 45 minutes.

Raw CT data are stored in a series of sinogram (.sin) files, each with information for 10 vertical cross-sections of data. The sinogram files for the glass bead fluidized bed are modified to correct for beam hardening (to be described in a following section). The center of rotation (COR) is also calculated for one of the volume files. The COR is a necessary parameter used in the reconstruction of volume files and accounts for the alignment of the detector. This parameter is iteratively found by reconstructing a single horizontal cross-section of the volumetric image using several COR values; the value yielding the clearest image is chosen as the COR for the volume file. COR values are determined for both the bottom and top slice of the volumetric image to account for rotational alignment. Since the detector remains in the same location for all tests, the same COR is used for all

reconstructions in this study (383 for both the top and bottom slices). Reconstruction of single slices is performed with the Recon2-D program developed by CNDE.

Once the raw sinogram files are generated and the COR is determined, the files are transferred to a 14-node cluster at CNDE for reconstruction. The reconstruction produces a 3-D volumetric image (.vol) through a filtered backprojection algorithm (Striegel, 2005). Volume files are then transferred to the X-ray computer and viewed using X-ray Image Processor (XRIP) software specifically developed for the XFloViz facility. The visualization software allows modification of viewing parameters like the spatial range, intensity range, and color mapping scale for a given file. Since volume files are always rectangular (they contain information in a 3-D matrix) and extraneous information exists outside the fluidized bed's cylindrical region of interest (ROI), a clipping feature is used to isolate the bed region. Once the desired parameters are set, 2-D images are generated for different viewing axes. Images are extracted showing x-y planes (z-slice) at various heights, the x-z plane passing through the center of the bed (y-slice), and the y-z plane passing through the center of the bed (x-slice), as illustrated schematically by Figure 3.15. A false color algorithm is applied to the resulting slice images with the XRIP software to improve contrast and to highlight important features. The colorizing method is further explained in a later section.

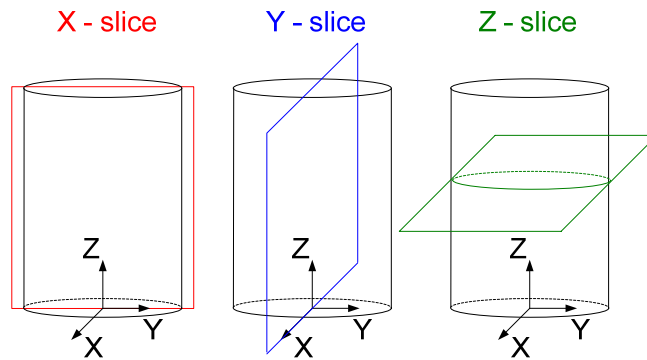


Figure 3.15: CT imaging planes.

3.5.2 Calibrations

Due to artifacts generated by CT imaging, a series of calibrations are applied to the raw data. These include a calibration for pixel normalization, beam hardening, and volumetric image stretching.

3.5.2.1 Pixel Normalization

To account for pixel non-uniformity, linear normalization is employed as outlined by Ford (2006), Heindel et al. (2008), and Striegel (2005). In ideal situations, every pixel in the detector/camera pair responds identically to incident X-ray energy; however, in real-world applications pixels do not behave ideally. In CT imaging, this non-uniform response manifests itself as “ring artifacts” and false density features on the resulting 3-D image. Therefore, a normalization calibration is applied to images as they are acquired to reduce this effect.

The normalization essentially performed a linear interpolation, using a dark and a light image according to (Ford, 2006)

$$I_{\text{new}} = I_{\text{image}} + (I_{\text{image}} - I_{\text{dark}}) \left(\frac{I_{\text{avg}}}{I_{\text{flat}} - I_{\text{dark}}} \right) \quad (3.2)$$

where I is the local pixel intensity and the subscripts indicate the calibrated image intensity (I_{new}), the uncalibrated image intensity (I_{image}), the dark frame intensity (I_{dark}), the light frame intensity (I_{flat}), and an average of the light and dark intensities (I_{avg}). Before a CT test, a dark radiographic image is captured without X-rays. A light (flat) image is also captured without an object in the imaging region using the same X-ray power settings as the test conditions. From these two files, the PS_CT imaging program automatically applies the calibration to the images during acquisition.

3.5.2.2 Beam Hardening

During reconstruction of CT volume files, an artifact called beam hardening is often present and must be removed for accurate density information (Ramakrishna et al., 2006). Beam hardening is an effect of the polyenergetic nature of X-rays; the linear X-ray attenuation coefficient, μ , for low energy X-rays is typically much larger than μ for high energy X-rays in most materials (Ramakrishna et al., 2006). Consequently, low energy X-rays are preferentially attenuated in high density materials, causing regions of the CT image to appear less dense than they truly are. For example, Figure 3.16 shows the effects of beam hardening on a static bed of glass beads. It should be noted that high-density regions in grayscale CT images appear lighter than low-density regions. The images on the left show a CT x-slice and z-slice the bed without being corrected; the images indicate high density material around the edges of the bed despite the uniform composition of the bulk material. The images on the right show the same images corrected for beam hardening. Beam hardening occurs in most materials; however, high density materials like glass or sand exhibit more beam hardening than lower density materials such as corncob or walnut shell.

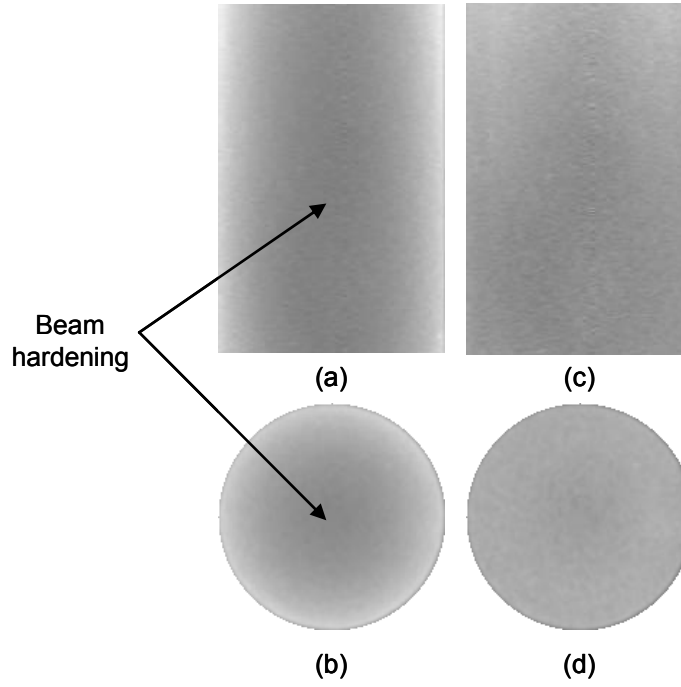


Figure 3.16: CT slices for bulk glass bead bed: (a) x-slice and (b) z-slice without corrections for beam hardening, (c) x-slice and (d) z-slice with corrections for beam hardening.

Two methods are typically used to reduce beam hardening in the CTs. In the first method, a filter is placed in front of the X-ray source to suppress low energy X-rays. This study utilizes copper and aluminum filters with thicknesses of 0.6 mm and 1.5 mm respectively. The number and type of filter depend on the material being visualized. The second method applies an “effective μ ” calibration to the raw CT data. The transmission of X-ray energy through a material is governed by the Beer-Lambert law,

$$I = I_0 e^{-\mu T} \quad (3.3)$$

The intensity of the transmitted X-ray energy which is incident on a detector, I , is a function of the X-ray intensity incident on the object, I_0 , the linear attenuation coefficient, μ , and the thickness of the object, T . The linear attenuation coefficient is a product of the mass attenuation coefficient and density; therefore, for a constant material the attenuation coefficient is only a function of density. Also, I_0 may be regarded as the intensity of the X-

ray energy that does not pass through the object (i.e., the intensity in air). Rearranging the Beer-Lambert law yields a more useful form,

$$\ln(I/I_0) = -\mu T \quad (3.4)$$

By plotting $\ln(I/I_0)$ versus T , a fifth-order polynomial curve-fit, $P(T)$, can be generated. Without beam hardening, this plot should yield a linear line; however, beam hardening causes $P(T)$ to deviate as thickness increases. An arbitrary line, $S(T)$, can be created that is tangent to the polynomial curve at small T locations. This resembles the linear attenuation coefficient in an ideal scenario without beam hardening. The subtraction of the curve-fit from the arbitrary line yields the effective μ correction factor, $F(T)$,

$$F(T) = S(T) - P(T) \quad (3.5)$$

The correction factor can be plotted against $\ln(I/I_0)$ to produce another fifth-order polynomial curve fit, $F(T)$. The $F(T)$ curve-fit can be applied to the raw CT data to remove beam hardening effects. Since the correction factor is dependent on the arbitrary line $S(T)$, the beam hardening correction is a somewhat iterative process. The beam hardening plots used for glass bead beds are shown in Appendix A.

Since beam hardening occurs due to varying thickness in a material, the relationship between the thickness and X-ray attenuation must be known. In the fluidized beds used in this study, the fluidizing material is in bulk granular form with air between individual particles. Because of the small particle sizes, it is difficult to quantify the relationship between X-ray attenuation and a single particle of the bed material.

To overcome this problem for the glass bead bed, a glass calibration “wedge” is utilized. By measuring the X-ray attenuation characteristics through given thicknesses of glass, an effective μ is calculated. The wedge consists of three 30×41 cm (12×16 in) sheets of DSB (double strength) soda-lime glass, cut into 24, 10.2 cm (4 in) wide sections of specific lengths, shown in Appendix A. By stacking sections of glass, an array of 12 thicknesses is

created. The section thicknesses are chosen to give highly detailed attenuation information through small thicknesses of glass and less detailed information at larger thicknesses to increase the data range. Each section in the wedge overlaps the previous section by 1.27 cm (0.5 in) to allow a wide region of intensities to be averaged for each of the 12 thicknesses. The wedge is composed of soda-lime glass to match the composition of glass beads used in the fluidized bed. Each glass section is sanded to reduce the risk of injury from glass shards. A wooden frame is constructed to contain the glass sections without movement and to reduce the risk of injury. Image of the glass wedges are available in Appendix A.

To perform the beam hardening calibration on the glass bead fluidized beds, a radiograph of the glass wedge is acquired with the scintillator detector/CCD camera pair. The X-ray parameters are identical to those used in CTs of fluidizing glass beads. The average intensity for each of the 12 sections is determined using the XRIP software, as well as the average intensity of surrounding air (I_0). The correction factor curve-fit, $F(T)$, is applied to raw CT sinogram data files using the SAS Beam Hardening program developed by CNDE. For this study, beam hardening calibrations are only applied to fluidized beds of glass beads where beam hardening is noticeable. Beam hardening is not observed in walnut shell and corncob CTs because both materials have low densities. Also, it should be noted that beam hardening corrections are dependent on the specific X-ray power settings used in the CT acquisition.

3.5.2.3 Volumetric Image Stretching

An additional calibration is applied as a result of stretching in the horizontal x- and y- directions during reconstruction of the volumetric image. For this study, data acquisition with 4×4 binning utilized 768 × 512 active pixels. Since reconstruction of each horizontal slice is contained in a 512×512 pixel region, the horizontal x- and y- directions are reduced by 66.7% (512/768 pixels). To overcome this stretching, the x- and y-axis on each CT image is increased by 150% (768/512 pixels) (or alternatively shrinking the z-axis by 66.7%) using a

batch process method in Adobe Photoshop. The resulting images have accurate aspect ratios, with a resolution of 15.6 pixels per cm (or 0.6 mm per pixel). Note that stretching of the volume files only affects the CT images but does not affect the actual CT intensity data. An example of volumetric image stretching in a bed of glass beads is shown in Figure 3.17. The left image shows the x-slice in a bed of bulk glass beads, generated by the software. The right image presents the same image corrected for stretching.

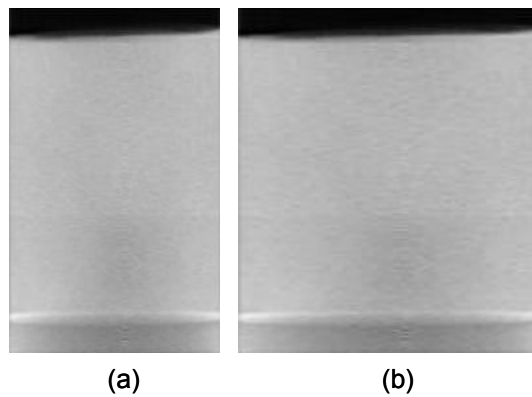


Figure 3.17: CT x-slice for glass bead bed: (a) original image, and (b) corrected for stretching.

3.5.3 Finding Gas Holdup from CT Data

In order to quantify the CT data, the time-averaged local gas holdup is calculated for all materials and flow combinations. Gas holdup (void fraction or volumetric gas fraction) is a ratio describing the amount of void space in a material. This is particularly useful in understanding heat and mass transfer phenomena, as mentioned in Chapter 2.

3.5.3.1 Gas Holdup Derivation

The local gas holdup (ϵ_g) can be determined from equation (3.6), by knowing the local X-ray attenuation for the flow (μ), the individual particle (μ_p), and the gas (μ_g) (Hammer et al.,

2006). Since attenuation is proportional to CT intensity, the local gas holdup can be calculated from CT intensity data for the flow (I), the particle (I_p), and the gas (I_g).

$$\varepsilon_g = \frac{\mu - \mu_p}{\mu_g - \mu_p} = \frac{I - I_p}{I_g - I_p} \quad (3.6)$$

The CT intensity for a single particle cannot be determined due to the small size of each particle; however, by manipulating the bulk phase gas holdup equation, the CT intensity for a bed of particles (I_b) can be substituted instead. Using equation (3.6), the void fraction for the bulk material can be calculated from CT intensities,

$$\varepsilon_{g,b} = \frac{I_b - I_p}{I_g - I_p} \quad (3.7)$$

For a granular material, the void fraction of the bulk material ($\varepsilon_{g,b}$) is constant, and is defined by

$$\varepsilon_{g,b} = 1 - \frac{\rho_b}{\rho_p} = \text{Constant} \quad (3.8)$$

The bulk density (ρ_b) and particle density (ρ_p) for each material are provided in property tables or may be experimentally calculated. Substituting and rearranging equations (3.6) and (3.7) yields the local gas holdup based on CT intensities for the fluidization (flow) condition, the gas, and the bulk material:

$$\varepsilon_g = \frac{I - I_b + (I_g - I)(\varepsilon_{g,b})}{I_g - I_b} \quad (3.9)$$

3.5.3.2 Gas Holdup from CT Data

In this study, a CT of the static bulk material and a CT of the empty vessel (air only) are collected for each material, with the same power settings used for CTs of the various flow

conditions. The XRIP program, mentioned earlier, uses these three files to convert CT intensities in each flow file into time-averaged local gas holdup information. From equation (3.9), gas holdup for each volumetric pixel, or voxel, in the flow file ($I(i, j, k)$) is calculated and the 3-D array of local gas holdup values is reassembled into another volumetric image file.

Due to image artifacts and noise, six different methods of calculating the gas holdup are evaluated in order to determine the best procedure for data analysis: (i) averaging gas and bulk files and using local flow data, (ii) smoothing the file generated by method (i), (iii) using local gas, bulk, and flow data, (iv) smoothing the file generated by method (iii), (v) pre-smoothing gas and bulk data and then using method (iii) for calculations, and (vi) smoothing the file generated by method (v). In the first two methods it is assumed that since the bulk and gas CT intensities are ideally uniform throughout the bed, the average intensity values throughout the reactor accurately describe the CT data. These averages, \bar{I}_b and \bar{I}_g and the local flow intensities are applied to equation (3.9). This method reduces the effects of local pixel noise from the air and bulk files; however, artifacts of the reactor are shown to significantly affect the data. The second approach, based on the averaging method, uses a smoothing approach on the resulting local gas holdup file. Essentially, for each voxel, the neighboring 27 voxels are averaged. Smoothing decreases some noise in the gas holdup file but image artifacts are still present. A similar smoothing approach is employed by Wu et al. (2007) to remove streaks in CT images. It is observed that the averaging method is ideal for homogeneous materials when few image artifacts are present; however, this approach induces too much error for fluidized bed applications.

In the remaining gas holdup calculation methods, each voxel in the gas holdup file is calculated using the local CT intensity values for the bulk ($I_b(i, j, k)$), air ($I_g(i, j, k)$), and flow files ($I(i, j, k)$). In the third calculation method, local voxel intensities are used directly in the calculations. While this method removes some of the image artifacts, it also introduces

some noise due to the heterogeneous nature of the bulk bed material. The fourth calculation method involves smoothing the locally calculated gas holdup file. In the fifth calculation type, bulk and air files are smoothed before calculation, and then the local bulk, air, and flow intensities are used directly in calculations. The final gas holdup calculation method involves pre-smoothing the gas and bulk files, then calculating the local gas holdups directly, and finally smoothing the resulting file.

3.5.3.3 Validating Gas Holdup

To verify equation (3.9), two CTs are captured of bulk glass beads in the reactor, and one of an empty reactor at identical X-ray power settings. Since the bulk material is a static system with a known bulk density, the bulk gas holdup is calculated from equation (3.8). With the bulk density for glass beads calculated as 1481 kg/m^3 and particle density of 2600 kg/m^3 (Table 3.1), the bulk gas holdup for glass beads is 0.43 according to equation (3.10).

$$\varepsilon_{g,b} = 1 - \frac{\rho_b}{\rho_p} = 1 - \frac{1481}{2600} = 0.43 \quad (3.10)$$

Gas holdup is calculated for the bulk material bed using the six methods mentioned previously and the results are compared to the expected value of 0.43. The results show that all six calculation methods produce similar gas holdup data with a deviation in the gas holdup file between 0.38 and 0.45; however, the data generally under-predict the bulk gas holdup. This may be due to experimental error in measuring the bed height and weight for bulk density; a slight error in bulk density propagates to a larger error in the bulk gas holdup calculation. Still, the data falls within an acceptable range of gas holdup and is used for calculations in this research. Plots of this validation and important equations are shown in Appendix C.

From these data, the ideal gas holdup calculation method is also identified for the study. It is observed that initially smoothing the bulk and air CT data, then using local voxel

information to calculate local gas holdup, and finally smoothing the resulting gas holdup data reduces noise and image artifacts more than the other approaches. The standard deviation, indicative of noise in the data, is also reduced with this method. As a result, this approach is employed to calculate local gas holdup from CT data in this research. Gas holdup images, tables, and plots showing the various calculation methods and the validation may be found in Appendix C. Additionally, the validation was performed on a fluidized bed of glass beads to ensure the calculation method remains applicable with a dynamic system; the validation is also provided in Appendix C.

3.5.3.4 Gas Holdup Summary

To recap, CTs are captured for each of the material and flow combinations described earlier. In addition, a CT of the empty reactor and a CT of a static bed are captured with the same X-ray power settings as the flow tests. The data are linearly normalized during data acquisition to remove the effects of pixel non-uniformity. For CTs of glass bead fluidized beds, a beam hardening calibration is applied to the raw sinogram files to remove the effects of preferential attenuation of X-rays in dense materials. The COR is next found for each material. Finally, CTs are reconstructed using a filtered backprojection algorithm. To calculate the gas holdup for each flow file, the bulk and air files are initially smoothed. The local flow, bulk, and air CT intensity data are subsequently fed into the gas holdup equation (equation (3.9)) to determine the time-averaged local gas holdup of the fluidized bed for each flow and material condition. The resulting gas holdup data is also smoothed to reduce noise. Finally, 2-D images are generated showing selected planes of the gas holdup image. The process is shown schematically in Figure 3.18.

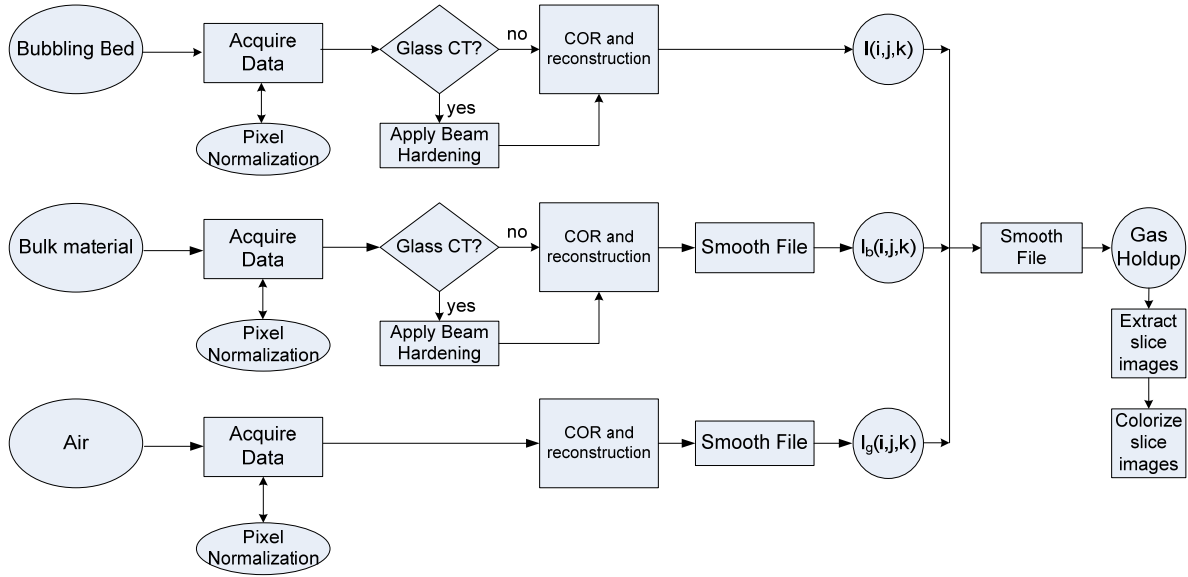


Figure 3.18: Flowchart for calculating local gas holdup from XCT data.

3.6 Radiography/Stereography/Particle Tracking

X-ray radiography provides a single 2-D plane projection of the density variation in a 3-D object. X-ray stereography is achieved by simultaneously acquiring radiographs from two different projections. For each fluidized bed material and flow combination, two radiographic images are simultaneously acquired at a frame rate of 20 frames per second (fps) at perpendicular orientations. These results can then be compared to CT/gas holdup data for identical fluidization conditions. In addition, a tracer particle is injected into a glass bead fluidized bed during a selected test with side air injection. Tracers are not injected into the walnut shell or corncob beds since the tracers developed in this study are found to sink upon injection. This study lays the groundwork for future studies using X-ray stereography that will capture dynamic fluidization features such as bubble size and rise velocity, and generate 3-D velocity profiles of injected particles at varying superficial and injector flow conditions. The first subsection in this section explains the procedure used to capture radiographic/stereographic images. As with CT imaging, radiographic images undergo a

series of calibrations to correct for inherent artifacts, and these are described in the second subsection. In addition, a coloring algorithm is applied to selected images to enhance the internal features; the coloring method is explained in subsection three. Corrected radiographic images are compiled into stereographic images which are next compiled into stereographic .avi movie files. For one stereographic movie, a particle is injected and tracked for one second with a manual particle tracking method, and is described in the last subsection.

3.6.1 Procedure

Stereographic data acquisition is similar to CT collection outlined earlier. Before capturing data, the X-ray sources are initially warmed-up. FxVisual software, developed by CNDE, is used to adjust the image acquisition parameters, display real-time X-ray images, control the rotation ring motion, and capture radiographic/stereographic information. In stereography low energy radiation is suppressed with copper and aluminum filters with thicknesses of 0.6 mm and 1.5 mm respectively. After warm-up, the X-ray power settings and camera binning levels are adjusted for the specific material in the imaging region. Stereographic X-ray power settings are slightly different than those used in CT scans due to differences in equipment. As with CT imaging, it is desired to set the X-ray power below saturation of the image. For 2×2 binning with the 12-bit frame grabber, saturation occurs at an image intensity value of 4095. Unfortunately, X-rays are unable to penetrate the glass bead fluidized bed without saturating the sides of the column. Since the image intensity values for radiographs/stereographs are not used in quantitative measurements in this study, saturation of the reactor walls is acceptable in glass fluidized beds. An X-ray voltage of 140 kV and current of 0.2 mA is used in stereographic imaging of glass bead beds, while an X-ray voltage of 120 kV and current of 0.2 mA is used in walnut shell and corncob beds; since

walnut shell and corncob beds have similar densities, the stereographic X-ray power settings are identical for the two materials.

After warm-up, a radiograph is acquired without the reactor in the imaging region, but with a grid placed in front of the detector for use in the unwarping calibration, to be discussed later. Also, light and dark images are acquired without an object in the imaging region for use in a pixel normalization calibration. The bed is next placed in the imaging region and the movie parameters are chosen in the acquisition software. Once setup is complete, stereographic images are collected and stored as individual images. Unlike CT imaging, the image intensifier detectors do not require excitation before data acquisition. The resulting images are calibrated and compiled into .avi movie files using the XRIP software. Particle tracking is next performed on selected stereographic frames as a proof-of-concept. Some of the gray-scale movie files are also colorized to highlight important internal features.

3.6.2 Calibrations

Three major calibrations are applied to the radiographic/stereographic images to improve contrast and to remove certain artifacts. Images are first converted from a 12-bit to a 16-bit format, then pixel normalized, and finally unwarped. Due to data writing restrictions on the X-ray PC, the calibrations are applied after data collection. This speeds up the collection process and allows acquisition of longer movies. Calibrations are applied with the internally developed XRIP software, also used for CT and gas holdup analysis. The software provides a batch method to apply desired calibrations to a selection of images. This feature is extremely useful since a short 30 second movie taken at 20 fps can result in 600 images for a radiographic movie or 1200 images for a stereographic movie, each requiring calibration. In addition, the software allows stereographic images to be placed side-by-side to show both views simultaneously. A cropping method is also available to focus on a desired region in the bed.

3.6.2.1 12-bit to 16-bit Conversion (Lightening)

When X-ray radiographic/stereographic images are collected with the FxVisual software, data are output as 16-bit .tiff images. Since 12 bits of information are collected by the XFloViz 12-bit frame-grabbers, only 12 bits of data are stored in the 16 bit format. As a result, the raw data has an intensity range of 0 to 4095 (12-bit) saved in a file with an intensity ranging from 0 to 65535. The resulting images, when opened with any program other than FxVisual, appear completely black. To allow other programs to open the radiographs, a conversion calibration multiplies the intensity of each pixel in the radiographic images by a factor of 4 in order to stretch the pixel intensity range - to match a 16-bit image. The resolution is unchanged by the calibration.

3.6.2.2 Pixel Normalization

As with CTs, a normalization calibration is applied to the data to account for pixel non-uniformity. A linear interpolation routine is again used with a flat and a dark image. Ten frames are collected and averaged for both flat and dark images to reduce noise in the calibration. Since the pixel intensity values are not used quantitatively, and the X-ray intensity is near or above saturation, the normalization calibration does not have major significance for stereographic imaging in this research.

3.6.2.3 Unwarping

When radiographs are taken with the image intensifier detectors, the resulting images are warped around the edges. To account for warping effects, an unwarping calibration is applied to each image. Figure 3.19 shows warping effects in a radiographic image of fluidized glass beads on the left, and the image after the unwarping calibration had been applied on the right.

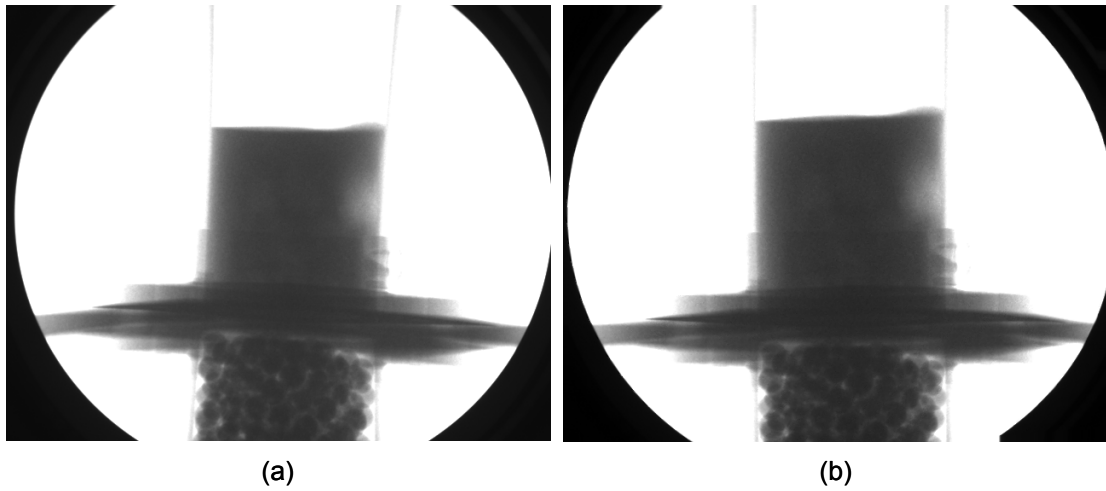


Figure 3.19: Radiographs of glass bead fluidized bed: (a) original warped image, and (b) resulting image after unwarping.

The unwarping algorithm is based on a third order polynomial curve fit of two variables: the x and y location. This method is outlined by Streigel (2005) and will be briefly mentioned here. With the imaging region cleared, a stainless steel plate with a 1.27 cm square grid of 2 mm holes is placed in front of a detector. When X-rays are incident on the plate, a radiograph of high-intensity points is generated. This image is used to create a file for the polynomial curve-fit coefficients described by Streigel (2005). Since unwarping is a function of detector orientation and location, all stereographs in this research are acquired with the image intensifier detectors in the same place.

3.6.3 Colorizing Images

To improve the contrast of the radiographic images, a false-color scheme can be applied to selected stereographic images. The XRIP software provides a colorizing method which converts 16-bit grayscale intensity values into a 16-bit RGB color-scale. The algorithm applies an independent value to a red, green, and blue channel based on the grayscale intensity value up to 65535. Four set-points define the equation for each color; the set-points are adjusted to provide a color scale that can significantly improve the contrast for a given set

of radiographs. A default color scheme is also available to color images with a continuous blue-green-red scale. The colorizing process is included in a batch process in order to apply the same coloring scheme to many images, for colored radiographic/stereographic movie generation. Figure 3.20 shows the colorizing of a radiographic image of a glass bead fluidized bed with a tracer particle. The contrasts of the tracer particle and air bubbles are shown to significantly improve through the colorizing process.

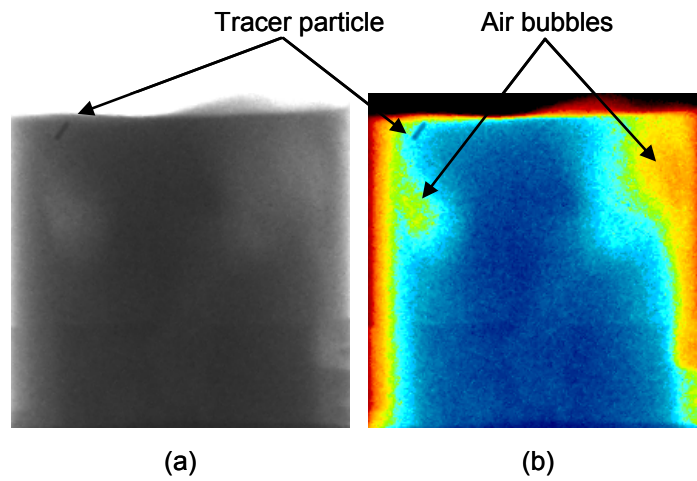


Figure 3.20: Radiographs of glass bead fluidized bed: (a) original image, and (b) the same image after colorizing.

3.6.4 Particle Tracking

For glass bead fluidization, stereographic frames are acquired at a rate of 20 fps. After 15 seconds of data collection, a single tracer particle is injected through the side port injector; an additional 45 seconds of stereographic data is acquired with the tracer in the bed. Resulting stereographic movies show the relationship between the dynamics of the injected particles and the fluidization hydrodynamics. As previously discussed, tracer particles in this research are only acceptable for glass bead fluidization; therefore, stereography of particle injection is not performed in walnut shell or corncob beds.

From the stereographic movies it is desired to track the movement of the tracer particle in the bed; however, a suitable automated particle tracking algorithm has not yet been developed for this setup. Consequently, this research presents a manual technique to find particle trajectories and velocities as a proof-of-concept. To manually track particles, stereographic frames are identified as a tracer particle is injected into a bed. For each 0.05 second increment (data is acquired at 20 fps) the center of the particle is visually located on both stereographic projections and is marked with a red dot to enhance the particle location. In some images the particle appears as a streak because it moves too quickly to obtain a definitive location; consequently, the center of the particle is estimated for calculations. The particle pixel location in x-z and y-z space is recorded based on reference coordinate systems, located on the top surface of the distributor plate and running along the center vertical axis of the bed. The process is repeated for subsequent stereographic frames captured at 0.05 second intervals. By knowing the time increment between stereographic image acquisition and the tracer particle location in each frame, the particle trajectory and velocity are determined. Constant particle motion is assumed between frames.

In this research, the proceeding particle tracking method is applied to a glass bead fluidized bed with $U_g = 1.5U_{mf}$ and $Q_s = 0.05Q_{mf}$, for one second of stereographic data. While the approach may be applied to the glass bead beds with varying flow conditions, only one case is analyzed to demonstrate that the method is successful. Manually locating tracer particles is a tedious process and an automated method would allow more conditions to be evaluated.

Chapter 4: Results and Discussion

Chapter 4 presents selected results from this research, and provides detailed discussion of these results. The discussion highlights the main trends that are observed and attempts to explain why these trends occurred. To begin, section 4.1 describes the results of minimum fluidization experiments. The section focuses on the two types of minimum fluidization; with and without side air injection. Section 4.2 contains the bulk of the analysis and describes local, time-averaged gas holdup results obtained from the X-ray CT data. This section will initially describe the effects of various flow conditions on gas holdup for each of the three bed materials. Next, the section will analyze the effects of bed material on gas holdup. Following gas holdup results, section 4.3 explains dynamic fluidization results obtained from stereographic movies. This section provides observations on the relationship between flow conditions and bed dynamics, and is followed by a discussion on the effects of bed material on stereographic imaging. Finally, section 4.4 presents preliminary particle tracking experiments in glass beads.

4.1 Minimum Fluidization Velocity

Minimum fluidization velocity is analyzed for all three bed materials and the results are presented in this section. The first subsection explains the minimum fluidization velocity results with no side air injection. The subsection also presents tables of the experimental flow conditions that are studied in later sections, and describes the relationship to minimum fluidization velocity (and flow rate). The second subsection focuses on minimum fluidization velocity results for all three bed materials with the introduction of side air. Comparisons are then made to understand how the bed material and side air injection affect minimum fluidization velocity.

4.1.1 Minimum Fluidization with No Side Air Injection

For fluidized beds of glass beads, walnut shell, and corncob, the minimum fluidization velocity without side air injection ($U_{mf,0}$) is experimentally determined according to the procedure outlined in Chapter 3. Additionally, the minimum fluidization air flow rate without side air injection ($Q_{mf,0}$) is calculated from $U_{mf,0}$. Average $U_{mf,0}$ is determined from 7 tests for glass beads and 10 tests for both walnut shell and corncob beds. Multiple tests ensure repeatability and improve the accuracy of the data; however, fewer tests are taken of the glass bead bed since the data appear to follow a typical fluidization curve. Table 4.1 shows $U_{mf,0}$, $Q_{mf,0}$, and the standard deviation of $U_{mf,0}$ for each material while selected raw data is available in Appendix B.

Table 4.1: Minimum fluidization velocity with no side air injection for glass beads, walnut shell, and corncob.

	Glass beads	Walnut shell	Corncob
$U_{mf,0}$, Average (cm/s)	21.7	18.4	17.1
$U_{mf,0}$, Standard Deviation (cm/s)	0.5	0.3	0.6
$Q_{mf,0}$, Average (Lpm)	105	89	83

From the data, it is apparent that $U_{mf,0}$ decreases with bed density. Glass beads have high density and result in $U_{mf,0} = 21.7$ cm/s. In contrast, walnut shell and corncob have much lower densities than glass and $U_{mf,0}$ is determined to be 18.4 cm/s and 17.1 cm/s, respectively. Similarly, walnut shell is slightly more dense than corncob and consequently, exhibits a slightly larger $U_{mf,0}$. It should be noted that the relationship between material and U_{mf} is not solely based on density, but is instead a complex function which includes many factors. The standard deviation of $U_{mf,0}$ shows the tests are repeatable, with a maximum deviation of only 0.6 cm/s.

The $U_{mf,0}$ tests without side air injection also show that the denser materials exhibit larger bed pressure drops. Since the volume of each bed material is constant, high density materials

have more mass than low density materials. In order for fluidization to occur, the force of the fluidizing air must overcome the weight of the bed. Consequently, a larger pressure drop is required to fluidize high density materials. To illustrate, Figure 4.1 shows the pressure drop between fluidization curves for glass beads, walnut shell, and corncob without side air injection.

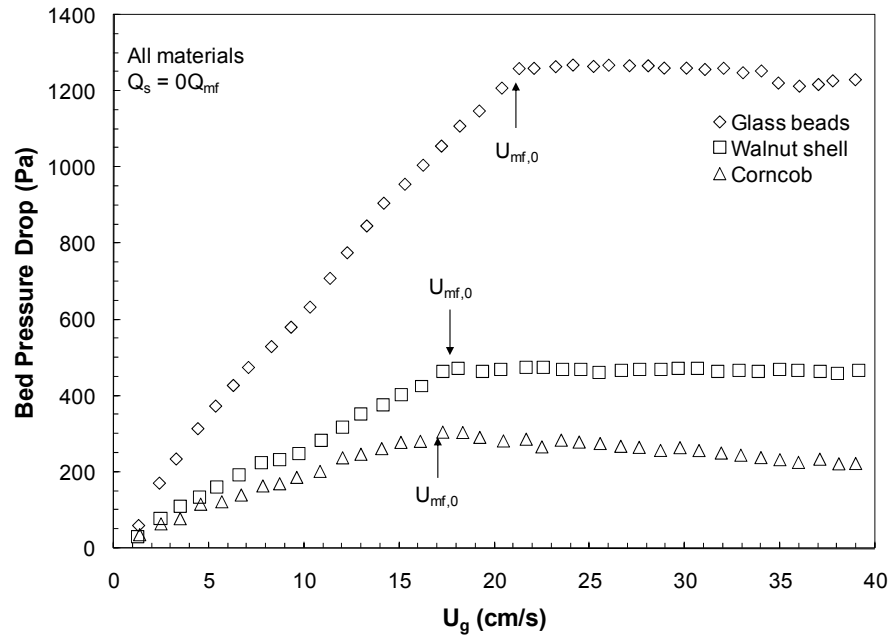


Figure 4.1: Sample $U_{mf,0}$ experimental curves for glass beads, walnut shell, and corncob with no side air injection.

As described in Chapter 3, a series of 25 test conditions is generated for each material; the conditions consist of combinations of five different bed gas velocities (U_g) and five different side air flow rates (Q_s). These velocities and flow rates are normalized to the experimental $U_{mf,0}$ and $Q_{mf,0}$ for each material. A summary of the U_g test conditions for each material is presented in Table 4.2. Similarly, the Q_s test conditions are summarized in Table 4.3. An expanded table, showing velocities and flow rates for all test conditions is available in Appendix B.

Table 4.2: Superficial gas velocity test conditions for glass beads, walnut shell, and corncob.

	Superficial gas velocity - U_g (cm/s)		
Bed material	Glass beads	Walnut shell	Corncob
$U_{mf,0}$, ($Q_s = 0$)	21.7	18.4	17.1
$U_g = 1.25U_{mf,0}$	27.1	22.9	21.4
$U_g = 1.50U_{mf,0}$	32.5	27.5	25.7
$U_g = 1.75U_{mf,0}$	37.9	32.1	29.9
$U_g = 2.00U_{mf,0}$	43.3	36.7	34.2
$U_g = 3.00U_{mf,0}$	65.0	55.1	51.3

Table 4.3: Side air injection flow rate test conditions for glass beads, walnut shell, and corncob.

	Side air injection flow rate - Q_s (Lpm)		
Bed material	Glass beads	Walnut shell	Corncob
$Q_{mf,0}$, ($Q_s = 0$)	105	89	83
$Q_s = 0Q_{mf,0}$	0.0	0.0	0.0
$Q_s = 0.05Q_{mf,0}$	5.3	4.5	4.2
$Q_s = 0.10Q_{mf,0}$	10.5	8.9	8.3
$Q_s = 0.15Q_{mf,0}$	15.8	13.4	12.5
$Q_s = 0.20Q_{mf,0}$	21.1	17.9	16.6

4.1.2 Minimum Fluidization with Side Air Injection

Since the flow conditions in this study are based on the minimum fluidization velocity with no side air injection, it is desired to see how side air injection affects the minimum fluidization velocity. For each material, air is injected at the corresponding flow rates identified in Table 4.3, and U_{mf} is determined using the same procedure mentioned in Chapter 3. Each condition is tested 2 to 3 times to improve accuracy and repeatability. The fluidization curves with side air injection are more difficult to analyze than the curves generated without side air. As Q_s increases, the slope of the pressure-velocity fluidization curve becomes more gradual, and thus, U_{mf} is increasingly difficult to calculate. In addition, with large values of Q_s there appears to be a non-linear region introduced to the fluidization curves below U_{mf} , which is repeatable for all materials. It is hypothesized that with side air injection, the fluidized beds undergo two fluidization points. Because side air decreases the

particle friction in the bed, the bed undergoes partial fluidization with U_g well below U_{mf} . As U_g increases past the partial fluidization point, the pressure-velocity slope becomes more gradual until reaching a constant pressure, which is the fully fluidized U_{mf} . For the purposes of this study, the fully fluidized U_{mf} is analyzed. Figure 4.2 identifies the apparent partial fluidization and full fluidization locations on the experimental fluidization curves for glass beads, walnut shell, and corncob with $Q_s = 0.20Q_{mf,0}$.

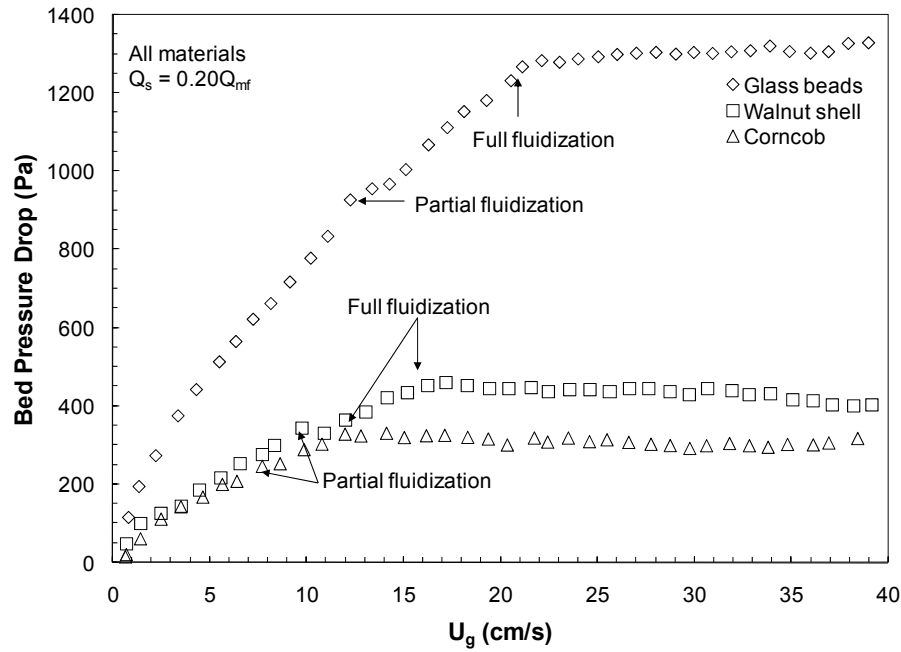


Figure 4.2: Fluidization curves for glass beads, walnut shell, and corncob with $Q_s = 0.20Q_{mf}$.

In addition to partial fluidization, the introduction of side air is found to increase the pressure drop across the bed when U_g is below U_{mf} . This effect is shown in Figure 4.3 for glass beads and in Appendix B for walnut shell and corncob beds. The fluidization curves for five Q_s conditions are also shown in Appendix B for each material. The average U_{mf} for each condition is presented in Table 4.4 with the \pm corresponding to one standard deviation. Standard deviation in U_{mf} with side air injection is observed to be larger than for $U_{mf,0}$ without side air in some cases. This is due to higher uncertainty in identifying U_{mf} ; side air

causes a gradual increase in the pressure-velocity curve instead of the sharp discontinuity as observed in $U_{mf,0}$ tests. Also, fewer U_{mf} experiments were performed with side air injection than with no side air; performing more U_{mf} experiments with side air will improve the accuracy of the results.

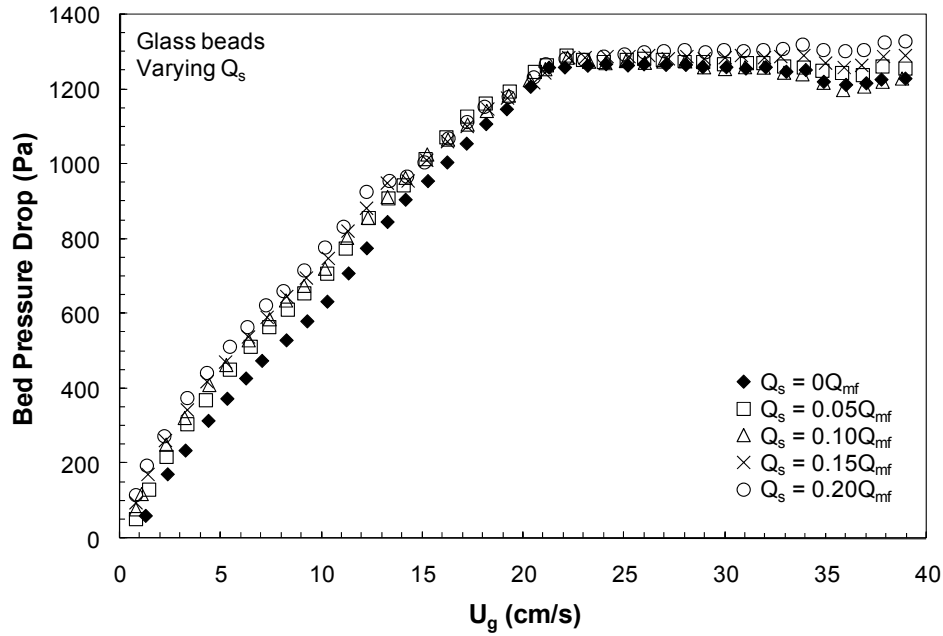


Figure 4.3: Fluidization curves for glass beads with five side air flow rates.

Table 4.4: U_{mf} for various side air flow rates in beds of glass beads, walnut shell, and corncob.

	$Q_s = 0Q_{mf}$	$Q_s = 0.05Q_{mf}$	$Q_s = 0.10Q_{mf}$	$Q_s = 0.15Q_{mf}$	$Q_s = 0.20Q_{mf}$
Glass beads U_{mf} (cm/s)	21.7 ± 0.5	22.2 ± 0.0	22.2 ± 0.0	22.2 ± 0.1	21.6 ± 0.7
Walnut shell U_{mf} (cm/s)	18.4 ± 0.3	18.3 ± 0.0	17.7 ± 0.8	16.9 ± 0.3	16.1 ± 0.1
Corncob U_{mf} (cm/s)	17.1 ± 0.6	15.1 ± 1.0	13.0 ± 1.5	12.6 ± 0.7	11.7 ± 0.6

To illustrate the effects of side air injection more clearly, U_{mf} for each material is plotted against the side air injection flow rate in Figure 4.4. As Q_s is increased for beds of walnut shell and corncob, U_{mf} decreases. Since more air is introduced into the bed, the friction between bed particles is reduced; therefore, U_{mf} is expected to decrease with increasing Q_s . Also, the corncob bed features the largest drop in U_{mf} under the five Q_s flow conditions. This

may be partly due to the low density of corncob. It is likely that Q_s has a greater impact on reducing the backpressure required to fluidize the bed than for glass beads. This also explains why U_{mf} for beds of glass beads do not significantly vary with Q_s ; a significant pressure is required to fluidize the heavier glass bed, regardless of Q_s .

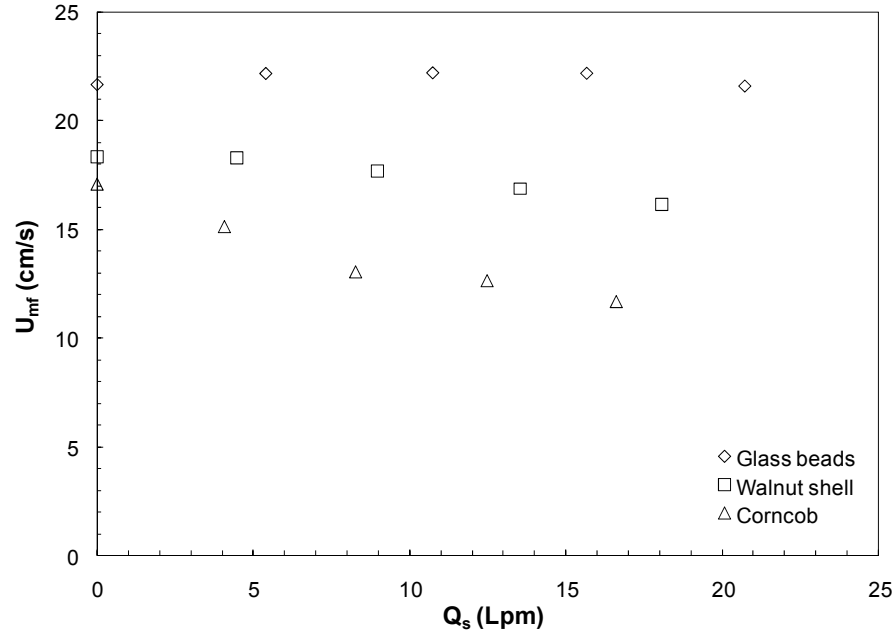


Figure 4.4: U_{mf} for various side air flow rates in beds of glass beads, walnut shell, and corncob.

4.2 Gas Holdup

In this section, X-ray computed tomography is used to calculate the local time-averaged gas holdup in fluidized beds of glass beads, walnut shell, and corncob with varying flow conditions. Combinations of five superficial gas velocities and five side air flow rates are examined for each material, as outlined in Tables 4.2 and 4.3, respectively. For simplicity, the remainder of this Chapter will drop the 0 subscript on $U_{mf,0}$ and $Q_{mf,0}$ when referring to the flow conditions, which are based on minimum fluidization without side air injection. This section will also refer to the local time-averaged gas holdup simply as the gas holdup. The

first subsection describes effects of varying U_g and Q_s on fluidization behavior. Analysis is performed on the effects of U_g and Q_s on glass beads, walnut shell, and corncob fluidized beds independently. In the second subsection, local gas holdup is compared between all three bed materials.

For gas holdup comparisons, a series of 2-D x-, y-, and z-slice images are acquired. Y-slices pass through the center of the bed and the injection port and are useful in understanding how air injection affects fluidization. Z-slices highlight the fluidization symmetry. Although the CT imaging region is composed of 350 z-slices, results at heights of 3.2 cm and 9.0 cm above the distributor plate are reported in this section; these heights correspond to the top of the side air injector and the top region of the bed ($H/D = 0.88$), respectively. X-slices also show the fluidization symmetry and are available in Appendix C.

In addition to the images, time-averaged local gas holdup data are plotted with respect to spatial location to provide more quantitative results in this section. Some fluctuations on the plots are observed, and are attributed to noise induced by the gas holdup calculations and CT imaging artifacts. Because the same bulk material and air files are used in gas holdup calculations, some regions of the plots may look like highly repeatable features. By comparing plots to images, noise on the plots can be differentiated from the important flow features. It should be noted that the lines connecting data points on the plots are only presented to show trends and do not imply continuous data.

4.2.1 Effect of Various Flow Conditions on Local Gas Holdup

For each material, the local time-averaged gas holdup is compared for each U_g and Q_s condition. Each collection of images in the following subsections show y- and z-slices for all five Q_s conditions for a given U_g condition. The edges of the images represent the boundaries of the fluidized bed; the bottom of each y-slice represents the top of the distributor plate and the edges of the y- and z- slices represent the bed chamber walls. Horizontal dashed lines on

the y-slices correspond to the locations of the z-slices, and “grayed” region on the bottom-right of the y-slices show the location of the side air injection port. At the top of each collection of slices is the color scale corresponding to gas holdup. It should be noted that in this subsection, the gas holdup color scales are identical for all slices in a given material but are different between materials. The scales are modified individually here for each material in order to improve color resolution. As a result, the bed materials cannot be directly compared by color; however, the actual gas holdup values are unaffected. Gas holdup data are also plotted to further illustrate trends identified on the x-, y-, and z-slice images.

4.2.1.1 Glass Beads

The local time-averaged gas holdup for y- and z-slice images are presented in Figure 4.5 for a glass bead fluidized bed with $U_g = 1.25U_{mf}$ and all five Q_s conditions. For glass bead beds, the gas holdup color scale ranges from $\epsilon_g = 0.2$ to $\epsilon_g = 1.0$ to highlight important flow features. Additionally, it should be noted that the theoretical bulk void fraction, $\epsilon_{g,b}$, for glass bead beds is approximately 0.43 (as shown in Table 3.1); this calculation is available in Appendix C.

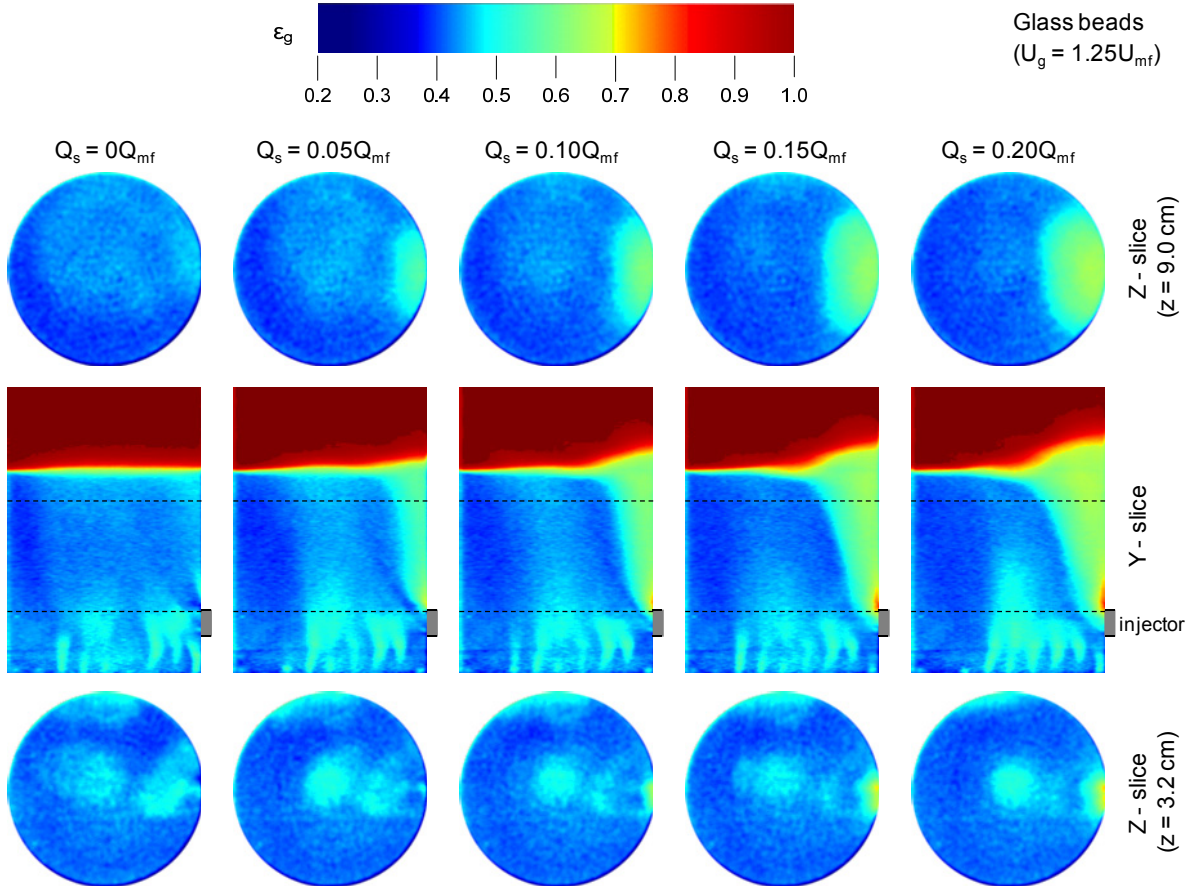


Figure 4.5: Gas holdup y- and z-slices for glass bead fluidization: $U_g = 1.25U_{mf}$, varying Q_s .

With no side air injection and $U_g = 1.25U_{mf}$, both y- and z-slice images in Figure 4.5 demonstrate that the bed fluidizes fairly uniformly. This is also illustrated by plotting local gas holdup as a function of x- and y- location for various axial heights from the distributor plate (z-slices). Figure 4.6 and Figure 4.7 show these plots for glass bead fluidization with $U_g = 1.25U_{mf}$ and $Q_s = 0Q_{mf}$. In Figure 4.6, local gas holdup along the y-axis at four heights (on the x-slice) is plotted. The boundaries of the bed are shown by vertical lines. Note that at $y = 5.2 \text{ cm}$ gas holdup sharply decreases to about 0.20 due to a small portion of the reactor wall caught in the region applied to gas holdup calculations. Figure 4.7 shows gas holdup at the identical four heights along the x-axis (on the y-slice passing through the injector). Both plots show that for all four heights, local gas holdup is approximately constant throughout the bed.

Since the two plots show similarly distributed data on perpendicular axes, the fluidization is assumed to be uniform and symmetrical throughout the bed when $Q_s = 0Q_{mf}$. This effect was also observed in the literature (Bhusarapu et al., 2006; Du et al., 2005).

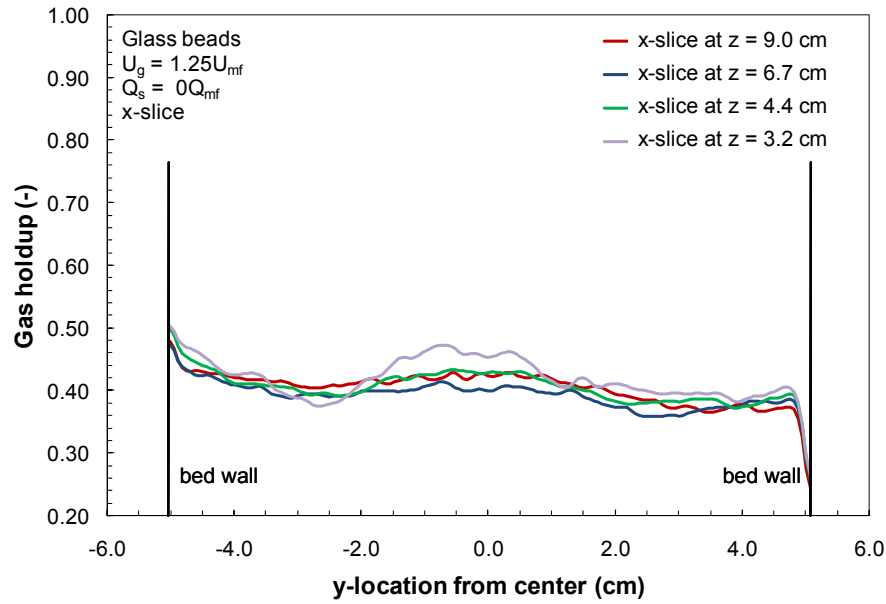


Figure 4.6: X-slice gas holdup for glass bead fluidization at four heights: $U_g = 1.25U_{mf}$, $Q_s = 0Q_{mf}$.

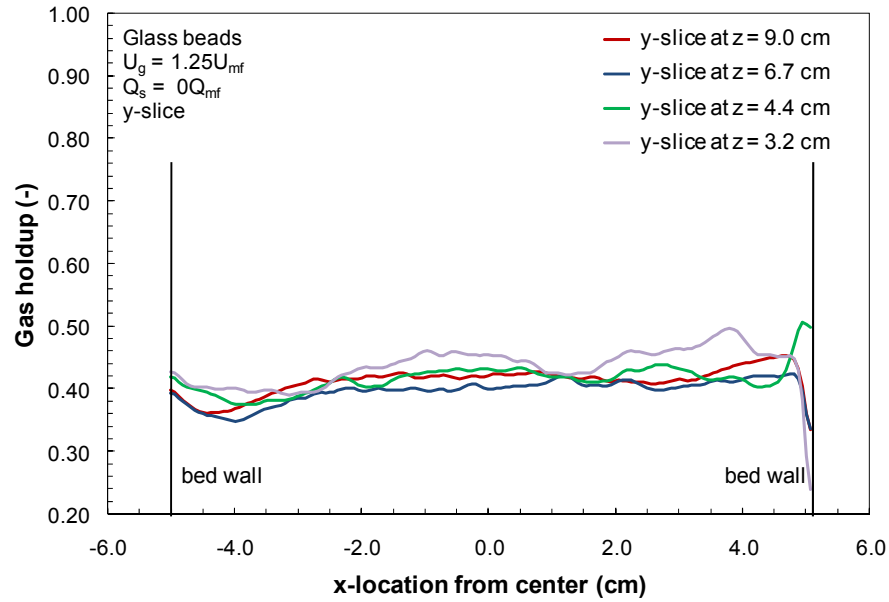


Figure 4.7: Y-slice gas holdup for glass bead fluidization at four heights: $U_g = 1.25U_{mf}$, $Q_s = 0Q_{mf}$.

The plots in Figure 4.6 and Figure 4.7 and the images in Figure 4.5 show the local gas holdup throughout the bed is distributed near the bulk gas holdup of 0.43. This suggests that for superficial gas velocities only slightly above the minimum fluidization velocity, the bed is barely fluidized, which is expected. Noise in the system and measurement errors cause some local gas holdup data to fall below the theoretical bulk gas holdup, and this was similarly seen in the validation of the gas holdup equations. It is also possible that regions of the bed experience packing phenomena during fluidization, which may cause local gas holdup data to fall below $\varepsilon_{g,b}$.

The y-slice images and plots for $Q_s = 0Q_{mf}$ demonstrate that the injection port influences the bed hydrodynamics, even without side air injection. In the image, a region of relatively high local gas holdup is observed directly above the injection port. Again this is validated by the plot in Figure 4.7 where a relatively high local gas holdup occurs on the y-slice around $x = 5.0$ cm for a height of $z = 4.4$ cm. Since the side injection port is not plugged in glass bead fluidization with $Q_s = 0Q_{mf}$, the injection system likely influences bed hydrodynamics more than if the side injection port is plugged. It is also possible that drag from the injector port causes slight asymmetry in the fluidization uniformity.

Y- and z-slice images also show that the fluidizing air coming from the distributor plate is not completely uniform. Regions of higher local gas holdup on the images indicate that fluidizing air preferentially flows by the walls and the center of the bed for $U_g = 1.25U_{mf}$. Preferential flow paths in the images are identified as regions of relatively high local gas holdup compared with the surrounding material. Figure 4.6 and Figure 4.7 also show this effect, most clearly for axial heights of 3.2 cm. Without side air, the y-slice images indicate the bed has a uniform time-averaged height.

Similar trends are seen in Figure 4.8, which plots the average planar gas holdup as a function of bed height for glass bead fluidization with $U_g = 1.25U_{mf}$ and no side air injection.

The plot shows that the average gas holdup slightly decreases in the bed as axial height increases; however, the average planar gas holdup is still fairly constant throughout the bed. As discussed earlier, the gas holdup below the bulk gas holdup indicates measurement errors, noise, and packing effects. The bed surface is also clearly shown in Figure 4.8 as the section of the curve which is nearly horizontal. It should be noted that the deviation in the gas holdup plot near $z = 1$ cm originates from an artifact in the CT reconstruction caused by the lower flange on the bed chamber; this artifact is relatively insignificant to the plot.

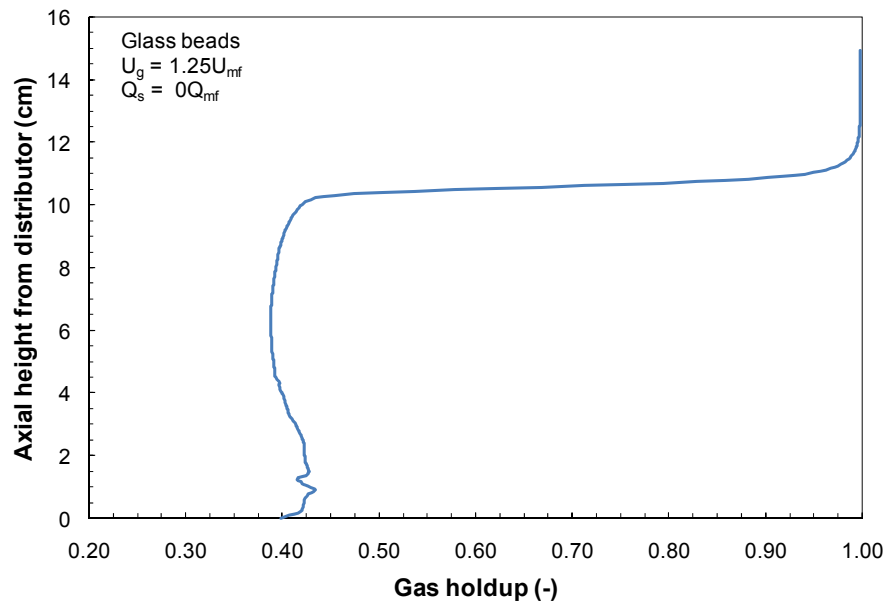


Figure 4.8: Average gas holdup by height for glass bead fluidization: $U_g = 1.25U_{mf}$, $Q_s = 0Q_{mf}$.

Figure 4.5 also highlights the effects of increasing side air injection on fluidization behavior; with side air injection, the region above the injector has a much higher local gas holdup than the surrounding bed due to the larger quantity of air flowing from the injector to the top of the bed. This dilute region resembles a boundary layer with a clearly definable limit and shows that the majority of the air flows near the reactor wall. The side injector air flow path gradually penetrates into the bed and this expansion increases with height from the injector. This occurs due to high velocity air from the injector mixing with bed material and

expanding into the bed. To further illustrate, Figure 4.9 shows local y-slice gas holdup plotted at four heights from the distributor plate for glass bead fluidization with $U_g = 1.25U_{mf}$ and $Q_s = 0.10Q_{mf}$. Directly above the injector at $z = 3.2$ cm, a region of high local gas holdup exists but does not extend far into the bed. As height increases, the magnitude of the local gas holdup in this region decreases slightly, but the width of the region significantly increases. Injection air also produces an asymmetric average bed height; above the injector the average bed height is much larger than the surrounding bed. The highest average bed height occurs near the wall directly above the injector. The bed height effects are most clearly shown in the y-slice images (Figure 4.5). While the images show non-symmetrical fluidization with side air injection, the z-slices show that fluidization remains fairly symmetrical about the x-axis. The plot of the local gas holdup along the y-axis (x-slice) for the bed in Figure 4.9 also demonstrates symmetrical fluidization, and is presented in Appendix C.

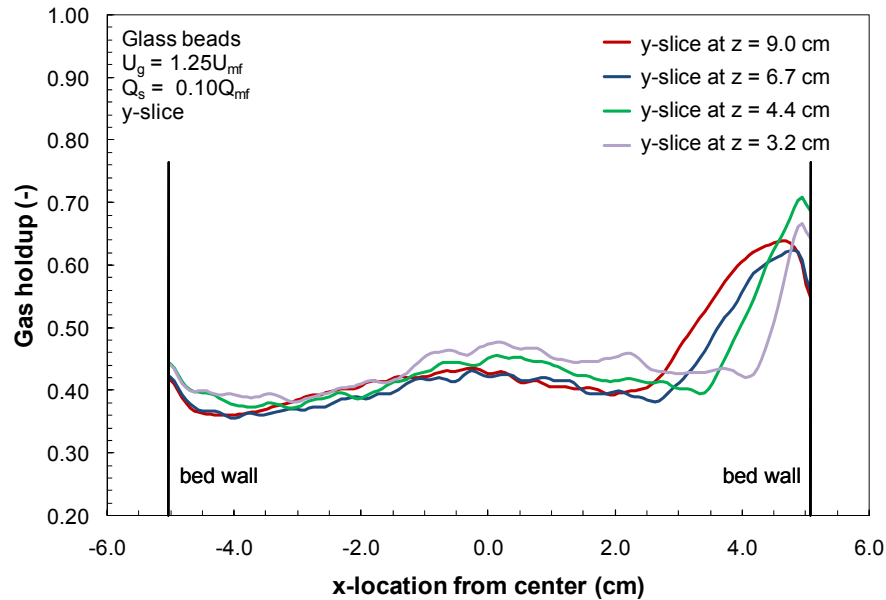


Figure 4.9: Y-slice gas holdup for glass bead fluidization at four heights: $U_g = 1.25U_{mf}$, $Q_s = 0.10Q_{mf}$.

As Q_s increases, the local gas holdup above the injector port increases, as expected. The boundary of the injection air flow path also extends further into the bed with increasing Q_s . This effect can be seen in the z-slice images of Figure 4.5; at $z = 3.2$ cm, a small region of high gas holdup occurs near the side air injection port while at $z = 9.0$ cm, the high gas holdup region has expanded over much of the bed. Plots of local gas holdup also illustrate this effect. Figures 4.10 and 4.11 present plots of y-slice local gas holdup along the x-axis for two heights and all five Q_s conditions. Figure 4.10 shows that local gas holdup directly above the injector increases as Q_s increases at $z = 3.2$ cm. Similarly, Figure 4.11 shows local gas holdup above the injector at $z = 9.0$ cm increases with Q_s but also expands further towards the center of the bed. For instance, at $Q_s = 0.05Q_{mf}$ the high gas holdup region caused by the side air injection extends from around $x = 3.0$ cm to the reactor wall. At $Q_s = 0.20Q_{mf}$, this region extends from around $x = 1.5$ cm to the reactor wall. Directly above the side injection port is a small region of very high local gas holdup, indicating that the side air injection creates a jetting effect as it is introduced. With increased Q_s , this high gas holdup region also increases in size. Images in Figure 4.5 and the plot in Figure 4.10 show how jetting from side air injection increases with Q_s . Increasing Q_s also increases the average bed height above the injector while the rest of the bed remains approximately the same height. This effect is clearly observed in the y-slice images (Figure 4.5).

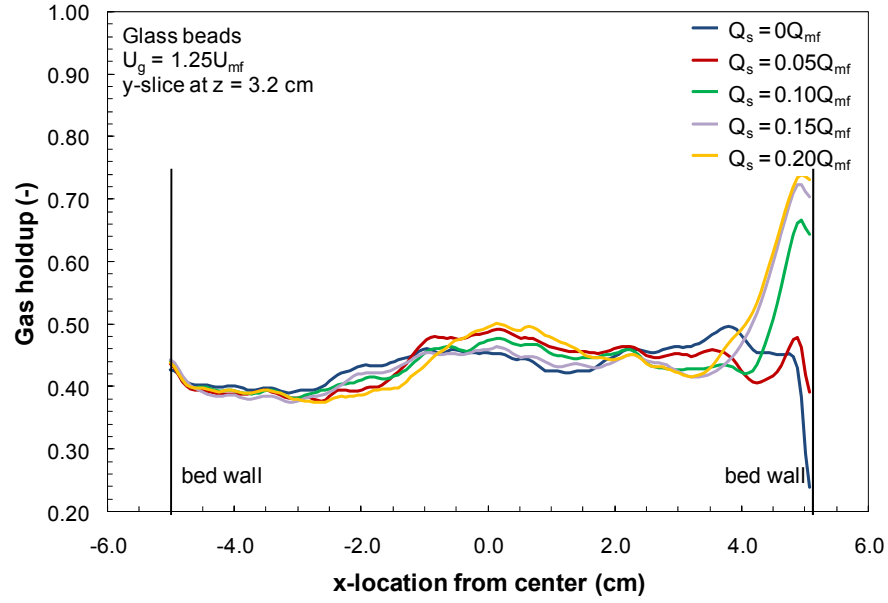


Figure 4.10: Y-slice gas holdup for glass bead fluidization at $z = 3.2$ cm: $U_g = 1.25U_{mf}$, varying Q_s .

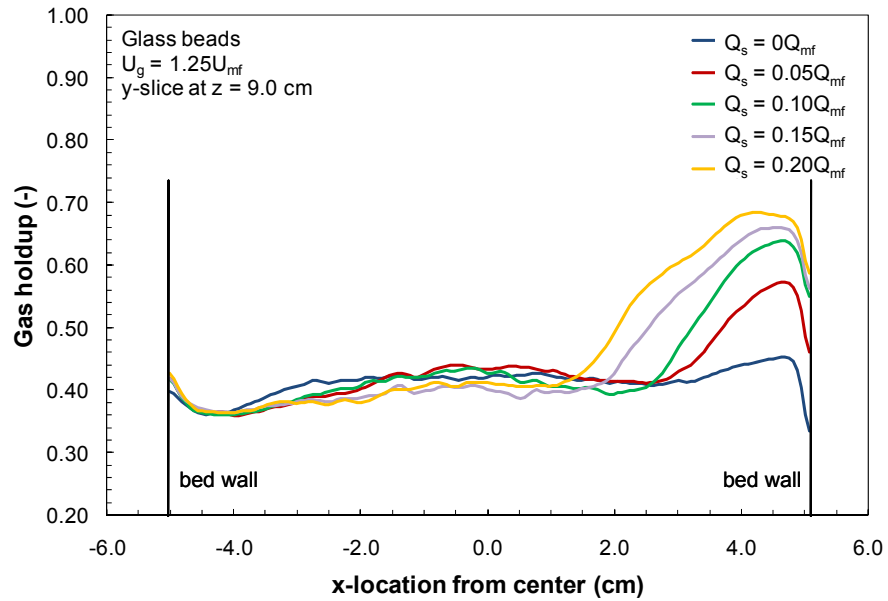


Figure 4.11: Y-slice gas holdup for glass bead fluidization at $z = 9.0$ cm: $U_g = 1.25U_{mf}$, varying Q_s .

Changes in Q_s are observed to affect fluidization uniformity along the x-axis (y-slice); however, fluidization is generally symmetric about the x-axis. Plots of x-slice local gas

holdup data for various Q_s conditions at specific axial heights show the gas holdup distribution is generally symmetric about the x-axis. These plots are available in Appendix C.

While changes in Q_s affect fluidization uniformity and are locally significant, side air injection is found to have little effect on the average planar gas holdup as a function of height. This signifies that for $U_g = 1.25U_{mf}$, side air injection only influences the local gas holdup in a limited bed region. Figure 4.12 plots average planar gas holdup as a function of axial height for all Q_s conditions at $U_g = 1.25U_{mf}$. The plot clearly demonstrates that the average gas holdup for each plane is generally constant for each Q_s condition. Deviations occur near the top of the bed where increasing Q_s affects the average gas holdup due to the side air flow path. As discussed earlier, the penetration of side air flow and the bed height above the injector both increase increased Q_s .

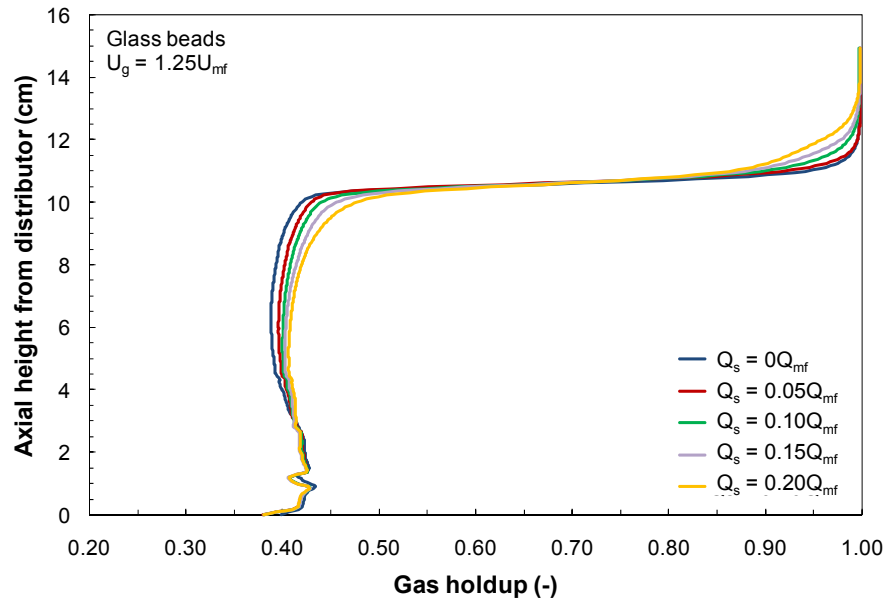


Figure 4.12: Average gas holdup by height for glass bead fluidization: $U_g = 1.25U_{mf}$, varying Q_s .

The effects of Q_s on fluidization of glass beads are also shown for $U_g = 1.5U_{mf}$ in Figure 4.13, $U_g = 1.75U_{mf}$ in Figure 4.14, $U_g = 2U_{mf}$ in Figure 4.15, and $U_g = 3U_{mf}$ in Figure 4.16.

By comparing gas holdup from these figures and Figure 4.5, as well as by analyzing plots of local gas holdup data, the effects of superficial gas velocity on glass bead fluidization hydrodynamics is observed. The most prominent effect of superficial gas velocity is that gas holdup generally increases with increases U_g . This increase in gas holdup is due to a higher volume of air passing through the bed, and confirms a trend identified by Ellenberger et al. (1995).

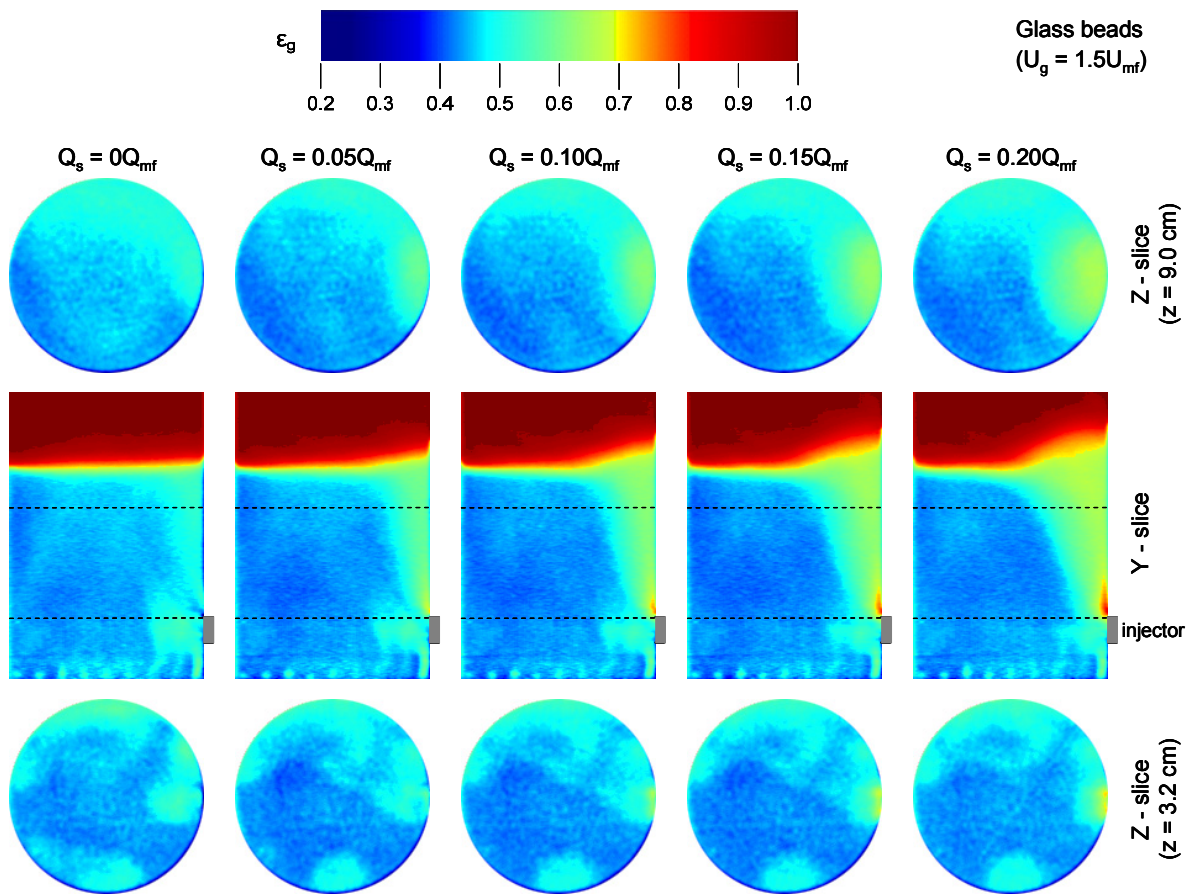


Figure 4.13: Gas holdup y- and z-slices for glass bead fluidization: $U_g = 1.5U_{mf}$, varying Q_s .

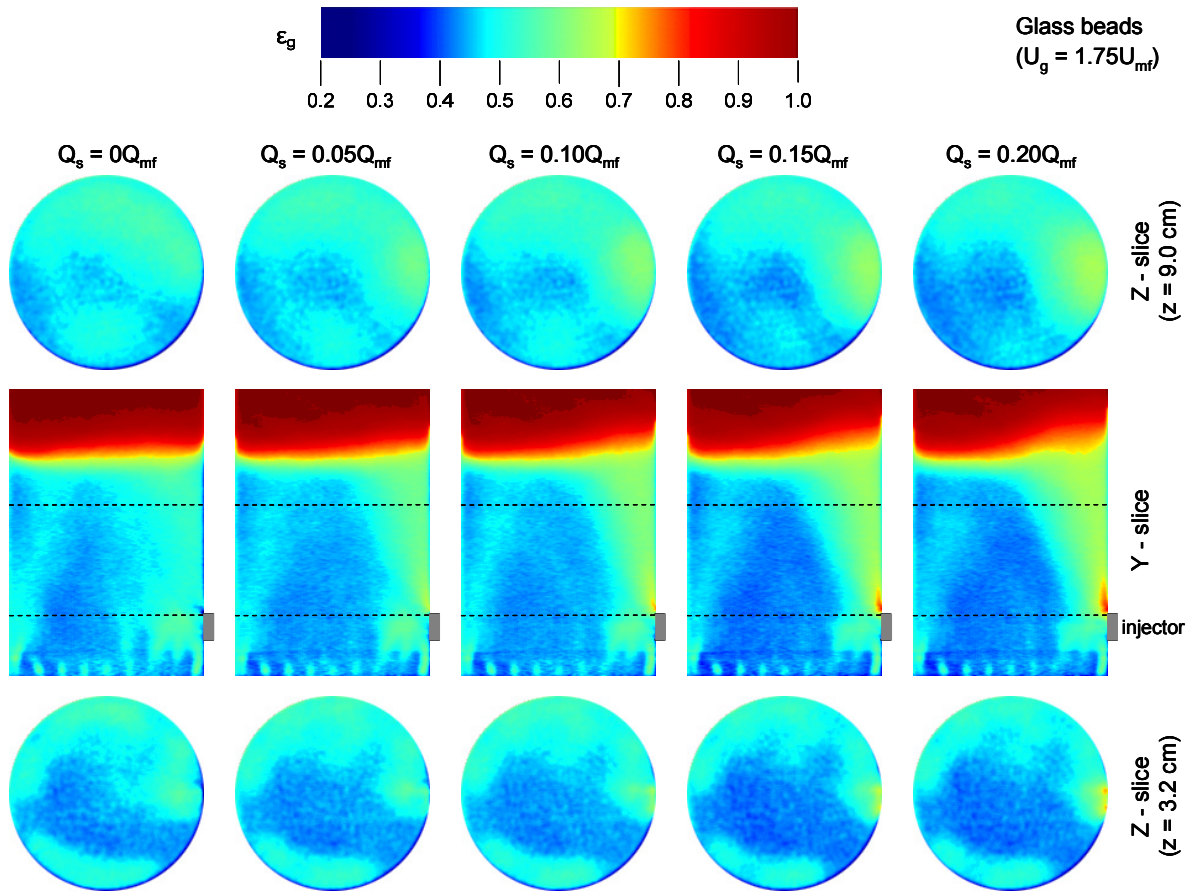


Figure 4.14: Gas holdup y- and z-slices for glass bead fluidization: $U_g = 1.75U_{mf}$, varying Q_s .

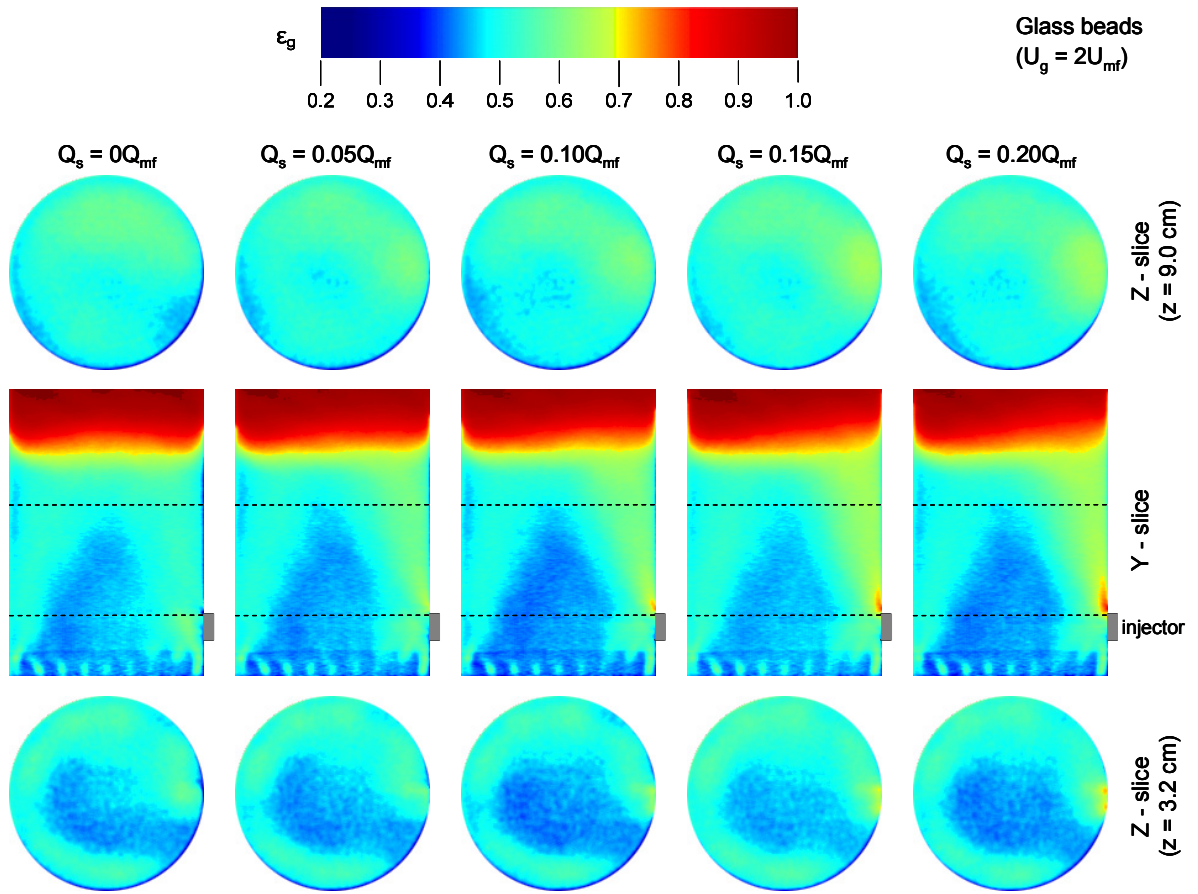


Figure 4.15: Gas holdup y- and z-slices for glass bead fluidization: $U_g = 2U_{mf}$, varying Q_s .

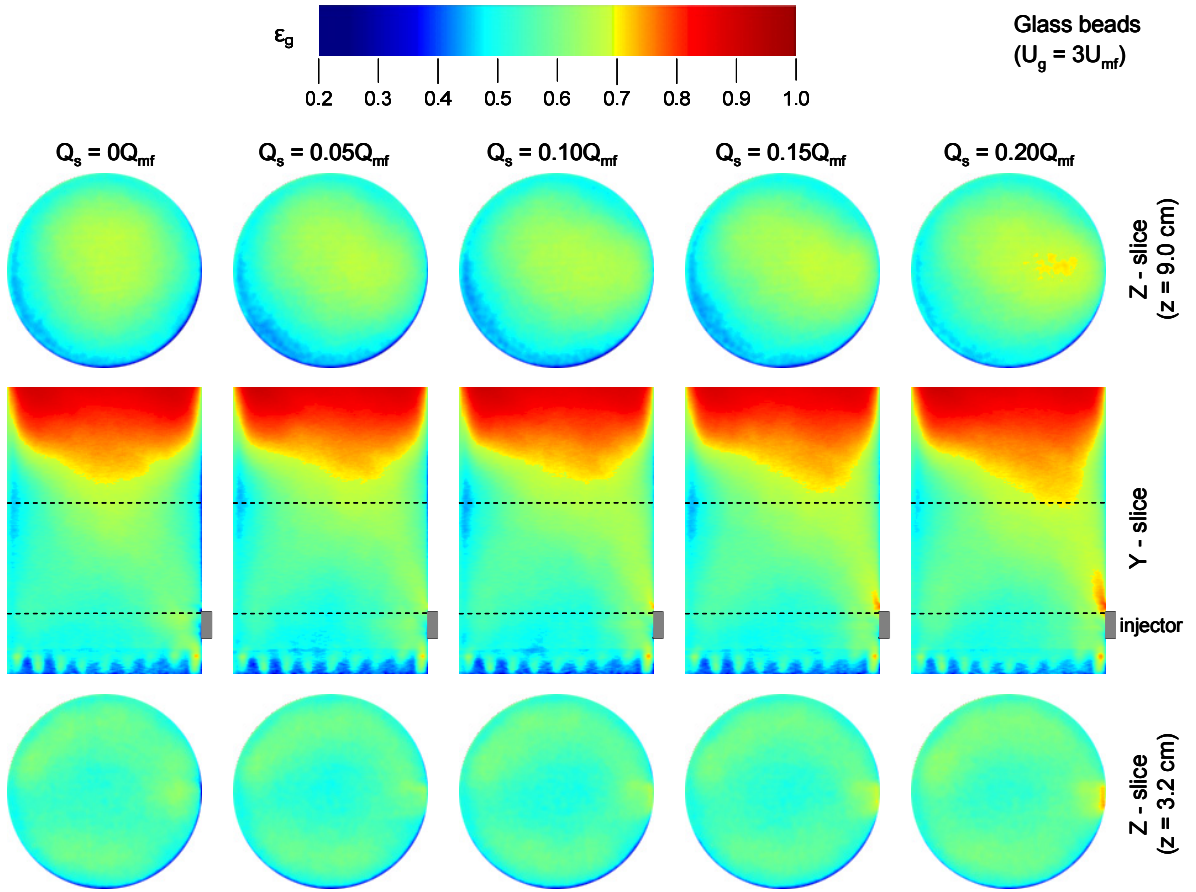


Figure 4.16: Gas holdup y- and z-slices for glass bead fluidization: $U_g = 3U_{mf}$, varying Q_s .

Another important feature illustrated by the gas holdup images is the internal flow structure caused by the fluidizing air from the distributor plate. For $U_g = 1.25U_{mf}$, relatively high local gas holdup is located in the bottom-center of the bed, indicating the time-averaged flow occurs mostly in the center. Above this region, the local gas holdup is generally uniform except by the side air injection flow path. As U_g increases to $1.5U_{mf}$ and $1.75U_{mf}$, the air dispersion from the distributor plate is no longer concentrated in the center, but instead around the walls of the bed. This is observed by the high gas holdup around the edges of the 3.2 cm z-slice images (Figure 4.13 and Figure 4.14). Further increasing the flow to $U_g = 2U_{mf}$ and $U_g = 3U_{mf}$ also shows the air from the distributor plate is concentrated around the edges of the reactor, but a distinct region of low gas holdup occurs in the center of the bed. Above

the region of low gas holdup, the high gas holdup region migrates towards the center until uniting in the top portion of the bed. This indicates that for glass beads, air flow from the distributor preferentially flows near the walls of the reactor. Bubbles travel from the reactor walls towards the center of the bed while also rising vertically. At a certain height, the bubbles appear to coalesce, which is shown by the boundary of the low gas holdup and high gas holdup regions near the top of the bed. In other words, a boundary exists at a critical height where annular flow coalesces, and this effect does not appear related to side air injection flow rate. These flow structures are clearly identified in the y-slice images (Figure 4.15 and Figure 4.16). Also, the 3.2 cm z-slice images show the high local gas holdup around the bottom walls of the bed while the 9.0 cm z-slices show the region near the bubble coalescence. This flow structure confirms the results observed by Lim et al. (2007). In the study the bubble profile had concentrated zones near the distributor walls but gradually migrated inwards until coalescing at a critical height.

Another structure shown in the $U_g = 2U_{mf}$ and $3U_{mf}$ y-slice images is a region of lower gas holdup on the edge of the column across from the injector and slightly below the bed surface. The low gas holdup region is also captured in the 9.0 cm z-slice images and is observed to span a section of the wall. This feature can be attributed to recirculation of the bed material down the walls of the reactor due to bubble coalescence in the center of the bed. The flow structures caused by the fluidizing air seem nearly unaffected by side air injection except near the injector port, where the side air injection flow path can be seen. X-slice images showing identical trends are available in Appendix C. The flow structure at the top of the bed resembles the results observed by Zhu et al. (2007). In that study, flow was approximately radially symmetric with a dilute center and a dense annulus; however, side air was not introduced in the fluidized beds.

U_g also influences the flow structures at the surface of the bed. With low U_g of $1.25U_{mf}$ and $1.5U_{mf}$, y-slice images show that the top of the bed is approximately level with the

exception of the region above the side injection port. Increasing U_g to $1.75U_{mf}$ and $2U_{mf}$ results in areas of high gas holdup located near the bed edges. Further increasing U_g to $3U_{mf}$ shows a dramatic low gas holdup region near the walls of the top of the bed with higher gas holdup towards the center, again confirming the results described by Zhu et al. (2007). This phenomenon is caused by bubbles breaking the surface near the bed center. As entrained bed particles are ejected by the bubbles, they contact the reactor walls and fall back into the bed. Additionally, this shows that high U_g ejects more particles from the bed than low U_g , indicating that bubbling occurs much more rapidly.

The gas holdup images also show the effects of U_g on bed expansion. From the y-slice images, it is evident that increasing U_g increases the average bed height. The images also show that increasing U_g results in the top of the bed becoming less distinguishable. For example, in Figure 4.5, y-slice images for $U_g = 1.25U_{mf}$ clearly show the upper bed boundaries. For $U_g = 1.5U_{mf}$ and $U_g = 1.75U_{mf}$ (Figure 4.13 and Figure 4.14), the upper boundary of the bed is distinguishable, but a gradient of gas holdup exists near the bed surface. With high U_g of $2U_{mf}$ and $3U_{mf}$ (Figure 4.15 and Figure 4.16), the bed heights are difficult to distinguish, indicating that for higher U_g fluidization is much more dynamic. This trend is also visually confirmed as larger bubbles with faster rise velocities break the surface of the bed with increased U_g . In addition, increasing the superficial gas velocity reduces the relative bed height above the injector. For $U_g = 1.25U_{mf}$ the bed height is significantly larger above the injector than the surroundings. In contrast, for $U_g = 2U_{mf}$ the relative bed height above the injector is similar to the height of the surrounding bed. This illustrates that fluidization uniformity improves as a result of increasing U_g . It should be noted that while the $U_g = 3U_{mf}$ images (Figure 4.16) show high local gas holdup directly above the side air injector, the surface of the bed appears much more uniform than at low U_g .

Increasing U_g also affects the average planar gas holdup, as illustrated by the plot in Figure 4.17 for glass beads with $Q_s = 0.10Q_{mf}$. The plot shows that with increased U_g the

average gas holdup in the bed increases. Additionally, above $z = 10$ cm the curves become more gradual with increasing U_g . This trend is caused by higher bed expansion and less distinguishable bed height, and will be described later. Also, the plot shows that the average gas holdup near the base of the bed does not change significantly with U_g . This indicates that fluidization is not complete near the surface of the distributor plate and this region is not significantly affected by changes in gas flow. In all U_g conditions the gas holdup through the bed appears to be somewhat uniform except near the bottom and top.

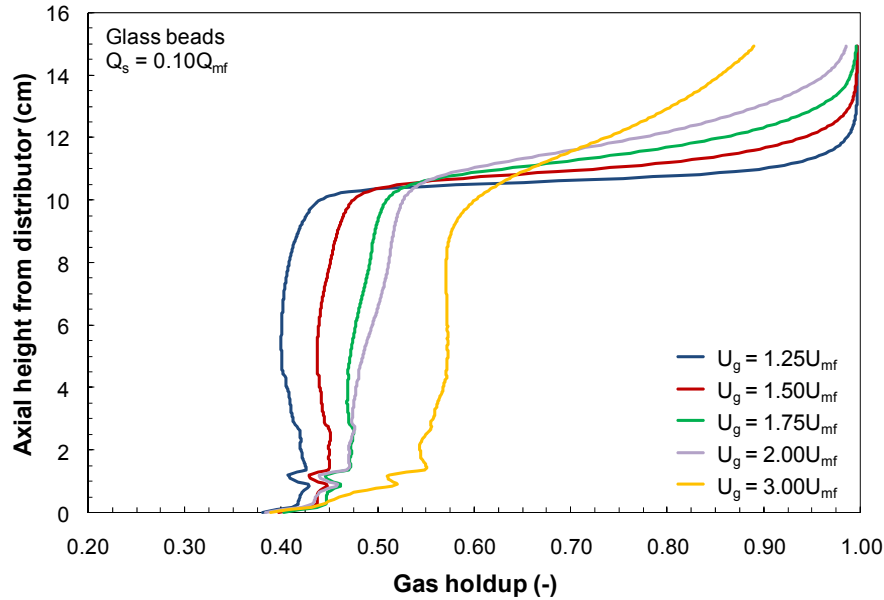


Figure 4.17: Average gas holdup by height for glass bead fluidization: $Q_s = 0.10Q_{mf}$, varying U_g .

In addition to influencing flow structures within the bed, U_g significantly affects the side air injection flow path. By increasing U_g , side air penetrates further into the bed. This effect is shown in the $U_g = 1.25U_{mf}$, $U_g = 1.5U_{mf}$ and $U_g = 1.75U_{mf}$ y-slice images where $Q_s = 0.10Q_{mf}$. In the $U_g = 1.25U_{mf}$ images, side air follows the reactor chamber wall vertically and does not appear to penetrate the bed except near the top. In the $U_g = 1.5U_{mf}$ and $U_g = 1.75U_{mf}$ images, side air expands further into the bed. Side air penetration is also observed in y-slice

plots of local gas holdup for various U_g conditions at axial heights of 3.2 cm and 9.0 cm, presented in Figure 4.18 and Figure 4.19, respectively. Both plots demonstrate that as U_g increases, the region of high local gas holdup by the side air injector penetrates further towards the bed center. The increase in side air penetration occurs because of an increase in the local gas holdup throughout the bed; with a high gas holdup, less force is required for the side air to penetrate the bed material. U_g does not appear to affect the magnitude of the high gas holdup region directly above the side air injector under identical Q_s conditions. By comparing Figures 4.18 and 4.19 to Figures 4.10 and 4.11, it is clear that changes in U_g affect injector air penetration more significantly than changes in Q_s . This is partly due to the low flow rate of side air compared to the fluidizing air flow rate.

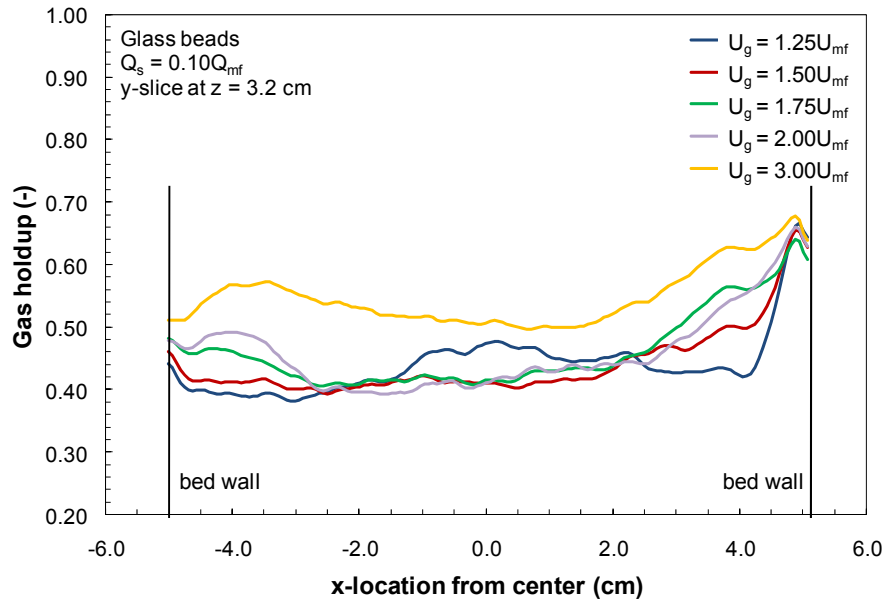


Figure 4.18: Y-slice gas holdup for glass bead fluidization at $z = 3.2$ cm: $Q_s = 0.10Q_{mf}$, varying U_g .

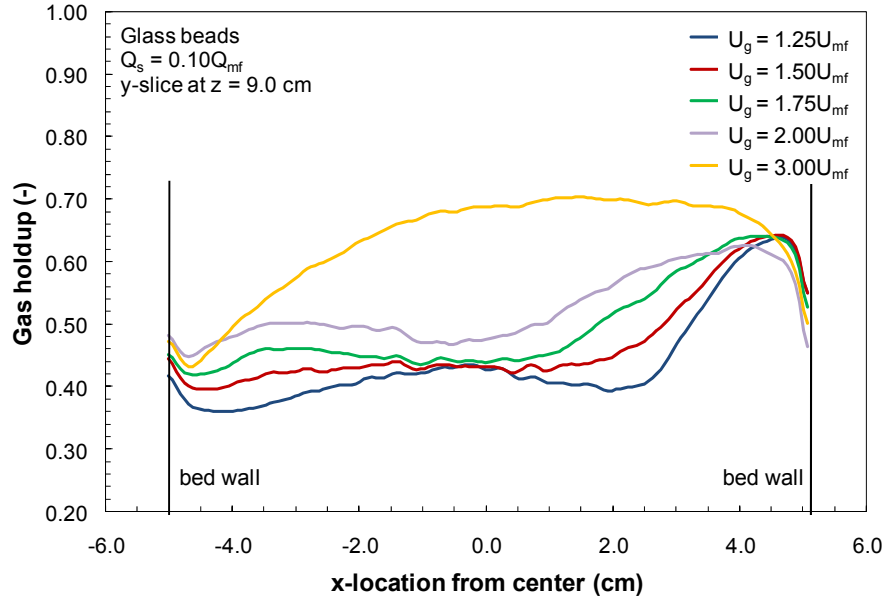


Figure 4.19: Y-slice gas holdup for glass bead fluidization at $z = 9.0$ cm: $Q_s = 0.10Q_{mf}$, varying U_g .

Not only does increasing U_g increase the side air penetration, it also changes the side air flow path boundary profile. In the y-slice images of Figure 4.5, the side air flow path boundaries for $U_g = 1.25U_{mf}$ are clearly observed for each Q_s . For $U_g = 1.5U_{mf}$ (Figure 4.13) and $U_g = 1.75U_{mf}$ (Figure 4.14), the boundaries are less distinct but still identifiable. At even higher U_g of $2U_{mf}$ (Figure 4.15) and $3U_{mf}$ (Figure 4.16), the side air flow path boundaries are much less distinguishable. The y-slice gas holdup plots in Figure 4.18 and Figure 4.19 also show this trend; at low U_g conditions a distinguishable peak of high local gas holdup is shown above the side air injector, but as U_g increases this peak becomes less drastic.

The changes in the boundary profiles also indicate another important trend; increasing U_g improves fluidization uniformity, regardless of Q_s . In other words, the effects of side air injection are greatly reduced with larger U_g . This occurs because the percentage of the side air flow relative to the total air flow through the entire bed (fluidizing air and side air), is greatly reduced as U_g increases. The y-slice images for $U_g = 1.25U_{mf}$ illustrate that with side air injection, non-uniform fluidization occurs and regions of high gas holdup exist above the

side air injector, while low gas holdup is seen in the surrounding bed. The y-slice images for $U_g = 2U_{mf}$ show that gas holdup is more symmetrically distributed through the bed with increasing U_g . The plots in Figure 4.18 and Figure 4.19 further show this trend towards symmetric fluidization with increasing U_g . As with changes in Q_s , plotting the local x-slice gas holdup along the y-axis demonstrates symmetric fluidization about the y-axis, regardless of U_g . Selected x-slice plots are available in Appendix C.

Superficial gas velocity is also shown to affect the region directly above the distributor plate, as previously described for the average planar gas holdup plot in Figure 4.17. Y-slice images for $U_g = 1.5U_{mf}$ (Figure 4.13) show regions of high gas holdup extending from the distributor plate into the bed, indicating that air jets into the bed as it is introduced by the distributor plate orifices. These jets are created by a high local gas velocity passing through each orifice hole in the distributor plate. Bed material between these orifices exhibits slightly lower gas holdup than the surroundings, showing that fluidization is not uniform at the surface of the distributor plate. As with the side air injection, the air penetration from the distributor plate increases with increasing U_g . In all cases, low gas holdup between the air jets suggests uniform fluidization does not occur directly above the distributor plate, between the distributor orifices.

While superficial gas velocity significantly affects fluidization hydrodynamics, it appears that changes in U_g do not significantly affect fluidization symmetry in the y-direction. For all Q_s , the z-slice images for each flow condition show relatively symmetrical fluidization behavior about the x-axis, which passes through the center of the bed and side air injector. Additionally, for all U_g conditions fluidization is affected by the side air injector design when no side air is introduced and the side is not plugged. Both the y- and z-slice images for $Q_s = 0Q_{mf}$ show a distinctive high gas holdup region above the side air injector. The effect of the injector design illustrates the importance of injector design on fluidization uniformity.

4.2.1.2 Walnut Shell

For walnut shell fluidized beds, a series of images are compiled like those displayed for glass beads. While the images provide insight into fluidization behavior, only the images for $U_g = 1.5U_{mf}$ and $3U_{mf}$ will be presented in this section, and the remaining images are available in Appendix C. Figure 4.20 shows y- and z-slice gas holdup images for walnut shell fluidizing at $U_g = 1.5U_{mf}$ under five Q_s conditions. Similarly, Figure 4.21 shows the walnut shell gas holdup images for $U_g = 3U_{mf}$. A gas holdup color scale ranging from $\epsilon_g = 0.4$ to $\epsilon_g = 1.0$ is applied to the walnut shell images to improve color resolution. A series of local gas holdup plots are also presented in this section and in Appendix C to quantitatively emphasize important features. The bulk gas holdup for walnut shell is 0.55 (shown in Table 3.1) and the calculation is provided in Appendix C. Many of the trends observed in walnut shell beds are also observed in glass bead beds and detailed explanations are provided in the previous section.

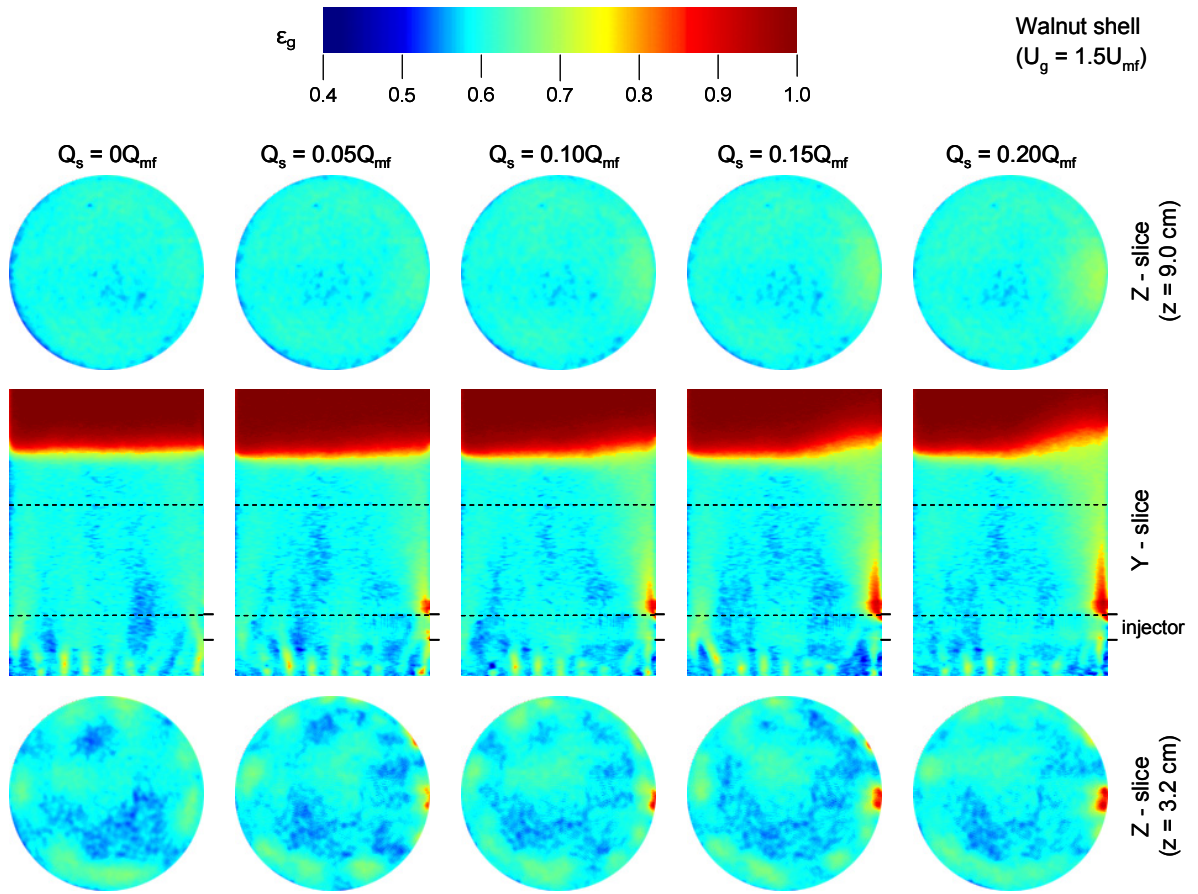


Figure 4.20: Gas holdup y- and z-slices for walnut shell fluidization: $U_g = 1.5U_{mf}$, varying Q_s .

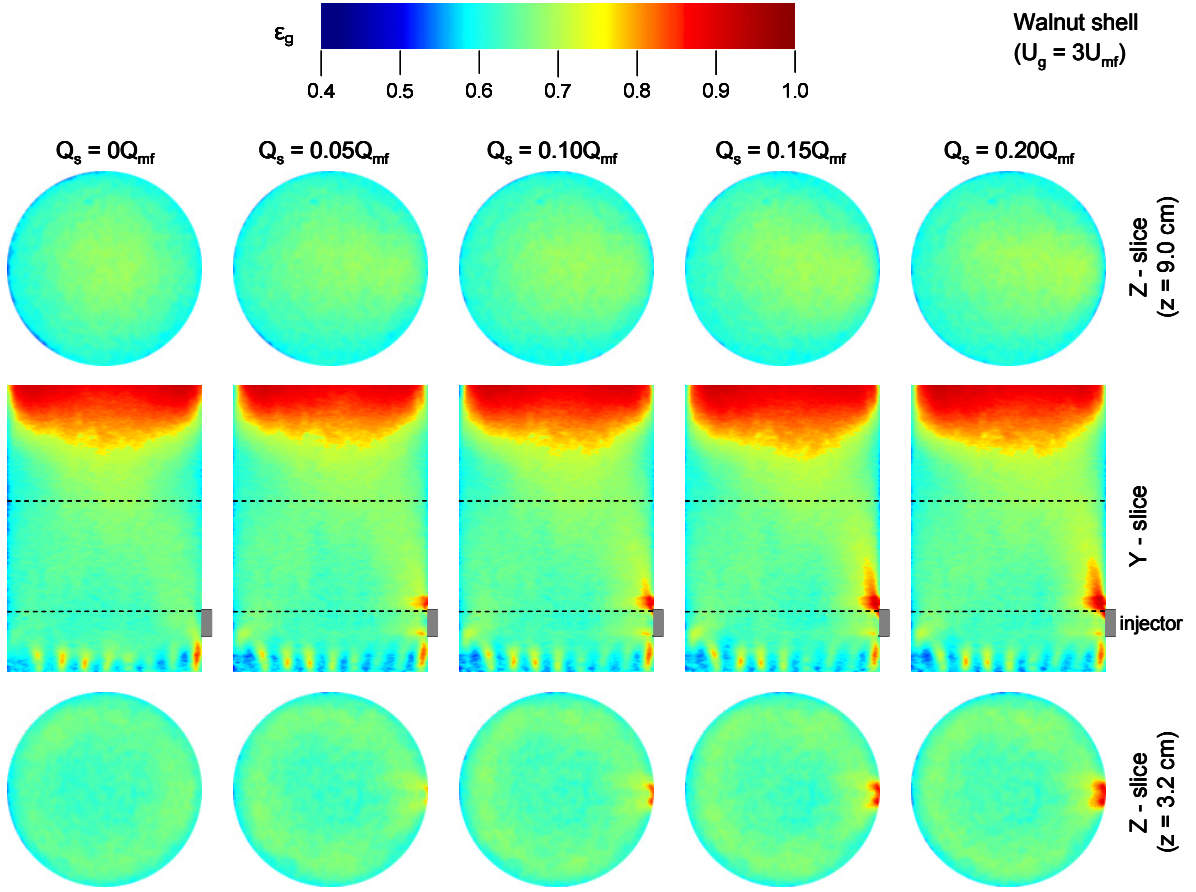


Figure 4.21: Gas holdup y- and z-slices for walnut shell fluidization: $U_g = 3U_{mf}$, varying Q_s .

As with glass beads, plots of local gas holdup along the x- and y-axes for various heights of the bed show that walnut shell fluidizes uniformly without side air injection. Figure 4.22 and Figure 4.23 plot the x- and y-slice local gas holdup for walnut shell fluidization with $U_g = 1.5U_{mf}$ and $Q_s = 0Q_{mf}$ at four axial heights, respectively. Despite apparent non-uniform air dispersion from the distributor plate, both plots and the images in Figure 4.21 show that without side air, walnut shell fluidization is generally uniform throughout the bed. Regions of relatively high gas holdup are observed on the $z = 3.2$ cm images in Figure 4.21, indicating preferential air distribution occurs near the distributor plate. As axial height increases, these regions are diminished and air is more uniformly dispersed throughout the bed. In other words, fluidizing air produces channels or jets as it is introduced into the bed, but it gradually

expands uniformly across the bed as height increases. Z-slice gas holdup images at $z = 9.0$ cm show fewer regions of high gas holdup than at $z = 3.2$ cm. These effects are also observed on local gas holdup plots; relatively high gas holdup occurs around $y = 4.5$ cm on the x-slice plot and around $x = -4.5$ cm on the y-slice plot for low axial heights. At larger heights, these regions are not as distinguished.

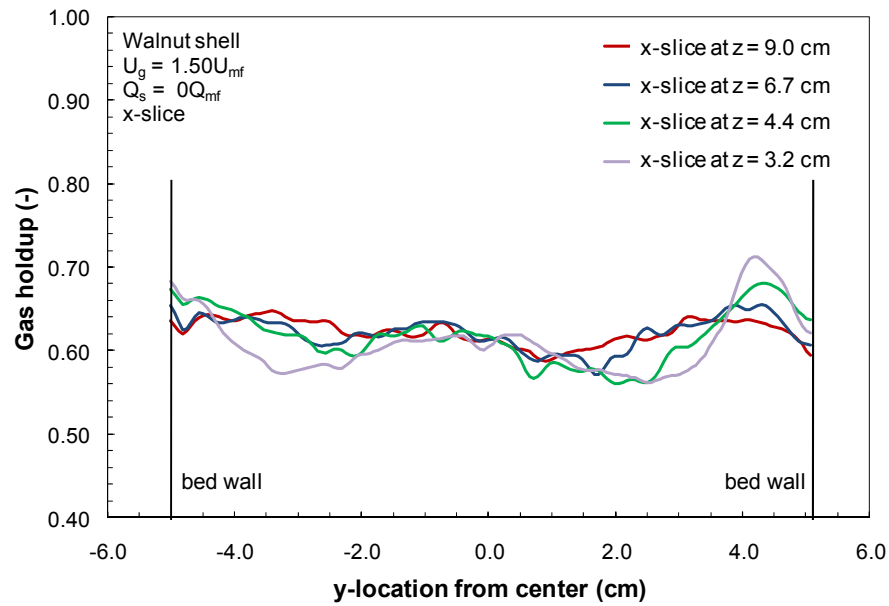


Figure 4.22: X-slice gas holdup for walnut shell fluidization at four heights: $U_g = 1.5U_{mf}$, $Q_s = 0Q_{mf}$.

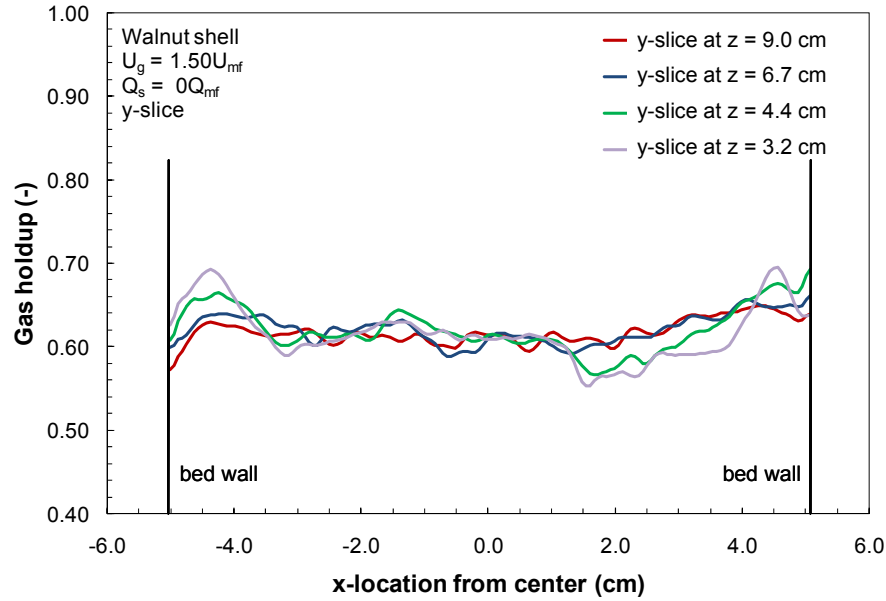


Figure 4.23: Y-slice gas holdup for walnut shell fluidization at four heights: $U_g = 1.5U_{mf}$, $Q_s = 0Q_{mf}$.

With side air injection, y- and z-slice images illustrate that a distinct flow path occurs above the injector. Directly above the side air injector is a small region of high local gas holdup which gradually decreases in magnitude but expands towards the center of the bed as height increases. To further illustrate, Figure 4.24 presents the y-slice local gas holdup plot at various heights for walnut shell fluidization with $U_g = 1.5U_{mf}$ and $Q_s = 0.10Q_{mf}$. A region of high gas holdup occurs near the side air injection port at $x = 5.2$ cm. As height increases, this locally high gas holdup region decreases in magnitude but extends further towards the center of the bed. As with channeling in the bed from the distributor plate, side air injection is shown to initially create a channeling or jetting effect when introduced to the bed but gradually expands through the bed as height increases.

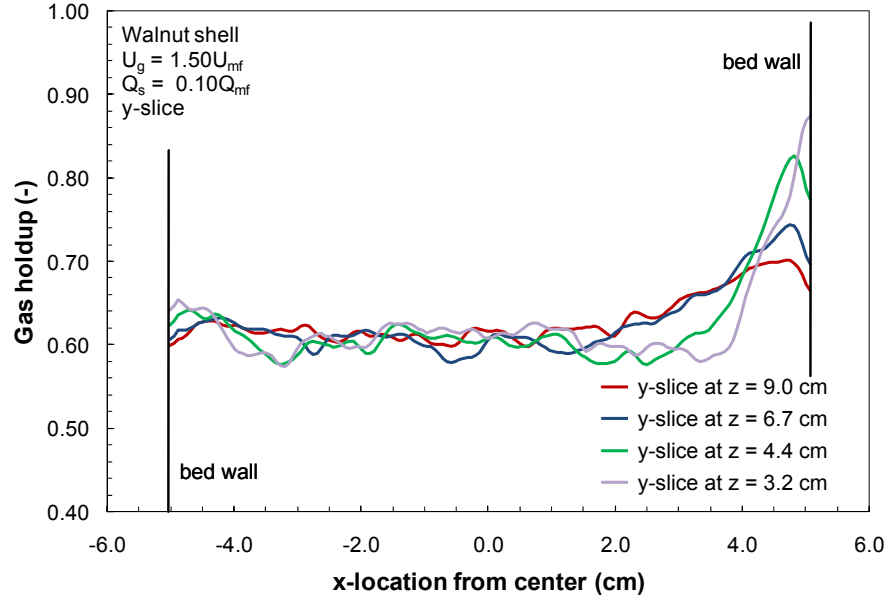


Figure 4.24: Y-slice gas holdup for walnut shell fluidization at four heights: $U_g = 1.5U_{mf}$, $Q_s = 0Q_{mf}$.

Figures 4.20 and 4.21 also show the effects of increasing Q_s on fluidization. As with glass beads, increasing Q_s when $U_g = 1.5U_{mf}$ increases the bed height above the injection port while few effects are seen in the surrounding bed height. The images also demonstrated that increasing Q_s increases the local gas holdup magnitude near the side air injection port. Plots showing this trend are presented in Figure 4.25 and Figure 4.26. These plots show y-slice local gas holdup at two different heights for walnut shell fluidization at $U_g = 1.5U_{mf}$ with various Q_s conditions. At a height of 3.2 cm (Figure 4.25), increasing Q_s greatly increases local gas holdup by the side air injection port. At $z = 9.0$ cm (Figure 4.26), increasing Q_s increases the local gas holdup magnitude above the injector, but also increases the penetration of the high gas holdup region towards the center of the bed. It can also be seen that at $z = 9.0$ cm, the side air injection flow path is less distinct than at the lower heights, indicating that side air injection is dispersed into the bed as bed height increases. Again it should be noted that some of the repeatable features in Figure 4.26 represent noise and reconstruction artifacts induced by the gas holdup calculations.

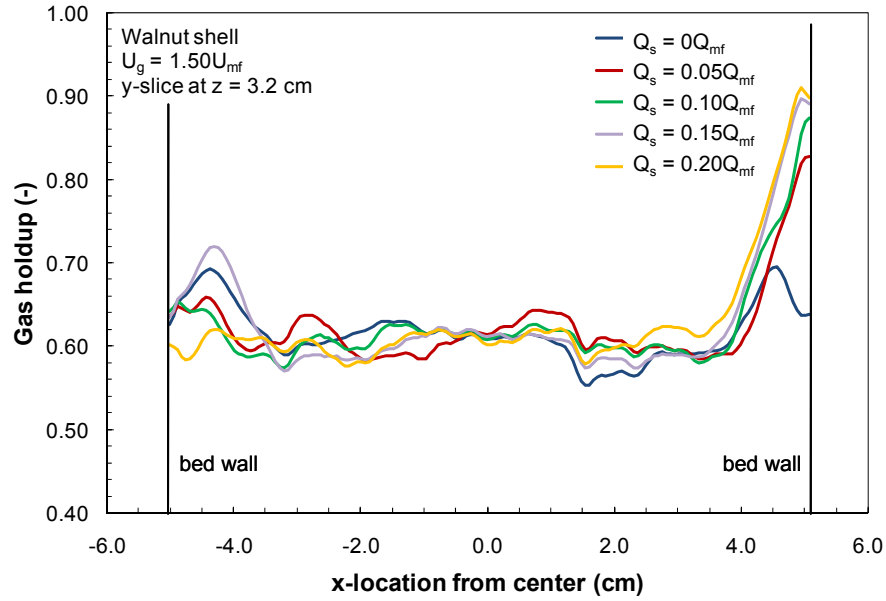


Figure 4.25: Y-slice gas holdup for walnut shell fluidization at $z = 3.2$ cm: $U_g = 1.50U_{mf}$, varying Q_s .

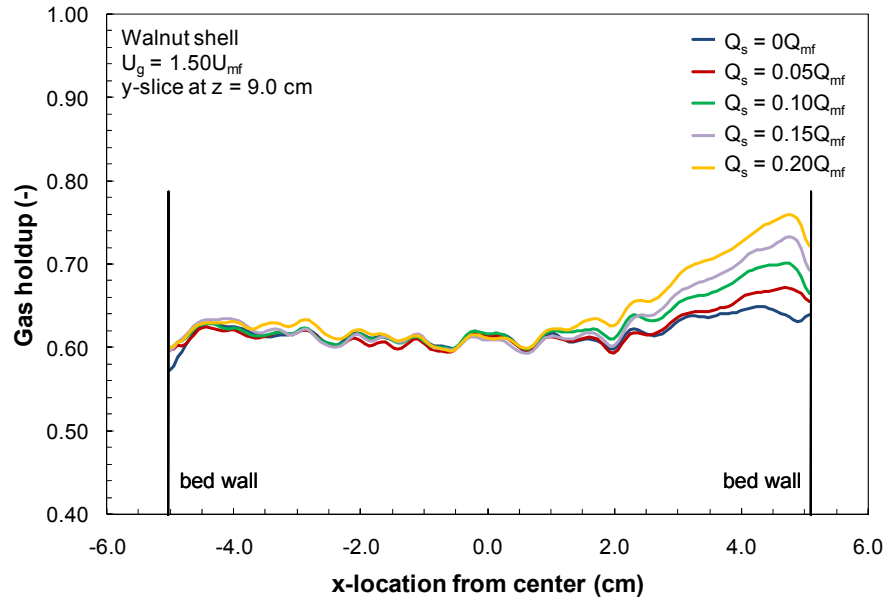


Figure 4.26: Y-slice gas holdup for walnut shell fluidization at $z = 9.0$ cm: $U_g = 1.50U_{mf}$, varying Q_s .

By comparing Figure 4.20 and Figure 4.21, and images available in Appendix C, trends in fluidization behavior due to changes in U_g are observed. Furthermore, plots of y-slice local

gas holdup for $Q_s = 0.10Q_{mf}$ at various U_g conditions are presented in Figure 4.27 and Figure 4.28 for two heights. As expected, increasing U_g increases gas holdup through the bed due to higher air volume in the system. Air channeling from the distributor plate appears to be less significant as U_g increases, although it is still identifiable. Y-slice images show a definite side air injection flow path for $U_g = 1.5U_{mf}$ while the path is much less distinguishable for $U_g = 3U_{mf}$. Figure 4.27 illustrates that at $z = 3.2$ cm, the magnitude of the local gas holdup in the side air injection flow path appears unaffected by altering U_g , however, Figure 4.28 demonstrates that higher U_g increases side air injection penetration at $z = 9.0$ cm. Figure 4.21 and Figure 4.28 also show that fluidization symmetry improves as U_g increases. For $U_g = 3U_{mf}$, the local gas holdup distribution appears to be nearly symmetrical about the bed centerline, regardless of the side air injection. As with glass beads, as U_g increases the injection air is found to have less impact on the fluidization uniformity. Similar to glass beads, as U_g increases the internal flow structure of the bed consists of high air flow around the bottom edges of the bed which gradually migrate towards the center of the bed, about halfway up the bed. The y-slice images in Figure 4.21 show regions of lower gas holdup along the walls close to the top of the bed due to recirculation of bed material. Y-slice images also illustrate that with increasing U_g , the bed height is larger near the walls than at the center. This is due to bubbles in the center of the bed ejecting particles towards the walls. As expected, increases in U_g increase the bed height, as observed in y-slice images.

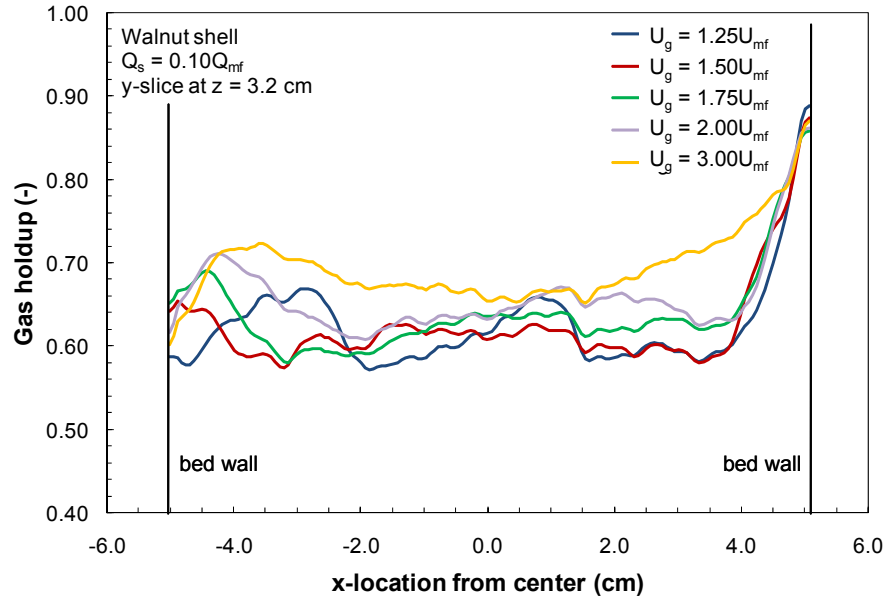


Figure 4.27: Y-slice gas holdup for walnut shell fluidization at $z = 3.2$ cm: $Q_s = 0.10Q_{mf}$, varying U_g .

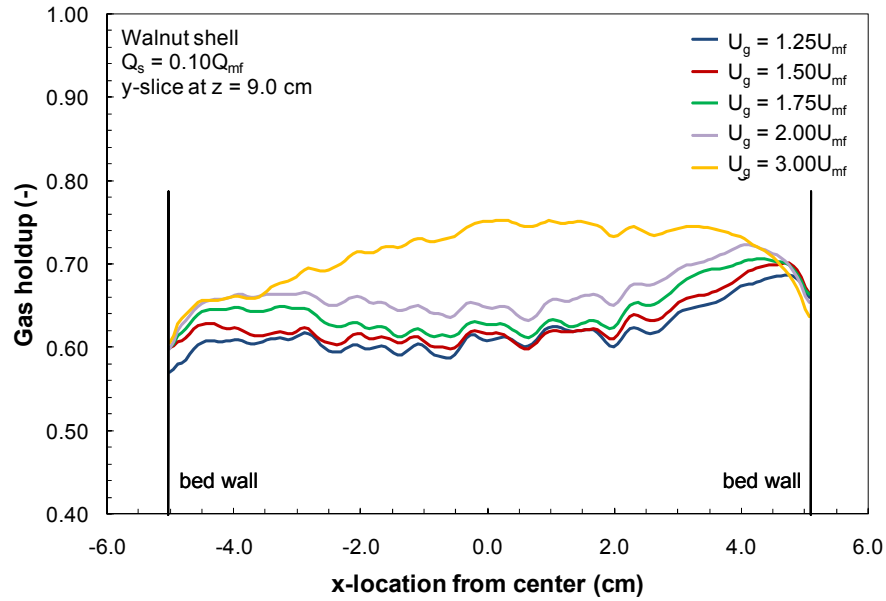


Figure 4.28: Y-slice gas holdup for walnut shell fluidization at $z = 9.0$ cm: $Q_s = 0.10Q_{mf}$, varying U_g .

4.2.1.3 Corncob

As with glass beads and walnut shell, collections of y- and z-slice gas holdup images under all five Q_s conditions are compiled for corncob beds. Like walnut shell, only the images for $U_g = 1.5U_{mf}$ in Figure 4.29 and $U_g = 3U_{mf}$ in Figure 4.30 are presented in this section for simplicity. Additional figures are available in Appendix C. For corncob, the gas holdup color scale is mapped between $\epsilon_g = 0.5$ and $\epsilon_g = 1.0$ to improve color resolution. Plots are also generated similar to those shown for glass beads and walnut shell. These provide additional insight into fluidization features, and are presented in Appendix C. The analysis focuses on the gas holdup z- and y-slice images. Bulk gas holdup for the corncob beds is 0.61 (shown in Table 3.1) and the calculation is presented in Appendix C.

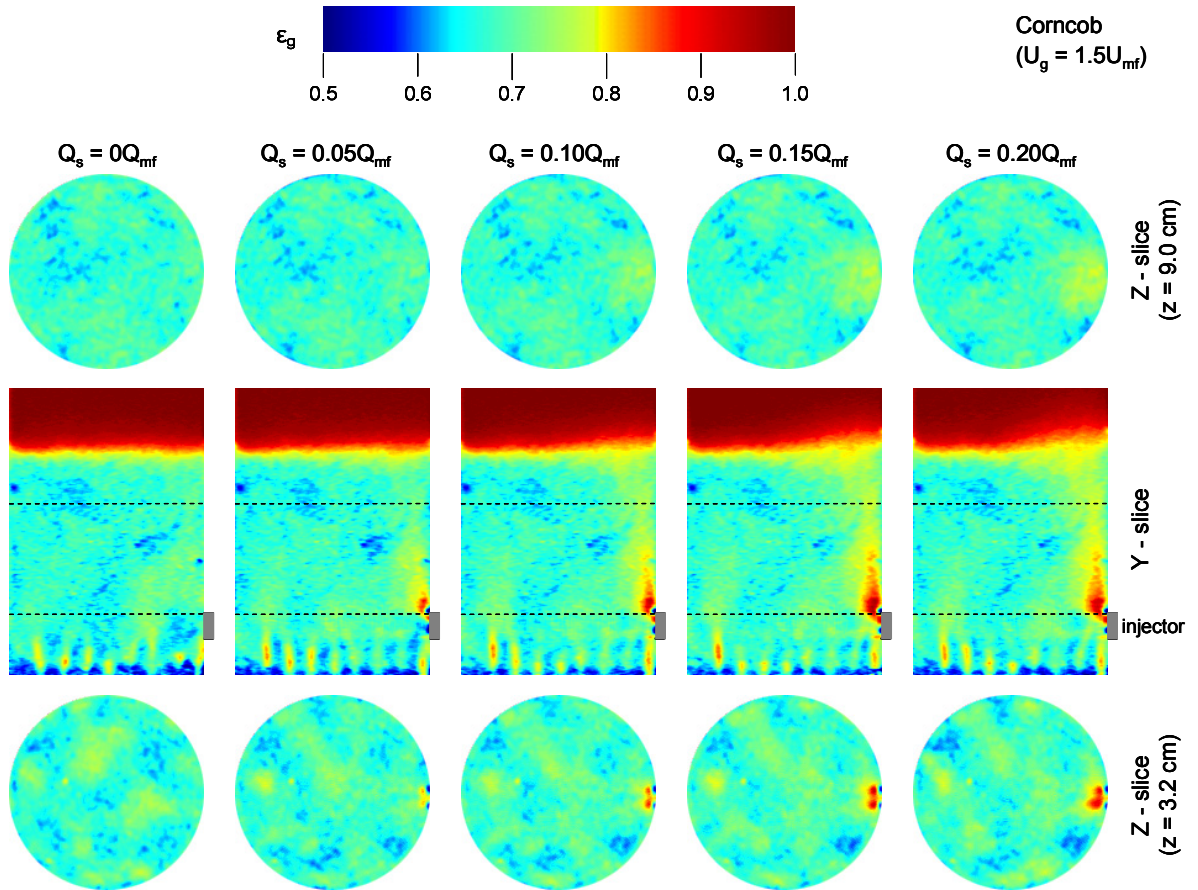


Figure 4.29: Gas holdup y- and z-slices for corncob fluidization: $U_g = 1.5U_{mf}$, varying Q_s .

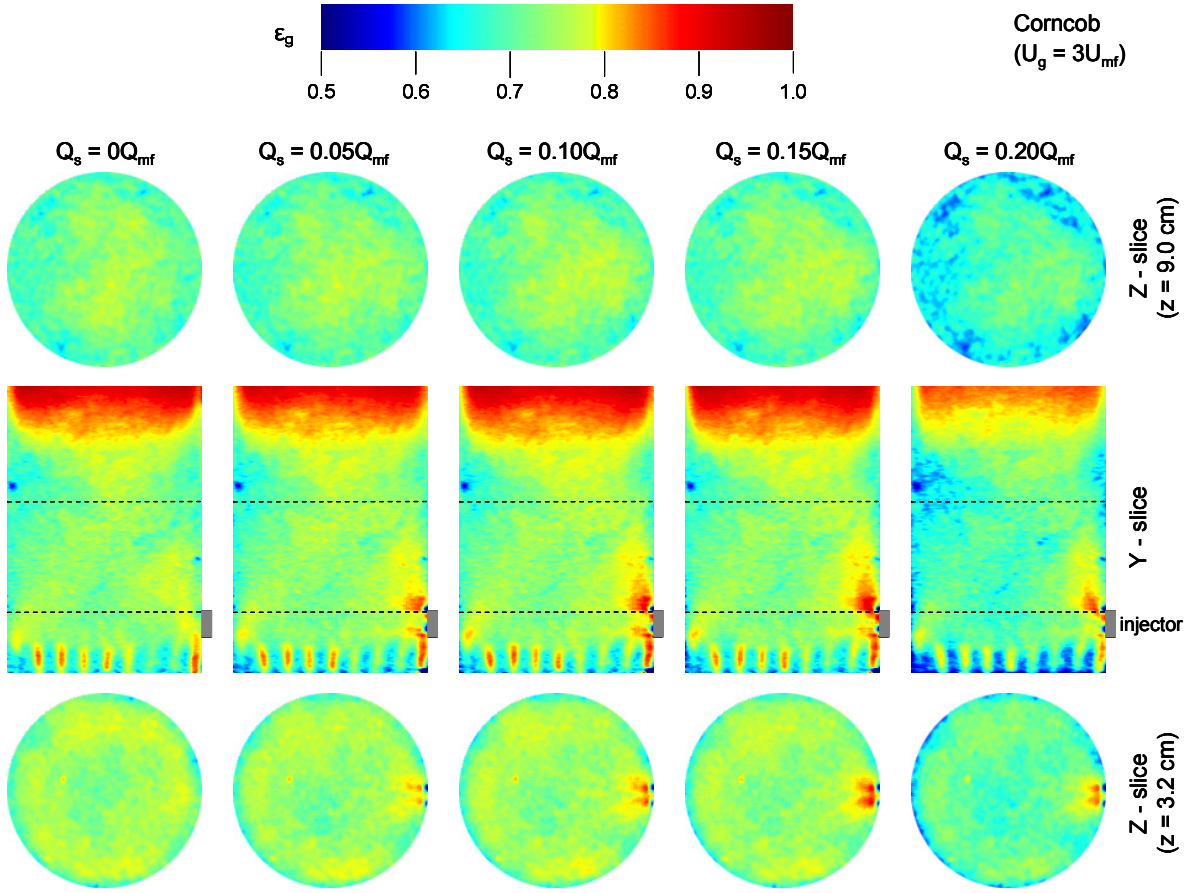


Figure 4.30: Gas holdup y- and z-slices for corncob fluidization: $U_g = 3U_{mf}$, varying Q_s .

Like glass beads and walnut shell, the z- and y-slice images show that fluidization without side air injection is fairly uniform. It should be noted that in the y-slice images there is a circular region of low gas holdup near top-left of the bed which is an artifact of the bulk corncob CT image used in gas holdup calculations. Plots of local x- and y- slice gas holdup for various heights at $U_g = 1.5U_{mf}$ also show that the bed uniformly fluidizes when no side air is injected (Appendix C). The y- and z-slice images also show paths of high gas holdup located near the bottom of the bed; as described earlier, air from the distributor plate creates channels, or jets, as it is introduced.

When side air is introduced, corncob shows features similar to those observed in glass beads and walnut shell beds. The y-slice images for $U_g = 1.5U_{mf}$ (Figure 4.29) show regions

of high gas holdup located directly above the side injection port, indicating that side air creates channels as it is injected into the corncob. With increasing height, the gas holdup magnitude above the side injection port gradually decreases while the expansion of the flow path increases, since side injection air flow is increasingly diffused through the bed.

Increasing Q_s slightly increases the bed height above the injection port for low U_g .

By comparing Figure 4.29 and Figure 4.30 and the corncob images in Appendix C, trends between fluidization and U_g are also observed. For corncob beds, as U_g increases, fluidization uniformity also increases. For y-slice images at $U_g = 1.5U_{mf}$, the fluidization air flow path is clearly observed; however, as U_g increases to $3U_{mf}$, the path of the side air is only noticeable near the side injector port. The magnitude of the high gas holdup region directly above the side air injector does not appear to be affected by changes in U_g . Similarly, as U_g increases the average bed height increases. The average bed height profile also becomes less uniform with increases U_g ; the height near the bed walls is higher than at the center due to bubbles in the center ejecting corncob towards the walls. Like glass beads and walnut shell, high U_g creates a flow structure with high gas holdup near the bottom edges of the bed, which gradually migrate towards the center of the column as height increases. Near the top of the bed is a region of lower gas holdup around the column edges showing recirculation of corncob.

4.2.2 Effects of Bed Material on Local Gas Holdup

In section 4.2.1 fluidization of glass beads, walnut shell, and corncob are analyzed under various U_g and Q_s conditions. While many features are similar between the three materials, the previous figures cannot be compared adequately since the color mapping scales are not equivalent between materials. To compare fluidization hydrodynamics between materials, Figure 4.31 and Figure 4.32 present a selection of gas holdup y-slice images for all three materials with three Q_s conditions ($Q_s = 0Q_{mf}$, $0.05Q_{mf}$, and $0.10Q_{mf}$) and two U_g conditions

($U_g = 1.5U_{mf}$ and $3U_{mf}$). These images have been mapped to the same color scale ranging from $\epsilon_g = 0.3$ to $\epsilon_g = 1.0$, and the static bulk images are also shown for reference. It should be noted that in the bulk material images, the reactor is filled with bed material; consequently, the images do not show the surface of the beds.

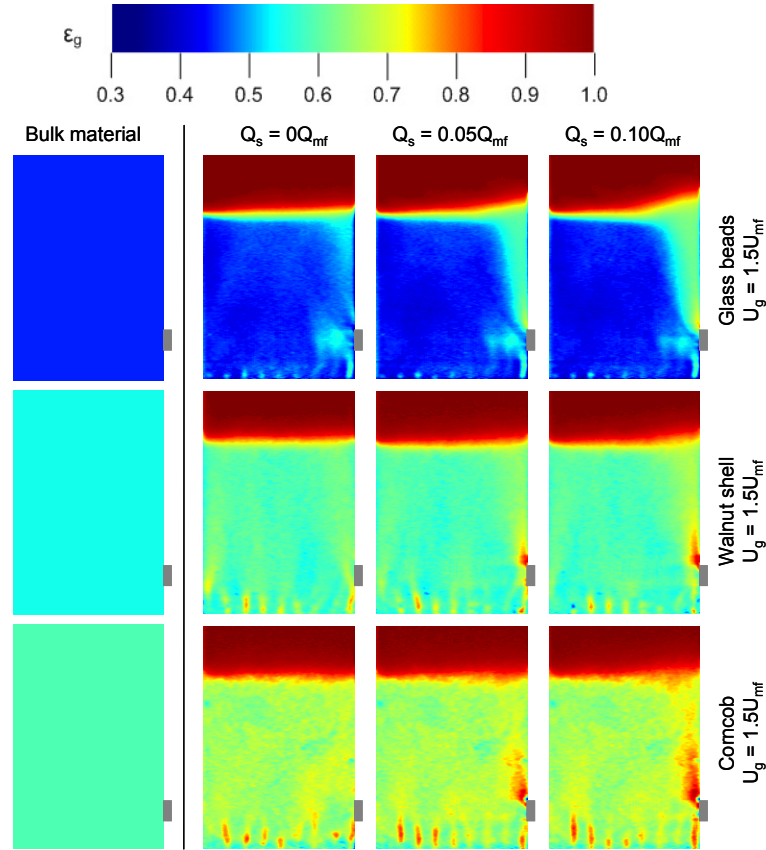


Figure 4.31: Gas holdup y-slices for all materials: $U_g = 1.5U_{mf}$, varying Q_s .

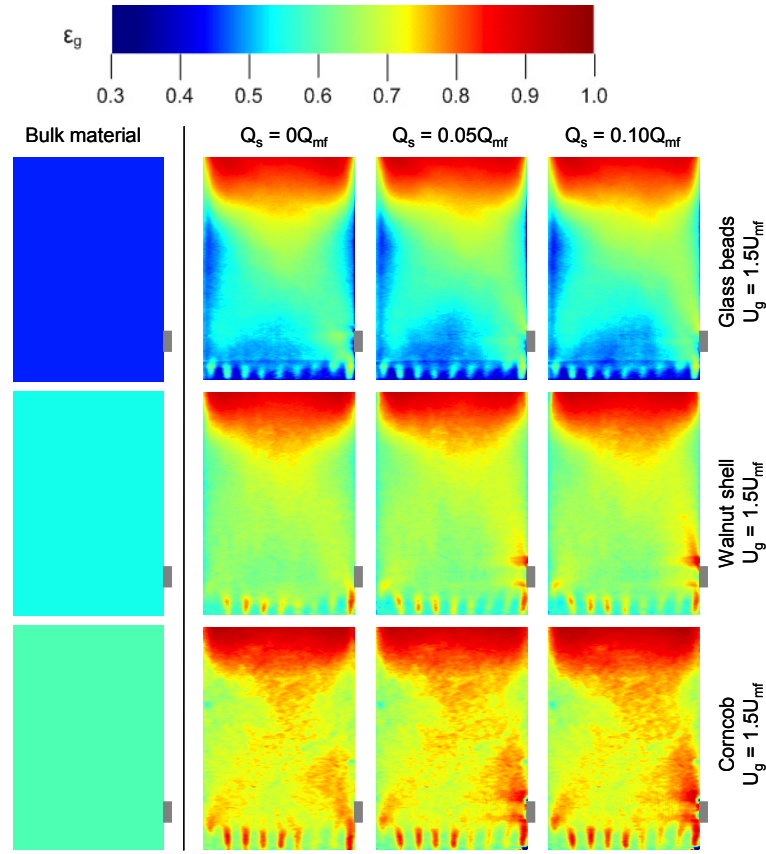


Figure 4.32: Gas holdup y-slices for all materials: $U_g = 3U_{mf}$, varying Q_s .

Figure 4.31 shows y-slices of all materials at $U_g = 1.5U_{mf}$. It is evident that as the density of the material decreases, the gas holdup increases. The glass bead beds are shown to have lower gas holdup than both walnut shell and corncob beds, while corncob beds exhibit higher gas holdup than walnut shell beds. This trend is also confirmed in Figure 4.33 which plots the average planar gas holdup by height for each material with $U_g = 1.5U_{mf}$ and no side air. From the plot, gas holdup appears consistent in each bed; however, the average ϵ_b for corncob is larger than for walnut shell and glass beads. This effect follows the bulk gas holdup for each material; $\epsilon_{g,b}$ of glass is lower than walnut shell which is in turn lower than corncob.

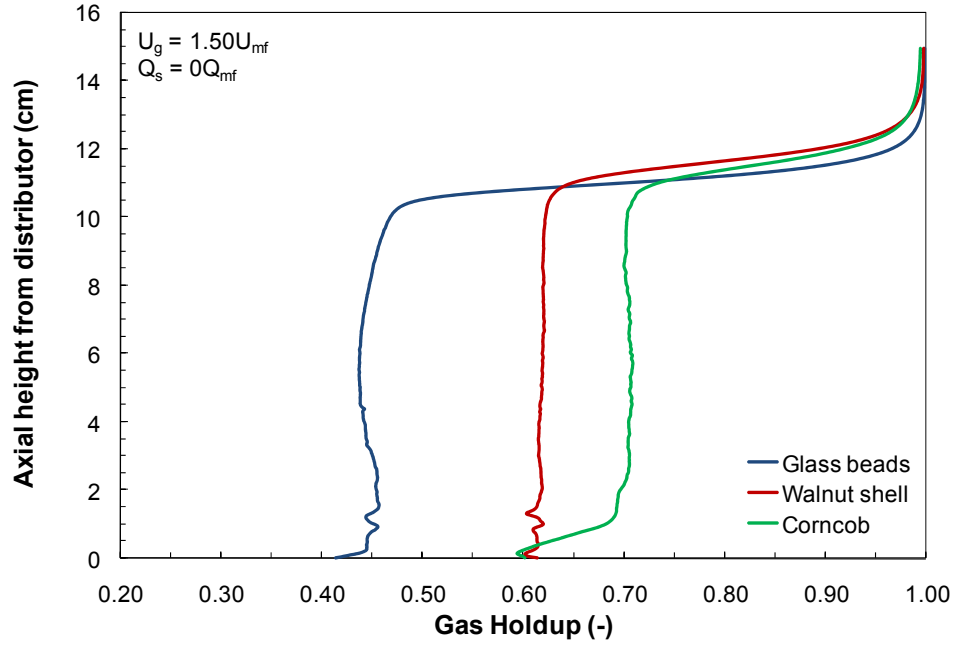


Figure 4.33: Average gas holdup by height for all materials: $Q_s = 0Q_{mf}$, $U_g = 1.5U_{mf}$.

The y-slice images in Figure 4.31 also illustrate the effects of material on noise in the calculations. Since X-ray attenuation in glass beads is much larger than in air, the signals obtained from CTs of glass have high resolution compared to the surrounding air. In walnut shell and corncob beds, the attenuation difference between the bed material and the surrounding air is much less than with glass, and reduces the resolution of the CT data. In addition, glass beads are extremely homogeneous and the bulk glass CT data used in the gas holdup calculations has a high uniformity. As a result, very little noise is introduced in the calculations by the bulk glass CT. In contrast, the bulk CT files for walnut shell and corncob are much more heterogeneous and, consequently, noise is introduced to the gas holdup calculations. To illustrate, corncob images at all three Q_s conditions in Figure 4.31 have a circular region of low gas holdup located in the top left corner of the bed; this is an artifact of the bulk CT corncob file. For the three materials examined, it follows that CT imaging of

glass bead beds is ideal since it provides the highest gas holdup resolution and lowest noise in calculations.

Figure 4.31 shows that the general fluidization behavior is similar for all three materials at $U_g = 1.5U_{mf}$ under the three Q_s conditions. The average gas holdup curves in Figure 4.33 also follow a similar shape for each material; a relatively constant average planar gas holdup exists throughout the bed except near the surface of the bed, at which point the gas holdup curves sharply increase. It is also observed that the corncob bed exhibits relatively low gas holdup near the bottom of the bed (Figure 4.33). This indicates that air is not evenly dispersed directly above the distributor plate in corncob beds, which is confirmed by the gas holdup images and discussed earlier.

In all materials, the majority of the beds appear to fluidize uniformly except near the side air injection port, as seen in the y-slice images. The region of high gas holdup near the side air injection port is the result of the side air injection. The side air is shown to disperse as it flows upwards through the bed and the side air flow path is very clearly defined for all Q_s conditions in glass bead beds. For walnut shell beds, the side air flow path can be distinguished but not as well as for glass. In the corncob bed the side air flow path is even less distinct. These effects show that decreasing material density diffuses the side air more throughout the bed. Additionally, since the images are time-averaged, this effect suggests that corncob and walnut shell fluidize more rapidly than glass beads, creating a more uniform time-averaged gas holdup distribution. The introduction of side air is found to have little effect on the average planar gas holdup for all materials. Figure 4.34 shows the average planar gas holdup for all three beds with $Q_s = 0.10Q_{mf}$ and $U_g = 1.50U_{mf}$. A comparison of Figure 4.33 to Figure 4.34 shows little difference in the gas holdup curves.

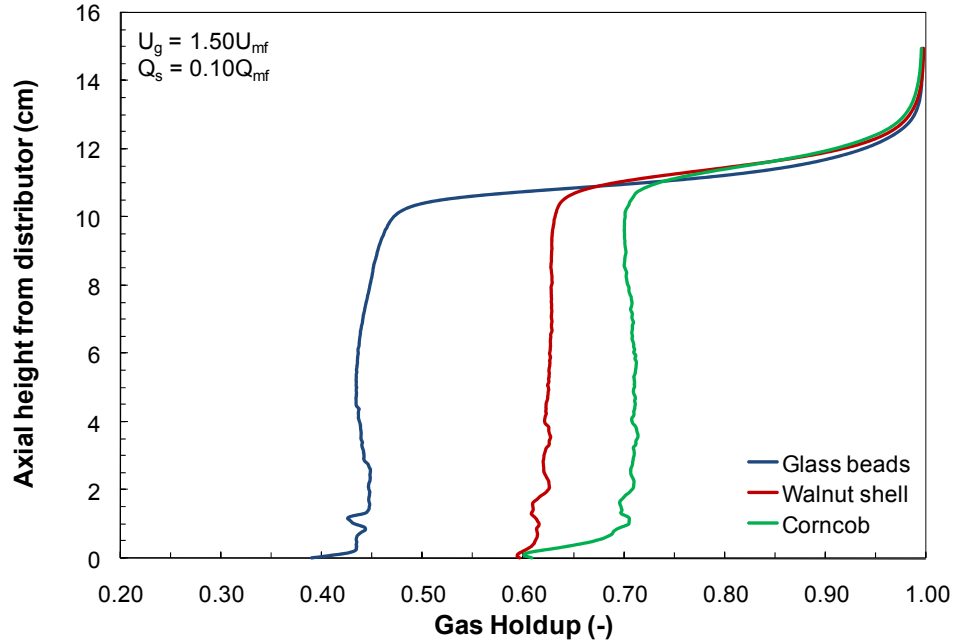


Figure 4.34: Average gas holdup by height for all materials: $Q_s = 0.10Q_{mf}$, $U_g = 1.5U_{mf}$.

The side air flow path also affects the bed height differently for each material. In glass beads the side air causes the bed height above the injector region to be noticeably larger than for the rest of the bed. This height difference is much less pronounced in walnut shell. The corncob exhibits an even smaller height difference. This effect again illustrates that injection air diffuses more rapidly in the lower density biomass beds.

The y-slice images without side air injection ($Q_s = 0Q_{mf}$) illustrate how side injector design and configuration affects fluidization. In the glass bead beds, the side injection port is not plugged and a region of higher gas holdup exists near the bed wall above the injector, indicating fluidization is affected by the open side injection port. Conversely, the side port is plugged in the $Q_s = 0Q_{mf}$ walnut shell and corncob images. The effects of the side injector design on fluidization hydrodynamics, if present, are not noticeable in these beds. This may also suggest that fluidization of low density materials is affected less by reactor geometry

than high density materials; however, due to the differences in side port configuration (plugged verses open) this trend requires more analysis for verification.

Another difference between the materials involves air penetration from the distributor plate. Figure 4.31 shows that air is distributed uniformly in the glass bead bed. In walnut shell, paths of high gas holdup extend from the distributor plate into the bed, indicating channeling occurs near the bed base. Channeling is even more pronounced in the corncob beds. Generally, as the density of the bed material decreases, gas has a higher tendency to form channels upon entering the bed. This effect is likely due to a reduction in force necessary to move low density particles from the air stream. While channeling is seen for walnut shell and corncob, it does not seem to affect the uniformity of the fluidization at higher locations in the bed. Figure 4.32 shows a similar trend at $U_g = 3U_{mf}$, although air channeling is also observed for the glass bead beds.

By comparing Figure 4.31 to Figure 4.32, effects of U_g on fluidization of different bed materials can be seen. Again many similarities exist between the materials. At higher U_g , a region of high gas holdup exists in the top center of all beds. The bed height on the edges of the bed is also much higher than in the center. This is due to bubbles coalescing and leaving the bed along the center axis, ejecting particles towards the sides of the reactor. Additionally, the flow structures mentioned earlier are also found for all materials at $U_g = 3U_{mf}$. Regions of higher gas holdup occur along the bottom edges of the bed indicating annular air flow. At larger bed heights, the high gas holdup regions converge near the center. Approaching the top of each bed, between the high gas holdup center and the walls, a region of low gas holdup is found and indicates recirculation of bed material.

Figure 4.32 also shows the major difference in varying U_g for three materials. As Q_s increases in the glass bead bed, the flow path extends from the side air injection port to the bed center. As a result, the glass bead fluidization is asymmetric and appears skewed towards the side air injection port. In walnut shell and corncob beds, the side air flow path is not as

clearly defined for all Q_s ; the y-slice images (Figure 4.32) show that fluidization is almost completely uniform even with side air injection.

It is also observed that as U_g increases, the average bed height becomes difficult to identify. At high U_g , large bubbles break at the surface more rapidly than at low U_g conditions. As a result, the time-averaged bed height is not constant but rather a gradient. This is shown in the y-slice images where a large gas holdup gradient exists through the central axis of the bed.

Increasing U_g also affects the average planar gas holdup for all materials similarly. Figure 4.35 shows the average planar gas holdup as a function of height for all materials with no side air and $U_g = 3U_{mf}$. The plot illustrates that the gas holdup for all three beds is relatively low at the base of the bed, and then remains fairly constant with increasing height until a point where the gas holdup again increases. The low gas holdup regions at the bottom of the beds indicate that air is less dispersed near the distributor plate, likely because of air jets from the distributor plate orifices. The gradual increase in gas holdup above $z = 10$ cm illustrates that the bed surface is much less defined for $U_g = 3U_{mf}$ than with $U_g = 1.5U_{mf}$ (Figure 4.33). The relative shape of the gas holdup curves, however, is similar for all materials. Also, the difference in gas holdup between the materials is fairly consistent with Figure 4.33.

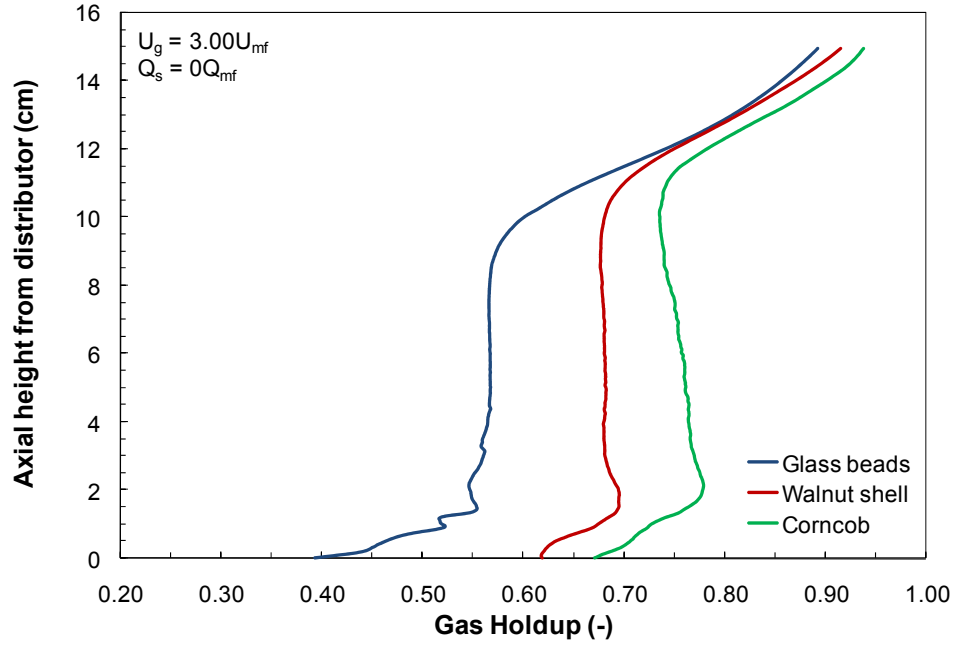


Figure 4.35: Average gas holdup by height for all materials: $Q_s = 0Q_{mf}$, $U_g = 3U_{mf}$.

4.3 Stereography

Section 4.3 provides analysis of the stereographic movies generated for the fluidized beds to show dynamic fluidization features. The U_g and Q_s conditions in the stereographic movies are identical to those used in CT acquisition. The movies support some of the results identified in CT imaging, but also provide insight into dynamic flow features. The first subsection describes the effects of changing Q_s and U_g on fluidization behavior. Analysis is done for each bed material independently. Next, a subsection describes how bed materials affect dynamic data acquired in stereography. In this research, stereographic data are used for qualitative analysis.

Stereographic imaging is composed of two perpendicular X-ray projections acquired simultaneously; one image is an x-z projection, and the other image is a y-z projection. In this section, a series of still frames from the movies are presented for each bed material. A

progression of still frames presents 0.20 seconds of data for both projections. The x-z projections are shown above the y-z projections in the following sections to allow more images to be shown, however, these images are placed side-by-side when compiled into movies. The injection port is shown in each projection and is located at the bottom-right wall in the x-z projection, and near the bottom-center in the y-z projection. The location of the injection tube also appears on the y-z projection as a vertical static object that is slightly darker than the surroundings. Also, in some images there are regions around the top-edges of the reactor where static electricity holds particles to the reactor walls. This is visible in the images but does not significantly affect fluidization behavior.

4.3.1 Effects of Various Flow Conditions

This subsection describes the effects of varying U_g and Q_s on stereographic data for glass beads, walnut shell, and corncob beds independently. Dynamic features are discussed and trends observed in CT imaging are confirmed.

4.3.1.1 Glass Beads

Figure 4.36 presents selected stereographic frames of glass bead fluidization with no side air injection for $U_g = 1.25U_{mf}$. From the images, relatively small diameter, spherical bubbles ($\sim 1\text{-}2$ cm in diameter) are shown to rise from the distributor plate towards the bed surface. Without side air injection, these bubbles appear to be distributed uniformly throughout the bed in both projections, indicating that fluidization is approximately uniform. Figure 4.36 also illustrates one of the main difficulties in stereographic imaging of glass beads; it is difficult to penetrate the center of the bed with X-rays without saturating the wall region in the image, and as a result, internal features are difficult to observe.

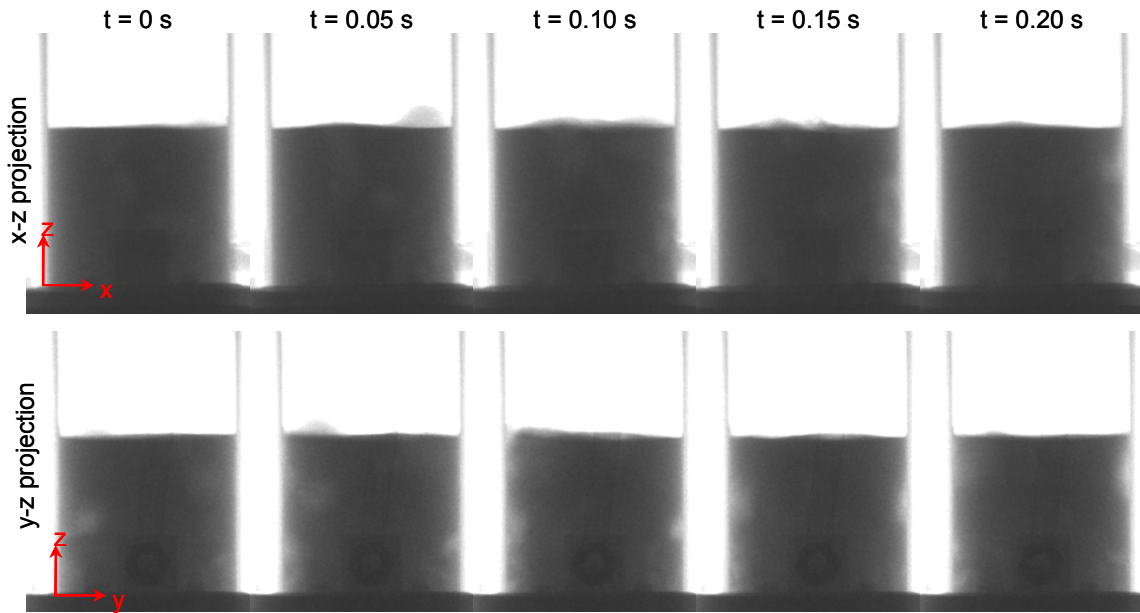


Figure 4.36: Stereographic images of glass bead fluidization: $U_g = 1.25U_{mf}$, $Q_s = 0Q_{mf}$.

To understand the effects of side air injection on glass bead fluidization, Figures 4.37-4.40 show stereographs of glass beads with side air injection at $Q_s = 0.05Q_{mf}$, $Q_s = 0.10Q_{mf}$, $Q_s = 0.15Q_{mf}$, and $Q_s = 0.20Q_{mf}$ respectively. When air is introduced through the side injection port, it is clear that a region of rapid bubbling occurs above the side air injector. For example, more bubbles appear to rise along the wall above the injector than in the surrounding bed in the x-z projection of Figure 4.37. This effect is seen in the local gas holdup plots where the time-averaged gas holdup above the injector is much larger than that of the surrounding bed at $U_g = 1.25U_{mf}$. Bubbles from the side air injector also appear to grow as they rise through the bed, which indicates bubble coalescence. Away from the side air injector the bed appears to fluidize uniformly. This is demonstrated in the y-z projections and the left-side of the x-z projections as uniformly sized bubbles appear uniformly dispersed throughout the bed. The effect is also verified by the local gas holdup plots presented in subsection 4.2.1.1.

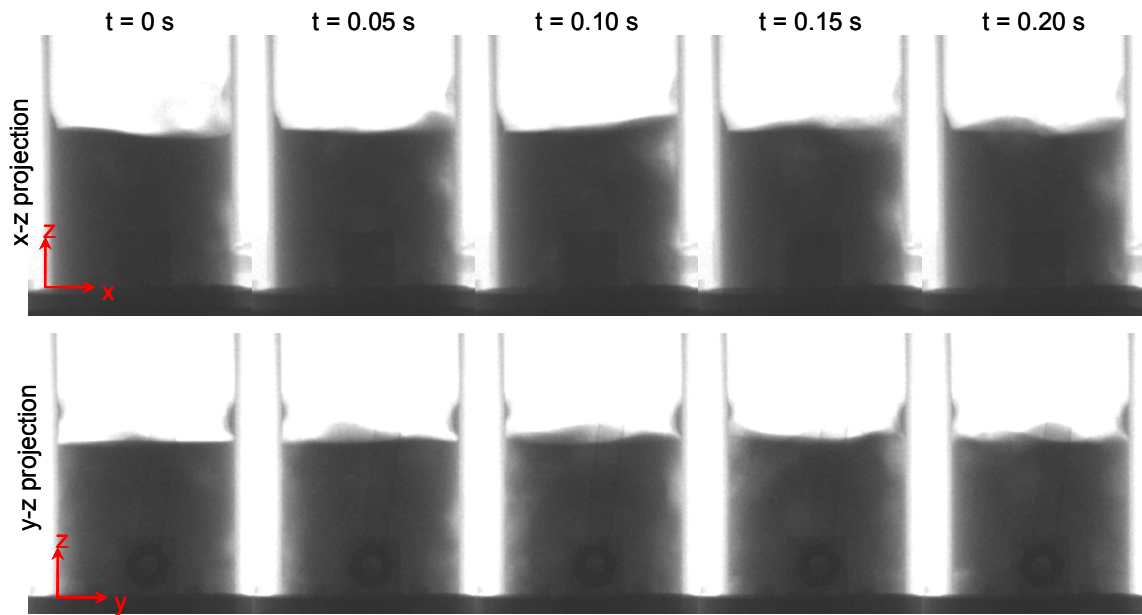


Figure 4.37: Stereographic images of glass bead fluidization: $U_g = 1.25U_{mf}$, $Q_s = 0.05Q_{mf}$.

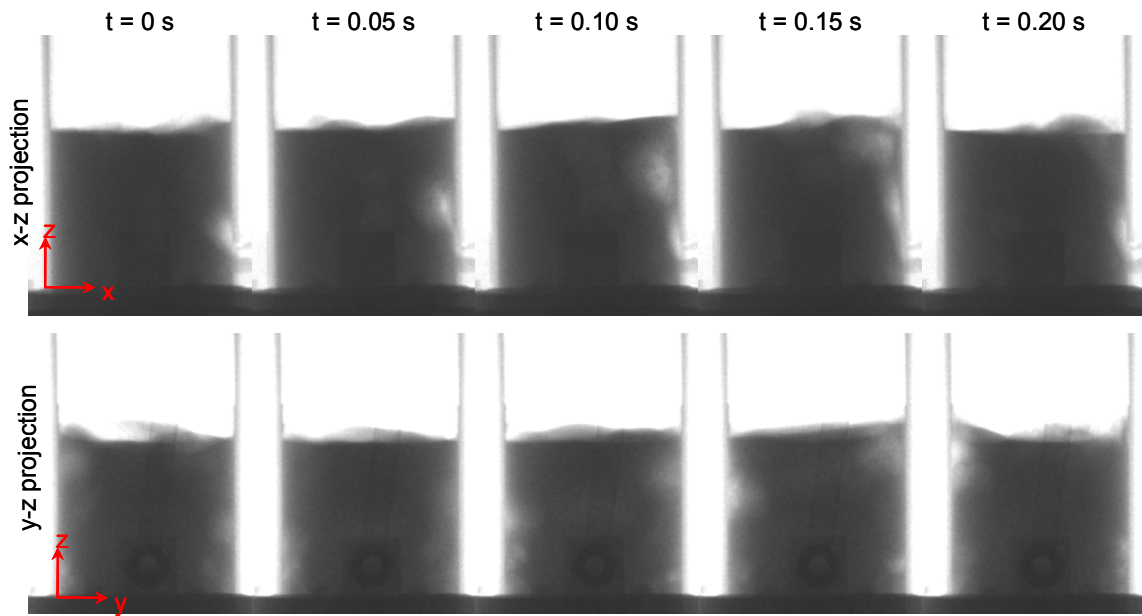


Figure 4.38: Stereographic images of glass bead fluidization: $U_g = 1.25U_{mf}$, $Q_s = 0.10Q_{mf}$.

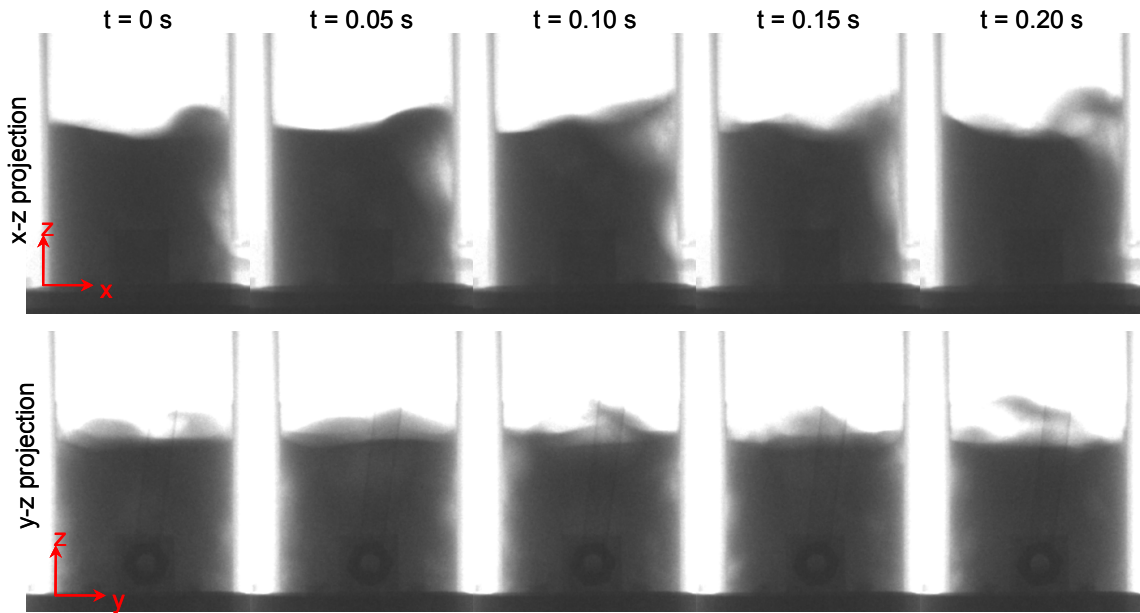


Figure 4.39: Stereographic images of glass bead fluidization: $U_g = 1.25U_{mf}$, $Q_s = 0.15Q_{mf}$.

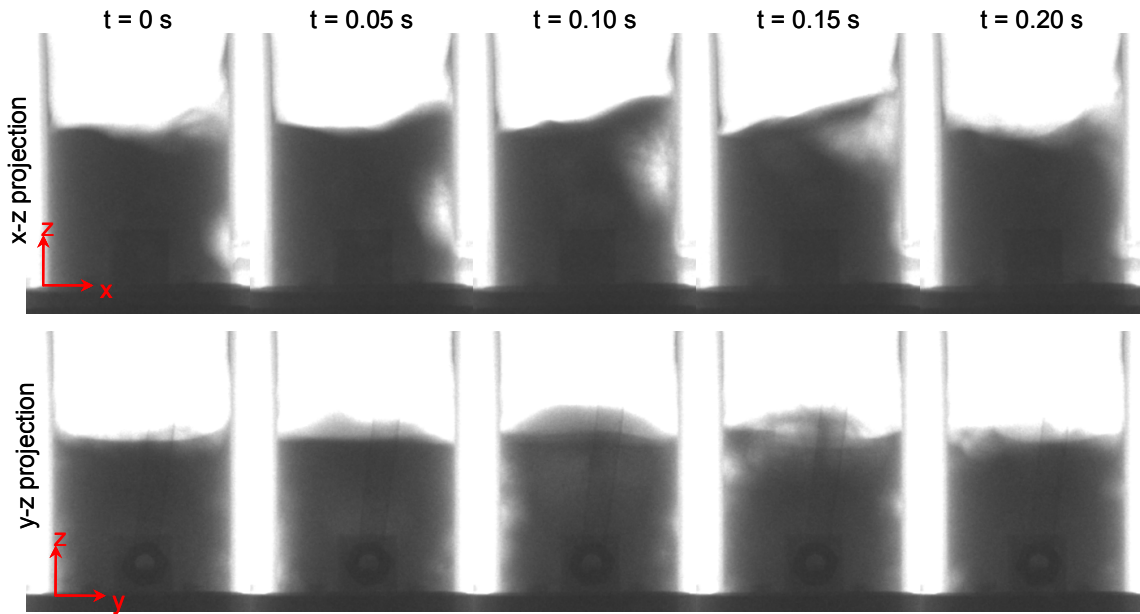


Figure 4.40: Stereographic images of glass bead fluidization: $U_g = 1.25U_{mf}$, $Q_s = 0.20Q_{mf}$.

Comparing Figure 4.36 through Figure 4.40, it is evident that varying Q_s has some influence on the bed hydrodynamics; however, these effects are mostly localized near the side injection port. The x-z projections illustrate that increasing Q_s also increases the average

bubble size above the side air injector. The bubbles above the injector for $Q_s = 0.05Q_{mf}$ (Figure 4.37) are much smaller than those visible for $Q_s = 0.20Q_{mf}$ (Figure 4.40).

Additionally, as Q_s increases, the bubbles appear to penetrate farther into the bed as shown in Figure 4.40. As expected, the bubble rise velocity also appears to increase with Q_s ; this occurs because a higher air velocity in the injector translates to higher air velocity in the bed. In all five figures, changes in Q_s do not seem to affect bed hydrodynamics outside of the side air injection region; both projections show many, small diameter bubbles dispersed throughout the bed regardless of Q_s . Additionally, the flow appears symmetrical in the y-z projections which correlate with the x-slice CT results.

Figures 4.41-4.44 present stereographic images of glass bead fluidization with various U_g and Q_s conditions to show the effects of increasing U_g on fluidization hydrodynamics. Figure 4.41 illustrates that with $U_g = 1.5U_{mf}$ and no side air injection, bubbles throughout the bed are larger than those in the $U_g = 1.25U_{mf}$ images. Similarly, the bubbles for $U_g = 3U_{mf}$ (Figure 4.43) are very large, indicating a high level of coalescence. Not only does bubble size increase with U_g , but the bubble speed also increases. By comparing the stereographic images, it can be seen that the bed is much more dynamic with $U_g = 3U_{mf}$ than with $U_g = 1.25U_{mf}$ and $1.5U_{mf}$. This effect is readily observed in the stereographic movies but difficult to capture in the still frames presented here. While individual bubble size appears to change with U_g , all beds appear to fluidize uniformly when no side air is injected.

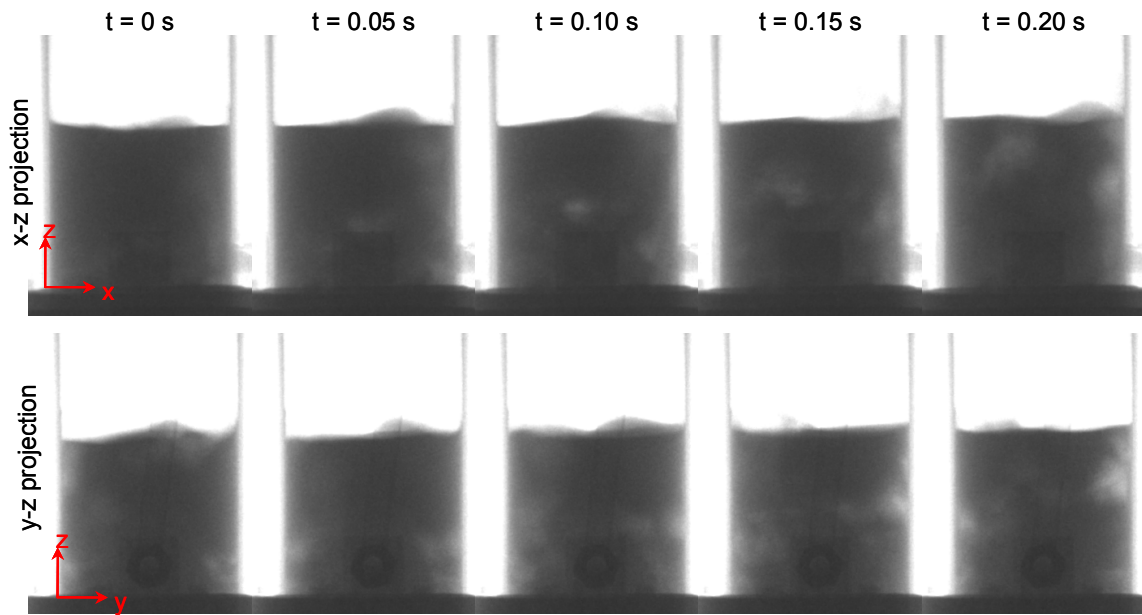


Figure 4.41: Stereographic images of glass bead fluidization: $U_g = 1.5 U_{mf}$, $Q_s = 0 Q_{mf}$.

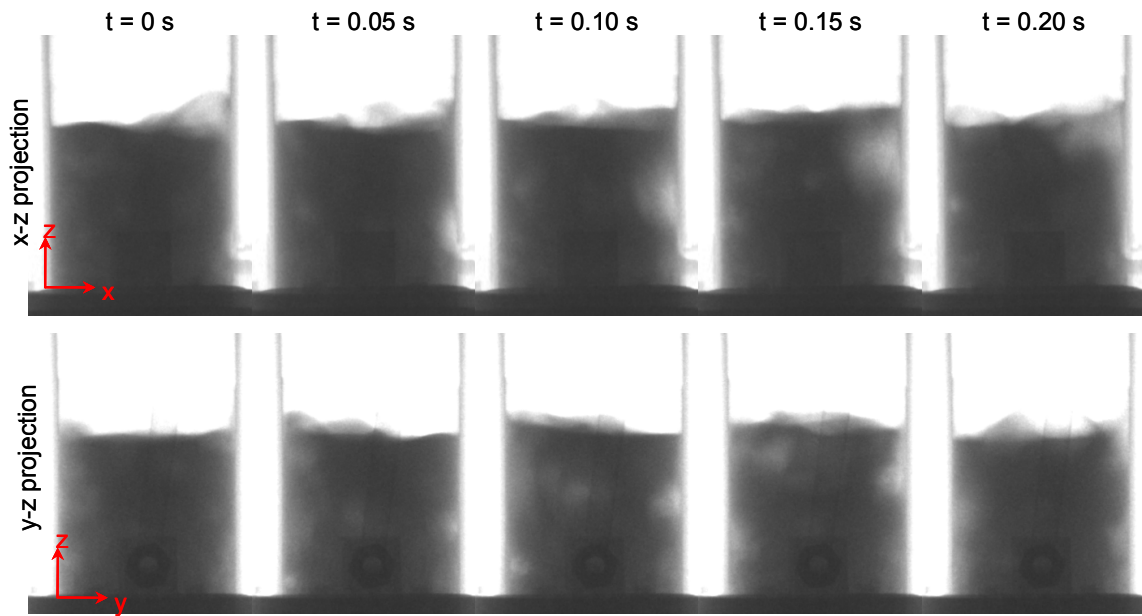


Figure 4.42: Stereographic images of glass bead fluidization: $U_g = 1.5 U_{mf}$, $Q_s = 0.10 Q_{mf}$.

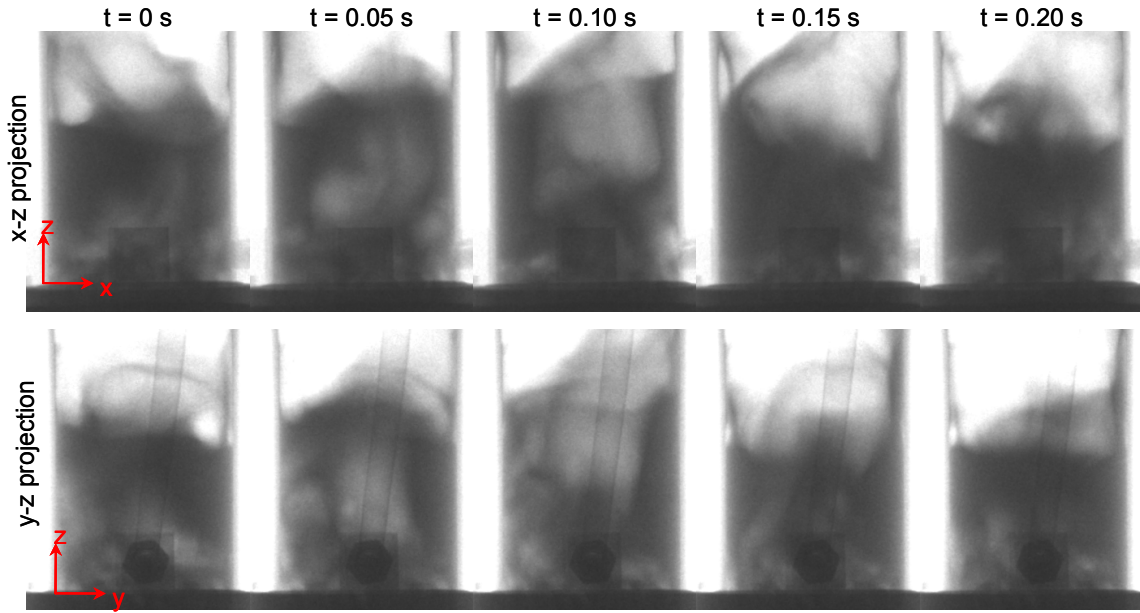


Figure 4.43: Stereographic images of glass bead fluidization: $U_g = 3U_{mf}$, $Q_s = 0Q_{mf}$.

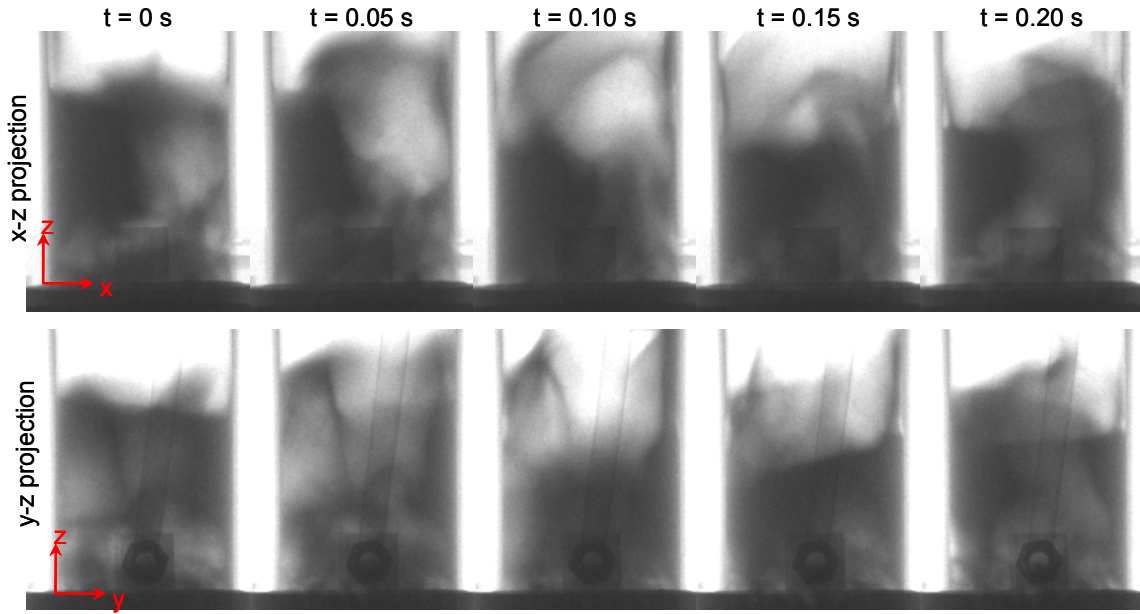


Figure 4.44: Stereographic images of glass bead fluidization: $U_g = 3U_{mf}$, $Q_s = 0.10Q_{mf}$.

The influence of side air injection on fluidization becomes less significant as U_g increases. For instance, the side air injection flow path is clearly seen when $U_g = 1.5U_{mf}$ (Figure 4.42), whereas the side air injection flow path under identical Q_s conditions is not

easily observed when $U_g = 3U_{mf}$ (Figure 4.44). Still, the intense bubbling appears to be slightly skewed towards the injector as side air is introduced for $U_g = 3U_{mf}$, showing that side air injection has a slight effect on glass bead fluidization hydrodynamics. This effect is described in detail for the gas holdup images (subsection 4.2.1.1).

These figures also show that increasing U_g increases the bed height, confirming observations from the gas holdup images. Note that it is difficult to make distinctions about bed height when $U_g = 3U_{mf}$ due to the highly dynamic interface; this illustrates the usefulness in collecting time-averaged local gas-holdup data. Despite increases in U_g , fluidization in the y-z projections appears to be symmetric. Again, this shows that fluidization is uniform far from the side air injector. U_g not only affects the bed hydrodynamics but also the X-ray penetration in the glass bead beds since more air is present in the bed, affecting attenuation. In the $U_g = 1.25U_{mf}$ images, it is difficult to clearly distinguish the internal features of the bed; however, internal features in the $U_g = 3U_{mf}$ images are more easily observed. This is also seen by the intensity of the bed material on the stereographic images. In beds with low U_g , the bed material appears darker than with high U_g , indicating higher X-ray attenuation occurs with less air flow. The increase in X-ray penetration with increasing U_g is caused by higher gas flowing through the system raising the gas holdup, thereby reducing the effective bed density. Since density is proportional to X-ray attenuation, increasing air flow is expected to improve penetration of dense materials.

4.3.1.2 Walnut Shell

Stereographic images of walnut shell fluidization with no side air injection and $U_g = 1.5U_{mf}$ are presented in Figure 4.45. It is observed that small bubbles approximately 1 - 2 cm in diameter are dispersed throughout the walnut shell bed, suggesting that fluidization occurs uniformly. It is also observed that internal features are highly visible in the walnut shell bed. The side injection port and tube are clearly seen in the y-z projections and extra bosses are

seen in the x-z projections. Since the walnut shell beds do not require X-ray saturation, the bed surface is also identifiable in the images. Bubbles are observed to break the surface of the bed, ejecting particles into the freeboard. It is also observed that the bed surface is fairly uniform with only minor disturbances due to bubbles breaking the surface.

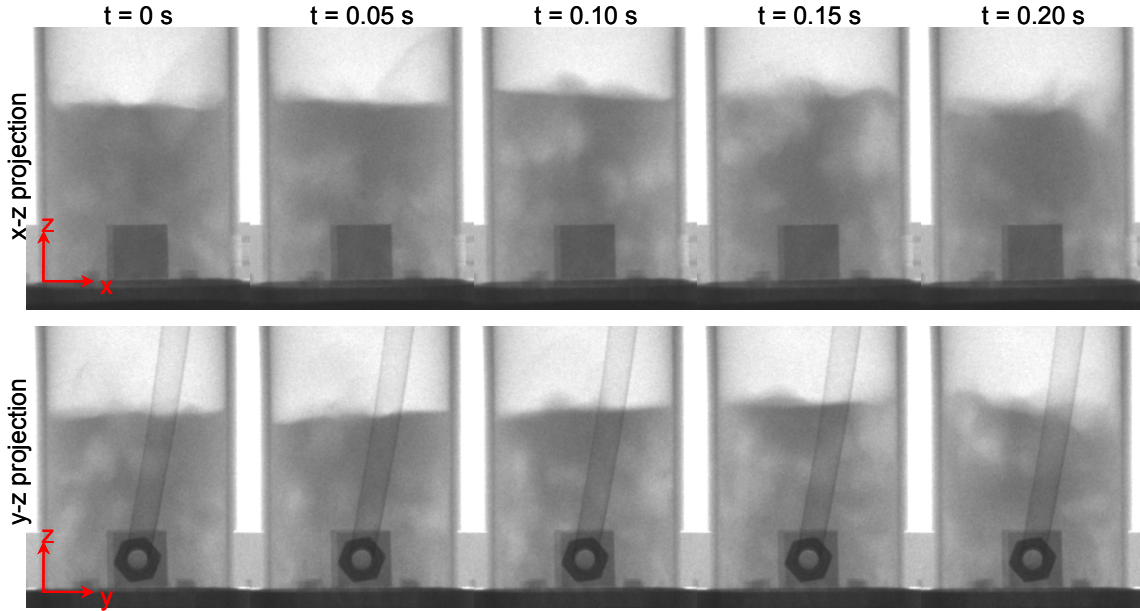


Figure 4.45: Stereographic images of walnut shell fluidization: $U_g = 1.5U_{mf}$, $Q_s = 0Q_{mf}$.

Figure 4.46 illustrates the effects of side air injection at $Q_s = 0.10Q_{mf}$ on walnut shell fluidization with $U_g = 1.5U_{mf}$. Stereographic projections demonstrate that as side air is introduced in walnut shell beds, relatively large air bubbles travel along the wall above the side air injection port, growing as they rise through the bed. Additionally, bubbling in the bed above the side air injection port is more rapid than in the surrounding bed. As observed in the time-averaged gas holdup results, the walnut shell bed appears to fluidize uniformly far from the side air injection flow path, indicated by uniformly dispersed bubbles.

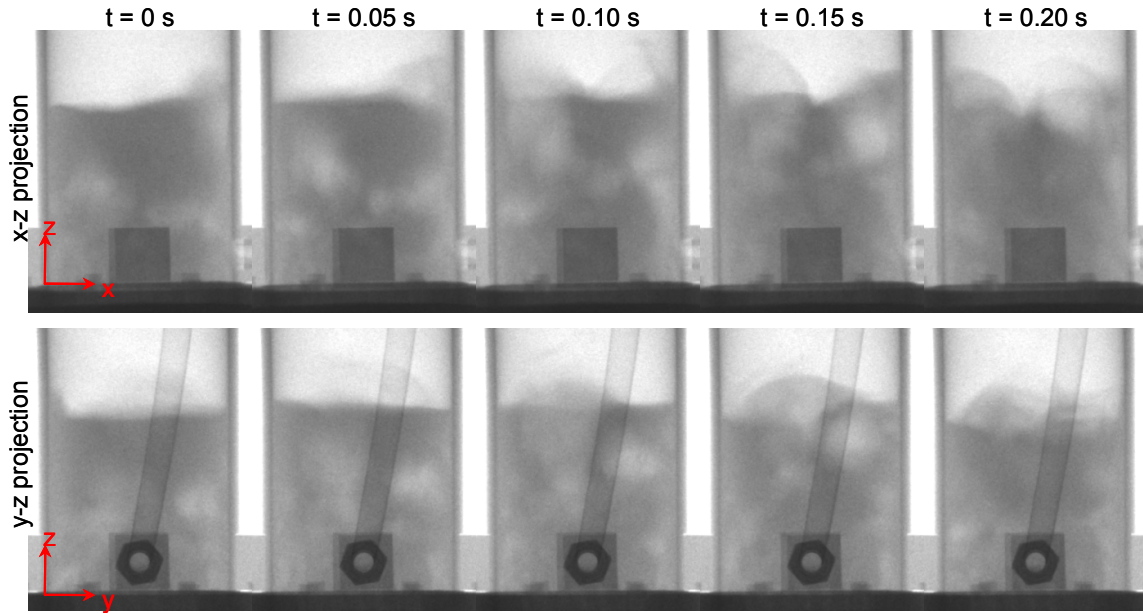


Figure 4.46: Stereographic images of walnut shell fluidization: $U_g = 1.5U_{mf}$, $Q_s = 0.10Q_{mf}$.

Increasing U_g in walnut shell fluidization significantly affects the bed hydrodynamics. To illustrate, Figure 4.47 presents stereographic frames of walnut shell fluidizing at $U_g = 3U_{mf}$ without side air injection. It is observed that as U_g increases from $U_g = 1.5U_{mf}$ (Figure 4.45) to $U_g = 3U_{mf}$, bubbles are considerably larger and rise much more rapidly. Consequently, as U_g increases, the bed becomes more dynamic. This result is expected since higher velocity through the distributor plate orifices translates to a larger air volume and upward air velocity in the bed. Additionally, with increased U_g , the surface of the bed is difficult to distinguish. Due to rapid bubbling, no definable bed boundary can be observed from the stereographic image; however, the bed expansion is noticeably larger with increased U_g . Despite the turbulent nature of the fluidization at high U_g , it appears the fluidization is uniform and large bubbles consistently break the surface near the center of the bed. This feature is more visible in stereographic movies than in still frames. It is also observed that X-ray penetration of the walnut shell slightly increases with increased U_g , due to a larger volume of air in the bed.

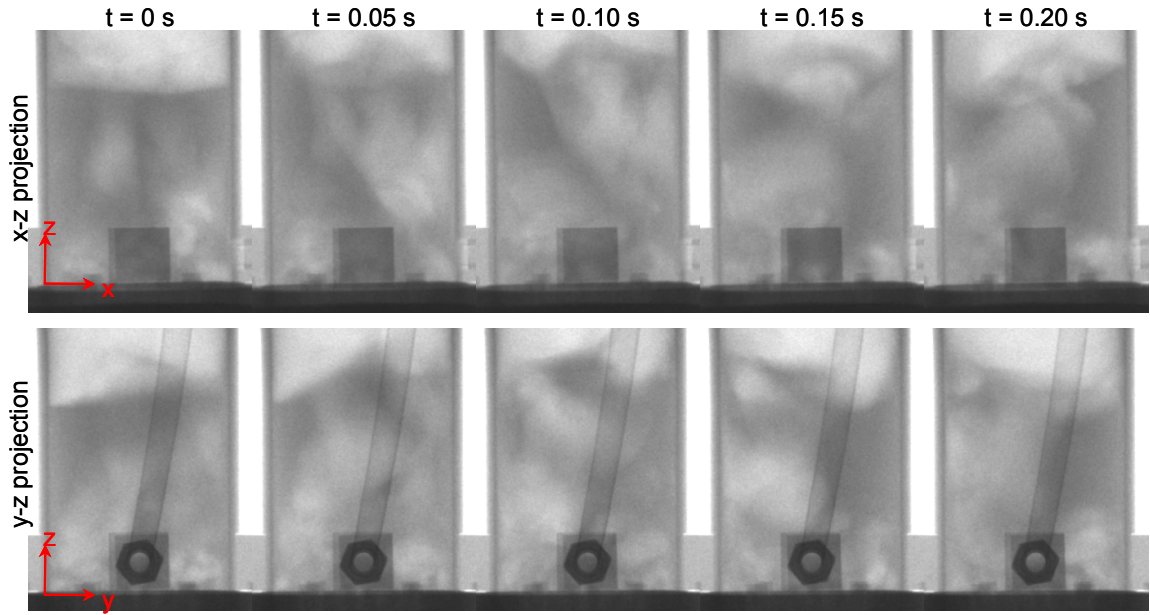


Figure 4.47: Stereographic images of walnut shell fluidization: $U_g = 3U_{mf}$, $Q_s = 0Q_{mf}$.

Increasing U_g also affects side air injection, as demonstrated by stereographic images of walnut shell fluidization with $U_g = 3U_{mf}$ and $Q_s = 0.10Q_{mf}$, in Figure 4.48. As U_g increases, the effects of side air injection on bed hydrodynamics are reduced. For $U_g = 1.5U_{mf}$, bubbling caused by side air injection is clearly observed; however, for $U_g = 3U_{mf}$ it is difficult to distinguish the effects of side air flow on the surrounding bed.

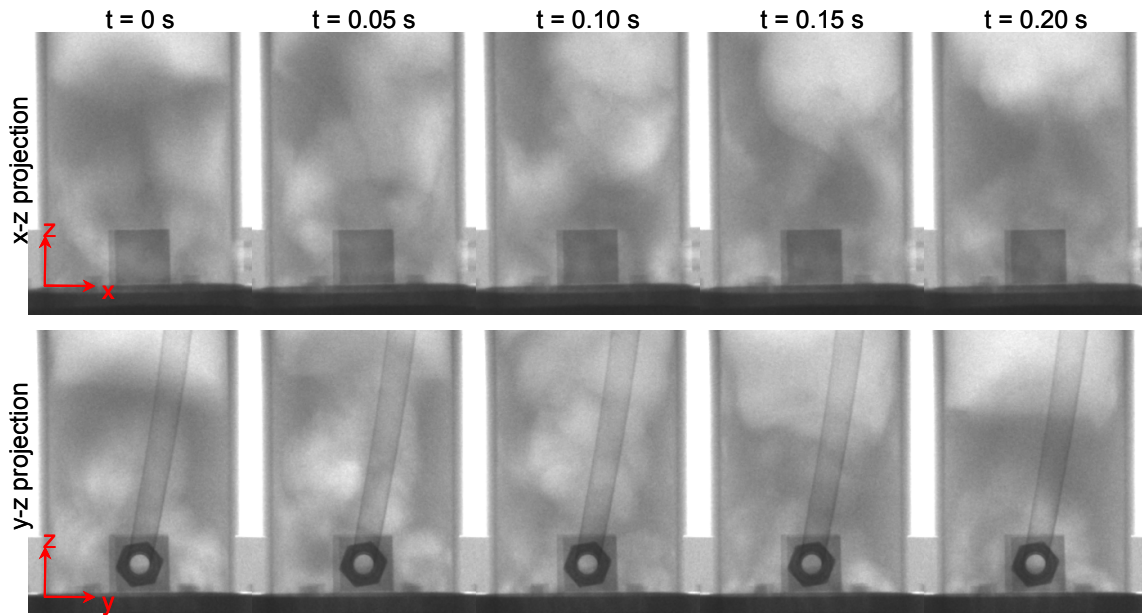


Figure 4.48: Stereographic images of walnut shell fluidization: $U_g = 3U_{mf}$, $Q_s = 0.10Q_{mf}$.

4.3.1.3 Corncob

Like glass bead and walnut shell beds, stereographic results of corncob beds highlight the effects of U_g and Q_s on fluidization hydrodynamics. Figure 4.49 presents stereographic frames of corncob fluidization with $U_g = 1.5U_{mf}$ and no side air. It is observed that many small bubbles ($\sim 1\text{-}2$ cm) are distributed evenly throughout the bed, indicating that fluidization is uniform with no side air injection. Additionally, X-rays easily penetrate corncob beds to show internal fluidization features without saturation of the bed walls. The side air injection port, extra bosses, and injection tube are also easily identifiable. Particle ejection from bubbles breaking the bed surface can be seen in the freeboard; however, the bed height appears fairly constant without side air injection.

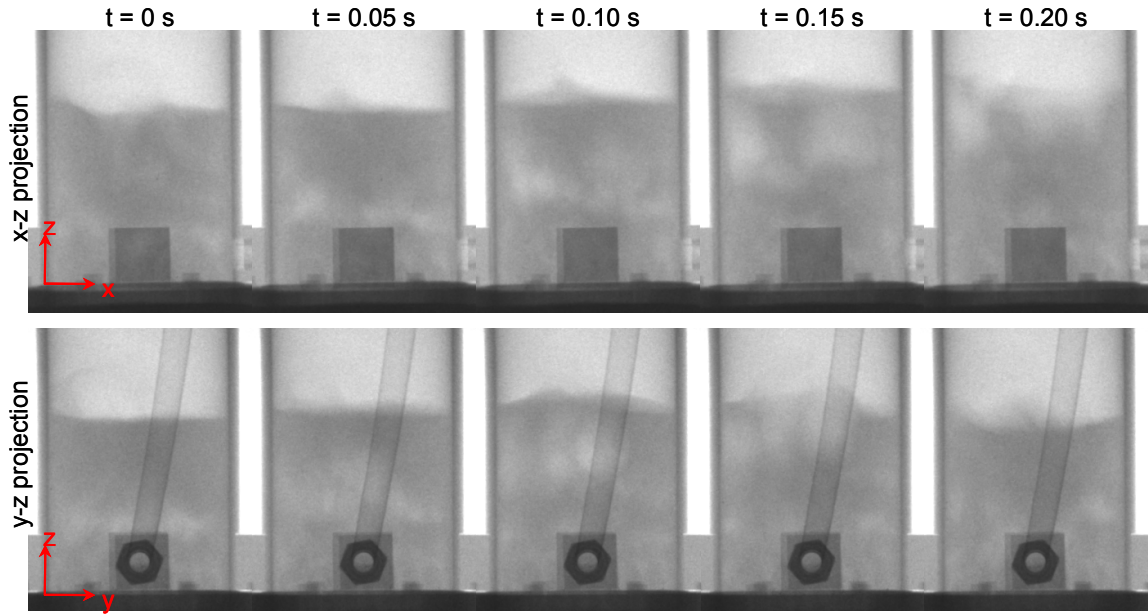


Figure 4.49: Stereographic images of corncob fluidization: $U_g = 1.5U_{mf}$, $Q_s = 0Q_{mf}$.

Figure 4.50 demonstrates the effects of side air injection at $Q_s = 0.10Q_{mf}$ on the corncob fluidized bed with $U_g = 1.5U_{mf}$. With side air injection, large bubbles coalesce along the wall above the side air injection port. These bubbles appear to rise more quickly than bubbles in the surrounding bed. It is also observed that the bubbles far from the side air injection flow path are fairly uniform, suggesting that fluidization uniformity is not affected by Q_s except near the side air injector.

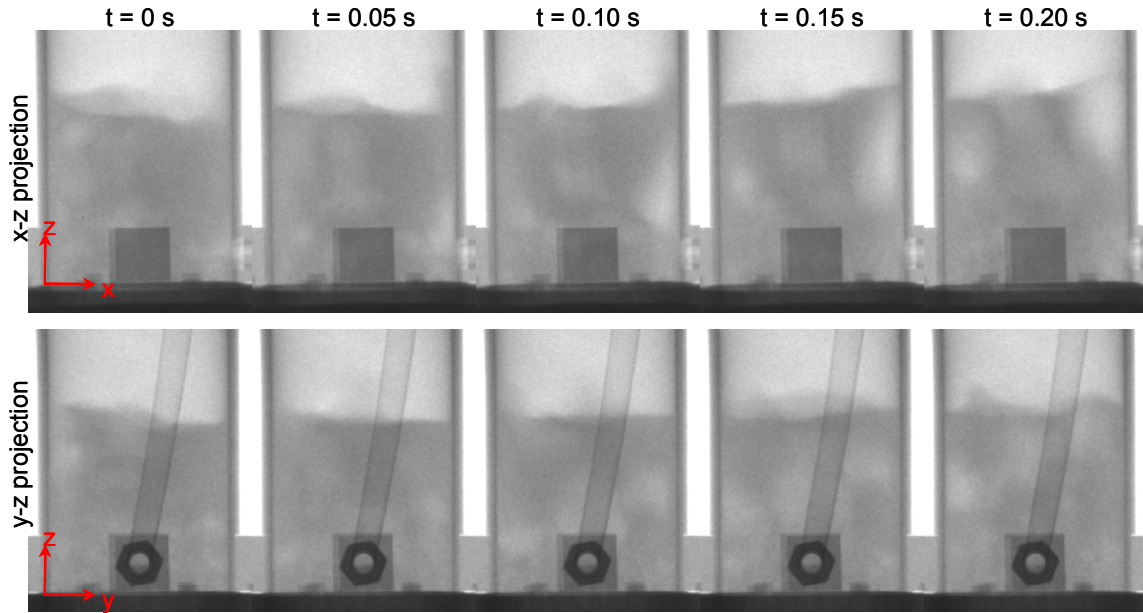


Figure 4.50: Stereographic images of corn cob fluidization: $U_g = 1.5U_{mf}$, $Q_s = 0.10Q_{mf}$.

By comparing corn cob fluidization without side air for $U_g = 1.5U_{mf}$ to Figure 4.51 for $U_g = 3U_{mf}$, the effects of increasing U_g are identified. As expected, increasing U_g increases bubble size and rise velocity. As a result, for $U_g = 3U_{mf}$, fluidization behavior is highly dynamic and the bed surface is not uniform with time. It is also observed that fluidization occurs uniformly with no side air injection, and is not significantly affected by U_g . Bubbles coalesce towards the center of the bed and are uniformly distributed. X-ray penetration is higher as U_g increases due to a larger bed gas holdup.

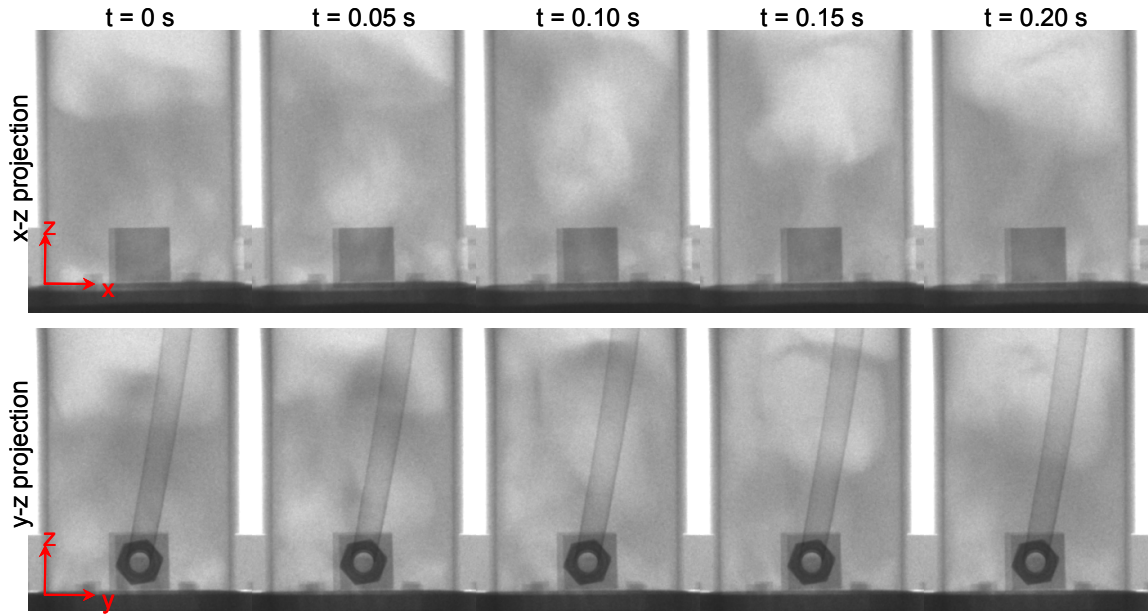


Figure 4.51: Stereographic images of corn cob fluidization: $U_g = 3U_{mf}$, $Q_s = 0Q_{mf}$.

Figure 4.52 shows the addition of side air at $Q_s = 0.10Q_{mf}$ on corn cob fluidization with $U_g = 3U_{mf}$. The figure illustrates that fluidization appears to be uniform, despite the addition of side air injection. Side air injection cannot be distinguished from the stereographic images and does not appear to greatly affect the hydrodynamics. As described in gas holdup results, as U_g increases, the effects of Q_s become less significant on fluidization behavior.

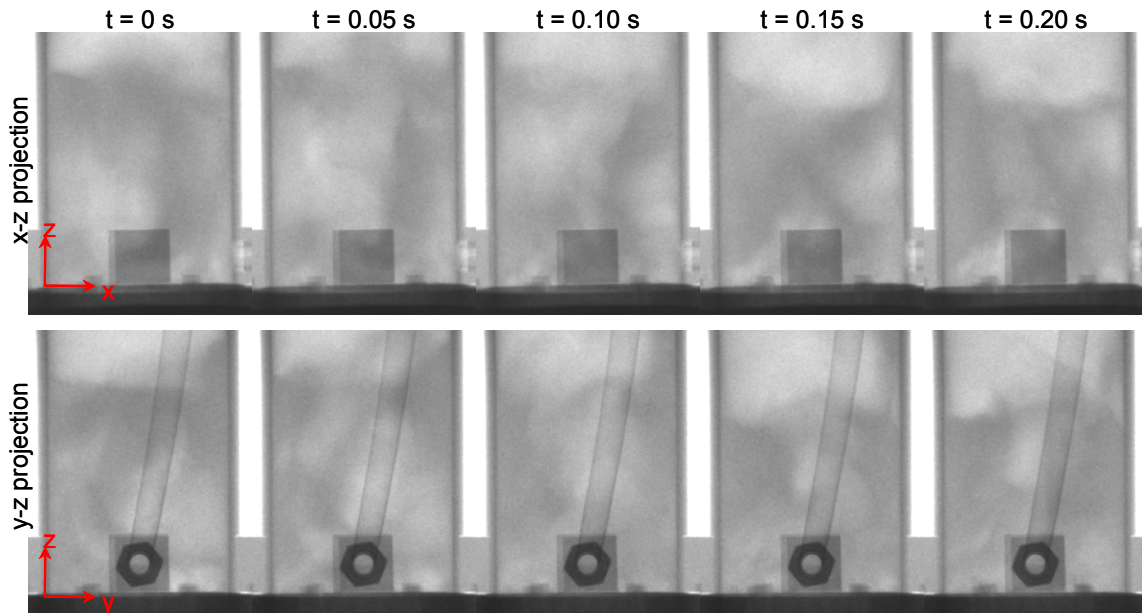


Figure 4.52: Stereographic images of corncob fluidization: $U_g = 3U_{mf}$, $Q_s = 0.10Q_{mf}$.

4.3.2 Effects of Bed Material

Stereographic data show similar trends for glass bead, walnut shell, and corncob beds. All three beds are observed to have small, uniformly dispersed bubbles at low U_g with no side air injection. As side air is introduced, bubbles preferentially rise along the wall above the side air injection port. Even with side air injection, the beds appear to fluidize uniformly far from the side air injection flow path. Increasing Q_s increases the rise velocity and size of these bubbles, as well as the penetration towards the bed center. As U_g increases, both the bubble size and rise velocity increase. This causes the bed to fluidize more rapidly with increasing U_g . Also, side air injection affects fluidization less as U_g increases; this effect is similarly observed gas holdup results. Glass beads exhibit the largest effects on fluidization behavior due to side air injection, followed by walnut shell and then corncob.

The most significant difference between the materials relates to the X-ray penetration. In glass beads, the bed walls and surface are saturated with X-rays in order to penetrate the center of the bed; even with saturation the internal fluidization features are difficult to see.

For the lower density walnut shell and corncob beds, saturation is not necessary and internal features are clearly identifiable. Similarly, X-ray penetration in corncob is even better than in walnut shell. Since density is related to X-ray attenuation, it is expected that the low density materials attenuate X-rays less than high density materials. These results show that radiographic/stereographic imaging is most effective on the walnut shell and corncob beds, and least effective on glass bead beds. It should be noted that this result is opposite of CT imaging where glass beads give the highest resolution with the lowest noise, followed by walnut shell and then corncob.

4.4 XPTV

Radiographic projections of tracer particle injection in a glass bead bed with $U_g = 1.50U_{mf}$ and $Q_s = 0.05Q_{mf}$ are shown in Figure 4.53 for 0.40 seconds of tracer particle movement. Appendix D shows the tracer particle for an additional 0.60 seconds. At time $t = 0$ s the tracer particle is injected into the bed through the side injection port, located at the bottom-right wall in the x-z projections and in the bottom-center of the y-z projections. The tracer particle locations are shown as red dots and the reference coordinate systems are labeled on each projection.

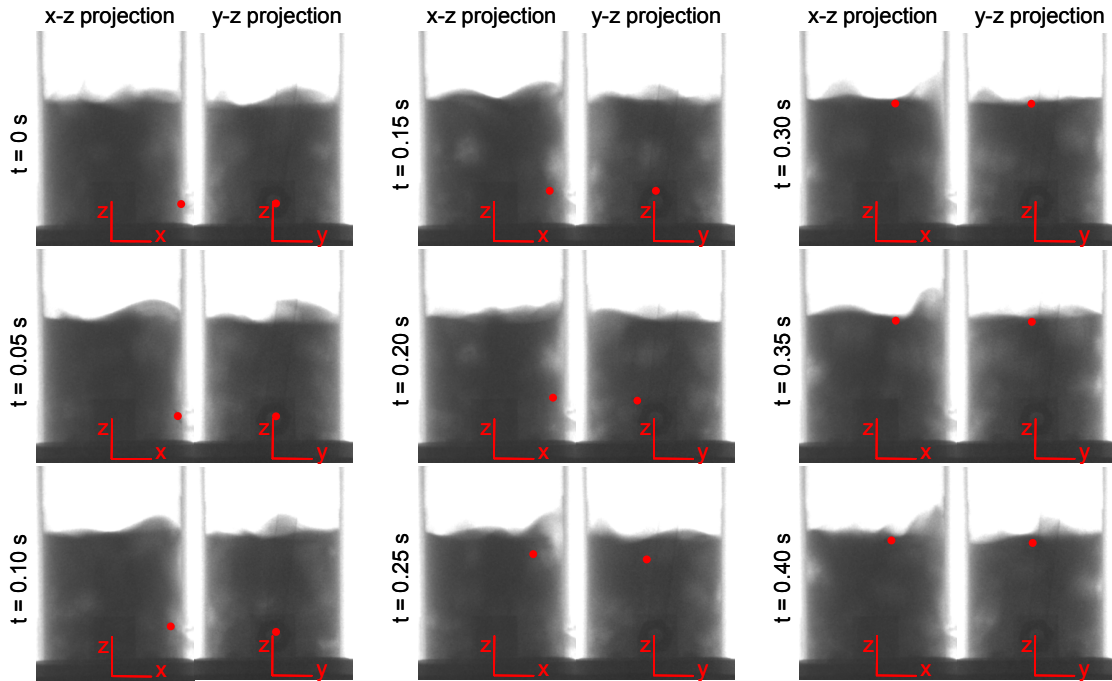


Figure 4.53: Particle tracking in glass bead fluidization: $U_g = 1.5U_{mf}$, $Q_s = 0.05Q_{mf}$.

From the projections, it is observed that the particle initially travels slowly upon injection into the bed. Between $t = 0.20$ and 0.30 s the particle travels a large vertical distance (in the positive z -direction) until reaching the surface of the bed. After $t = 0.30$ s, the particle gradually moves downwards towards the bottom of the bed (in the negative z -direction). The x - z projections show that from $t = 0$ to 0.50 s, the particle generally travels from the wall to the center of the reactor; however, after 0.50 seconds, the tracer remains near the center of the bed in the x -direction. The tracer particle is also observed to have little motion in the y -direction, and remains near the center of the bed throughout the images.

Based on the reference coordinate systems, the tracer location in x - y - z space is determined for each stereographic frame, and are presented in Appendix D. The tracer locations are also plotted in the x - z , y - z , and x - y planes in Figure 4.54, Figure 4.55, and Figure 4.56, respectively. In the plots, the reactor walls are identified as black lines, and the location of the side injection port appears as a gray rectangle or circle. Arrows indicate the

direction of the particle travel after the initial injection. The plots highlight similar trends to those noticed in the stereographic projections. The x-z and y-z plots show that the particle initially travels slowly in the bed after injection, followed by a large vertical z-displacement between $t = 0.20$ to 0.30 seconds and then gradual downward particle movement in the negative z-direction after $t = 0.30$ seconds. The particle is again observed to travel towards the center of the column from the side injection port, however, relatively little movement is seen in the y-direction. It is also observed that between $t = 0.15$ and 0.20 s, the tracer particle sharply deviates from the previous trajectory. This effect is explained later.

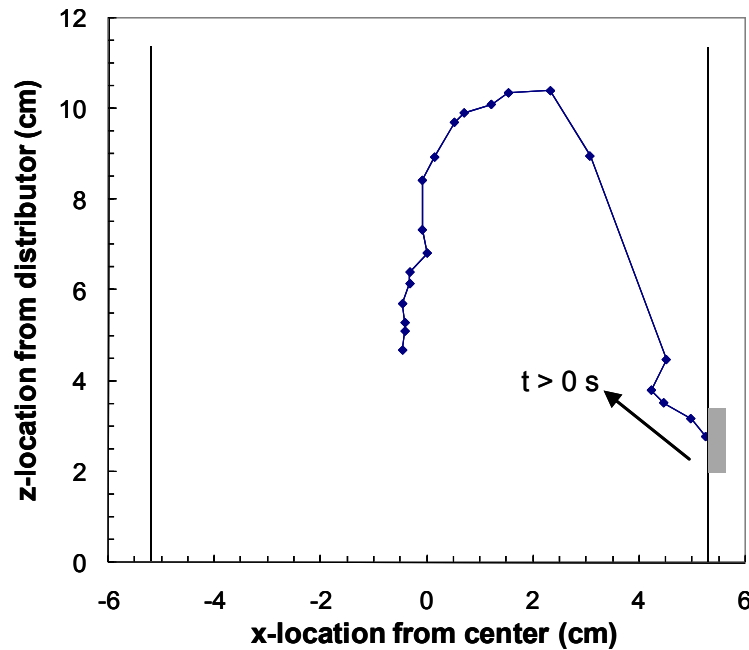


Figure 4.54: Injected tracer particle trajectory in x-z plane (each data point represents a time interval of 0.05 sec).

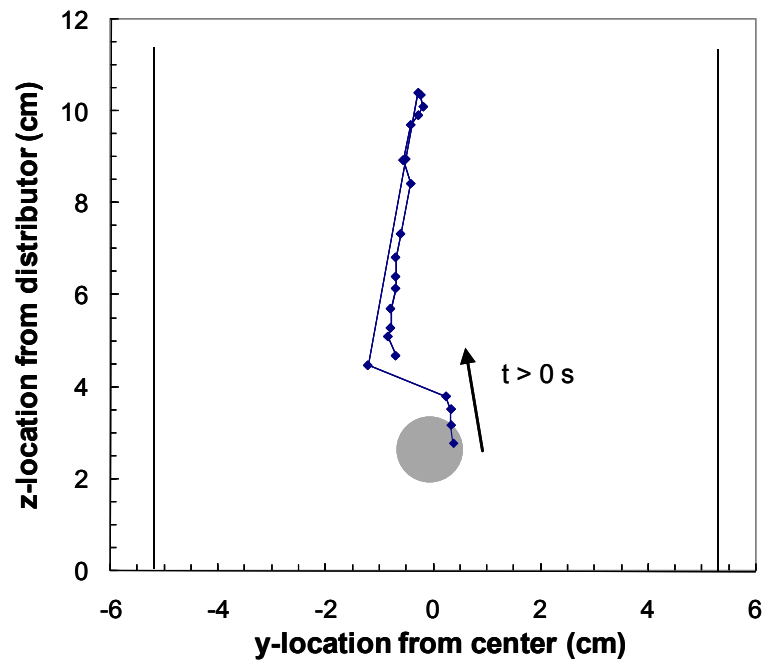


Figure 4.55: Injected tracer particle trajectory in y-z plane (each data point represents a time interval of 0.05 sec).

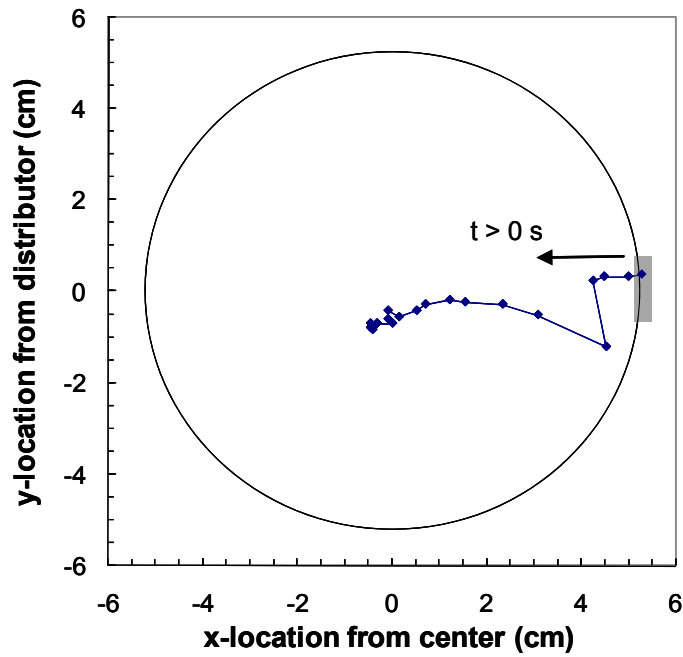


Figure 4.56: Injected tracer particle trajectory in x-y plane (each data point represents a time interval of 0.05 sec).

In addition to calculating tracer particle locations for each stereographic frame, the instantaneous tracer x-, y-, and z-velocities are calculated, and plotted as a function of time in Figure 4.57. The raw data is also presented in a table in Appendix D. The velocity plot confirms trends observed in location plots. Low velocities before $t = 0.15$ s suggest the particle initially moves slowly in the bed. At $t = 0.15$ s the particle changes trajectory which is seen by the spike in x- and y-velocities. At $t = 0.20$ s, a large increase in z-velocity indicates the tracer rises rapidly in the bed. After $t = 0.35$ s, x- and y-velocity are nearly zero while z-velocity is negative, confirming the gradual downward motion of the particle.

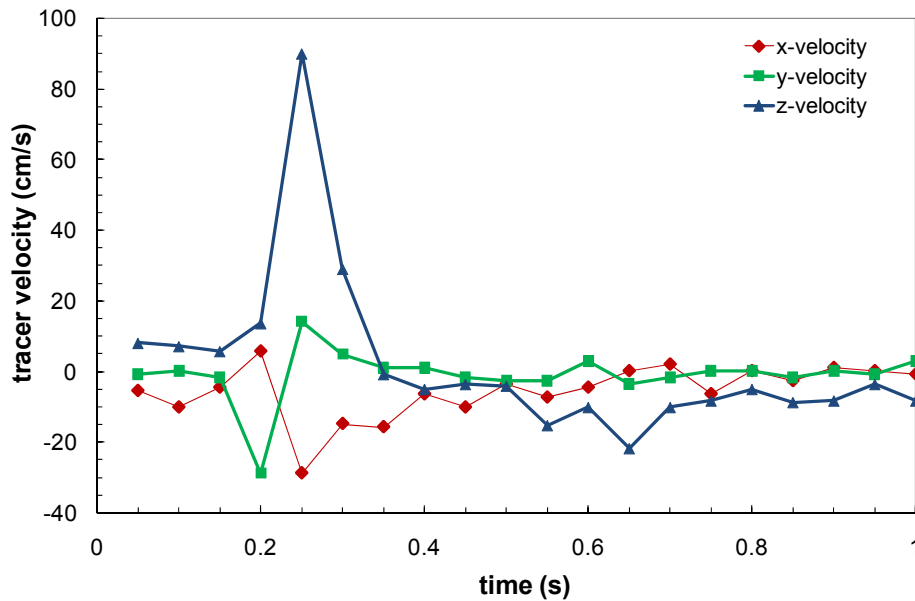


Figure 4.57: Injected tracer particle velocity in x-, y-, and z-directions.

The images and plots illustrate an important feature of particle injection into a fluidized bed. As discussed earlier, a large velocity spike at $t = 0.20$ s indicates the particle rapidly rises in the z-direction. This result was also observed by Shen et al. (2007). Comparing the particle motion to rising bubbles in the stereographic projections, it is also evident that the particle rise velocity is much larger than the rise velocities of surrounding bubbles. This effect can be understood by revisiting the side air injection velocity and superficial gas

velocity. For glass beads fluidized with $U_g = 1.50U_{mf}$, the superficial air velocity is 27.1 cm/s. The side air injection velocity at $Q_s = 0.05Q_{mf}$ is 90.5 cm/s, and is calculated from the side air injector diameter and the side air flow rate. These velocities are presented in a table in Appendix B. Additionally, the maximum z-velocity (rise velocity) of the tracer particle occurs at $t = 0.25$ s and is 89.5 cm/s. Comparing these velocities, the rise velocity of the tracer particle is nearly identical to the side air injection velocity. This indicates that at 0.20 s, the tracer particle is entrained in the side air injection flow, causing the particle to rapidly rise to the surface. As a result, fluidization hydrodynamics do not appear to affect the tracer particle motion until after the particle has reached the surface of the bed. Also, the trajectory of the particle injection in the x-direction from $t = 0.15$ to 0.50 s appears to follow the shape of the side air flow path observed in gas holdup images. This again illustrates the occurrence of a preferential flow path caused by side air injection. Once on the bed surface, the tracer particle travels outside of the side air flow path and fluidization hydrodynamics begin to affect the motion of the particle.

This effect also explains the observations made earlier. The tracer particle initially travels slowly after injection into the bed ($t < 0.15$ s). It is likely that upon injection, the particle is not immediately entrained in the side air flow path, and its motion is instead governed by the fluidization hydrodynamics. At $t = 0.15$ s, a sharp deviation in tracer trajectory occurs which suggests the tracer particle enters the side air flow path. Also, after $t = 0.50$ s the tracer particle sinks in the negative z-direction in the center of the bed. This indicates that after $t = 0.50$ s the particle is no longer in the side air injection flow path and the motion is only governed by fluidization. Since large gas holdup occurs near the top-center of the bed, it is expected that the tracer particle will sink since its buoyancy decreases with increased gas holdup (increased gas holdup decreases the bed density).

To illustrate further, Figure 4.58 presents the particle trajectory in the x-z plane superimposed on the gas holdup y-slice image for glass bead fluidization with $U_g = 1.50U_{mf}$

and $Q_s = 0.05Q_{mf}$. The figure confirms the observations about injection particle dynamics. After $t = 0.15$ s, the tracer clearly travels within the side air flow path shown on the time-averaged gas holdup image, at which point it rapidly rises towards the bed surface. The particle trajectory correlates well with the shape of the side air injection flow path.

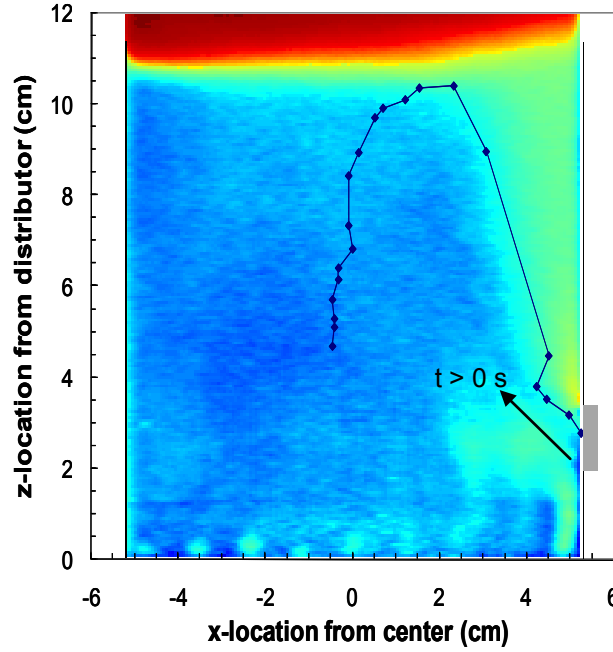


Figure 4.58: Tracer particle x-z location superimposed on gas holdup y-slice for glass bead fluidization: $U_g = 1.50U_{mf}$, $Q_s = 0.05Q_{mf}$ (each data point represents a time interval of 0.05 sec).

The trends observed in the particle tracking proof-of-concept illustrate the usefulness of particle tracking in a fluidized bed. Quantitative results show important dynamic features such as tracer particle location and velocity as a function of time. While these trends provide insight into particle injection in a fluidized bed of glass beads, further tests should be performed to validate the results. The development of an automated particle tracking algorithm would also improve reliability and accuracy of the results while reducing the calculation time. Finally, since tracer particles can attain velocities as high as the side air velocity (which can be up to 362 cm/s for glass beads with $Q_s = 0.20Q_{mf}$), faster cameras are necessary to improve time resolution and reduce the uncertainty in particle location.

Chapter 5: Conclusions and Recommendations

5.1 Conclusions

This research generated high quality experimental data with noninvasive X-ray techniques in order to validate CFD simulations which can ultimately improve the efficiency of biomass injection into a fluidized bed gasifier. The significant findings of this study were:

- The bed material was an important consideration when performing X-ray computed tomography and radiography/stereography on fluidized beds. CT imaging was more effective on glass bead beds than walnut shell or corncob beds since glass beads exhibited higher X-ray attenuation. This high attenuation increased the range of X-ray intensity values, which in turn increased the resolution of the CT data. Also, glass beads were ideal for gas holdup calculations due to higher bulk material homogeneity than in walnut shell and corncob beds. As a result, the noise in glass bead fluidization gas holdup data was lower than for walnut shell and corncob beds. Conversely, X-ray radiography/stereography was most effective on corncob and walnut shell beds. X-ray attenuation of the walnut shell and corncob beds was much lower than in glass beads due to lower material densities. As a result, it was easier to penetrate the walnut shell and corncob beds with X-rays and the internal features were highly visible. It was difficult to visualize tracer particles in glass bead beds due to the similar attenuation properties between the tracer and the glass beads. Since walnut shell and corncob exhibited low X-ray attenuation, tracer particles may be more distinguishable in these beds.
- Increasing the superficial gas velocity decreased the effects of side air injection for beds of glass beads, walnut shell, and corncob. From time-averaged gas holdup data at low U_g , it was observed that a side air injection flow path was clearly defined from the side

injection port to the surface of the bed. As U_g increased, the boundary of this path became less distinguishable. The surface of the bed was also observed to become more uniform with increasing U_g . Consequentially, increasing U_g improved the fluidization uniformity and decreased the significance of side air injection on bed hydrodynamics.

The following presents conclusions relating to the objectives described in Chapter 1.

Objective 1: Review current literature to better understand fluidization, biomass and its relationship to thermochemical conversion, nonintrusive testing methods that can be used to visualize internal fluidization features, and current needs in CFD simulation.

Conclusion 1: In Chapter 2, a review of current literature presented important fundamentals of fluidization behavior and fluidized beds, and highlighted important fluidization parameters such as gas holdup and the minimum fluidization velocity. Next, biomass and biomass fluidization was explained with an emphasis on common thermochemical conversion processes, such as gasification, that utilize fluidized beds to convert biomass into useful products. The review discussed the importance of noninvasive flow visualization for opaque multiphase flow systems, like fluidized beds. Two X-ray techniques were summarized; X-ray computed tomography and X-ray radiography/stereography/particle tracking velocimetry. Finally, the review described the need for high-quality experimental fluidized bed data in order to validate CFD simulations. CFD was described as one method of improving efficiency for processes like gasification.

Objective 2: Compare the effects of bed material on the minimum fluidization velocity to better understand the relationship between fluidization of the inert catalyst bed material and biomass fluidization.

Conclusion 2: Minimum fluidization velocity was experimentally determined without side air injection for fluidized beds of three different materials; glass beads, ground walnut shell, and ground corncob. Results showed that $U_{mf,0}$ decreased with bed material density; however, an explicit correlation could not be determined since U_{mf} is a complex function that includes many factors. Experimental plots showed that the pressure drop across the bed increased with increasing material density. The five side air flow conditions ($Q_s = 0Q_{mf,0}$, $Q_s = 0.05Q_{mf,0}$, $Q_s = 0.10Q_{mf,0}$, $Q_s = 0.15Q_{mf,0}$, $Q_s = 0.20Q_{mf,0}$) and five superficial gas velocities ($U_g = 1.25U_{mf,0}$, $U_g = 1.5U_{mf,0}$, $U_g = 1.75U_{mf,0}$, $U_g = 2U_{mf,0}$, and $U_g = 3U_{mf,0}$) used in the minimum fluidization experiments and X-ray imaging, were normalized to $U_{mf,0}$ and $Q_{mf,0}$ for each material.

Objective 3: Evaluate the effects of side gas injection, typical of biomass feed systems in gasifiers, on the minimum fluidization velocity.

Conclusion 3: The minimum fluidization velocity for each material with five different side air injection flow conditions was evaluated. Plots showed that the addition of side air caused the pressure-velocity curve to rise gradually, unlike the linear curve observed without side air injection. It was hypothesized that side air injection created two fluidization points; partial fluidization occurred at a U_g below U_{mf} , while complete fluidization occurred at U_{mf} . As Q_s increased, U_{mf} for corncob and walnut shell beds decreased, however, this effect was not seen in glass bead beds. Corncob beds exhibited the greatest reduction in U_{mf} with increasing Q_s .

Objective 4: Apply X-ray CT imaging to calculate time-averaged local gas holdup for fluidized beds in order to visualize time-averaged internal flow features.

Conclusion 4: Time-averaged local gas holdup was calculated for each material and flow combination using CT imaging. From the 3-D data, 2-D slices and plots of local gas

holdup were used to identify trends. For all materials, fluidization occurred uniformly without side air injection; however, the side air injector port was found to slightly influence bed hydrodynamics when it remained open. At a low superficial gas velocity ($U_g = 1.25U_{mf,0}$), some local gas holdup results were below the theoretical bulk gas holdup value. It was speculated that this effect was due to bed material packing, noise, and measurement errors.

Objective 5: Compare the effects of side gas injection on fluidization using local gas holdup data.

Conclusion 5: As side air was introduced in all beds, a preferential air flow path was observed which extended from the side air injection port to the bed surface. The side air flow path gradually penetrated the bed with increasing axial height from the side air injection port. With increasing Q_s , the side air flow path was also found to penetrate farther towards the center of the bed and the magnitude of the gas holdup within the flow path increased. Additionally, side air injection created a localized region of very high gas holdup directly above the side air injection port, which was observed to increase in size with increased Q_s . At low U_g , the side air flow path also disrupted the uniformity of the bed surface, causing the bed height above the injection port to be larger than the surrounding bed height. Despite influencing fluidization uniformity near the side air injector, fluidization appeared uniform in the remainder of the bed, regardless of Q_s .

Objective 6: Assess the effects of varying superficial gas velocity on fluidization using local gas holdup information.

Conclusion 6: By increasing U_g , the local gas holdup was observed to increase in all beds due to a higher volume of air passing through the material. Internal flow structures were also affected as U_g increased. Generally, air flow from the distributor plate was

concentrated around the reactor walls, leaving a region of low gas holdup in the center of the bed. The region of high gas holdup along the walls migrated towards the bed center as height increased, indicating that bubbles traveled from the walls towards the bed center. A small region of relatively low gas holdup was also observed near the walls in the top portion of the bed and was the result of recirculating bed material. As U_g increased, side air flow penetrated further into the glass bead beds for a fixed Q_s . Changes in U_g were shown to affect injector air penetration more significantly than changes in Q_s . Increasing U_g also improved fluidization uniformity, causing the side air flow path to be less distinct. The average bed height was more symmetrical with higher U_g , again demonstrating more uniform fluidization. The average bed height was less distinct with increased U_g , and regions of low gas holdup were observed along the walls at the top of the bed; this effect was attributed to large bubbles rapidly breaking the surface in the center of the bed and ejecting bed material towards the reactor walls. Additionally, at high U_g air jets from the distributor plate orifices were observed in the CT images near the bottom of the bed and uniform fluidization did not occur directly above the distributor plate. For regions away from the distributor plate, the beds appeared to fluidize uniformly for all Q_s and U_g combinations, except near the side air injection port.

Objective 7: Distinguish the effects of bed material on fluidization, with and without side air injection, through gas holdup information.

Conclusion 7: The effects of Q_s and U_g on local time-averaged gas holdup and fluidization hydrodynamics were similarly observed in beds of glass beads, walnut shell, and corncob with only slight differences. The higher density glass beads exhibited lower gas holdup than the lower density walnut shell or corncob beds; this effect also followed the bulk gas holdup for each material. Gas holdup resolution in glass bead beds was higher than in walnut shell and corncob beds due to the large X-ray attenuation in glass. Similarly, more

noise was introduced in the corncob and walnut shell beds due to the heterogeneous nature of the bulk material. The side air injection flow path was observed to diffuse more in the corncob and walnut shell than the glass beads; this effect was also seen by a more symmetrical time-averaged bed height in corncob and walnut shell beds. Additionally, corncob and walnut shell fluidization appeared more uniform than glass bead fluidization. At high U_g , the side air injection did not significantly affect fluidization symmetry in corncob and walnut shell while glass bead fluidization was skewed towards the side air injection port.

Objective 8: Demonstrate the application of X-ray stereographic imaging towards understanding dynamic fluidization features.

Conclusion 8: Stereographic imaging of fluidized beds showed dynamic features not observed in the time-averaged gas holdup data, and also validated some effects described in the gas holdup results. Bubble size and velocities were seen in stereographic movies, as well as the effects of side air injection and changes in superficial gas velocity. Results of stereographic imaging were qualitative in this work.

Objective 9: Evaluate the effects of side gas injection on fluidization hydrodynamics using stereographic imaging.

Conclusion 9: Stereographic imaging in beds without side air injection showed many small uniformly dispersed bubbles. A region of rapid bubbling was observed above the side air injection port as side air was introduced. Bubbles from the side air injector appeared to grow as they traveled upwards. The size and rise velocity of these bubbles also increased and penetrated toward the center of the bed with increasing Q_s . The bubbles remained uniformly dispersed in the bed away from the side air injection port and were relatively unaffected by side air injection.

Objective 10: Compare the effects of varying superficial gas velocity on fluidization hydrodynamics through stereographic imaging.

Conclusion 10: Stereographic images demonstrated that increasing U_g in glass bead beds increased both bubble size and rise velocity. Without side air injection, fluidization appeared to be uniform. The influence of side air injection on fluidization was less significant as U_g increased, indicating that more uniform fluidization occurred at higher U_g . The bed height also increased as U_g increased. X-ray penetration of glass bead fluidization increased with U_g due to an increase in gas holdup. At low U_g , it was difficult to distinguish internal features of the flow due to high X-ray attenuation. In addition, the reactor walls were saturated with X-ray energy to improve penetration in the center of the glass bead bed, resulting in a loss of image quality near the bed walls.

Objective 11: Contrast the effects of bed material on fluidization hydrodynamics and on stereographic imaging.

Conclusion 11: The effects of U_g and Q_s were similarly observed in stereographic images of glass beads, walnut shell, and corncob beds. X-ray penetration in walnut shell and corncob beds was much higher than in glass bead beds, and as a result, internal features of walnut shell and corncob beds were more clearly identifiable. Also, saturation of the bed walls was unnecessary in corncob and walnut shell beds. It was determined that walnut shell and corncob were more suitable as fluidization materials in stereographic X-ray imaging while glass beads were better for X-ray CT imaging.

Objective 12: Present a proof-of-concept technique for tracking a particle upon injection into a fluidized bed through a side injection port.

Conclusion 12: Particle tracking was performed on a tracer injected through the side port in a fluidized bed of glass beads. A visual tracking method was employed to determine the locations and velocities of the tracer particle as a function of time. The results showed that the tracer particle initially traveled slowly upon injection, but at a certain time the tracer rapidly rose towards the surface of the bed. Next the particle was found to migrate towards the center of the bed and fall towards the bottom of the bed. It was hypothesized that the dynamics of the tracer particle were governed by the side air flow as it traveled towards the bed surface; however, once reaching the surface, the particle traveled outside the side air flow path and the fluidization hydrodynamics primarily affected the tracer motion. These results should be validated by additional experiments after a reliable automated particle tracking method is developed.

5.2 Recommendations

For future studies, further minimum fluidization experiments should be performed under identical side air injection conditions described in this study in order to improve the reliability of the data. Additional minimum fluidization experiments should be performed with high side air flow rates (such as $Q_s = 0.30Q_{mf,0}$ or $Q_s = 0.50Q_{mf,0}$) for a more complete understanding of how side air injection affects fluidization.

Fluidization should also be examined for various bed materials at different bed heights to understand how bed height affects fluidization with side air injection. Additional studies should be performed on varying reactor geometries to determine the effects of side air injection on fluidization hydrodynamics. These experiments could provide beneficial information about reactor scale-up; one of the largest obstacles in CFD modeling. Some preliminary work has been done in this area but more research is necessary for verification (Franka et al., 2008).

Fluidization with side air injection through multiple injection ports should be compared to the results from this study. This has practical relevance in gasification systems which utilize multiple biomass injection ports. Multiple configurations should be tested under a variety of Q_s conditions.

A particle tracking algorithm must be developed that has a high probability of particle detection and can create particle trajectory and velocity information. This algorithm is necessary since visually tracking particles is ineffective and is susceptible to significant human error. To improve the probability of particle recognition, alternative tracer particles should be developed that have a much higher attenuation than the bed material. The density of new tracer particles must be carefully designed so the particle does not sink upon injection into a bed. Two types of particles should be designed for each bed; (i) a biomass-like particle to represent biomass injection into a gasifier and (ii) a neutrally buoyant particle to show the dynamic flow characteristics of the bed material.

Also, the trends observed in the particle tracking results, discussed in Chapter 4, should be validated by performing additional particle injection experiments. Since this research only presented a proof-of-concept approach to particle tracking, a thorough study of injection particle behavior is necessary to verify the observations in this research. These experiments would be simplified with an automated particle tracking routine.

To reduce the error in particle tracking, stereographic images should be acquired at a frame rate that is much greater than 20 fps. In this study, tracer particles were difficult to identify during particle injection due to the slow camera frame rate when compared to particle velocity. This may necessitate an increase in binning level (reducing the image resolution) or the purchase of faster CCD cameras.

References

- Abdullah, M.Z., Husain, Z., and Yin Pong, S.L., 2003, "Analysis of cold-flow fluidization test results for various biomass fuels," *Biomass & Bioenergy*, 24, pp. 487-494.
- Asadullah, M., Miyazawa, T., Shin-ichi, I., Kunimori, K., and Tmishige, K., 2003, "Demonstration of real biomass gasification drastically promoted by effective catalyst," *Applied Catalysis*, 246, pp. 103-116.
- Bhusarapu, S., Al-Dahhan, M.H., and Duduković, M.P., 2006, "Solids flow mapping in a gas-solid riser: mean holdup and velocity fields," *Powder Technology*, 163, pp. 98-123.
- Boland, D., and Geldart, D., 1971, "Electrostatic charging in gas fluidised beds," *Powder Technology*, 5(5), pp. 289-297.
- Boyer, C., Duquenne, A.M., and Wild, G., 2002, "Measuring techniques in gas-liquid and gas-liquid-solid reactors," *Chemical Engineering Science*, 57, pp. 3185-3215.
- Brandani, S., and Zhang, K., 2006, "A new model for the prediction of the behavior of fluidized beds," *Powder Technology*, 163, pp. 80-87.
- Bridgwater, A.V., and Peacocke, G.V.C., 2000, "Fast pyrolysis processes for biomass," *Renewable and Sustainable Energy Reviews*, 4, pp. 1-73.
- Bridgwater, A.V., 2003, "Renewable fuels and chemicals by thermal processing of biomass," *Chemical Engineering Journal*, 91, pp. 87-102.
- Brown, R.C., 1997, "ME 539: fluidized bed processes," Course Notes for ME539/ChE539, Iowa State University, Ames, IA.
- Bruni, G., Solimene, R., Marzocchella, A., Salatino, P., Yates, J.G., Lettieri, P., and Fiorentino, M., 2002, "Self-segregation of high-volatile fuel particles during devolatilization in a fluidized bed reactor," *Powder Technology*, 128, pp. 11-21.
- Callen, A., Moghtaderi, B., and Galvin, K.P., 2007, "Use of parallel inclined plates to control elutriation from a gas fluidized bed," *Chemical Engineering Science*, 62, pp. 356-370.
- Chaouki, J., Larachi, F., and Dudukovic, M.P., 1997, "Noninvasive tomographic and velocimetric monitoring of multiphase flows," *Industrial and Engineering Chemical Research*, 36, pp. 4476-4503.
- Constantineau, J.P., Grace, J.R., Lim, C.J., and Richards, G.G., 2007, "Generalized bubbling-slugging fluidized bed reactor model," *Chemical Engineering Science*, 62, pp. 70-81.

- Cui, H., and Grace J.R., 2007, "Fluidization of biomass particles: a review of experimental multiphase flow aspects," *Chemical Engineering Science*, 62, pp. 45-55.
- Davidson, J. F., and Harrison, D., 1963, *Fluidised Particles*, University Press, London, NW.
- Demirbas, A., 2007, "Combustion systems for biomass fuel," *Energy Sources, Part A: Recovery, Utilization, and Environmental Effects*, 29(4), 303 - 312.
- Deza, M., Battaglia, F., and Heindel, T.J., 2007, "Computational modeling of biomass in a fluidized bed gasifier," *Proceedings of 2007 ASME International Mechanical Engineering Congress and Exposition*, Seattle, Washington, IMECE2007-43097, pp. 1-8.
- Du, B., Warsito, W., and Fan, L.S., 2005, "ECT studies of gas-solid fluidized beds of different diameters," *Industrial and Engineering Chemical Research*, 44, pp. 5020-5030.
- Dudukovic, M.P., 2002, "Opaque multiphase flows: experiments and modeling," *Experimental Thermal and Fluid Science*, 26, pp. 747-761.
- Ellenberger, J., and Krishna, R., 1995, "A unified approach to the scale-up of gas-solid fluidized bed and gas-liquid bubble column reactors," *Chemical Engineering Science*, 49(24), pp. 5391-5411.
- Felipe, C.A.S., and Rocha, S.C.S, 2007, "Prediction of minimum fluidization velocity of gas-solid fluidized beds by pressure fluctuation measurements - analysis of the standard deviation methodology," *Powder Technology*, 174, pp. 104-113.
- Ford, J., December 2006, "Using X-ray computed tomography to measure local gas holdup in a stirred tank reactor," *MS Thesis*, Iowa State University.
- Ford, J.J., Heindel, T.J., and Jensen, T.C., 2007, "Imaging a gas-sparged stirred-tank reactor with X-ray CT," *Proceedings of the 5th Joint ASME/JSME Fluids Engineering Conference*, San Diego, CA: ASME Press, Paper FEDSM2007-37022.
- Franka, N., Heindel, T.J., and Battaglia, F., 2007, "Visualizing cold-flow fluidized beds with X-rays," *Proceedings of the 2007 ASME International Mechanical Engineering Exposition and Congress*, Seattle, Washington, Paper: IMECE2007-43073.
- Franka, N., Drake, J.B., and Heindel, T.J., 2008, "Minimum fluidization velocity and gas holdup in fluidized beds with side port air injection," *Proceedings of the 2008 ASME Fluids Engineering Division Summer Meeting*, Jacksonville, Florida, Paper: FEDSM2008-55100.
- Gauthier, D., Zerguerras, S., and Flamant, G., 1999, "Influence of the particle size distribution of powders on the velocities of minimum and complete fluidization," *Chemical Engineering Journal*, 74, pp. 181-196.

Geldart, D., 1973, "Types of gas fluidization," *Powder Technology*, 7, pp. 285-292.

Gera, D., Mathur, M.P., Freeman, M.C., and Robinson, A., 2002, "Effect of large aspect ratio of biomass particles on carbon burnout in a utility boiler," *Energy and Fuels*, 16, pp. 1523-1532.

Glicksman, L., Carr, E., and Noymer, P., 2008, "Particle injection and mixing experiments in a one-quarter scale model bubbling fluidized bed," *Powder Technology*, 180, pp. 284-288.

Grace, J.R., Leckner, B., Zhu, J., and Cheng, Y., 2006, "Chapter 5: Fluidized Beds," in *Multiphase Flow Handbook*, Crowe, C.T., CRC Press, First edition, pp. 5.1-5.93.

Grassler, T., and Wirth, K.E., 2000, "X-ray computer tomography – potential and limitation for the measurement of local solids distribution in circulating fluidized beds," *Chemical Engineering Journal*, 77, pp. 65-72.

Guardiola, J., Rojo, V., and Ramos, G., 1996, "Influence of particle size, fluidization velocity and relative humidity on fluidized bed electrostatics," *Journal of Electrostatics*, 37, pp. 1-20.

Halow, J.S., "Electrical capacitance imaging of fluidized beds," in *Non-invasive Monitoring of Multiphase Flows*, Chaouki, J., Larachi, F., and Dudukovic, M.P., Elsevier Science B.V., Amsterdam, Netherlands, pp. 263-307, (1997).

Hammer, E.A., Johansen, G.A., Dyakowski, T., Roberts, E.P.L., Cullivan, J.C., Williams, R.A., Hassan, Y.A., and Claiborn, C.S., 2006, "Chapter 14: Advanced Experimental Techniques," in *Multiphase Flow Handbook*, Crowe, C.T., CRC Press, First edition, pp. 14.1-14.125.

Han, L., and Al-Dahhan, M.H., 2007, "Gas-liquid mass transfer in a high pressure bubble column reactor with different sparger designs," *Chemical Engineering Science*, 62, pp. 131-139.

Harteveld, W.K., 2005, "Bubble columns structures or stability?" PhD Thesis, Delft Technical University, Delft, Netherlands.

Harteveld, W.K., Mudde, R.F., and van den Akker, H.E.A., 2003, "Dynamics of a bubble column: influence of gas distribution on coherent structures," *The Canadian Journal of Chemical Engineering*, 81, pp. 389-394.

Heindel, T.J., Hubers, J.L., Jensen, T.C., Gray, J.N., and Striegel, A.C., 2005, "Using X-rays for multiphase flow visualization," *Proceedings of the 2005 ASME Fluids Engineering Division Summer Meeting and Exhibition*, Houston, TX: ASME Press, Paper FEDSM2005-77359.

Heindel, T.J., Gray, J.N., and Jensen, T.C., 2008, "An X-ray system for visualizing fluid flows," *Flow Measurement and Instrumentation*, 19(2), pp. 67-78.

Hernandez-Atonal, F.D., Ryu, C., Sharifi, V.N, and Swithenbank, J., 2007, "Combustion of refuse-derived fuel in a fluidised bed," *Chemical Engineering Science*, 62, pp. 627-635.

Hilal, N., Ghannam, M.T., and Anabtawi, M.Z., 2001, "Effect of bed diameter, distributor and inserts on minimum fluidization velocity," *Chemical Engineering Technology*, 24, pp. 161-165.

Hokel, B.W., 1996, "Radiation safety study guide for users of analytical X-ray systems," Environment, Safety, Health and Assurance, Ames Laboratory, Ames, IA, pp. 1-60.

Hubers, J.L., Striegel, A.C., Heindel, T.J., Gray, J.N., Jensen, T.C., 2005 "X-ray computed tomography in large bubble columns," *Chemical Engineering Science*, 60(22), pp. 6124-6133.

Hulme, I., and Kantas, A., 2004, "Determination of bubble diameter and axial velocity for a polyethylene fluidized bed using X-ray fluoroscopy," *Powder Technology*, 147, pp. 20-23.

Jones, S., May 2007, "Gas-liquid mass transfer in an external airlift loop reactor for syngas fermentation," *PhD dissertation*, Iowa State University, Ames, Iowa.

Joshi, and Ranade, 2003, "Computational fluid dynamics for designing process equipment: expectations, current status, and path forward," *Industrial and Engineering Chemical Research*, 42, pp. 1115-1128.

Kant Pandit, J., Wang, X.S., and Rhodes, M.J., 2007, "A DEM study of bubble formation in Group B fluidized beds with and without cohesive inter-particle forces," *Chemical Engineering Science*, 62, pp. 159-166.

Kantzas, A., Wright, I., and Kalogerakis, N., 1997, "Quantification of channelling in polyethylene resin fluid beds using X-ray computer assisted tomography (CAT)," *Chemical Engineering Science*, 52(13), pp. 2023-2035.

Kertzscher, U., Seeger, A., Affeld, K., Goubergrits, L., and Wellnhofer, E., 2004, "X-ray based particle tracking velocimetry-a measurement technique for multi-phase flows and flows without optical access," *Flow Measurement and Instrumentation*, 15, pp. 199-206.

Ketcham, R.A., and Carlson, W.D., 2001, "Acquisition, optimization and interpretation of X-ray computed tomographic imagery: applications to the geosciences," *Computers and Geosciences*, 27, pp. 381-400.

Krishna, R., Ellenberger, J., and Hennephof, D.E., 1993, "Analogous description of the hydrodynamics of gas-solid fluidized beds and bubble columns," *The Chemical Engineering Journal*, 53, pp. 89-101.

Kumar, S.B., and Duduković, M.P., "Computer assisted gamma and X-ray tomography: applications to multiphase flow systems," in *Non-invasive Monitoring of Multiphase Flows*, Chaouki, J., Larachi, F., and Dudukovic, M.P., Elsevier Science B.V., Amsterdam, Netherlands, pp. 47-103, (1997).

Lim, C.N, Gilbertson, M.A., and Harrison, A.J.L., 2007, "Bubble distribution and behaviour in bubbling fluidised beds," *Chemical Engineering Science*, 62, pp. 56-69.

McIlveen-Wright, D.R., Pinto, F., Armesto, L., Caballero, M.A., Aznar, M.P., Cabanillas, A., Huang, Y., Franco, C., Gulyurtlu, I., and McMullan, J.T., 2006, "A comparison of circulating fluidised bed combustion and gasification power plant technologies for processing mixtures of coal, biomass and plastic waste," *Fuel Processing Technology*, 87, pp. 793-801.

Mohan, D., Pittman, C.U.J., and Steele, P.H., 2006, "Pyrolysis of wood/biomass for bio-oil: a critical review," *Energy and Fuels*, 20, pp. 848-889.

Müller, C.R., Davidson, J.F., Dennis, J.S., Fennell, P.S., Gladden, L.F., Hayhurst, A.N., Mantle, M.D., Rees, A.C., and Sederman, A.J., 2007, "Rise velocities of bubbles and slugs in gas-fluidized beds: Ultra-fast magnetic resonance imaging," *Chemical Engineering Science*, 62, pp. 82-93.

Newton, D., Fiorentino, M., and Smith, G.B., 2001, "The application of X-ray imaging to the developments of fluidized bed processes," *Powder Technology*, 120, pp. 70-75.

Park, A.A., and Fan, L., 2007, "Electrostatic charging phenomenon in gas-liquid-solid flow systems," *Chemical Engineering Science*, 62, pp. 371-386.

Pederson, T., 2005, "NDE independent study of X-ray CT beam hardening correction," Independent Study Paper, Iowa State University, Ames, IA, pp. 1-22.

Peirano, E., Delloume, V., Johnsson, F., Leckner, B., and Simonin, O., 2002, "Numerical simulation of the fluid dynamics of a freely bubbling fluidized bed: influence of the air supply system," *Powder Technology*, 122, pp. 69-82.

Ramakrishna, K., Muralidhar, K., and Munshi, P., 2006, "Beam-hardening in simulated X-ray tomography," *NDT&E International*, 39, pp. 449-457.

Rao, T.R., and Bheemarasetti, J.V.R., 2001, "Minimum fluidization velocities of mixtures of biomass and sands," *Energy*, 26, pp. 633-644.

Rasul, M.G., 1998, "Fluidization characteristics of bagasse in a gas-fluidized bed," *Particle and Particle Systems Characterization*, 15, pp. 243-247.

Revel, J., Gatumel, C., Dodds, J.A., and Taillet, J., 2003, "Generation of static electricity during fluidization of polyethylene and its elimination by air ionization," *Powder Technology*, 135-136, pp. 192-200.

Riehle, C., 2000, "Measuring and calculating solid carry over in a CFB cold-flow model for different materials," *Powder Technology*, 107, pp. 207-211.

Sahoo, A., and Roy, G.K., 2005, "Mixing characteristic of homogeneous binary mixture of regular particles in a gas-solid fluidized bed," *Powder Technology*, 159, pp. 150-154.

Seeger, A., Affeld, K., Goubergrits, L., Kertzsch, U., and Wellenhofer, E., 2001, "X-ray-based assessment of the three-dimensional velocity of the liquid phase in a bubble column," *Experiments in Fluids*, 31, pp. 93-201.

Shen, L., Xiao, J., Niklasson, F., and Johnsson, F., 2007, "Biomass mixing in a fluidized bed biomass gasifier for hydrogen production," *Chemical Engineering Science*, 62, pp. 636-643.

Singh, R.K., and Roy, G.K., 2005, "Prediction of minimum bubbling velocity, fluidization index and range of particulate fluidization for gas-solid fluidization in cylindrical and non-cylindrical beds," *Powder Technology*, 159, pp. 168-172.

Stein, M., Martin, T.W., Seville, J.P.K., McNeil, P.A., and Parker, D.J., 1997, "Positron emission particle tracking: particle velocities in gas fluidised beds, mixers and other applications," in *Non-invasive Monitoring of Multiphase Flows*, Chaouki, J., Larachi, F., and Dudukovic, M.P., Elsevier Science B.V., Amsterdam, Netherlands, pp. 310-333.

Striegel, A., 2005, "Development of data acquisition software for X-ray radiography, computed tomography, and stereography for multiphase flows," MS Thesis, Iowa State University, Ames, IA.

Su, X., Hol, P.D., Talcott, S.M., Staudt, A.K., and Heindel, T.J., 2006, "The effect of bubble column diameter on gas holdup in fiber suspensions," *Chemical Engineering Science*, 61, pp. 3098-3104.

Tortora, P.R., Ceccio, S.L., O'Hern, T.J., Trujillo, S.M., and Torczynski, J.R., 2006, "Quantitative measurement of solids distribution in gas-solid riser flows using electrical impedance tomography and gamma densitometry tomography," *International Journal of Multiphase Flow*, 32, pp. 972-995.

Toye, D., Marchot, P., Crine, M., Pelsser, A.-M., and L'Homme, G., 1998, "Local measurements of void fraction and liquid holdup in packed columns using X-ray computed tomography," *Chemical Engineering and Processing*, 37, pp. 511-520.

Utikar, R.P., and Ranade, V.V., 2007, "Single jet fluidized beds: experiments and CFD simulations with glass and polypropylene particles," *Chemical Engineering Science*, 62, pp. 167-183.

Van Dijk, J.J., Hoffmann, A.C., Cheesman, D., and Yates, J.G., 1998, "The influence of horizontal internal baffles on the flow pattern in dense fluidized beds by X-ray investigation," *Powder Technology*, 98, pp. 273-278.

Van Ommen, J.R., Teuling, M., Nijenhuis, J., and van Wachem, B.G.M., 2006, "Computational validation of the scaling rules for fluidized beds," *Powder Technology*, 163, pp. 32-40.

Wang, H.G., Yang, W.Q., Senior, P., Raghavan, R.S., and Duncan, S.R., 2008, "Investigation of batch fluidized-bed drying by mathematical modeling, CFD simulation and ECT measurement," *American Institute of Chemical Engineers Journal*, 54(2), pp.427-444.

Wu, B., Yu, G., Bellehumeur, C., and Kantzas, A., 2007, "Dynamic flow behavior measurements in gas-solid fluidized beds using different non-intrusive techniques and polyethylene powder," *Flow Measurement and Instrumentation*, 18, pp. 197-203.

Wu, C.Z., Huang, H., Zheng, S.P., and Yin, X.L., 2002, "An economic analysis of biomass gasification and power generation in China," *Bioresource Technology*, 83, pp. 65-70.

Xie, N., Franka, N., Battaglia, F., Brown, R.C., 2007, "Simulations of elutriation phenomenon in fluidized beds," *Powder Technology*, In Review.

Yang, W., *Fluidization, Solids Handling, and Processing*, First edition, Industrial Applications of Three-Phase Fluidization Systems, Reese, J., Silva, E.M., Yang, S., and Fan, L., Chapter 9, Noyes Publications, Westwood, NJ, pp. 582-682 (1999).

Zhu, H., Zhu, J., Li, G., and Fengyun, L., 2007, "Detailed measurements of flow structure inside a dense gas-solids fluidized bed," *Powder Technology*, 180, pp. 339-349.

Appendix A: Experimental Setup

Appendix A presents a collection of photos, schematics, tables and plots relating to the experimental equipment and procedures to supplement the figures shown in Chapter 3.

Experimental Setup

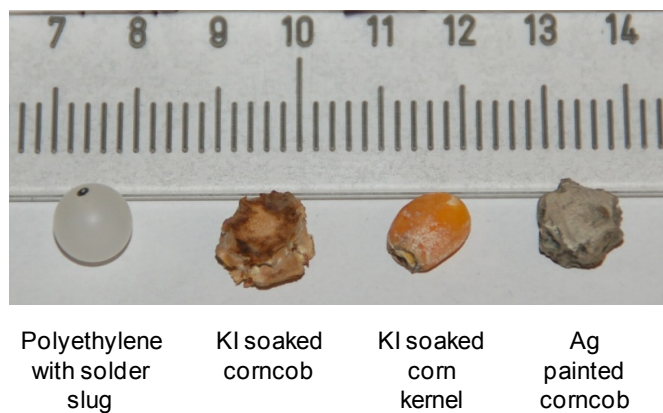


Figure A.1: Four tracer particles developed in this research (measurements in cm).

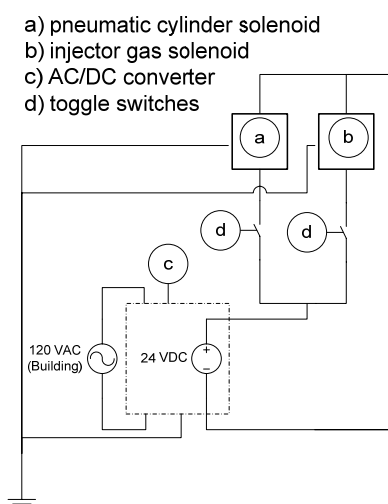


Figure A.2: Wiring schematic for solenoids.



Figure A.3: Sifting glass beads: (a) pouring glass in sieve, (b) cleaning sieve, and (c) shaking sieve with shaker.

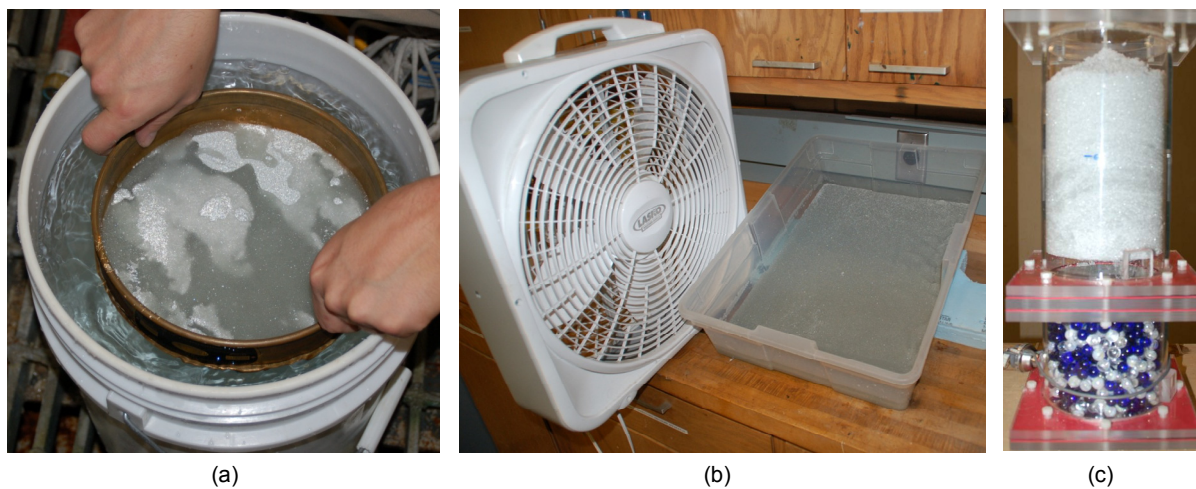


Figure A.4: Glass bead preparation: (a) washing, (b) initial fan drying, and (c) drying in fluidized bed.



Figure A.5: Weighing glass beads.

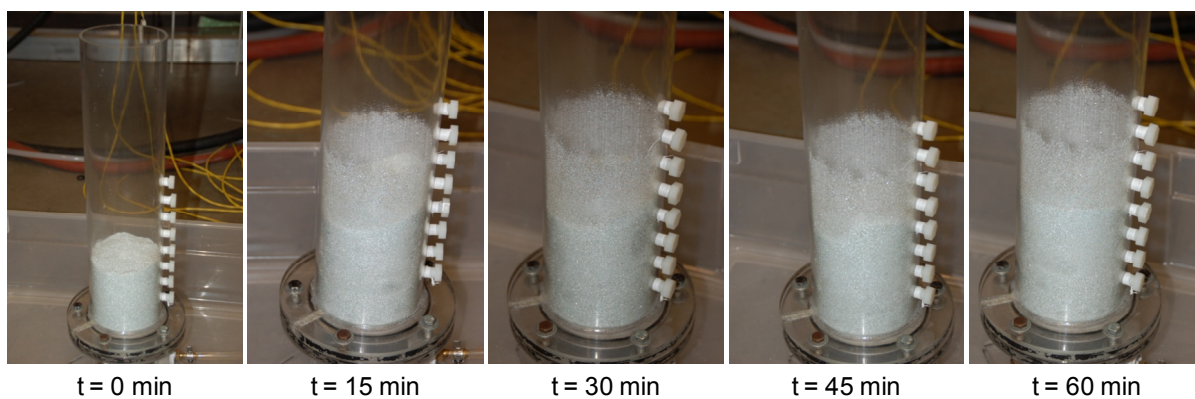


Figure A.6: Static electricity test for glass bead fluidization for one hour.

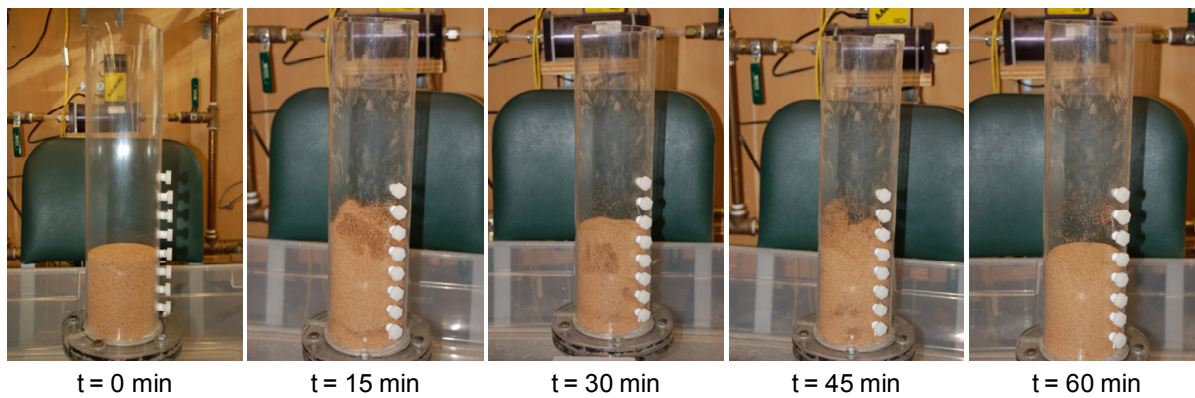


Figure A.7: Static electricity test for walnut shell fluidization for one hour.

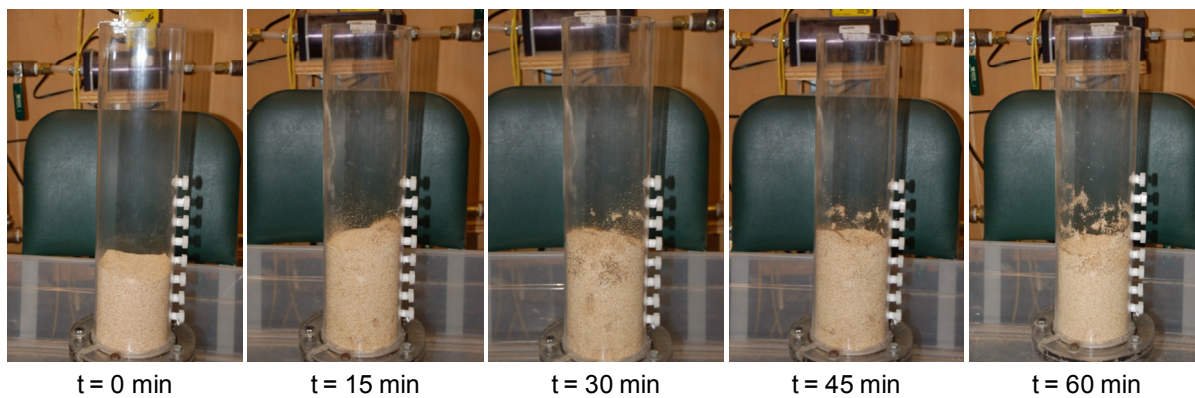


Figure A.8: Static electricity test for corn cob fluidization for one hour.

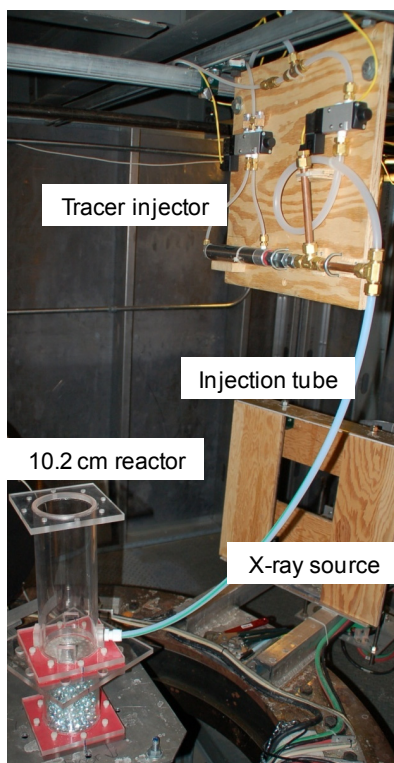


Figure A.9: Fluidized bed setup in X-ray vault.

Data Acquisition Setup and Calibration

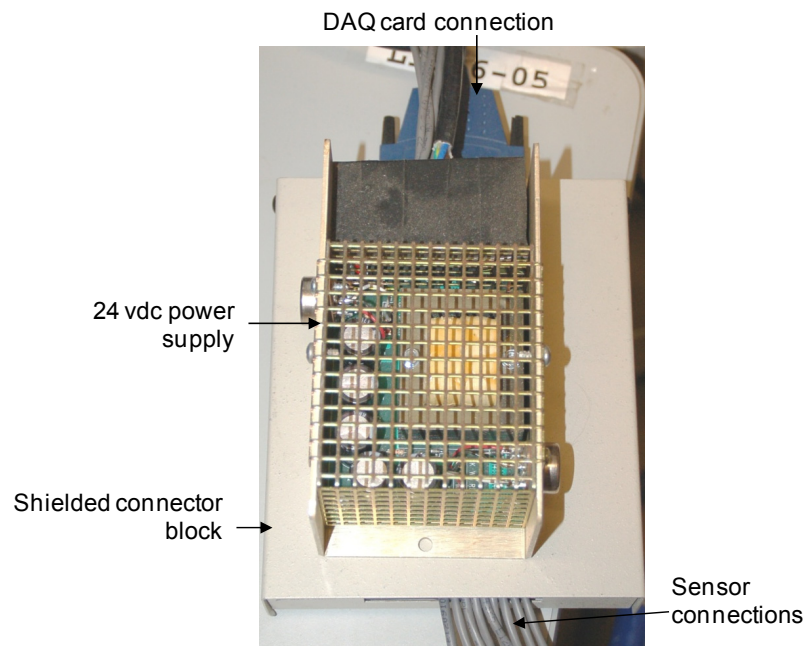


Figure A.10: DAQ equipment.

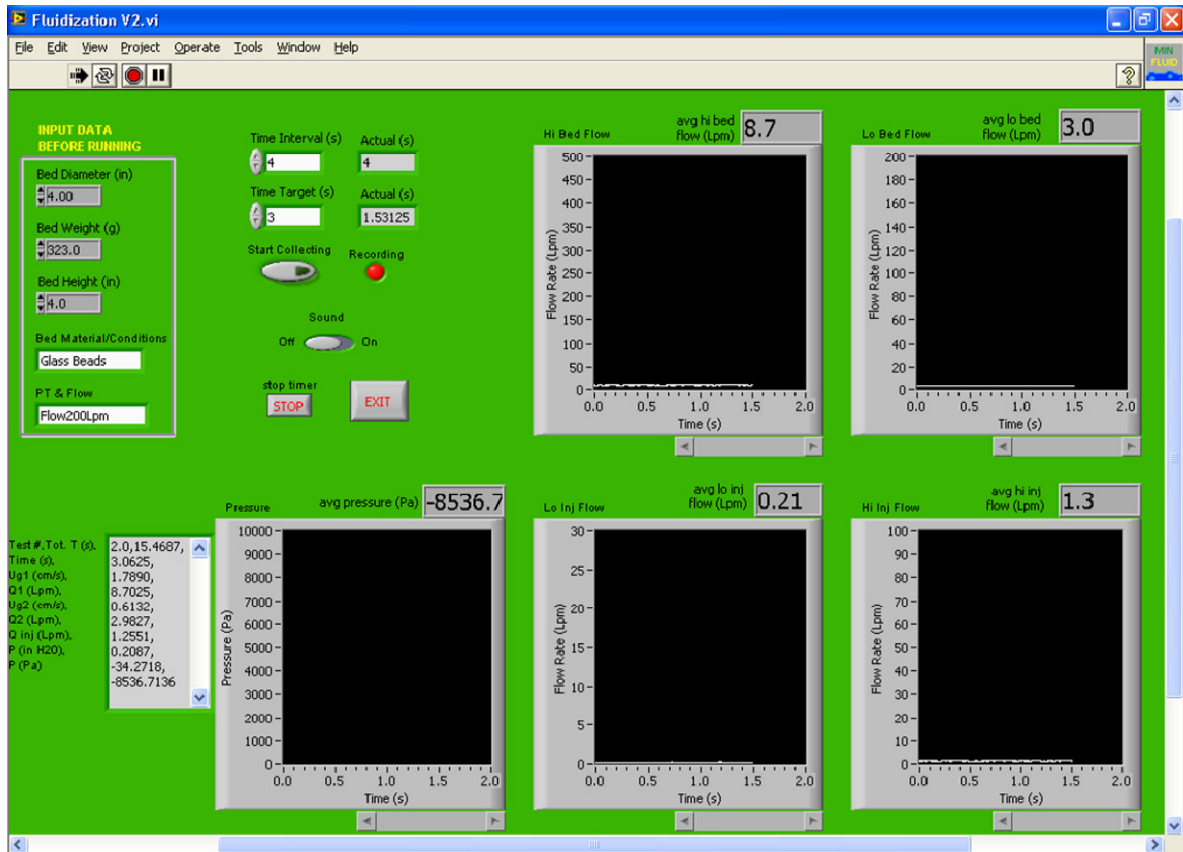


Figure A.11: LabView 8.0 DAQ GUI.



Figure A.12: Flow meter calibration drum.

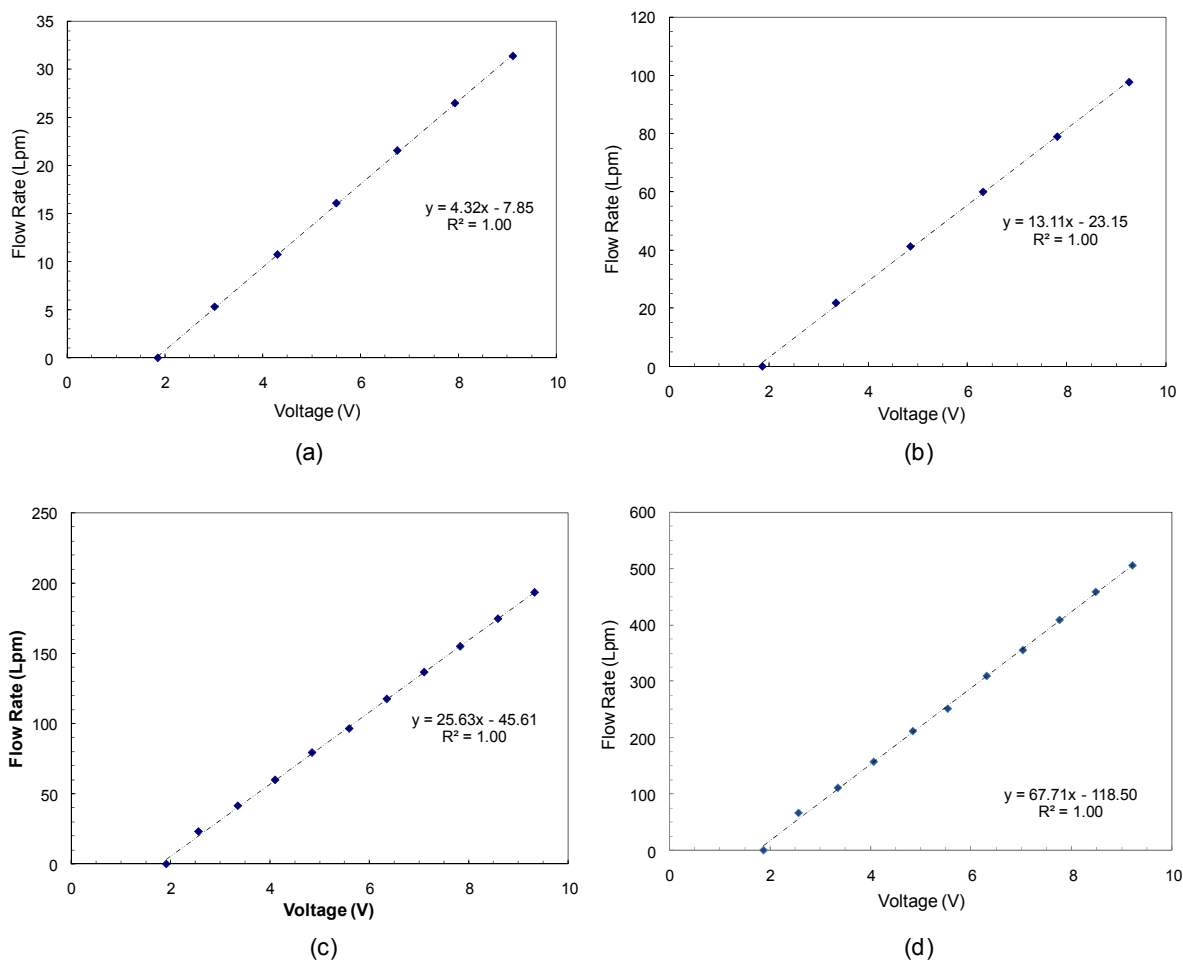


Figure A.13: Calibration curves for (a) 30 Lpm, (b) 100 Lpm, (c) 200 Lpm, and (d) 500 Lpm flow meters.



Figure A.14: Pressure transducer calibration.

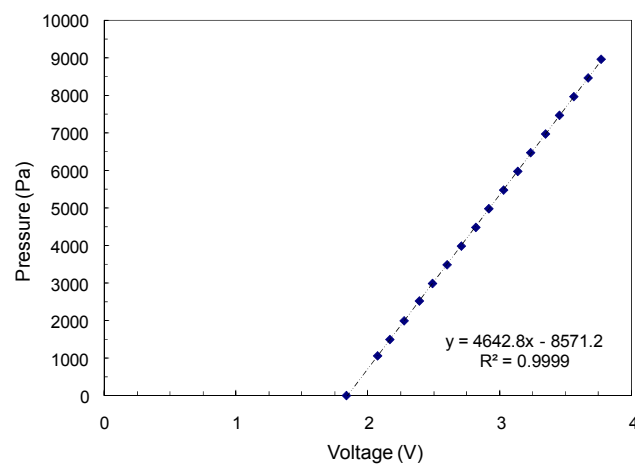


Figure A.15: Pressure transducer calibration curve.

Beam Hardening

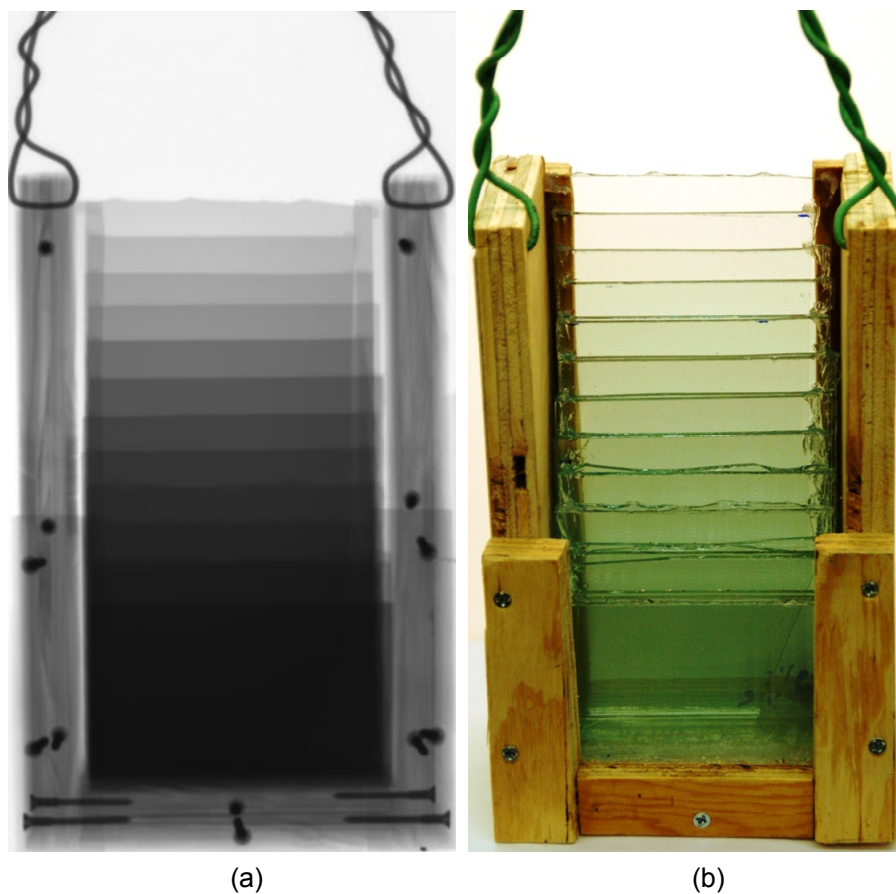


Figure A.16: Glass wedge for beam hardening calibrations: (a) radiographic image, and (b) digital photo.

Table A.1: Glass wedge specifications.

Section #	# plates/ section	Plate length (in)	Plate length (cm)	Total thickness (in)	Total thickness (cm)
1	1	8.0	20.32	0.12	0.30
2	1	7.5	19.05	0.24	0.60
3	1	7.0	17.78	0.35	0.90
4	1	6.5	16.51	0.47	1.20
5	2	6.0	15.24	0.71	1.80
6	2	5.5	13.97	0.94	2.40
7	2	5.0	12.70	1.18	3.00
8	2	4.5	11.43	1.42	3.60
9	2	4.0	10.16	1.65	4.20
10	2	3.5	8.89	1.89	4.80
11	4	3.0	7.62	2.36	5.99
12	4	2.5	6.35	2.83	7.19

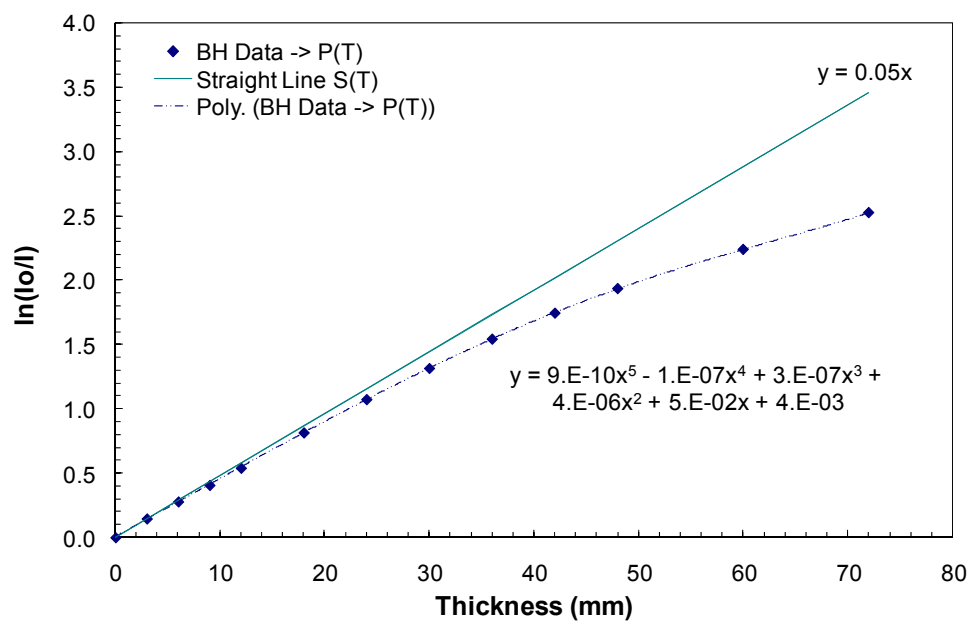


Figure A.17: Intensity vs glass wedge thickness for beam hardening calibration (P(T) and S(T)).

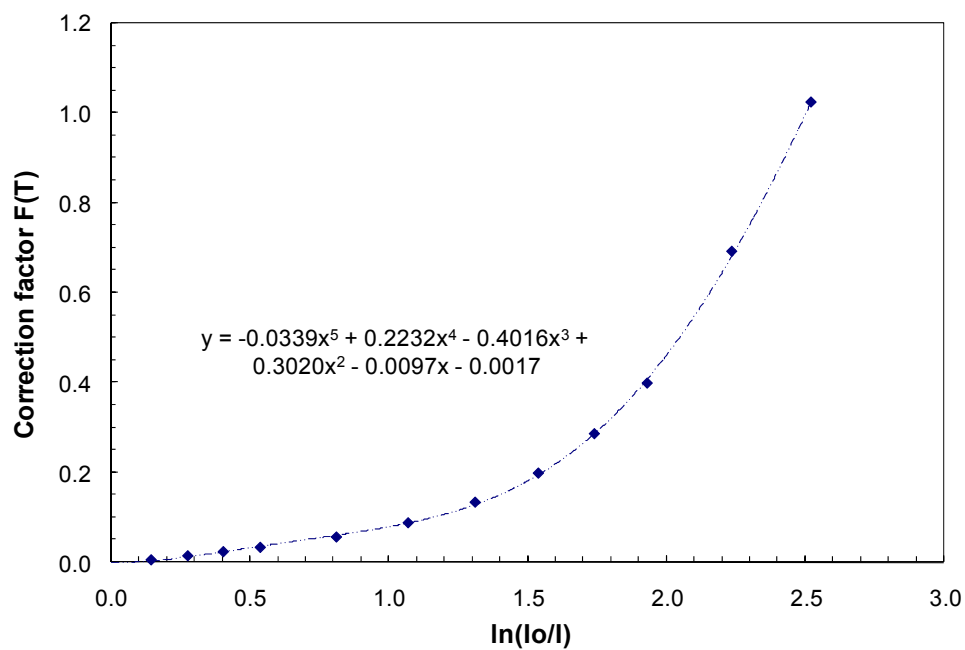


Figure A.18: Beam hardening correction factor vs intensity (F(T)).

Table A.2: Beam hardening calibration raw data.

Beam Hardening Correction for Glass (wedge) 150kV 3.5mA 4x4binning 1sec exposure 1CU 1Al Filter

	Plate Length (in)	Thickness (in)	Thickness (mm)	Intensity	<i>From data</i> ln(Io/I)	<i>From curve fit</i> ln(Io/I) P(T)	<i>Arbitrary line</i> S(T)	<i>F(T) = S(T) - P(T)</i> Correction Factor F(T)
T0	N/A	0	0	49964.9	0.00000	0.00400	0.00000	-0.00400
T1	8	0.118	2.9972	43177.3	0.14601	0.13891	0.14387	0.00496
T2	7.5	0.236	5.9944	37843.2	0.27787	0.27383	0.28773	0.01390
T3	7	0.354	8.9916	33299.3	0.40578	0.40856	0.43160	0.02303
T4	6.5	0.472	11.9888	29153.7	0.53874	0.54274	0.57546	0.03272
T5	6	0.708	17.9832	22160.9	0.81299	0.80752	0.86319	0.05568
T6	5.5	0.944	23.9776	17113.4	1.07146	1.06351	1.15092	0.08742
T7	5	1.18	29.972	13445.5	1.31268	1.30548	1.43866	0.13318
T8	4.5	1.416	35.9664	10710	1.54014	1.52845	1.72639	0.19794
T9	4	1.652	41.9608	8752.07	1.74203	1.72851	2.01412	0.28561
T10	3.5	1.888	47.9552	7235.8	1.93228	1.90366	2.30185	0.39819
T11	3	2.36	59.944	5337.12	2.23663	2.18588	2.87731	0.69143
T12	2.5	2.832	71.9328	4012.35	2.52194	2.42928	3.45277	1.02349

F(T)	$y = -0.0339x^5 + 0.2232x^4 - 0.4016x^3 + 0.3020x^2 - 0.0097x - 0.0017$ Final plot of correction factor
S(T)	$y = 0.048x$ Straight line slope of arbitrary line
P(T)	$y = 9E-10x^5 - 1E-07x^4 + 3E-07x^3 + 4E-06x^2 + 0.045x + 0.004$ Polynomial (5th degree) of ln(I/Io) vs Thickness

Appendix B: Minimum Fluidization Velocity Results

Appendix B provides a selection of data and plots acquired in minimum fluidization experiments to supplement the minimum fluidization velocity findings in Chapter 4.

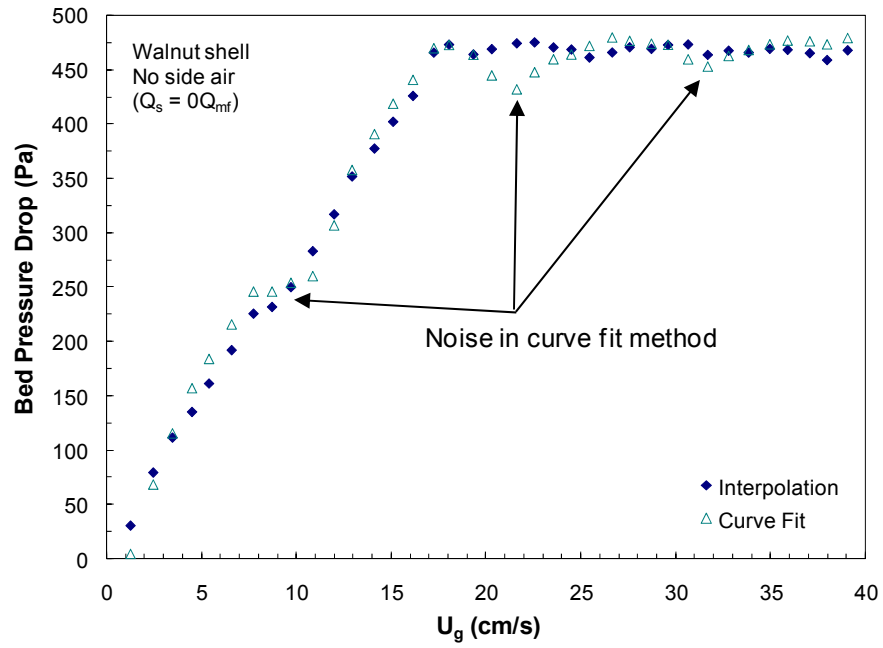


Figure B.1: U_{mf} curves for walnut shell and $Q_s = 0Q_{mf,0}$ with two methods: linear interpolation of empty bed data and curve-fit of empty bed data.

Table B.1: Example minimum fluidization test data for glass beads with $Q_s = 0Q_{mf,0}$.

Q _s		0Q _{mf,0}	Bed Material		Glass beads (500-600µm)				
Bed ID (in)		4	PT # and Flow #		PT (5 psig) - Flow (200 Lpm)				
Bed Height (in)		4	Test #3	8/16/2007					
Bed Weight (g)		1220	Empty #3	8/16/2007					
Bulk Density (kg/m ³)		1481.1							
Theoretical Force (Pa)		1476.2							
Experimental data - full bed						Empty Bed - raw		Empty bed - interpolate	Bed only
Time Interval	U _g	Q _g	Q _s	Pressure	Pressure	U _g	P	P	P
(s)	(cm/s)	(Lpm)	(Lpm)	(in H2O)	(Pa)	(cm/s)	(Pa)	(Pa)	(Pa)
5	39.7	193.3	0.2	30.4	7579	39.8	6428	6397	1182
5	38.8	188.5	0.2	29.4	7312	38.0	5929	6126	1186
5	37.8	184.1	0.2	28.4	7063	36.2	5396	5874	1189
5	36.8	179.2	0.2	27.2	6785	34.1	4849	5571	1213
5.047	35.8	174.2	0.2	26.2	6516	32.0	4323	5285	1230
5.016	34.9	169.9	0.2	25.3	6290	30.1	3857	5056	1234
5	33.9	164.9	0.2	24.2	6028	27.9	3388	4795	1233
5	32.9	160.3	0.2	23.2	5788	26.2	3051	4558	1230
5	31.8	154.8	0.2	22.1	5514	24.1	2641	4276	1238
5.032	31.0	151.0	0.2	21.4	5324	22.0	2252	4080	1243
5	30.0	145.9	0.2	20.4	5084	20.5	1977	3827	1257
5.032	29.0	140.9	0.2	19.5	4856	18.3	1677	3607	1249
5.047	28.0	136.1	0.2	18.7	4667	16.3	1425	3395	1272
5.062	27.1	131.7	0.2	18.0	4489	14.4	1200	3221	1268
5.032	26.0	126.7	0.2	17.2	4286	12.3	969	3020	1266
5	25.1	122.1	0.2	16.4	4094	10.4	763	2834	1259
5	24.1	117.2	0.2	15.7	3909	8.3	631	2638	1271
5	23.1	112.6	0.2	14.9	3718	6.4	520	2462	1256
5	22.2	108.0	0.2	14.2	3544	4.3	404	2284	1260
5	21.2	103.2	0.2	13.5	3356	2.4	311	2110	1247
5	20.5	99.5	0.2	12.8	3180	0.7	242	1975	1205
5	19.2	93.3	0.2	11.8	2934			1798	1136
5	18.2	88.4	0.2	11.1	2753			1660	1093
5.015	17.2	83.6	0.2	10.4	2583			1540	1043
5	16.3	79.4	0.2	9.7	2428			1432	996
5.094	15.3	74.5	0.2	9.0	2252			1312	940
5.016	14.2	69.1	0.2	8.3	2074			1182	892
5	13.3	64.7	0.2	7.7	1922			1082	840
5	12.2	59.1	0.2	6.9	1715			953	762
5.078	11.3	54.8	0.2	6.3	1558			857	701
5.031	10.4	50.5	0.2	5.6	1398			761	638
5	9.3	45.1	0.2	5.1	1276			692	585
5.016	8.2	39.9	0.2	4.7	1160			625	535
5.156	7.2	35.2	0.2	4.2	1048			569	479
5	6.4	31.1	0.2	3.8	959			521	437
5.031	5.3	25.9	0.2	3.4	841			461	380
5	4.2	20.6	0.2	2.8	709			399	310
5	3.4	16.4	0.2	2.4	608			357	251
5.032	2.4	11.8	0.2	2.0	494			311	183
5	1.4	6.8	0.2	1.4	348			270	78
5	0.7	3.6	0.2	1.0	243			243	0

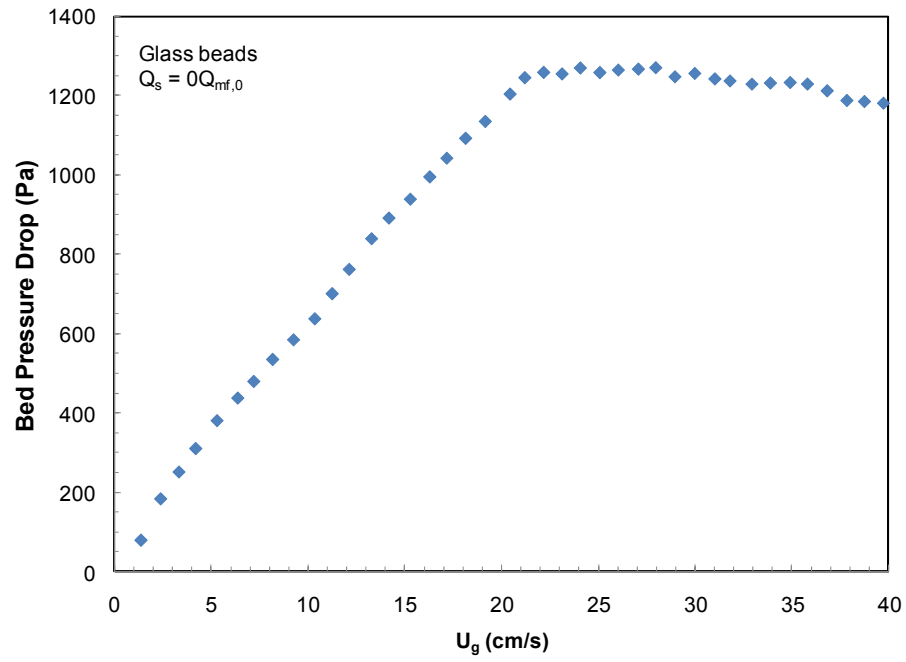


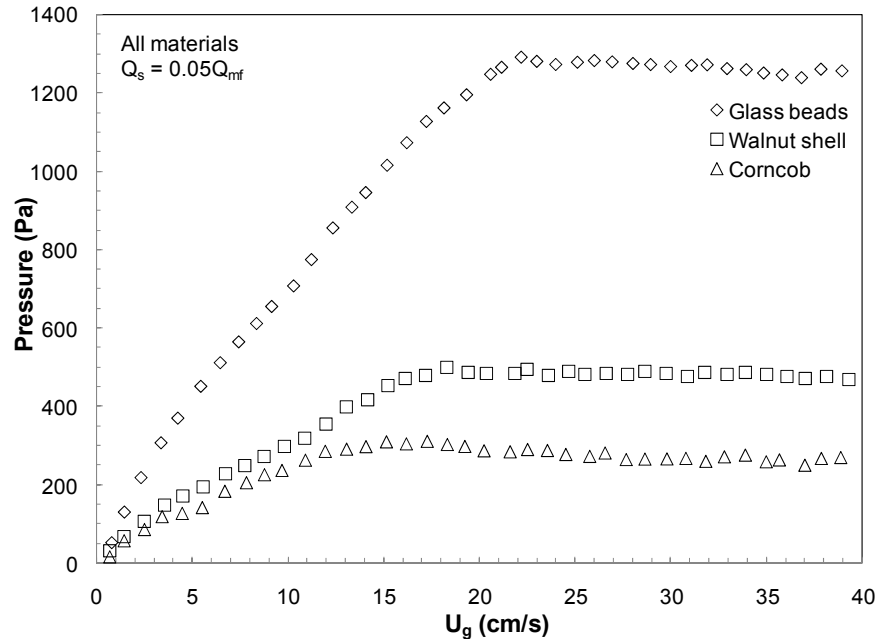
Figure B.2: Example minimum fluidization curve for glass beads with $Q_s = 0Q_{mf,0}$ (corresponding to Table B.1)

Table B.2: All $U_{mf,0}$ results for all materials with no side air.

	Glass beads	Walnut shell	Corncob
$U_{mf,0}$, Test 1	22.2	18.3	17.1
$U_{mf,0}$, Test 2	21.3	18.2	17.2
$U_{mf,0}$, Test 3	21.3	18.3	18.3
$U_{mf,0}$, Test 4	21.2	18.3	17.3
$U_{mf,0}$, Test 5	21.2	18.3	17.2
$U_{mf,0}$, Test 6	22.1	18.1	17.3
$U_{mf,0}$, Test 7	22.2	19.3	16.1
$U_{mf,0}$, Test 8		18.2	17.5
$U_{mf,0}$, Test 9		18.3	16.2
$U_{mf,0}$, Test 10		18.3	16.7
$U_{mf,0}$, Average	21.7	18.4	17.1
$U_{mf,0}$, Deviation	0.5	0.3	0.6

Table B.3: Experimental flow conditions for U_{mf} , CT, stereography, and particle tracking.

	Glass beads		Walnut shell		Corncob	
	Velocity (cm/s)	Flow rate (Lpm)	Velocity (cm/s)	Flow rate (Lpm)	Velocity (cm/s)	Flow rate (Lpm)
$U_{mf,0}$, $Q_{mf,0}$	21.7	105	18.4	89	17.1	83
$U_g = 1.25U_{mf,0}$	27.1	132	22.9	112	21.4	104
$U_g = 1.50U_{mf,0}$	32.5	158	27.5	134	25.7	125
$U_g = 1.75U_{mf,0}$	37.9	184	32.1	156	29.9	146
$U_g = 2.00U_{mf,0}$	43.3	211	36.7	179	34.2	166
$U_g = 3.00U_{mf,0}$	65.0	316	55.1	268	51.3	250
$Q_s = 0.05Q_{mf,0}$	90.5	5.3	76.7	4.5	71.5	4.2
$Q_s = 0.10Q_{mf,0}$	181.0	10.5	153.4	8.9	143.0	8.3
$Q_s = 0.15Q_{mf,0}$	271.5	15.8	230.1	13.4	214.5	12.5
$Q_s = 0.20Q_{mf,0}$	362.0	21.1	306.9	17.9	286.0	16.6

**Figure B.3: Sample U_{mf} curves for all materials with $Q_s = 0.05Q_{mf,0}$.**

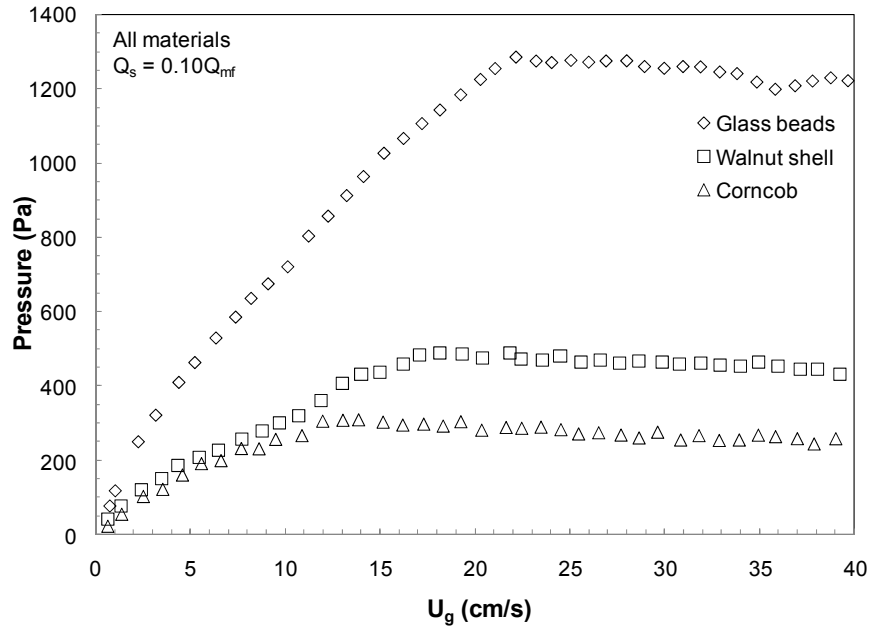


Figure B.4: Sample U_{mf} curves for all materials with $Q_s = 0.10Q_{mf,0}$.

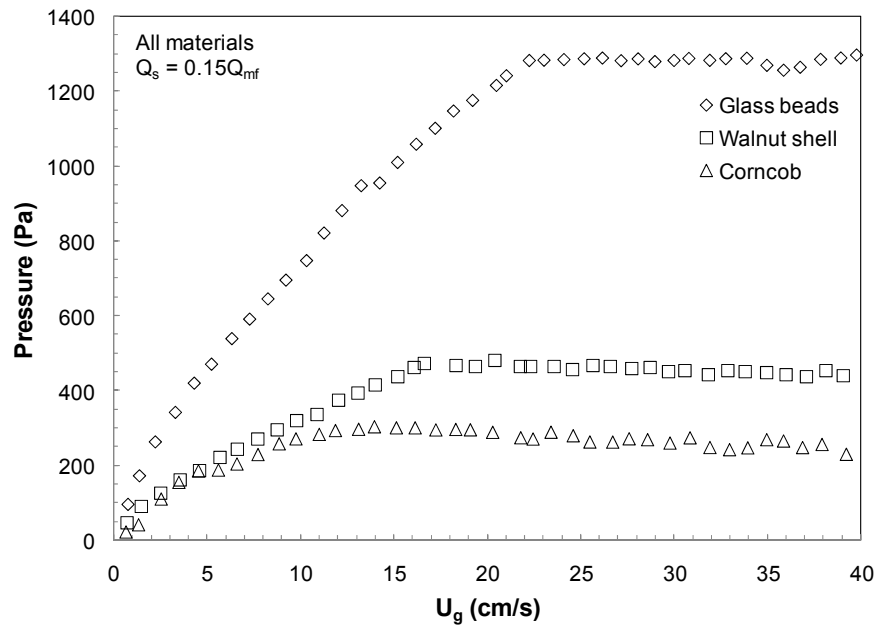


Figure B.5: Sample U_{mf} curves for all materials with $Q_s = 0.15Q_{mf,0}$.

Table B.4: Sample U_{mf} data for all materials with $Q_s = 0Q_{mf,0}$.

$Q_s = 0Q_{mf,0}$					
Glass beads		Walnut shell		Corncob	
8/15/2007	Test 3	10/19/2007	Test 6	10/10/2007	Test6
U_{mf} (cm/s)	21.30	U_{mf} (cm/s)	18.07	U_{mf} (cm/s)	17.27
Q_s avg (lpm)	0	Q_s avg (lpm)	0	Q_s avg (lpm)	0
Q_s stdev (lpm)	0	Q_s stdev (lpm)	0	Q_s stdev (lpm)	0
U_g (cm/s)	P (Pa)	U_g (cm/s)	P (Pa)	U_g (cm/s)	P (Pa)
39.8	1227	42.1	453	42.0	209
39.0	1230	41.1	480	41.2	205
37.8	1227	39.9	473	40.1	218
37.0	1217	39.1	468	39.0	223
36.0	1213	38.0	459	38.1	222
34.9	1221	37.1	465	37.1	235
34.0	1253	35.9	468	36.0	226
33.1	1248	35.0	469	35.0	233
32.0	1260	33.9	466	34.0	239
31.1	1257	32.8	467	32.9	245
30.1	1260	31.7	464	31.9	251
28.9	1260	30.7	473	30.7	257
28.1	1266	29.6	473	29.7	265
27.1	1266	28.7	469	28.7	258
26.0	1268	27.6	471	27.6	266
25.2	1265	26.7	466	26.6	269
24.1	1268	25.5	461	25.5	276
23.2	1264	24.5	468	24.4	280
22.1	1260	23.6	470	23.5	285
21.3	1259	22.6	475	22.5	267
20.4	1208	21.6	474	21.7	288
19.2	1148	20.3	469	20.5	283
18.2	1108	19.4	464	19.2	292
17.2	1056	18.1	473	18.3	305
16.3	1005	17.3	466	17.3	306
15.3	955	16.2	426	16.1	282
14.2	906	15.1	402	15.1	279
13.3	846	14.1	377	14.1	263
12.3	776	13.0	352	13.0	248
11.4	708	12.0	317	12.0	238
10.3	633	10.9	283	10.8	202
9.3	580	9.7	250	9.6	187
8.3	529	8.7	231	8.7	170
7.1	474	7.8	225	7.8	164
6.3	427	6.6	192	6.7	140
5.3	373	5.4	161	5.7	122
4.4	314	4.5	135	4.6	116
3.3	234	3.5	111	3.5	77
2.4	171	2.5	79	2.5	64
1.3	60	1.3	30	1.3	35
0.8	-12	0.7	-9	0.7	-5

Table B.5: Sample U_{mf} data for all materials with $Q_s = 0.05Q_{mf,0}$.

$Q_s = 0.05Q_{mf,0}$					
Glass beads		Walnut shell		Corncob	
8/21/2007	Test 1	10/19/2007	Test 1	10/12/2007	Test 1
U_{mf} (cm/s)	22.16	U_{mf} (cm/s)	18.30	U_{mf} (cm/s)	15.14
Q_s avg (lpm)	5.40	Q_s avg (lpm)	4.50	Q_s avg (lpm)	4.09
Q_s stdev (lpm)	0.03	Q_s stdev (lpm)	0.06	Q_s stdev (lpm)	0.02
U_g (cm/s)	P (Pa)	U_g (cm/s)	P (Pa)	U_g (cm/s)	P (Pa)
39.7	1252	41.9	493	42.3	254
38.9	1256	41.3	475	41.1	256
37.8	1261	40.2	472	40.4	249
36.8	1239	39.3	467	38.9	269
35.8	1246	38.1	476	37.9	267
34.8	1251	37.0	470	37.0	249
33.9	1259	36.0	476	35.7	263
32.9	1262	35.0	481	35.0	258
31.9	1272	33.9	484	33.9	275
31.1	1270	32.9	480	32.8	271
30.0	1267	31.8	486	31.8	259
28.9	1272	30.9	476	30.8	267
28.0	1275	29.7	482	29.8	265
26.9	1279	28.6	488	28.7	265
26.0	1283	27.7	480	27.7	264
25.1	1278	26.6	483	26.6	281
24.0	1273	25.5	480	25.8	272
23.0	1281	24.6	487	24.5	277
22.2	1291	23.6	478	23.6	287
21.1	1266	22.5	492	22.5	289
20.6	1247	21.8	484	21.6	284
19.3	1195	20.4	482	20.2	286
18.1	1162	19.4	486	19.2	297
17.2	1127	18.3	499	18.3	302
16.2	1073	17.2	479	17.3	310
15.2	1015	16.1	471	16.2	304
14.0	945	15.2	452	15.1	309
13.3	908	14.2	416	14.1	297
12.3	855	13.0	399	13.1	290
11.2	774	12.0	355	11.9	285
10.3	707	10.9	317	10.9	262
9.1	654	9.8	297	9.7	236
8.3	611	8.7	272	8.8	225
7.4	564	7.7	248	7.8	205
6.4	511	6.7	227	6.7	183
5.4	450	5.6	194	5.5	141
4.2	369	4.5	170	4.5	126
3.4	306	3.5	146	3.4	118
2.3	217	2.5	106	2.5	85
1.4	129	1.4	67	1.4	56
0.8	51	0.7	31	0.7	15

Table B.6: Sample U_{mf} data for all materials with $Q_s = 0.10Q_{mf,0}$.

$Q_s = 0.10Q_{mf,0}$					
Glass beads		Walnut shell		Corncob	
8/21/2007	Test 1	10/19/2007	Test 1	10/12/2007	Test 1
U_{mf} (cm/s)	22.18	U_{mf} (cm/s)	17.09	U_{mf} (cm/s)	12.00
Q_s avg (lpm)	10.71	Q_s avg (lpm)	9.00	Q_s avg (lpm)	8.35
Q_s stdev (lpm)	0.07	Q_s stdev (lpm)	0.05	Q_s stdev (lpm)	0.01
U_g (cm/s)	P (Pa)	U_g (cm/s)	P (Pa)	U_g (cm/s)	P (Pa)
39.7	1221	41.9	446	42.1	241
38.8	1229	41.1	439	41.0	235
37.8	1220	40.2	437	40.3	244
36.9	1207	39.2	431	39.0	258
35.8	1198	38.1	446	37.9	244
34.9	1217	37.1	445	37.0	258
33.8	1240	36.0	455	35.9	264
32.9	1244	35.0	464	35.0	268
31.9	1258	34.0	454	34.0	255
31.0	1259	32.9	456	32.9	254
30.0	1254	31.9	463	31.8	267
29.0	1259	30.8	459	30.9	255
28.0	1274	29.8	464	29.7	276
26.9	1274	28.7	468	28.7	260
26.0	1271	27.6	460	27.7	268
25.1	1275	26.6	471	26.6	274
24.1	1270	25.6	463	25.5	271
23.2	1274	24.5	481	24.6	283
22.2	1284	23.6	469	23.5	289
21.1	1254	22.4	473	22.5	286
20.3	1224	21.9	489	21.7	289
19.3	1183	20.4	474	20.4	281
18.2	1142	19.3	486	19.3	304
17.2	1105	18.2	488	18.4	292
16.3	1065	17.1	483	17.3	298
15.2	1026	16.2	459	16.2	295
14.2	963	15.0	438	15.2	303
13.3	912	14.0	430	13.9	309
12.3	856	13.0	407	13.1	308
11.3	803	11.9	360	12.0	306
10.2	720	10.7	319	10.9	267
9.1	674	9.7	301	9.5	256
8.2	635	8.8	279	8.6	231
7.4	585	7.7	257	7.7	232
6.4	529	6.5	226	6.6	199
5.3	463	5.5	209	5.6	191
4.4	409	4.4	185	4.6	160
3.2	321	3.5	149	3.6	122
2.3	250	2.4	120	2.5	102
1.1	118	1.4	77	1.4	54
0.8	77	0.7	41	0.7	22

Table B.7: Sample U_{mf} data for all materials with $Q_s = 0.15Q_{mf,0}$.

$Q_s = 0.15Q_{mf,0}$					
Glass beads		Walnut shell		Corncob	
8/21/2007	Test 1	10/19/2007	Test 1	10/12/2007	Test 1
U_{mf} (cm/s)	22.27	U_{mf} (cm/s)	16.63	U_{mf} (cm/s)	11.89
Q_s avg (lpm)	15.68	Q_s avg (lpm)	13.51	Q_s avg (lpm)	12.63
Q_s stdev (lpm)	0.09	Q_s stdev (lpm)	0.03	Q_s stdev (lpm)	0.02
U_g (cm/s)	P (Pa)	U_g (cm/s)	P (Pa)	U_g (cm/s)	P (Pa)
39.8	1298	42.0	417	42.2	238
38.9	1290	41.0	425	41.2	239
37.9	1287	40.2	439	40.4	227
36.8	1265	39.1	438	39.2	231
35.9	1257	38.1	452	37.9	257
35.0	1271	37.1	435	36.9	249
33.9	1289	36.0	442	35.9	266
32.8	1288	35.0	447	35.0	270
31.9	1284	33.8	449	34.0	248
30.8	1289	32.9	453	33.0	243
30.0	1284	31.9	442	31.9	249
29.0	1281	30.6	453	30.9	274
28.1	1288	29.7	450	29.8	261
27.2	1283	28.8	460	28.6	270
26.2	1290	27.8	459	27.6	272
25.2	1288	26.6	463	26.7	263
24.1	1286	25.7	465	25.5	263
23.1	1284	24.6	454	24.6	280
22.3	1283	23.6	462	23.4	290
21.0	1243	22.3	463	22.5	271
20.5	1217	21.8	464	21.8	275
19.2	1177	20.4	480	20.3	289
18.2	1148	19.4	464	19.1	296
17.2	1102	18.3	466	18.3	297
16.2	1059	16.6	470	17.3	296
15.2	1011	16.1	459	16.2	301
14.3	956	15.2	436	15.1	301
13.3	948	14.0	414	14.0	304
12.2	882	13.1	391	13.1	297
11.3	822	12.0	373	11.9	294
10.3	748	10.9	334	11.0	284
9.2	696	9.8	319	9.8	272
8.3	646	8.8	294	8.9	258
7.3	591	7.7	269	7.7	230
6.3	539	6.6	243	6.6	205
5.3	471	5.7	221	5.6	188
4.3	420	4.6	185	4.6	186
3.3	342	3.5	160	3.5	155
2.2	263	2.5	126	2.6	111
1.4	172	1.5	90	1.4	42
0.8	96	0.7	47	0.7	23

Table B.8: Sample U_{mf} data for all materials with $Q_s = 0.20Q_{mf,0}$.

$Q_s = 0.20Q_{mf,0}$					
Glass beads		Walnut shell		Corncob	
8/21/2007	Test 1	10/19/2007	Test 1	10/16/2007	Test 1
U_{mf} (cm/s)	21.12	U_{mf} (cm/s)	16.22	U_{mf} (cm/s)	12.00
Q_s avg (lpm)	20.70	Q_s avg (lpm)	18.10	Q_s avg (lpm)	16.70
Q_s stdev (lpm)	0.11	Q_s stdev (lpm)	0.02	Q_s stdev (lpm)	0.04
U_g (cm/s)	P (Pa)	U_g (cm/s)	P (Pa)	U_g (cm/s)	P (Pa)
39.9	1332	42.0	391	42.0	289
39.0	1328	41.1	405	41.2	284
37.9	1327	40.2	397	40.2	289
36.9	1305	39.1	404	38.4	316
36.0	1302	38.2	400	37.0	305
34.9	1306	37.1	405	36.1	300
33.9	1320	36.1	414	34.8	301
32.9	1308	35.0	418	33.8	294
31.9	1305	33.9	433	32.9	298
30.9	1301	32.8	429	31.8	304
30.0	1303	31.9	440	30.6	298
29.0	1299	30.7	446	29.8	291
28.0	1304	29.7	429	28.8	298
27.0	1302	28.7	437	27.8	302
26.0	1298	27.7	445	26.6	306
25.0	1293	26.7	445	25.5	313
24.0	1287	25.6	438	24.6	308
23.0	1278	24.6	443	23.5	317
22.1	1283	23.6	444	22.4	307
21.1	1267	22.5	437	21.8	318
20.5	1231	21.6	449	20.4	300
19.3	1181	20.4	446	19.4	315
18.1	1153	19.4	445	18.3	319
17.2	1111	18.3	452	17.1	324
16.3	1068	17.2	461	16.2	323
15.1	1004	16.2	454	15.1	319
14.3	967	15.2	436	14.1	330
13.4	955	14.1	423	12.8	323
12.2	927	13.1	386	12.0	327
11.1	834	12.0	366	10.8	302
10.2	778	10.9	330	9.9	288
9.1	717	9.8	343	8.6	252
8.1	662	8.3	299	7.7	245
7.2	622	7.7	277	6.4	207
6.3	565	6.6	253	5.7	199
5.5	513	5.6	217	4.7	167
4.3	442	4.5	187	3.5	143
3.4	375	3.5	145	2.5	111
2.2	273	2.5	128	1.4	61
1.3	194	1.4	100	0.7	21
0.8	116	0.7	49	0.7	15

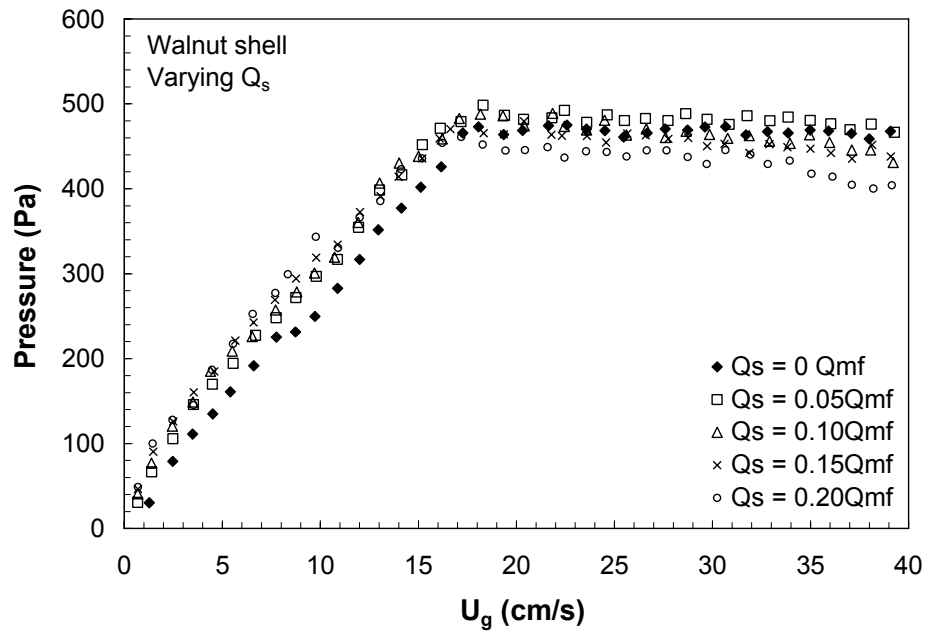


Figure B.6: U_{mf} for walnut shell at all five Q_s conditions.

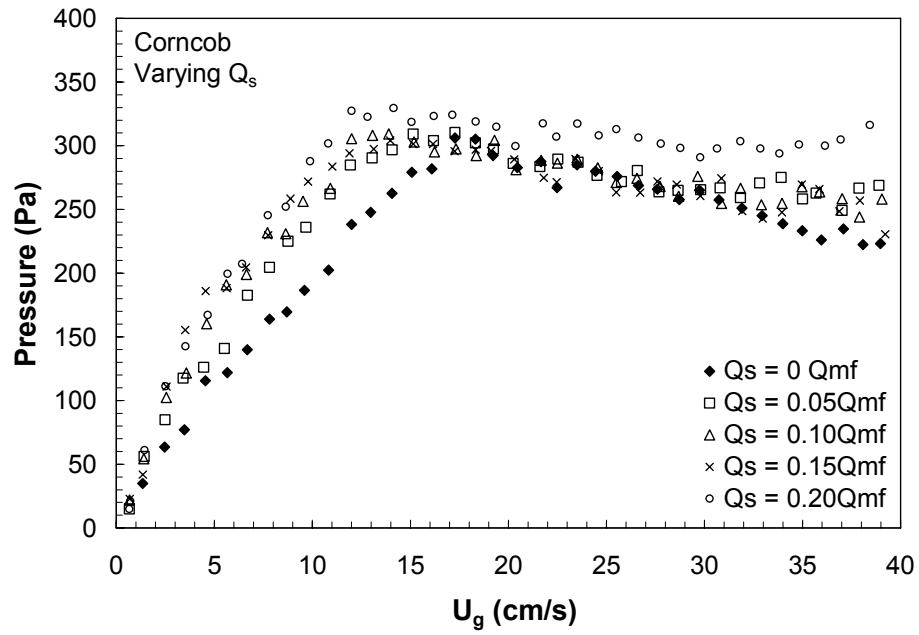


Figure B.7: U_{mf} for corncob at all five Q_s conditions.

Appendix C: CT and Gas Holdup Results

Appendix C provides x-, y-, and z- slice gas holdup images not presented in Chapter 4. Some selected gas holdup plots are also presented to support the trends described in Chapter 4.

Gas Holdup Validation

The bulk void fraction (gas holdup) for all three beds is determined experimentally. By knowing the bulk density (ρ_b) and the particle density (ρ_p), $\varepsilon_{g,b}$ is calculated from the following equations.

$$\varepsilon_{g,b}(\text{glass}) = 1 - \frac{\rho_b}{\rho_p} = 1 - \frac{1481 \text{ kg/m}^3}{2600 \text{ kg/m}^3} = 0.43 \quad (\text{C.1})$$

$$\varepsilon_{g,b}(\text{walnut}) = 1 - \frac{\rho_b}{\rho_{p,avg}} = 1 - \frac{592 \text{ kg/m}^3}{1300 \text{ kg/m}^3} = 0.55 \quad (\text{C.2})$$

$$\varepsilon_{g,b}(\text{corncob}) = 1 - \frac{\rho_b}{\rho_{p,avg}} = 1 - \frac{392 \text{ kg/m}^3}{1000 \text{ kg/m}^3} = 0.61 \quad (\text{C.3})$$

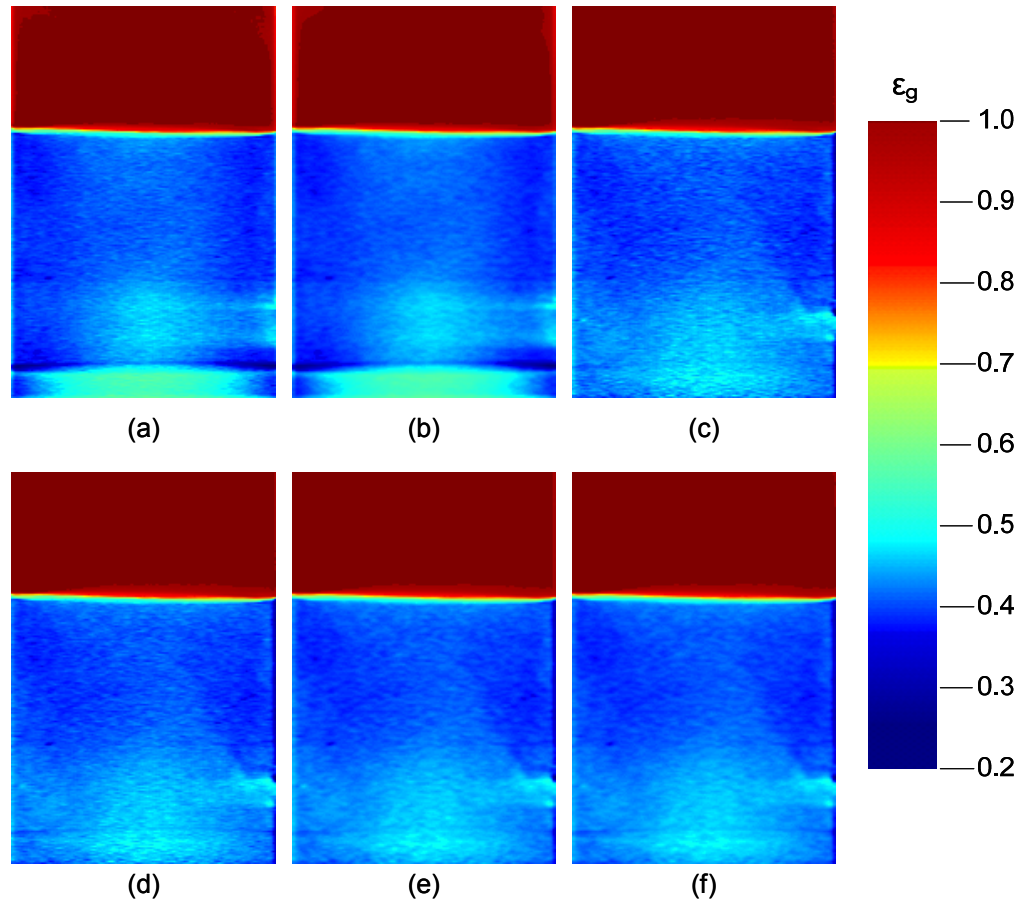


Figure C.1: Gas holdup y-slice images in bulk glass beads ($Q_s = U_g = 0$) for six calculation methods: a) average, b) average (smoothed after), c) local, d) local (smooth before), e) local (smooth after), and f) local (smooth before and after).

Table C.1: Local y-slice gas holdup average and standard deviation at $z = 7.0$ cm for bulk glass beads using various calculation methods.

Calculation method	Average	Average (smoothed after)	Local	Local (smoothed before)	Local (smoothed after)	Local (smoothed both)
Average ε_b	0.378	0.377	0.373	0.372	0.372	0.371
Standard deviation ε_b	0.015	0.013	0.016	0.016	0.013	0.014

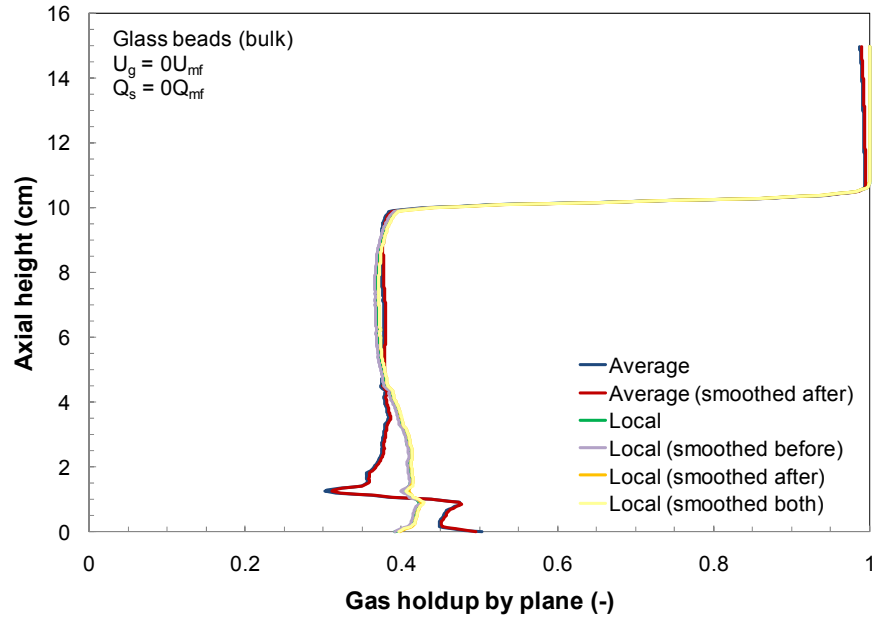


Figure C.2: Average gas holdup by height for bulk glass beads using various calculation methods.

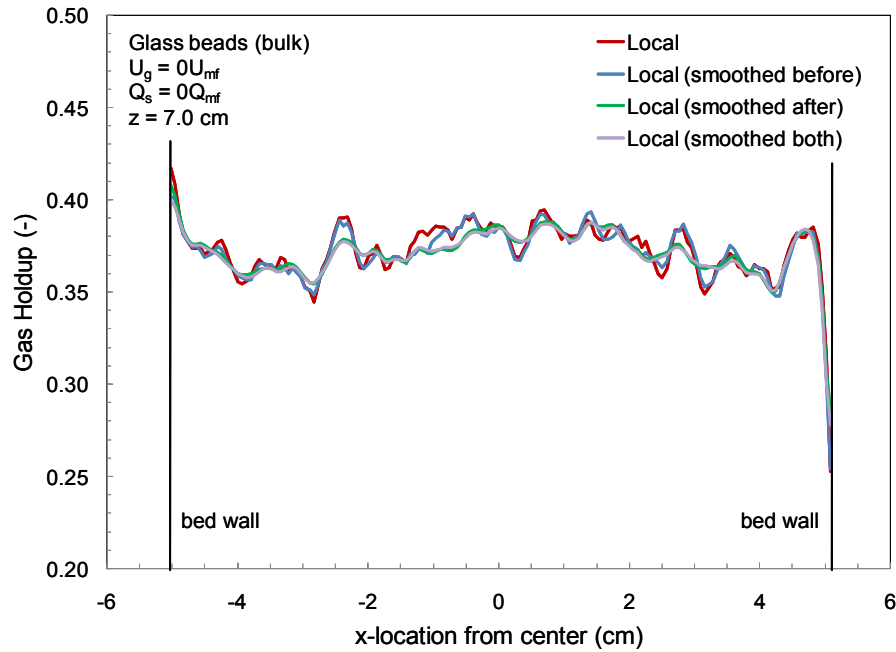


Figure C.3: Local y-slice gas holdup for bulk glass beads at $z = 7.0 \text{ cm}$ using various calculation methods.

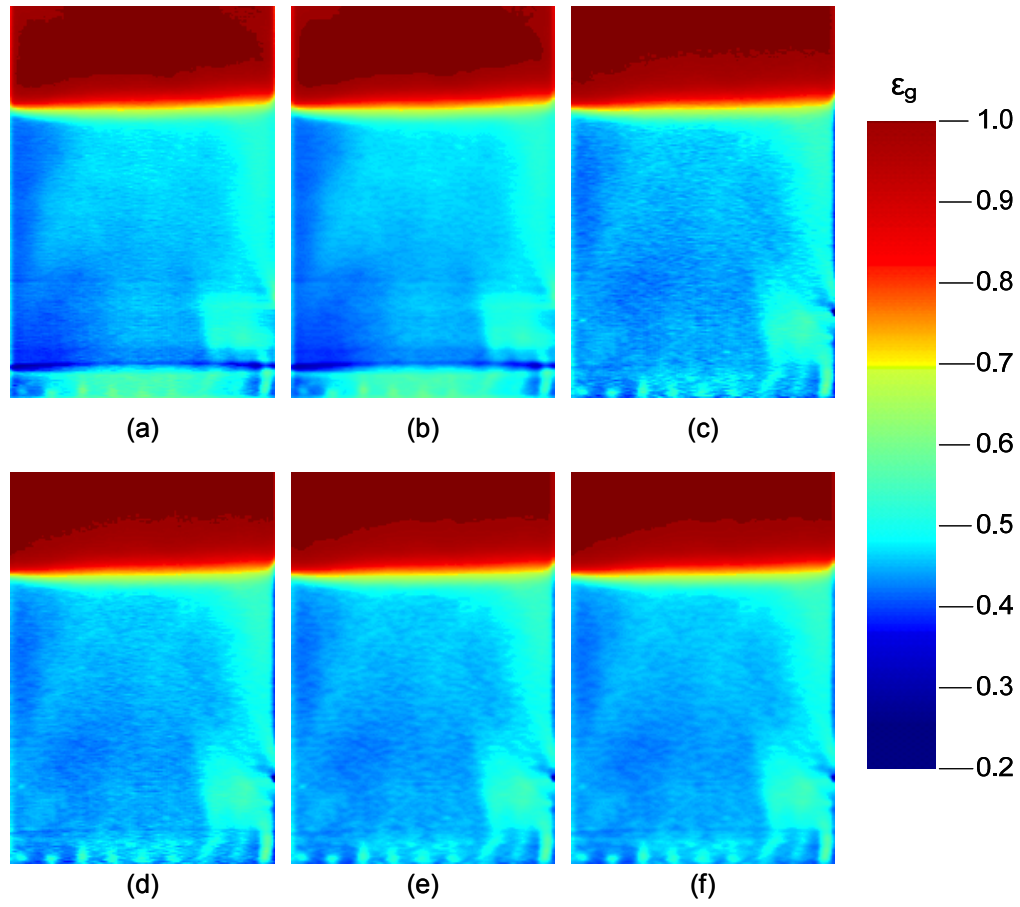


Figure C.4: Gas holdup y-slice images for glass bead fluidization with $U_g = 1.50U_{mf}$ and no side air injection for six calculation methods: a) average, b) average (smoothed after), c) local, d) local (smooth before), e) local (smooth after), and f) local (smooth before and after).

Table C.2: Local y-slice gas holdup average and standard deviation at $z = 7.0$ cm for bulk glass beads using various calculation methods.

Calculation method	Average	Average (smoothed after)	Local	Local (smoothed before)	Local (smoothed after)	Local (smoothed both)
Average ε_b	0.450	0.450	0.443	0.442	0.443	0.442
Standard deviation ε_b	0.023	0.022	0.023	0.023	0.022	0.022

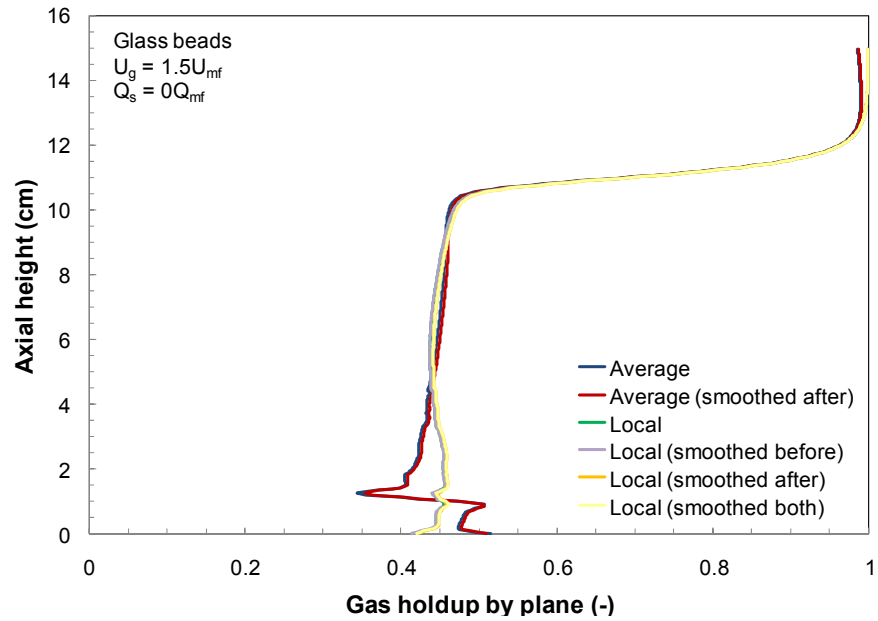


Figure C.5: Average gas holdup by height for glass bead fluidization using various calculation methods:
 $U_g = 1.50U_{mf}$, $Q_s = 0Q_{mf}$.

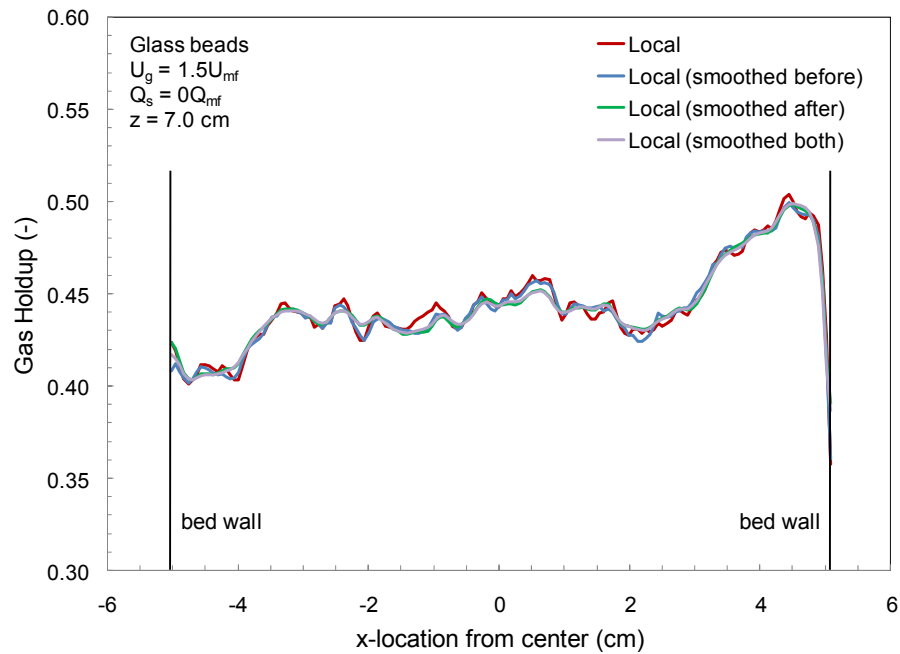
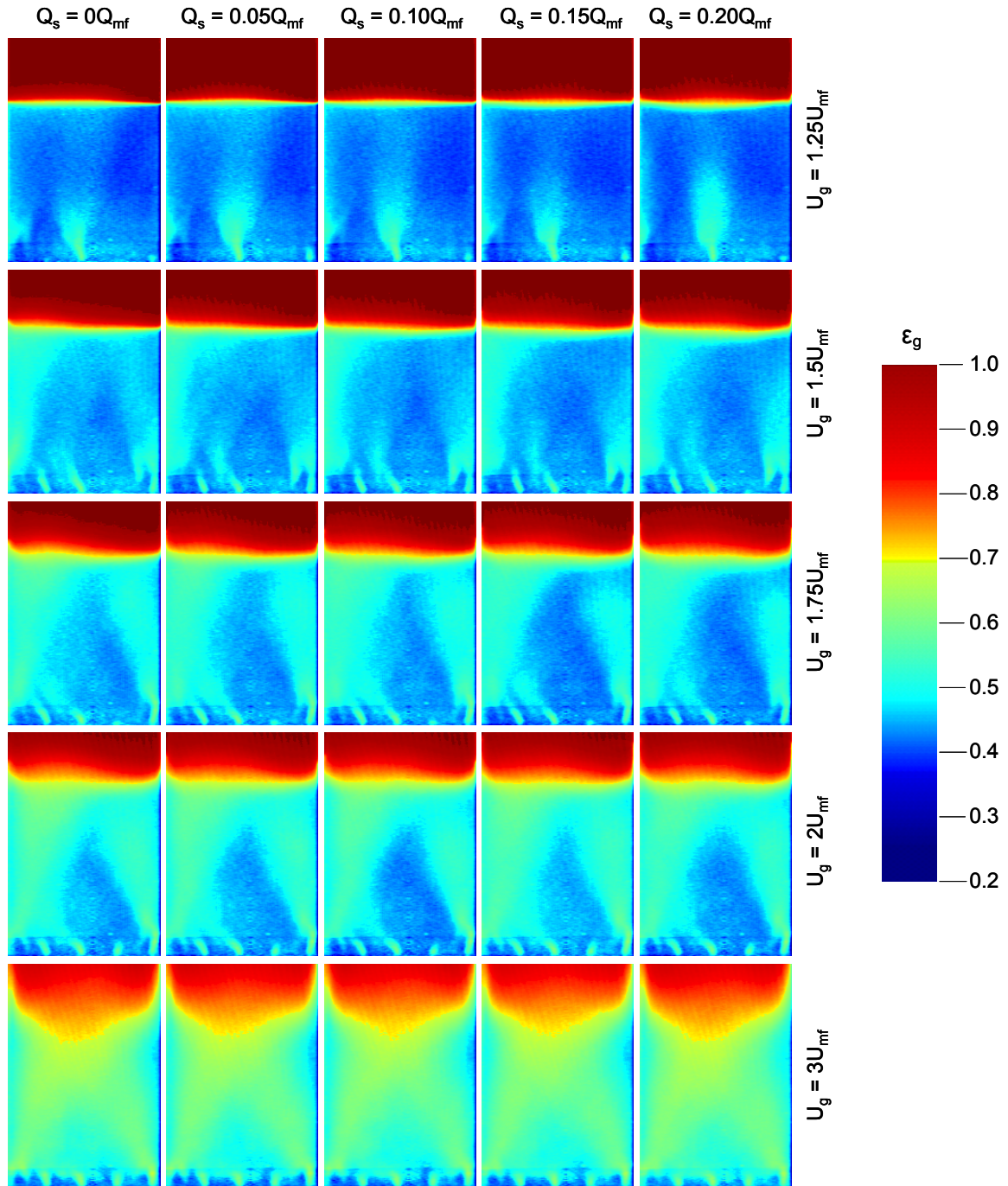


Figure C.6: Local y-slice gas holdup for glass bead fluidization at $z = 7.0 \text{ cm}$ using various calculation methods: $U_g = 1.50U_{mf}$, $Q_s = 0Q_{mf}$.

Glass Bead Gas Holdup

Figure C.7: Gas holdup x-slices for glass bead fluidization: varying U_g and Q_s .

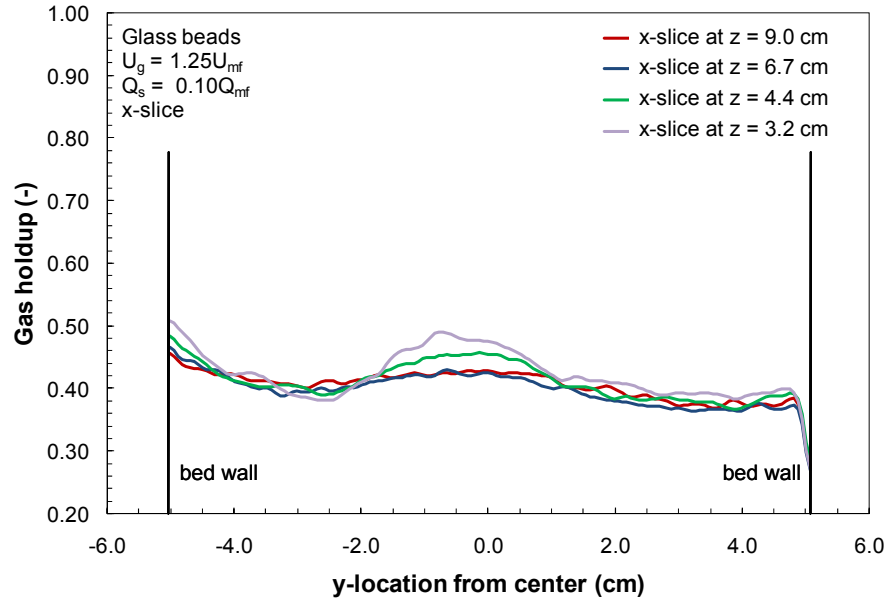


Figure C.8: X-slice gas holdup for glass bead fluidization at four heights: $U_g = 1.25U_{mf}$, $Q_s = 0.10Q_{mf}$.

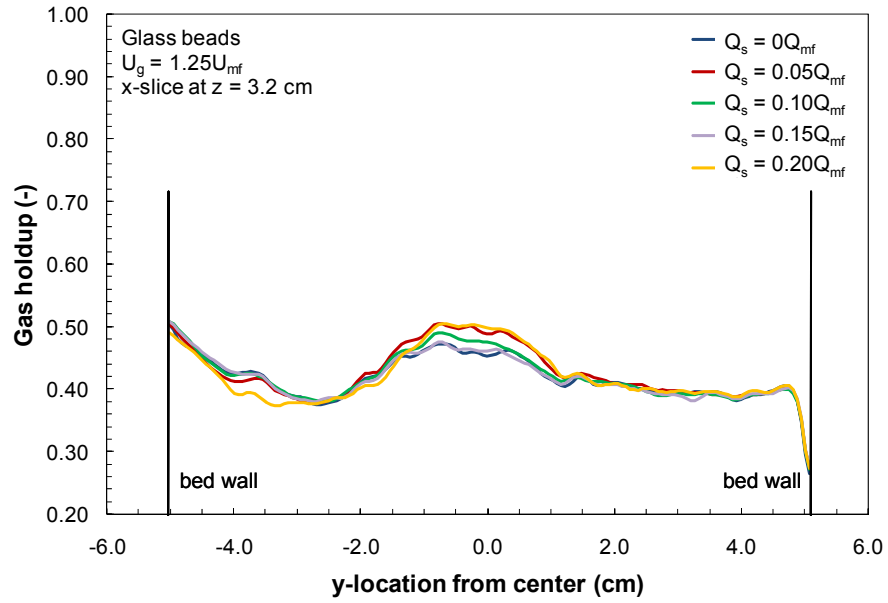


Figure C.9: X-slice gas holdup for glass bead fluidization at $z = 3.2$ cm: $U_g = 1.25U_{mf}$, varying Q_s .

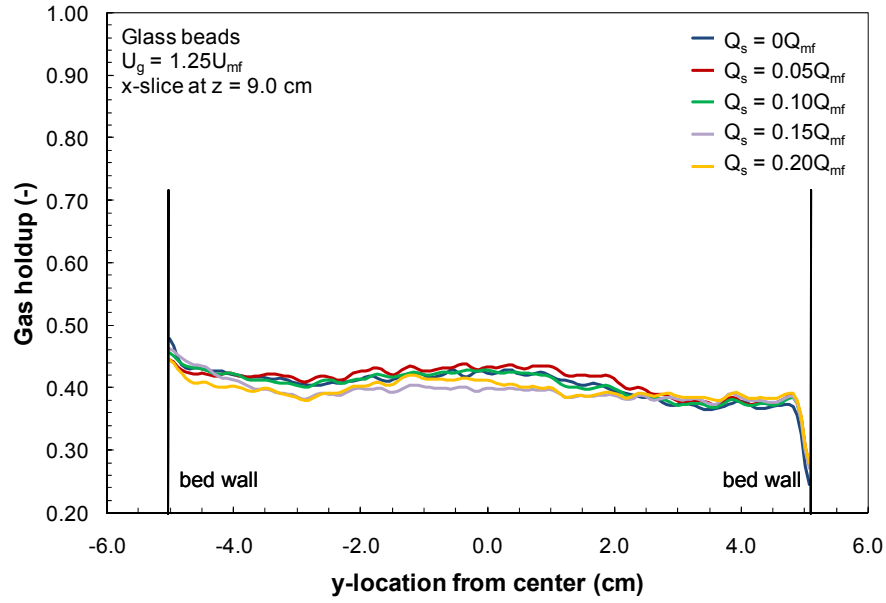


Figure C.10: X-slice gas holdup for glass bead fluidization at $z = 9.0$ cm: $U_g = 1.25U_{mf}$, varying Q_s .

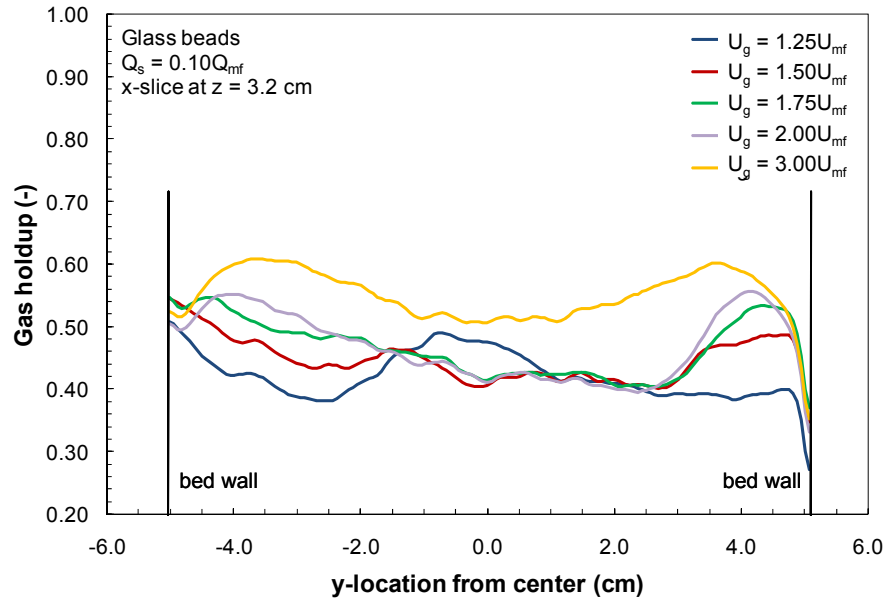


Figure C.11: X-slice gas holdup for glass bead fluidization at $z = 3.2$ cm: $Q_s = 0.10Q_{mf}$, varying U_g .

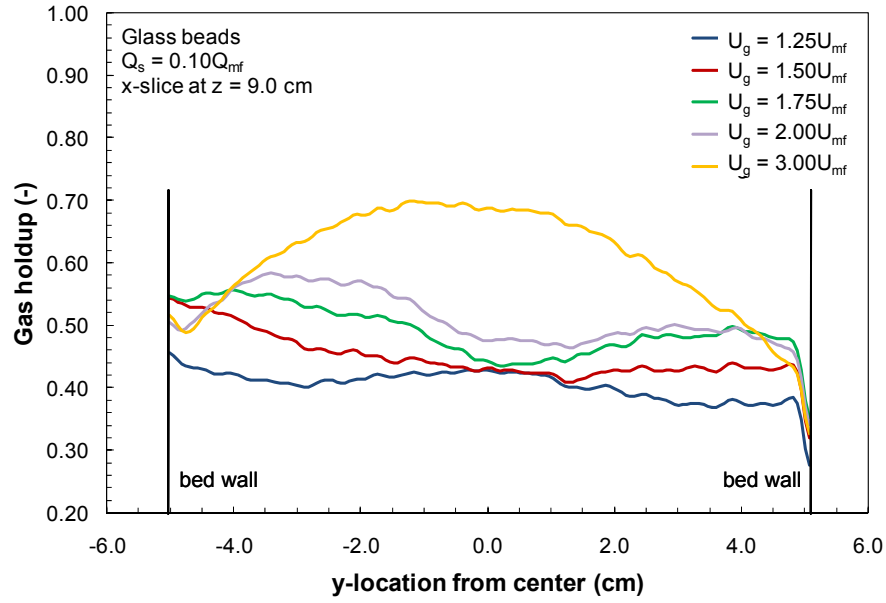


Figure C.12: X-slice gas holdup for glass bead fluidization at $z = 9.0$ cm: $Q_s = 0.10Q_{mf}$, varying U_g .

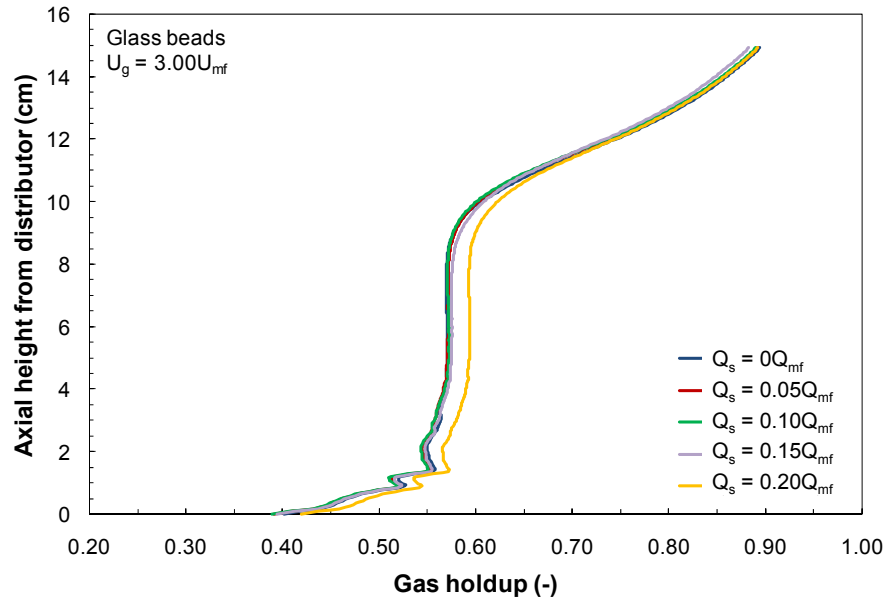


Figure C.13: Average gas holdup by height for glass bead fluidization: $U_g = 3U_{mf}$, varying Q_s .

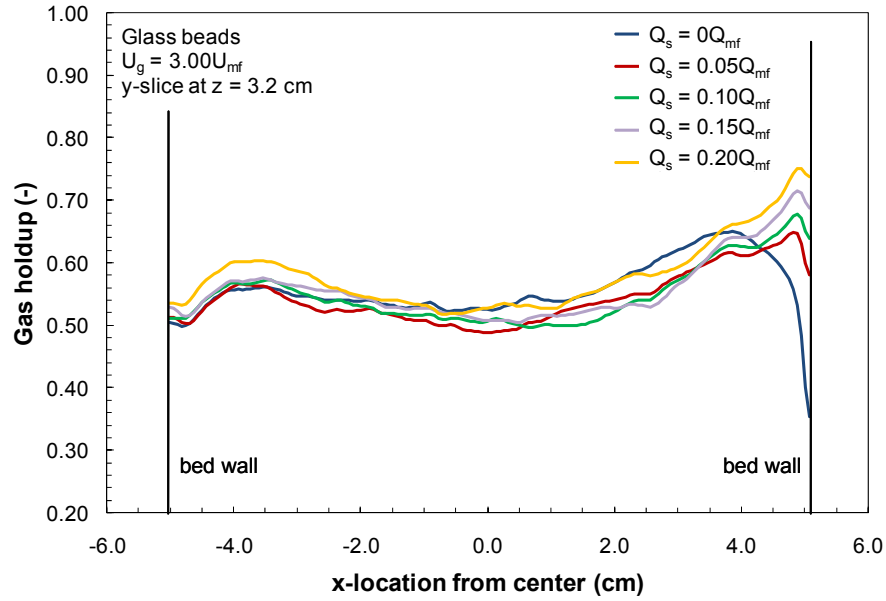


Figure C.14: Y-slice gas holdup for glass bead fluidization at $z = 3.2$ cm: $U_g = 3U_{mf}$, varying Q_s .

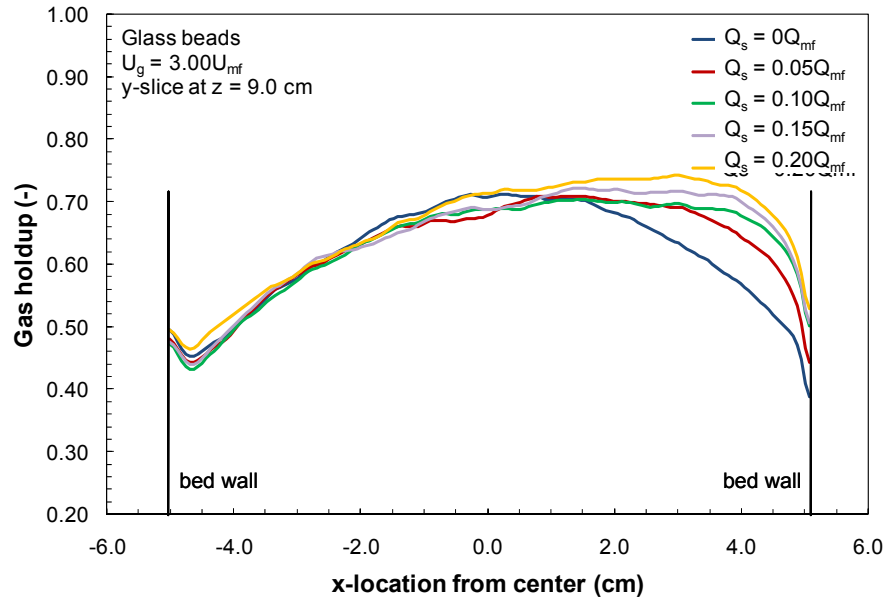


Figure C.15: Y-slice gas holdup for glass bead fluidization at $z = 9.0$ cm: $U_g = 3U_{mf}$, varying Q_s .

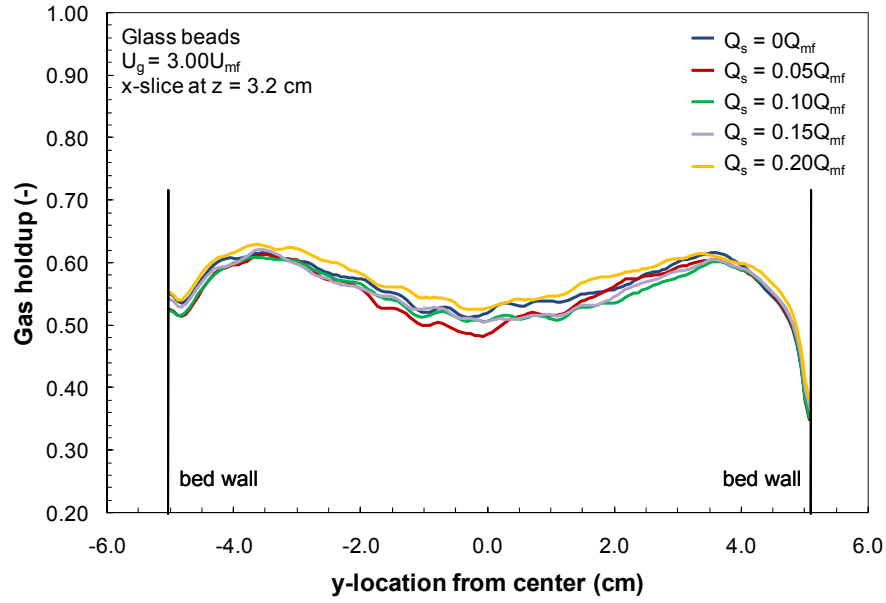


Figure C.16: X-slice gas holdup for glass bead fluidization at $z = 3.2$ cm: $U_g = 3U_{mf}$, varying Q_s .

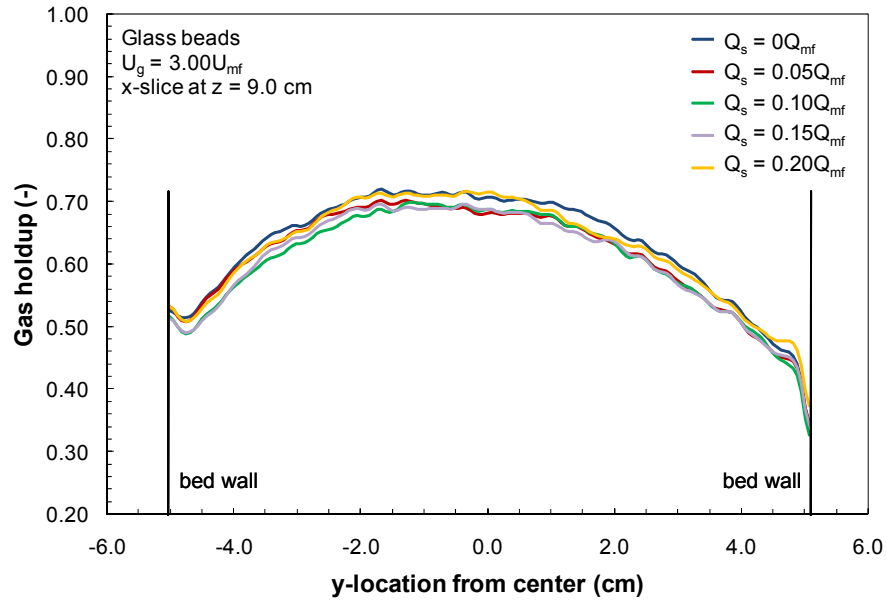


Figure C.17: X-slice gas holdup for glass bead fluidization at $z = 9.0$ cm: $U_g = 3U_{mf}$, varying Q_s .

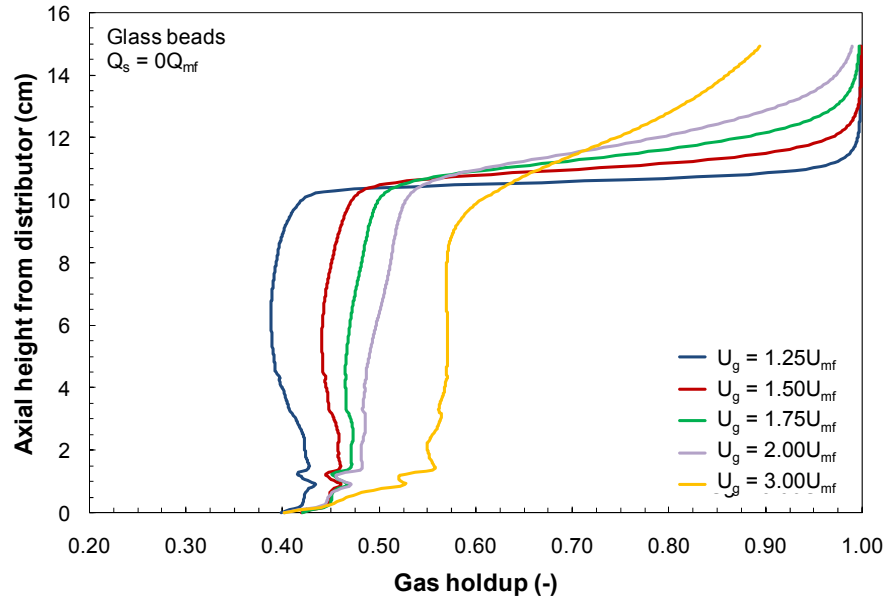


Figure C.18: Average gas holdup by height for glass bead fluidization: $Q_s = 0Q_{mf}$, varying U_g .

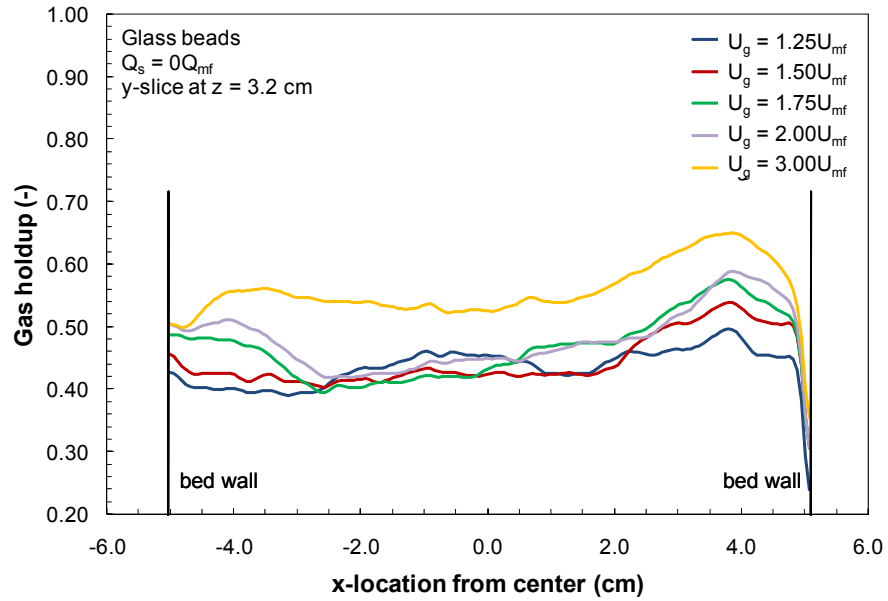


Figure C.19: Y-slice gas holdup for glass bead fluidization at $z = 3.2$ cm: $Q_s = 0Q_{mf}$, varying U_g .

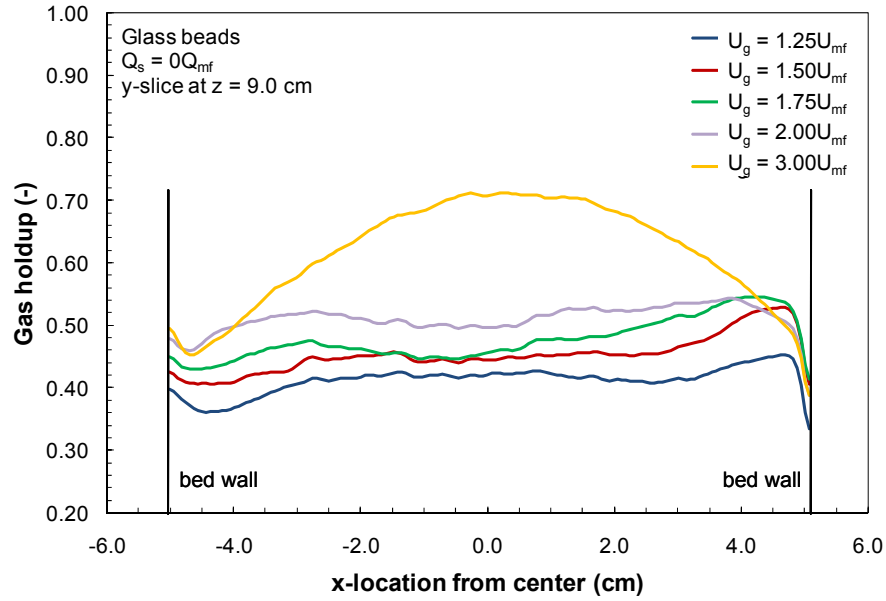


Figure C.20: Y-slice gas holdup for glass bead fluidization at $z = 9.0$ cm: $Q_s = 0Q_{mf}$, varying U_g .

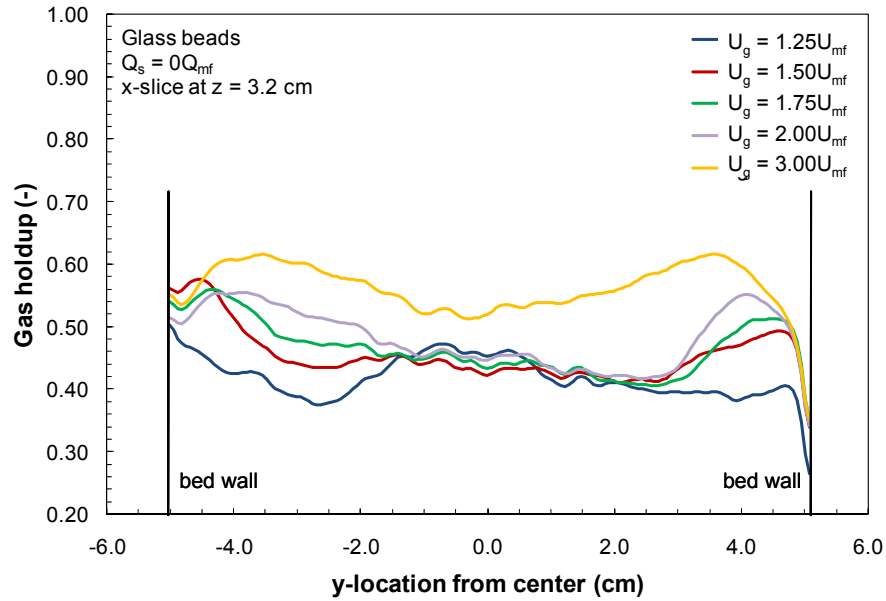


Figure C.21: X-slice gas holdup for glass bead fluidization at $z = 3.2$ cm: $Q_s = 0Q_{mf}$, varying U_g .

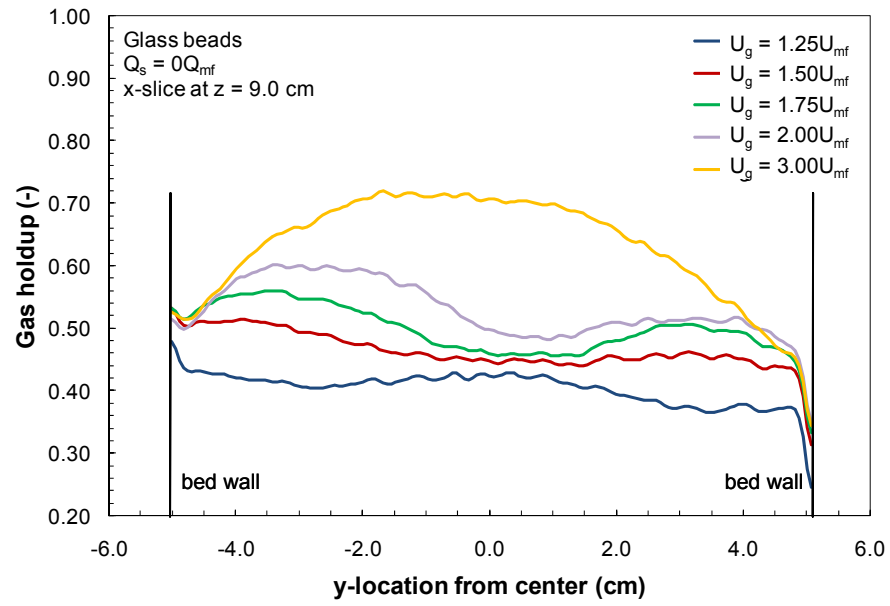


Figure C.22: X-slice gas holdup for glass bead fluidization at $z = 9.0$ cm: $Q_s = 0Q_{mf}$, varying U_g .

Walnut Shell Gas Holdup

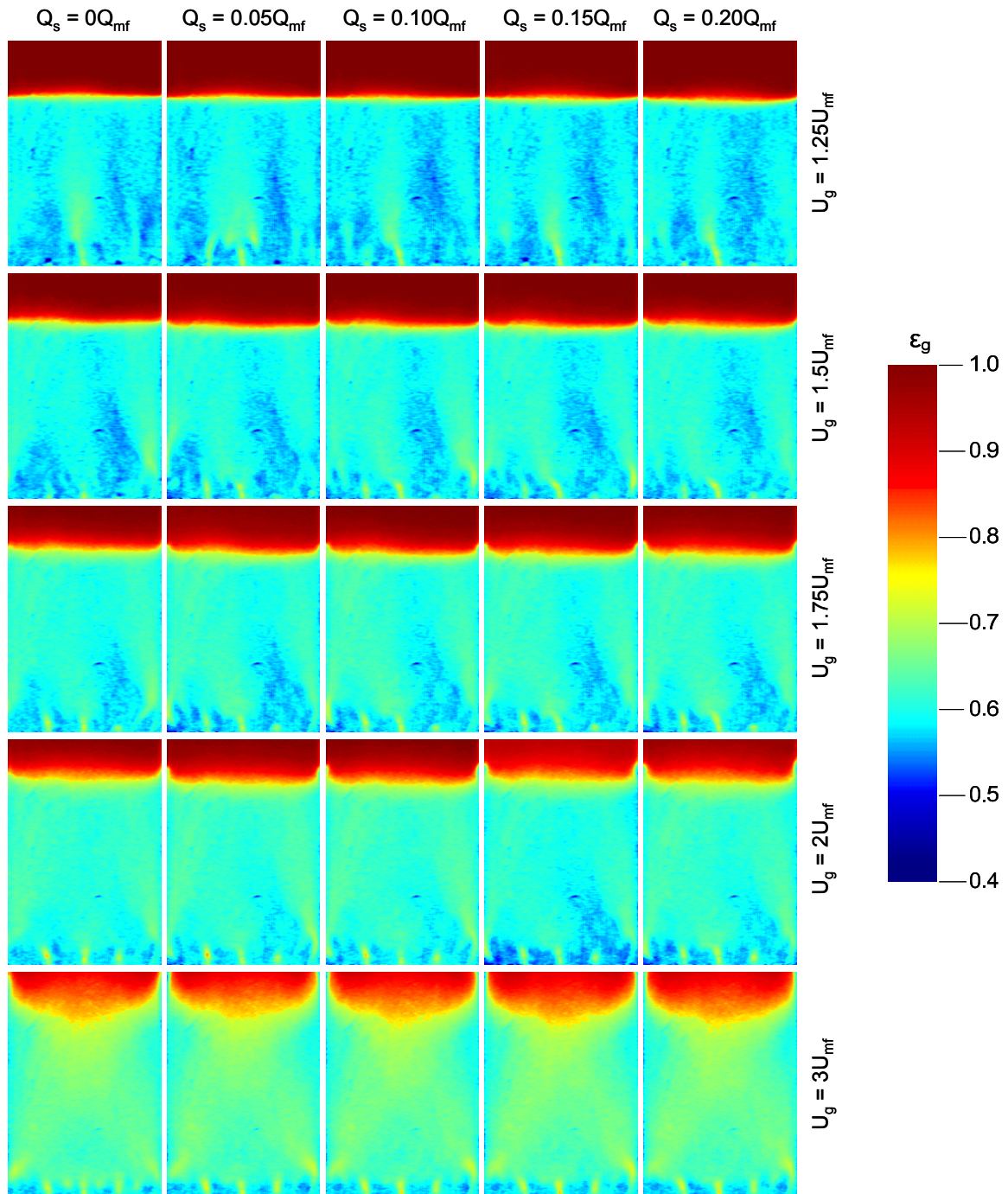


Figure C.23: Gas holdup x-slices for walnut shell fluidization: varying U_g and Q_s .

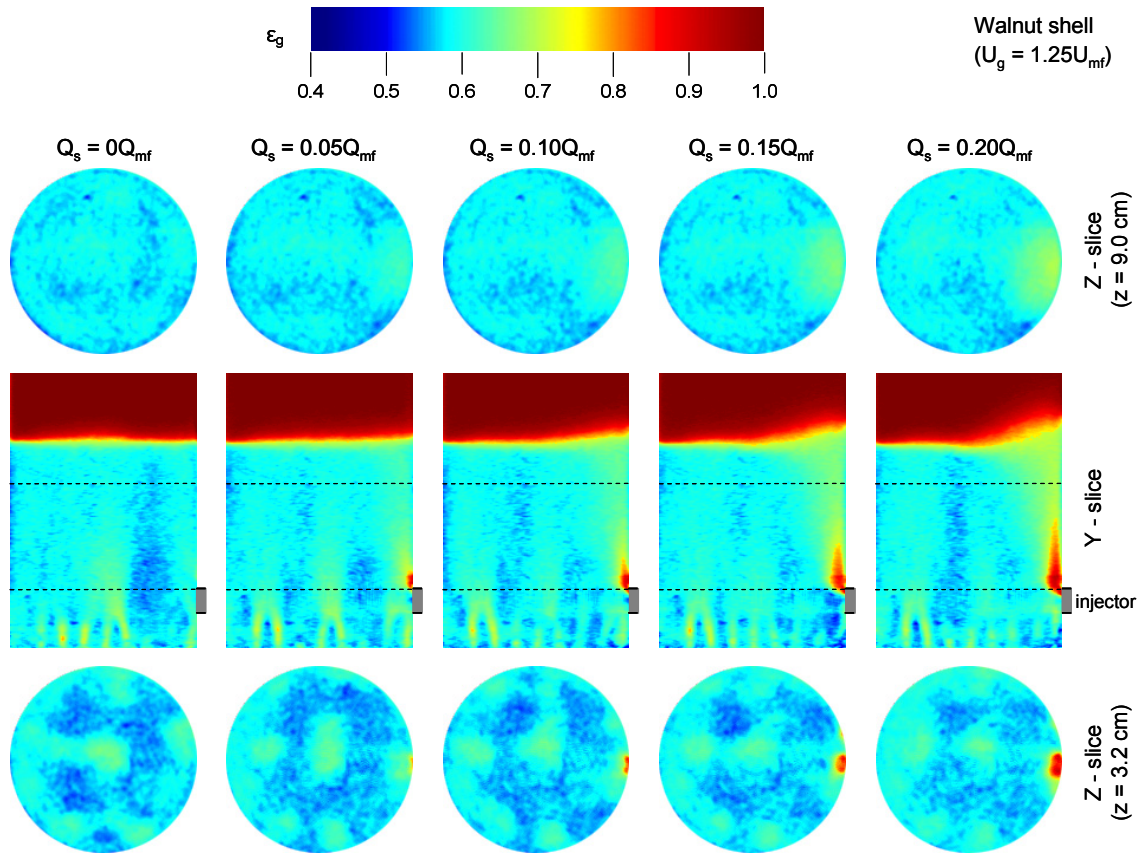


Figure C.24: Gas holdup y- and z-slices for walnut shell fluidization: $U_g = 1.25U_{mf}$, varying Q_s .

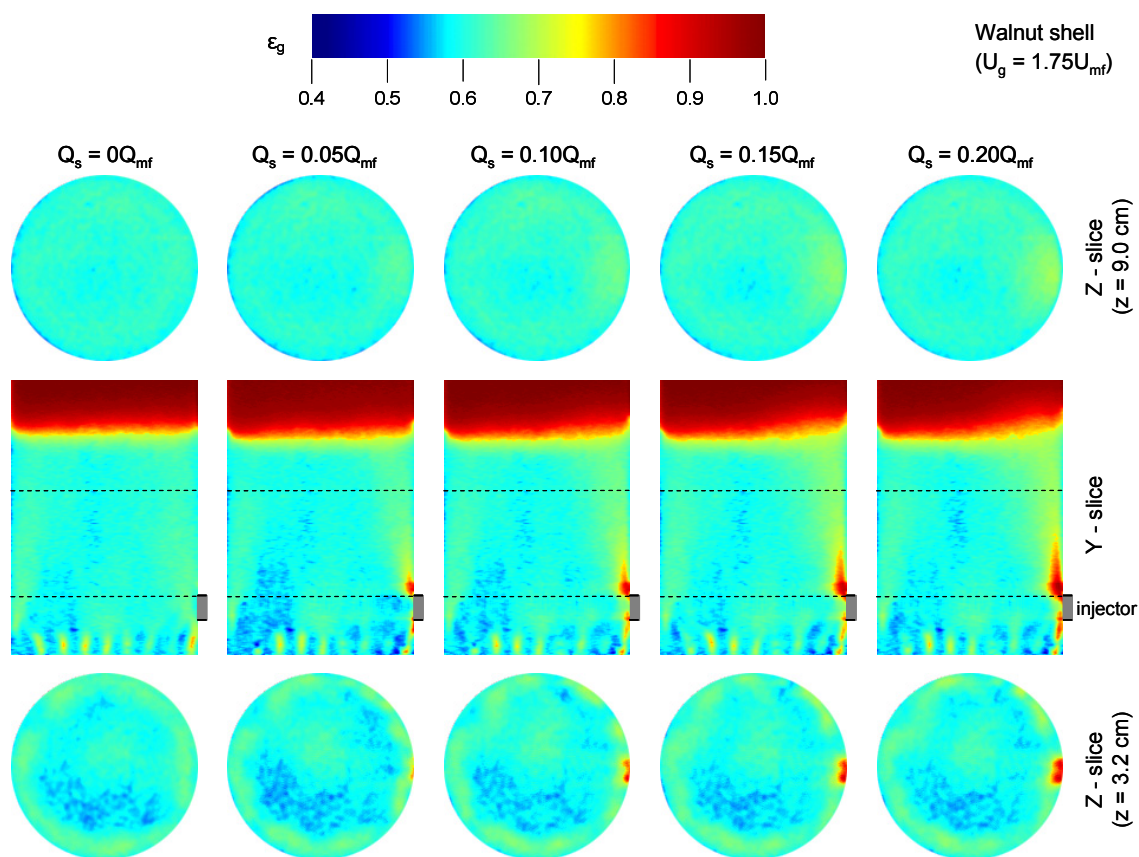


Figure C.25: Gas holdup y- and z-slices for walnut shell fluidization: $U_g = 1.75U_{mf}$, varying Q_s .

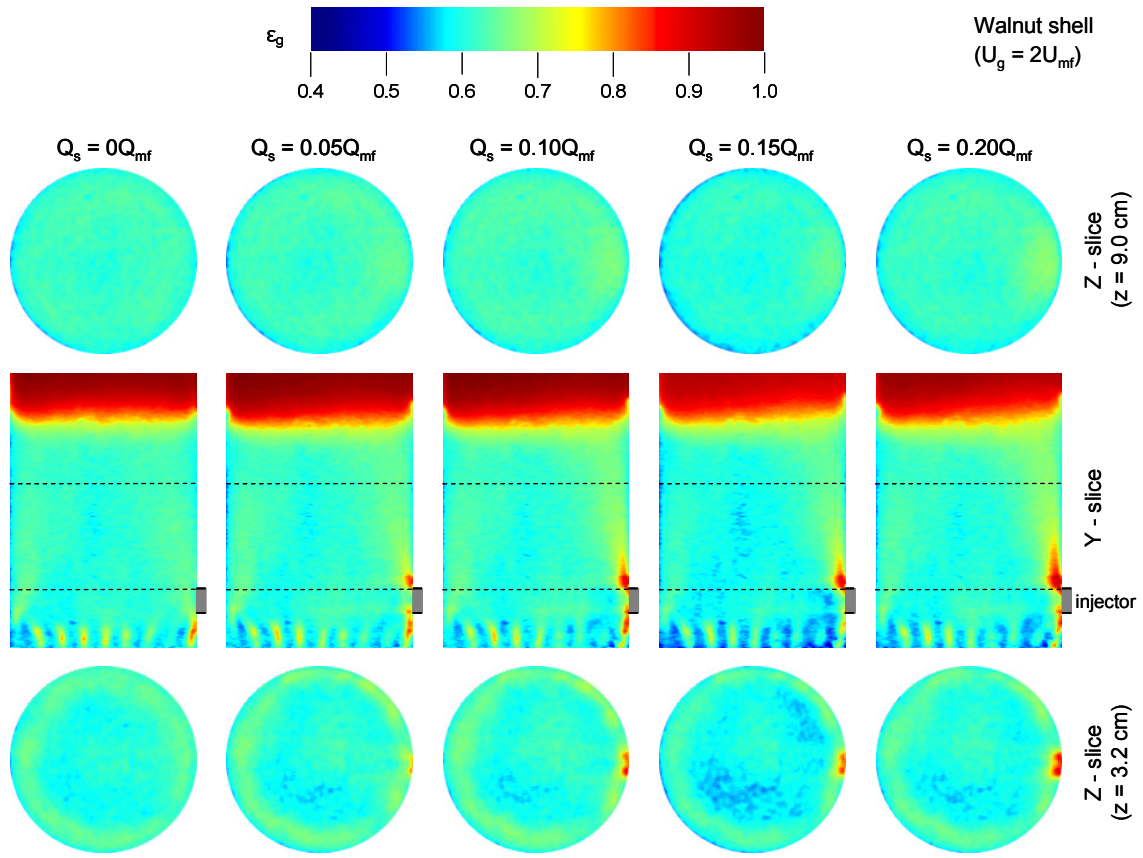


Figure C.26: Gas holdup y- and z-slices for walnut shell fluidization: $U_g = 2U_{mf}$, varying Q_s .

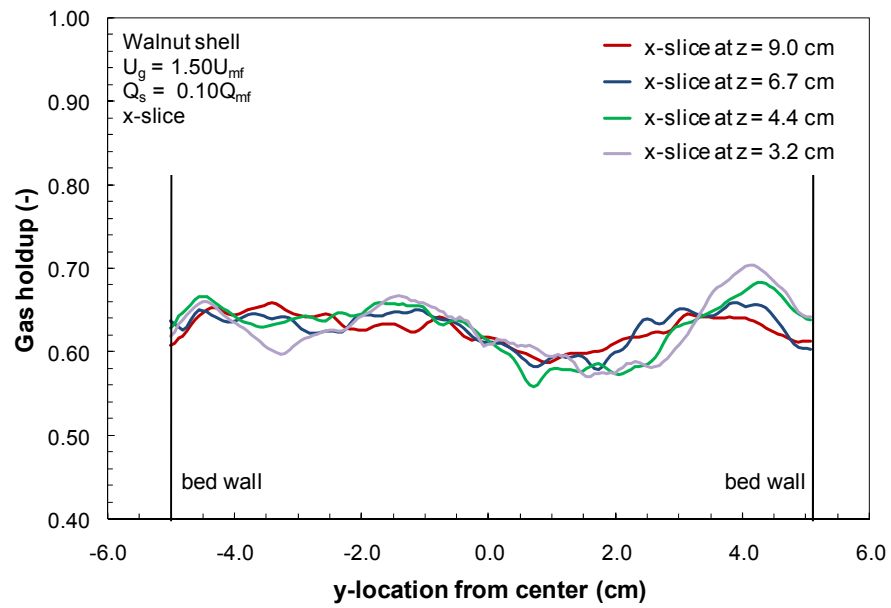


Figure C.27: X-slice gas holdup for walnut shell fluidization at four heights: $U_g = 1.5U_{mf}$, $Q_s = 0.10Q_{mf}$.

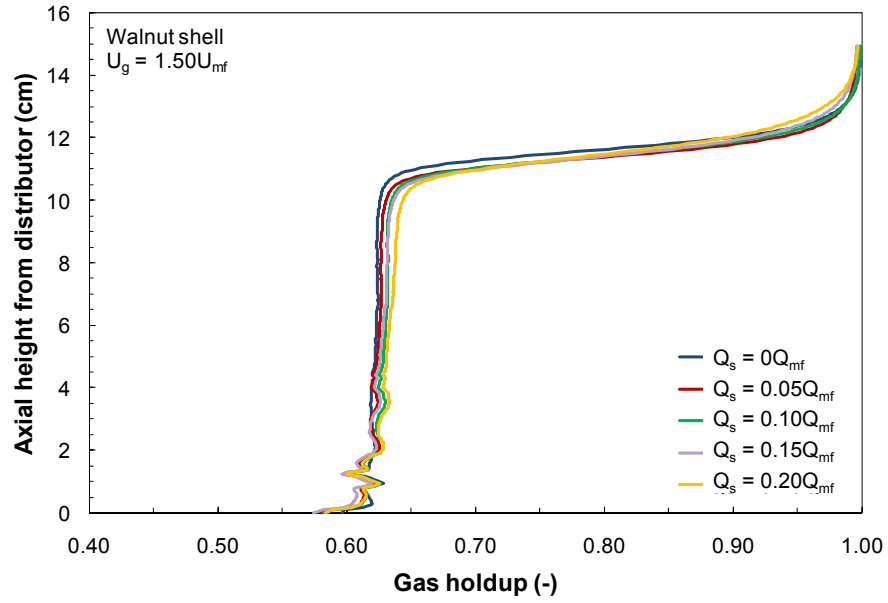


Figure C.28: Average gas holdup by height for walnut shell fluidization: $U_g = 1.5U_{mf}$, varying Q_s .

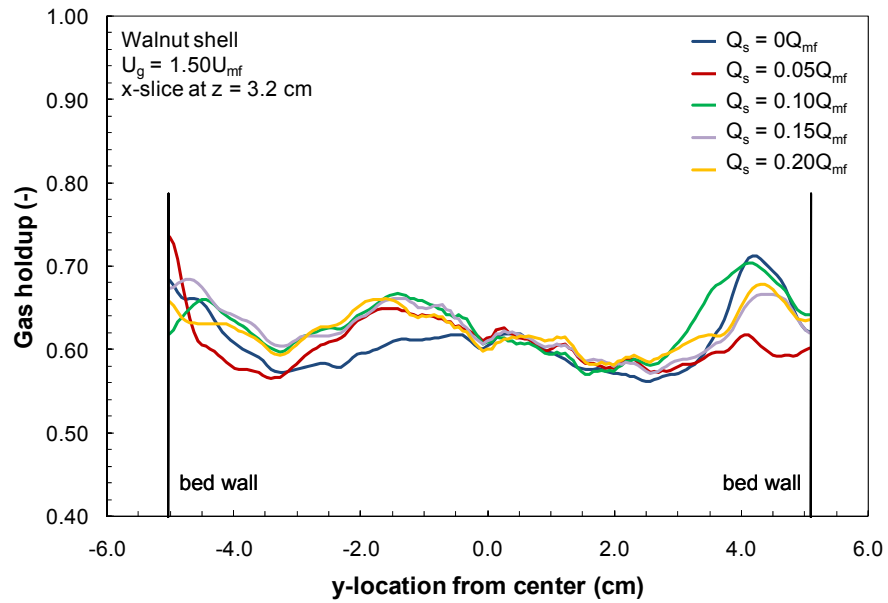


Figure C.29: X-slice gas holdup for walnut shell fluidization at $z = 3.2$ cm: $U_g = 1.5U_{mf}$, varying Q_s .

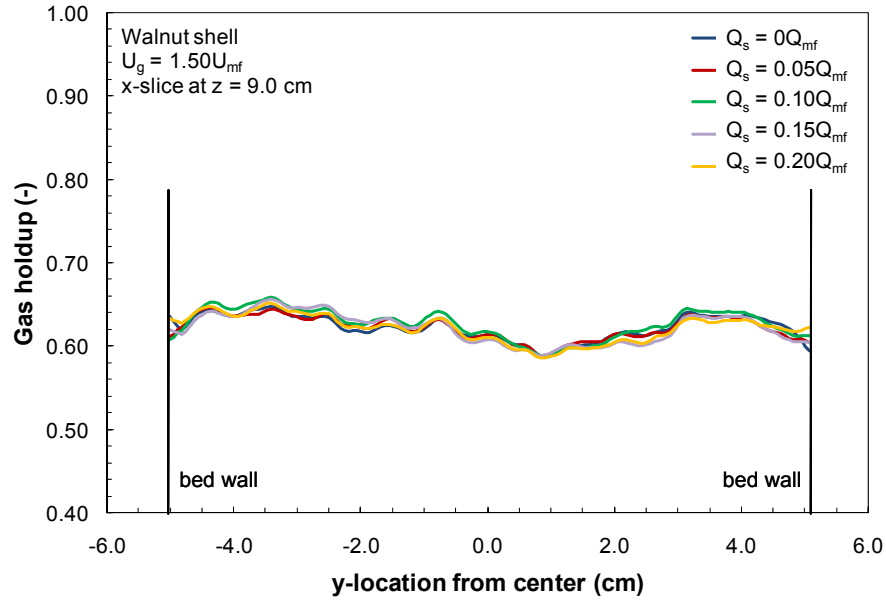


Figure C.30: X-slice gas holdup for walnut shell fluidization at $z = 9.0$ cm: $U_g = 1.50U_{mf}$, varying Q_s .

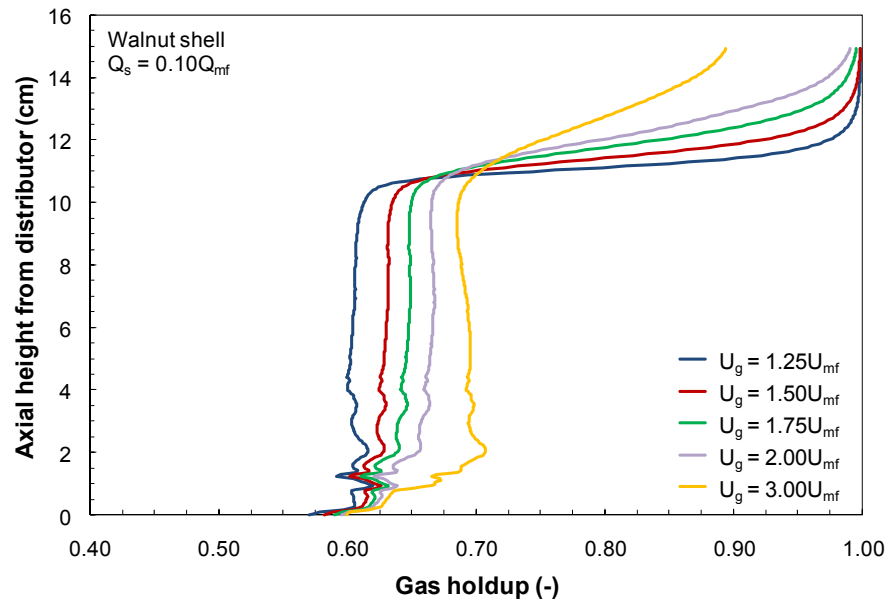


Figure C.31: Average gas holdup by height for walnut shell fluidization: $Q_s = 0.10Q_{mf}$, varying U_g .

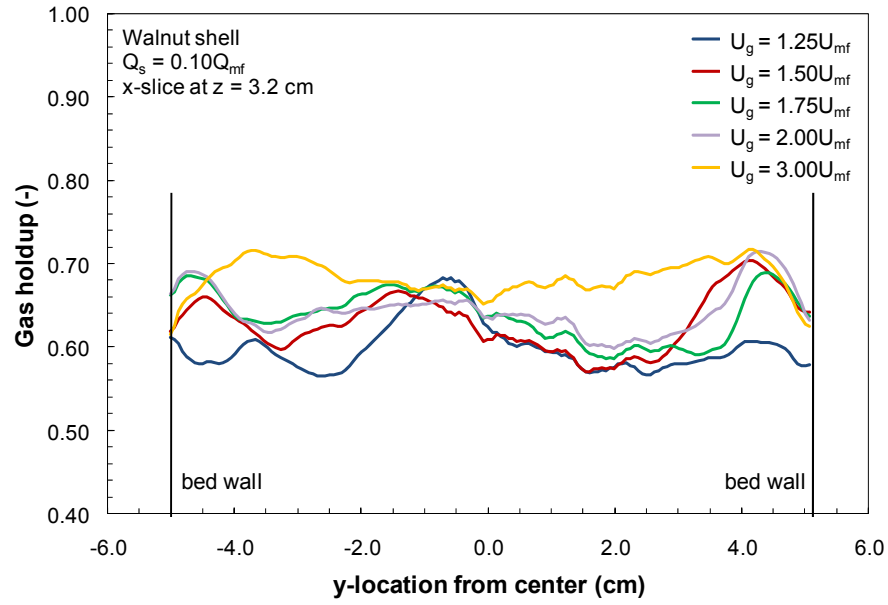


Figure C.32: X-slice gas holdup for walnut shell fluidization at $z = 3.2$ cm: $Q_s = 0.10Q_{mf}$, varying U_g .

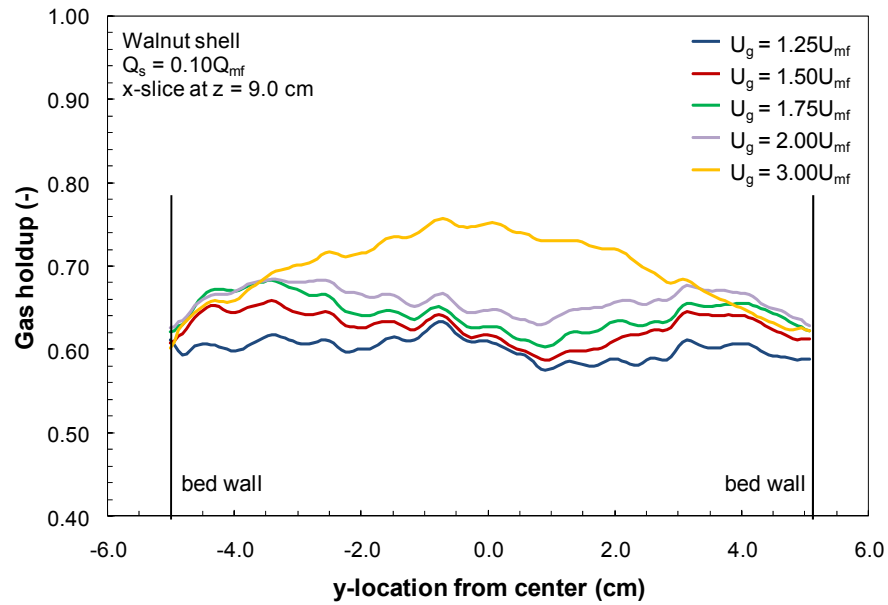


Figure C.33: X-slice gas holdup for walnut shell fluidization at $z = 9.0$ cm: $Q_s = 0.10Q_{mf}$, varying U_g .

Corncob Gas Holdup

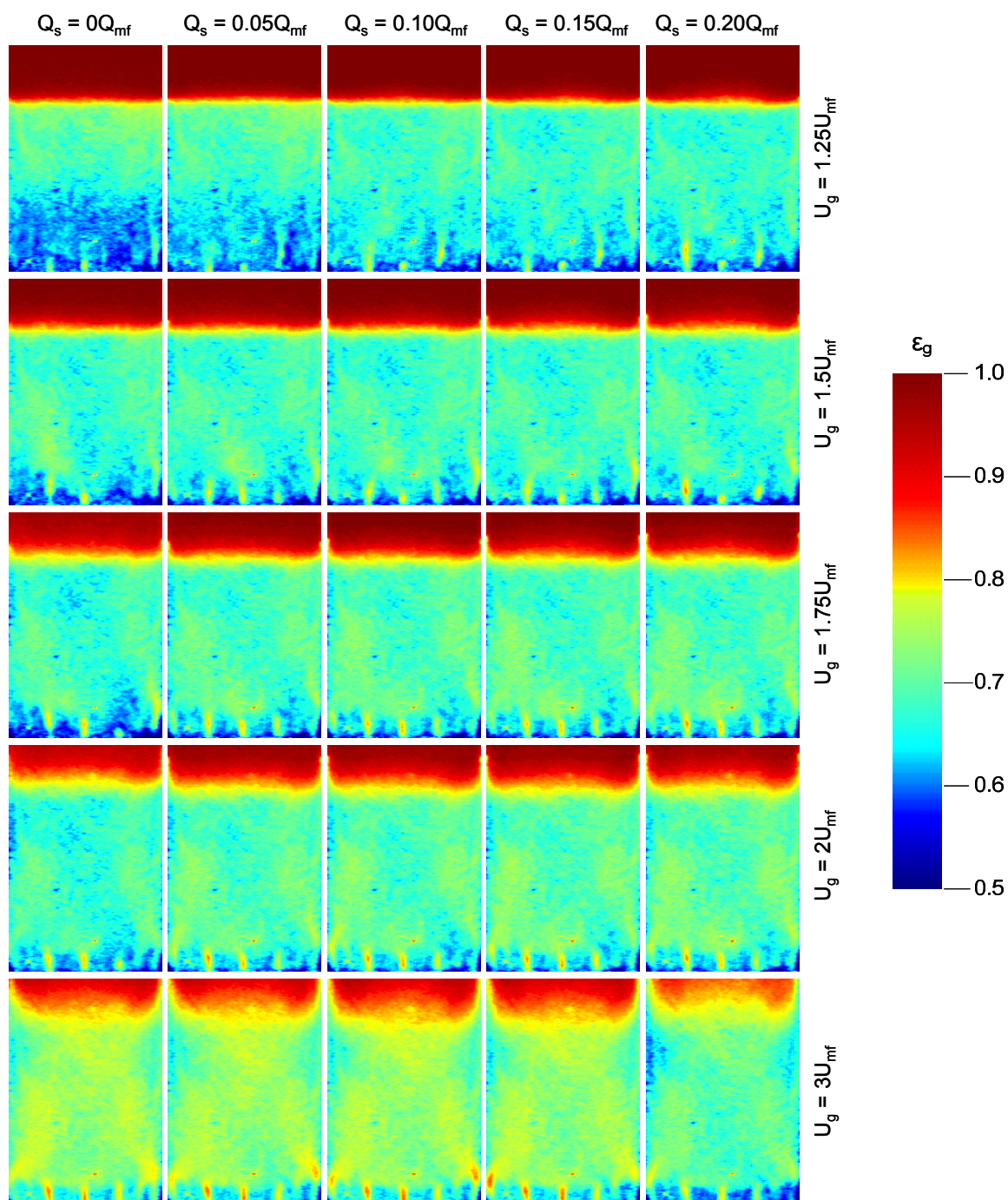


Figure C.34: Gas holdup x-slices for corn cob fluidization: varying U_g and Q_s .

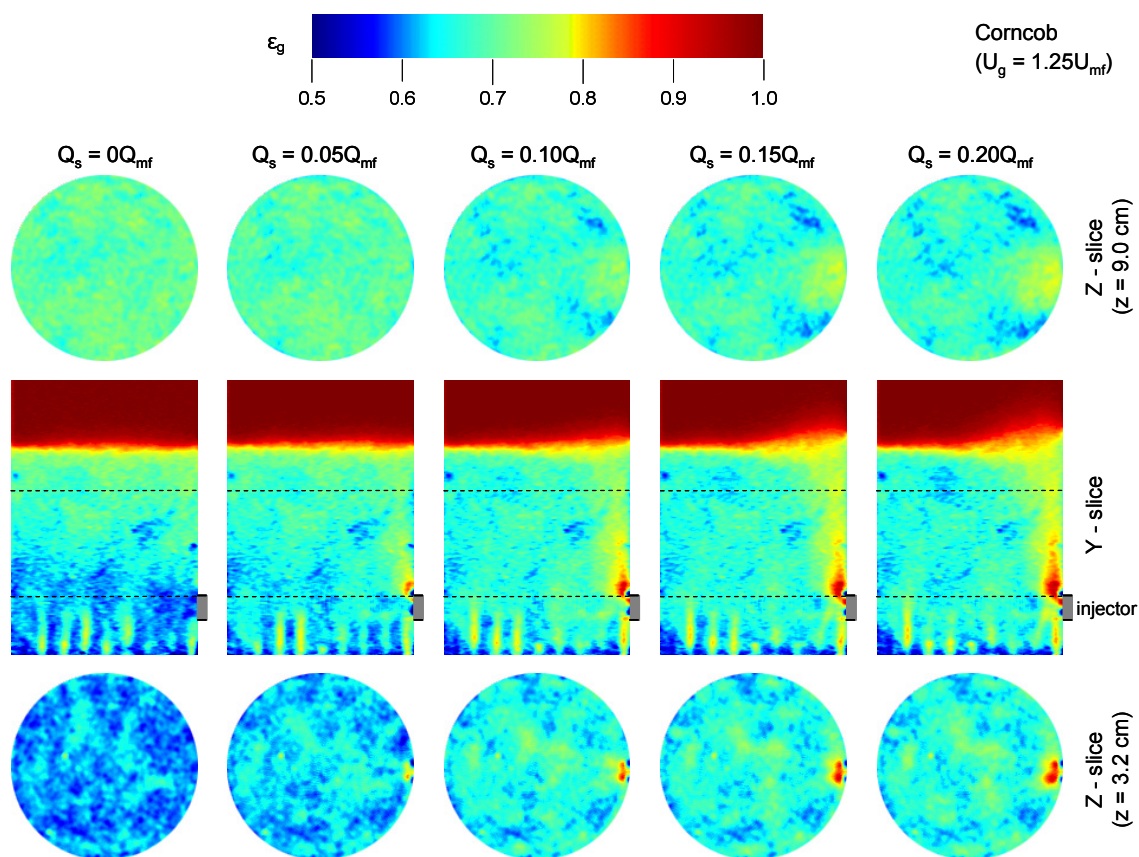


Figure C.35: Gas holdup y- and z-slices for corncob fluidization: $U_g = 1.25U_{mf}$, varying Q_s .

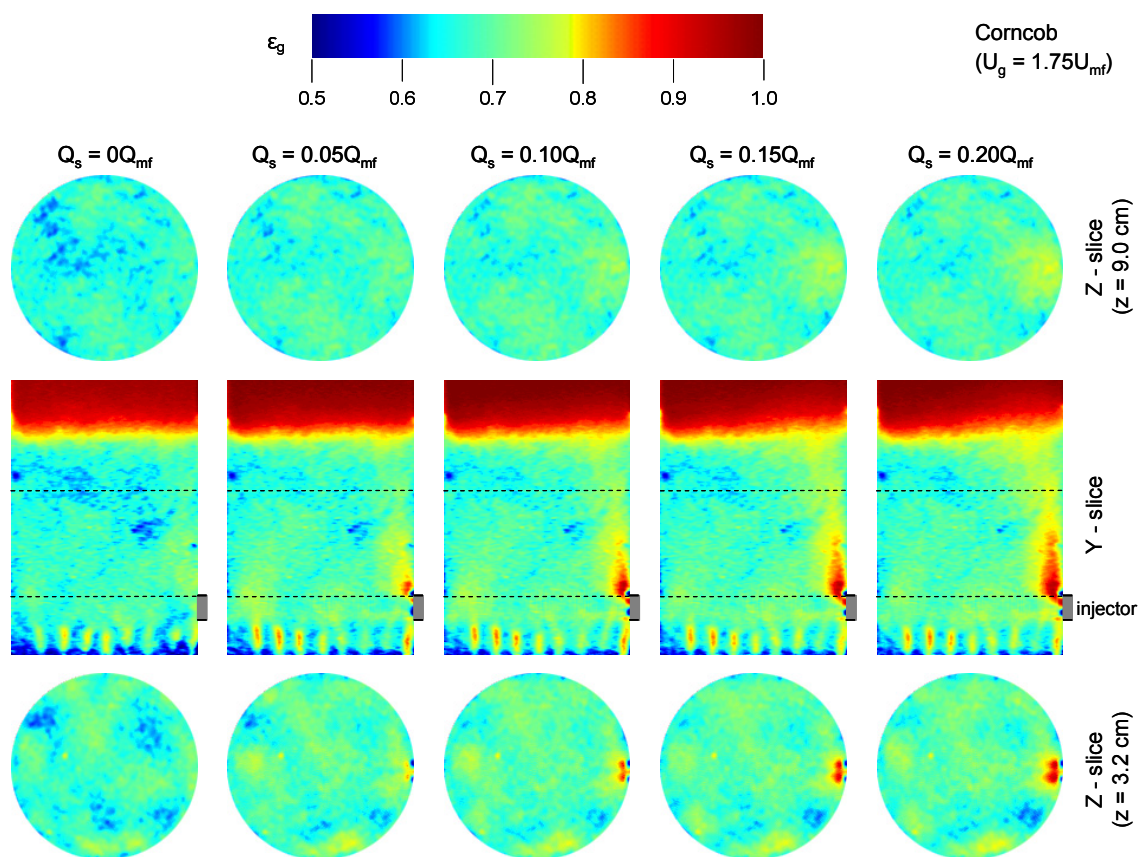


Figure C.36: Gas holdup y- and z-slices for corn cob fluidization: $U_g = 1.75U_{mf}$, varying Q_s .

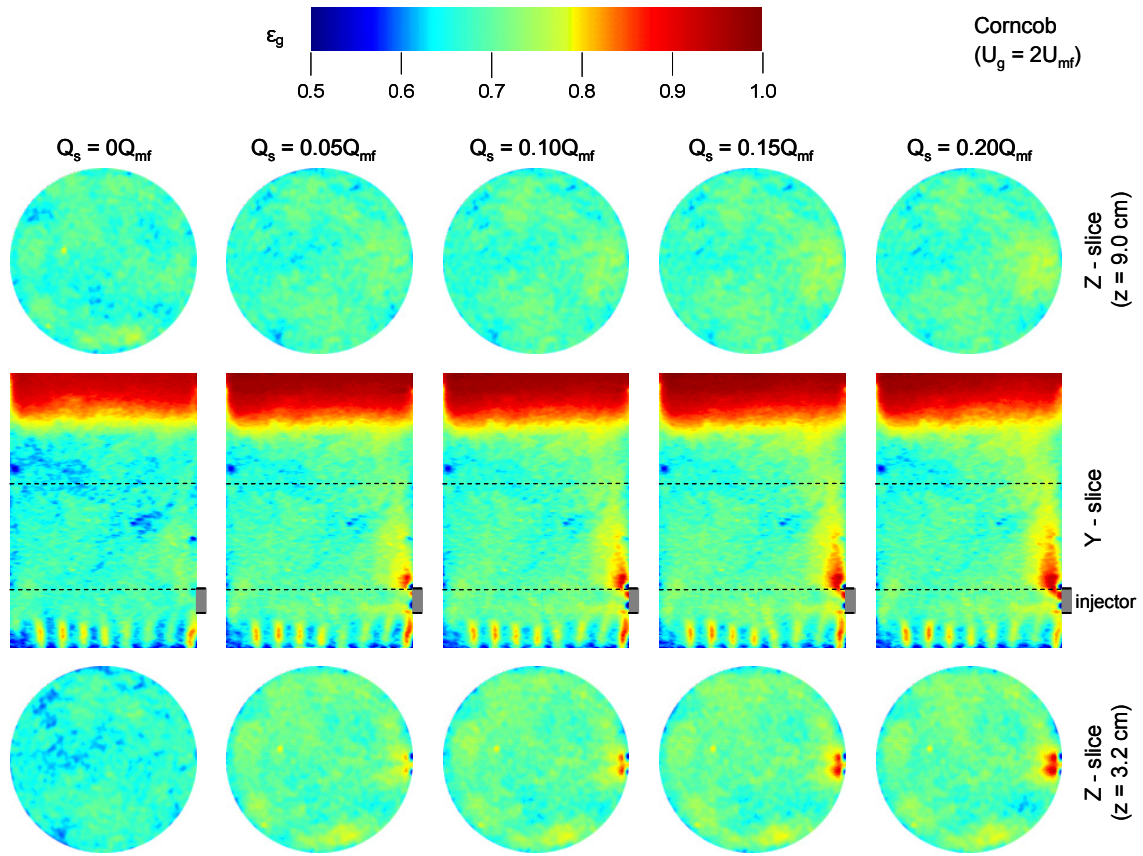


Figure C.37: Gas holdup y- and z-slices for corncob fluidization: $U_g = 2U_{mf}$, varying Q_s .

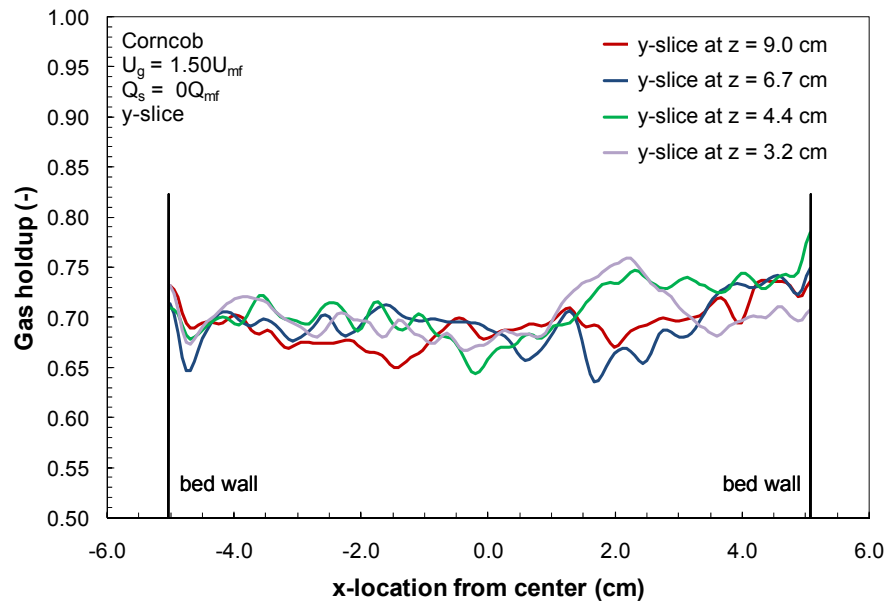


Figure C.38: Y-slice gas holdup for corncob fluidization at four heights: $U_g = 1.5U_{mf}$, $Q_s = 0Q_{mf}$.

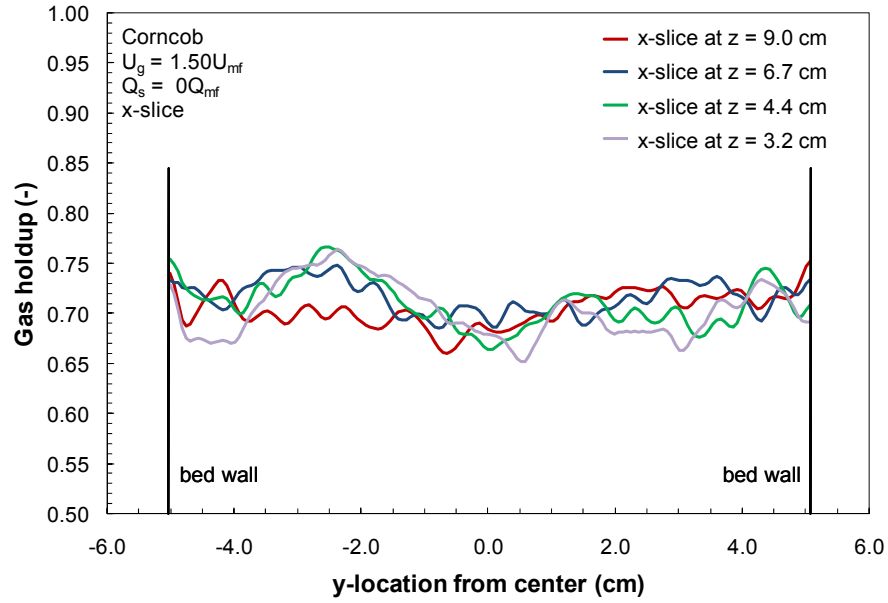


Figure C.39: X-slice gas holdup for corn cob fluidization at four heights: $U_g = 1.50U_{mf}$, $Q_s = 0Q_{mf}$.

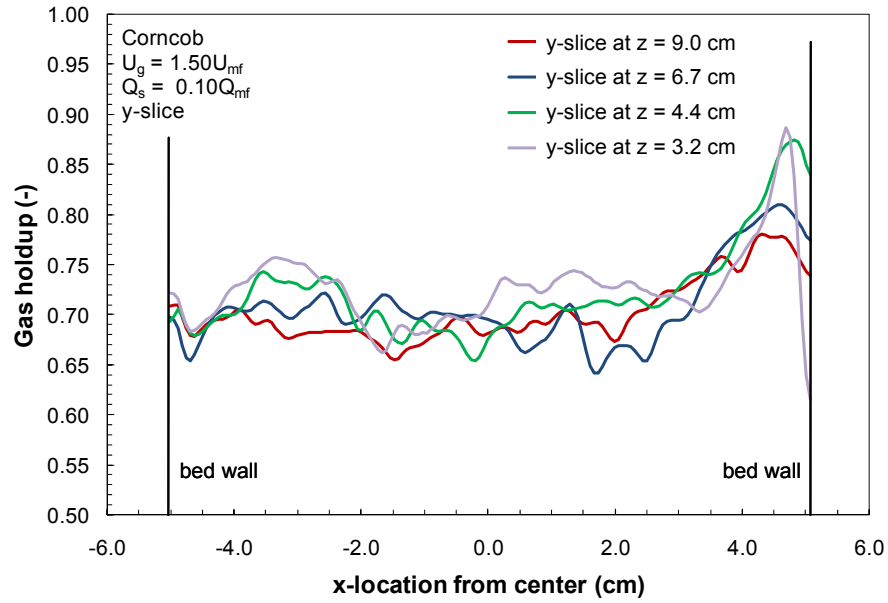


Figure C.40: Y-slice gas holdup for corn cob fluidization at four heights: $U_g = 1.50U_{mf}$, $Q_s = 0.10Q_{mf}$.

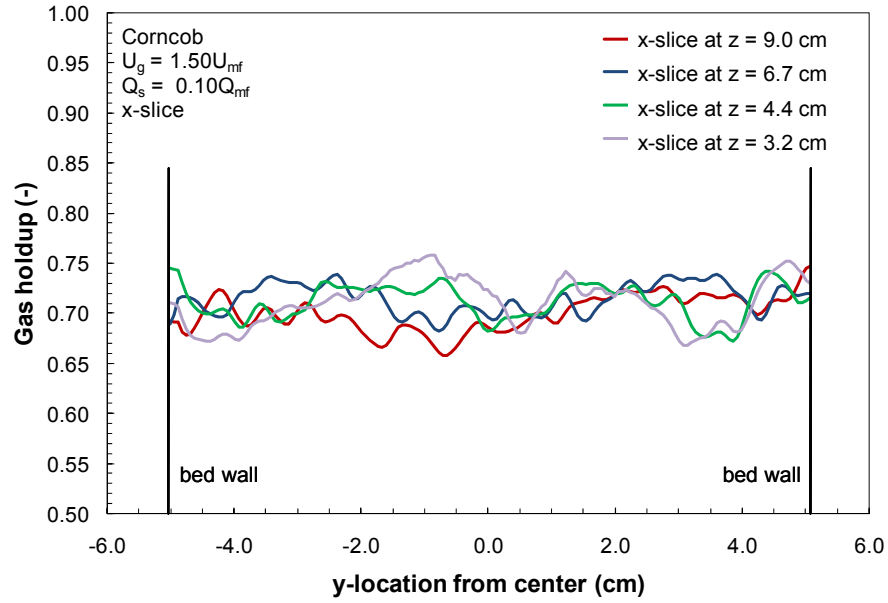


Figure C.41: X-slice gas holdup for corncob fluidization at four heights: $U_g = 1.50U_{mf}$, $Q_s = 0.10Q_{mf}$.

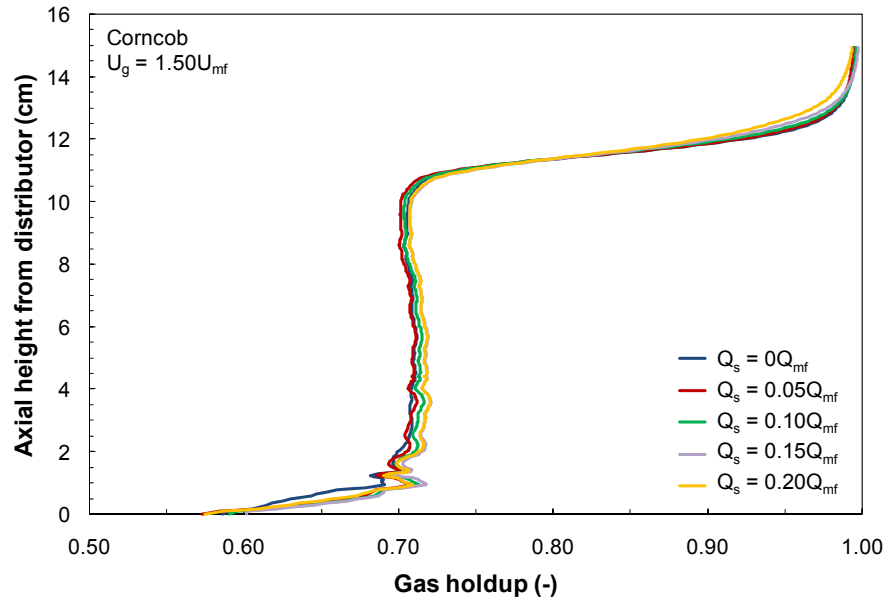


Figure C.42: Average gas holdup by height for corncob fluidization: $U_g = 1.50U_{mf}$, varying Q_s .

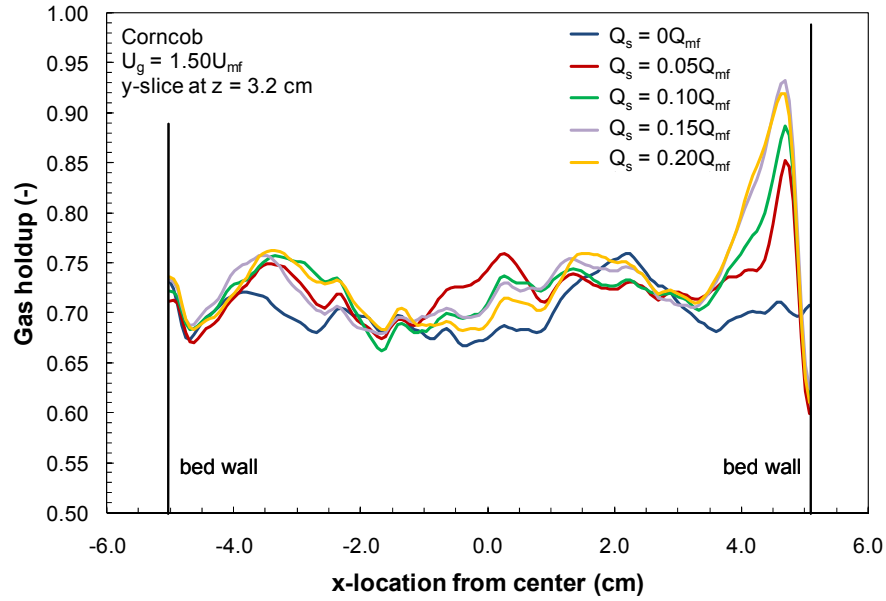


Figure C.43: Y-slice gas holdup for corn cob fluidization at $z = 3.2$ cm: $U_g = 1.50U_{mf}$, varying Q_s .

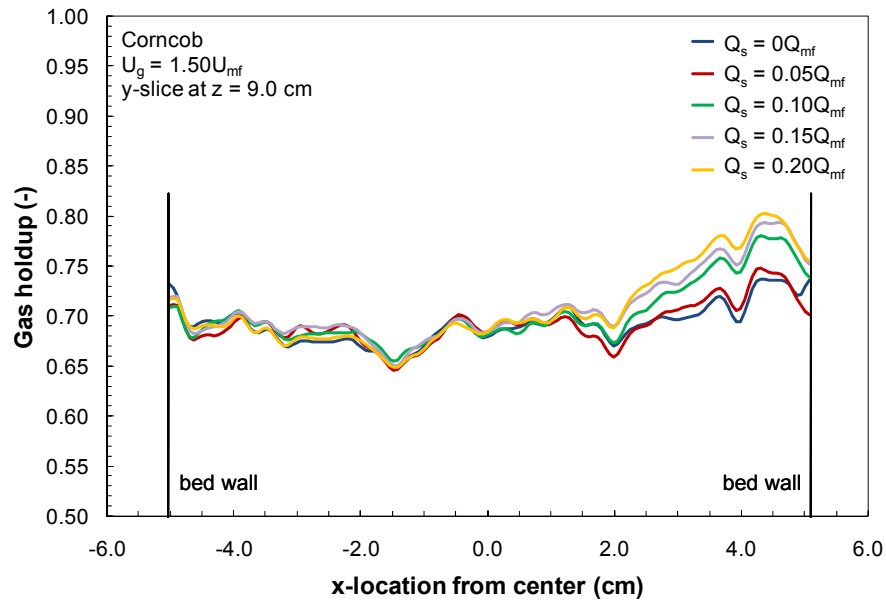


Figure C.44: Y-slice gas holdup for corn cob fluidization at $z = 9.0$ cm: $U_g = 1.50U_{mf}$, varying Q_s .

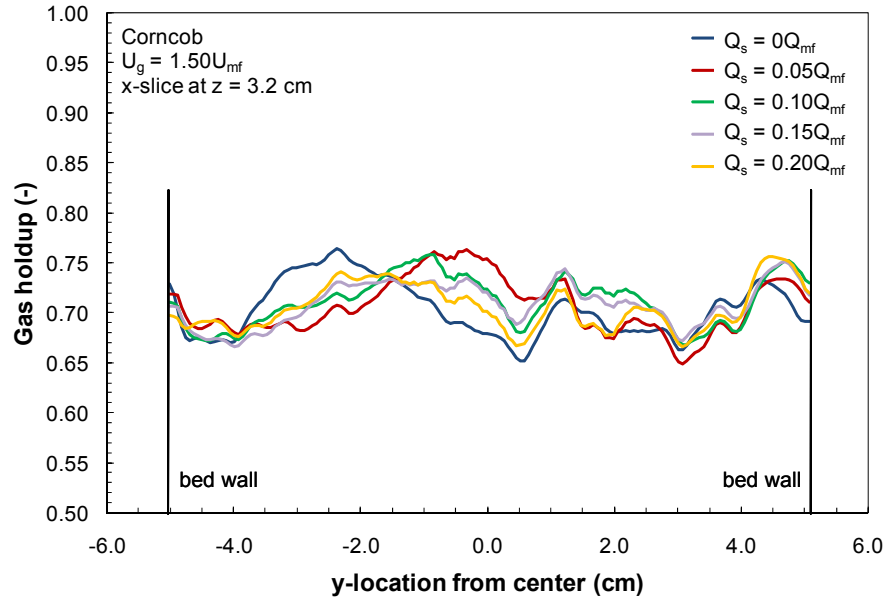


Figure C.45: X-slice gas holdup for corn cob fluidization at $z = 3.2$ cm: $U_g = 1.50U_{mf}$, varying Q_s .

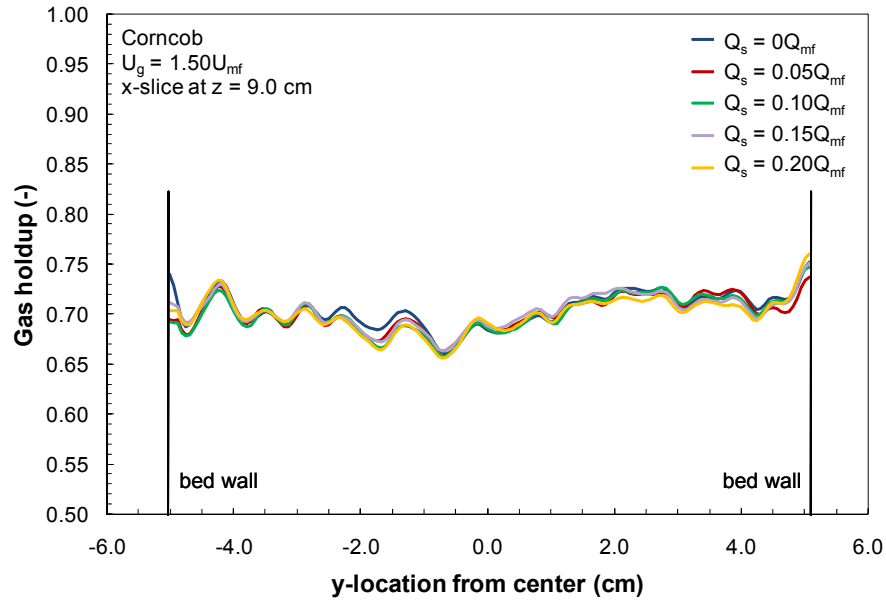


Figure C.46: X-slice gas holdup for corn cob fluidization at $z = 9.0$ cm: $U_g = 1.50U_{mf}$, varying Q_s .

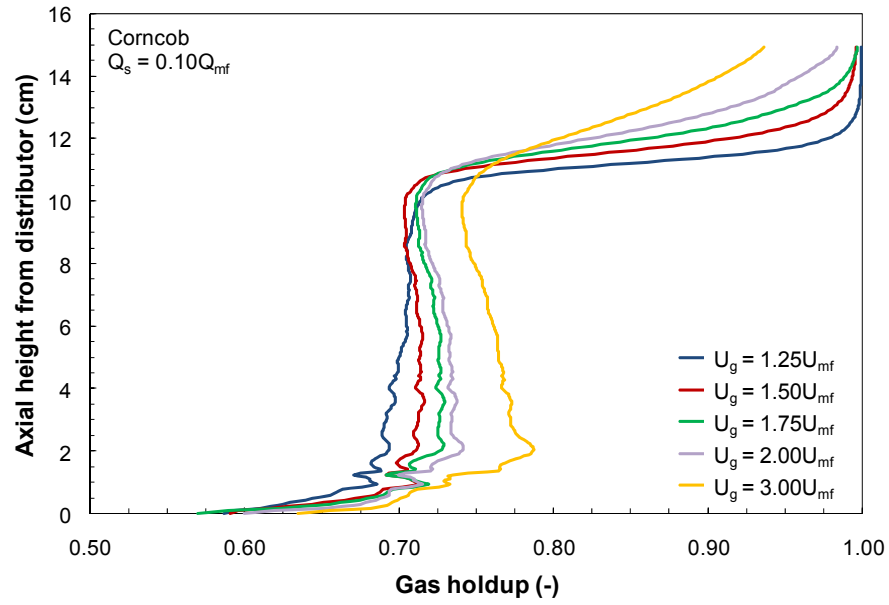


Figure C.47: Average gas holdup by height for corn cob fluidization: $Q_s = 0.10Q_{mf}$, varying U_g .

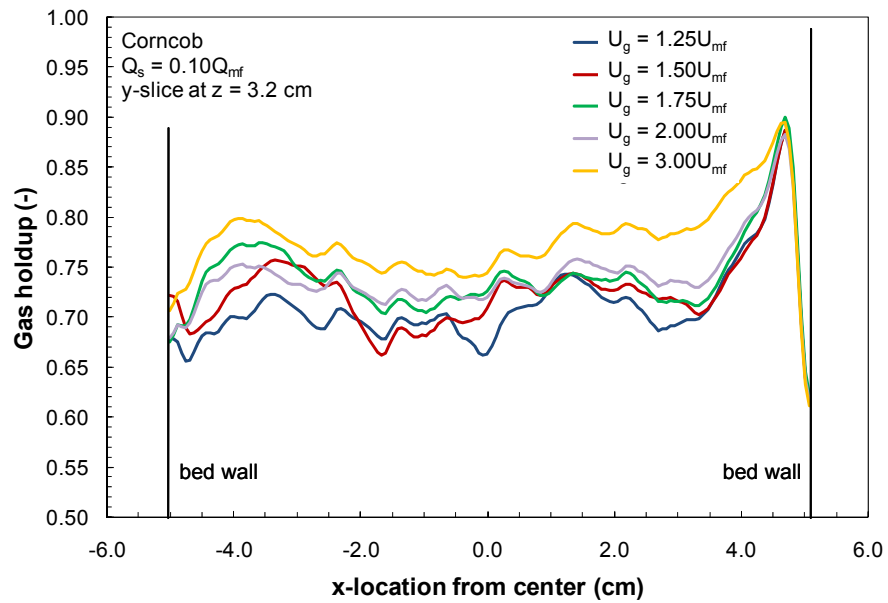


Figure C.48: Y-slice gas holdup for corn cob fluidization at $z = 3.2$ cm: $Q_s = 0.10Q_{mf}$, varying U_g .

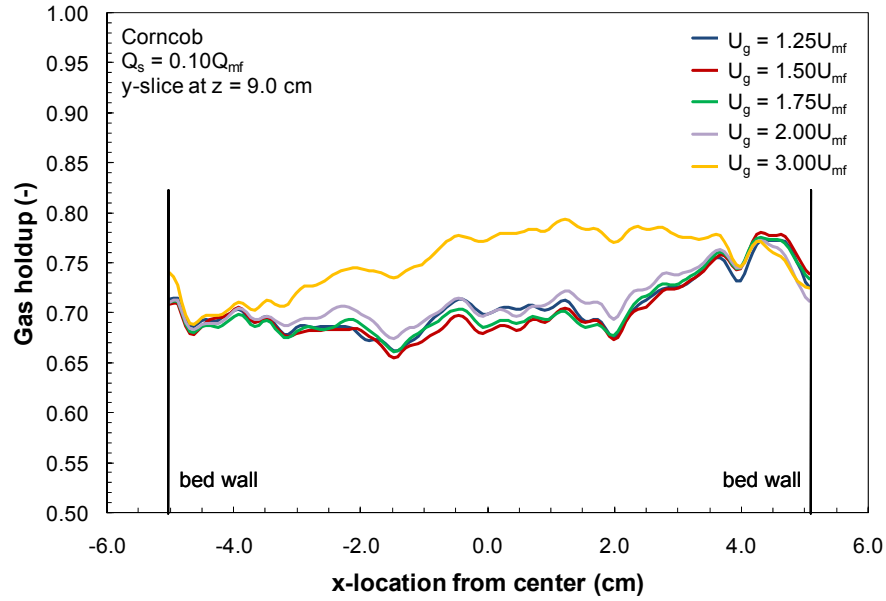


Figure C.49: Y-slice gas holdup for corn cob fluidization at $z = 9.0$ cm: $Q_s = 0.10Q_{mf}$, varying U_g .

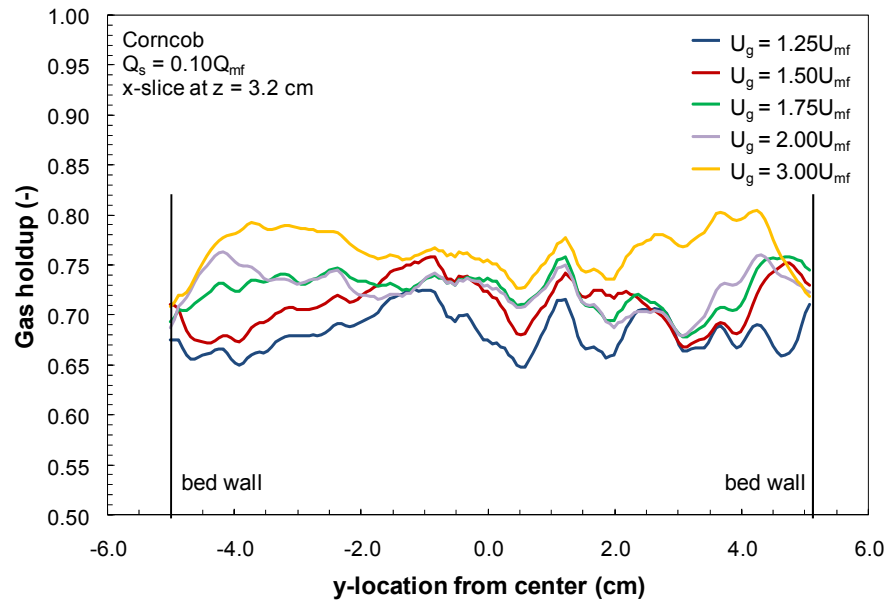


Figure C.50: X-slice gas holdup for corn cob fluidization at $z = 3.2$ cm: $Q_s = 0.10Q_{mf}$, varying U_g .

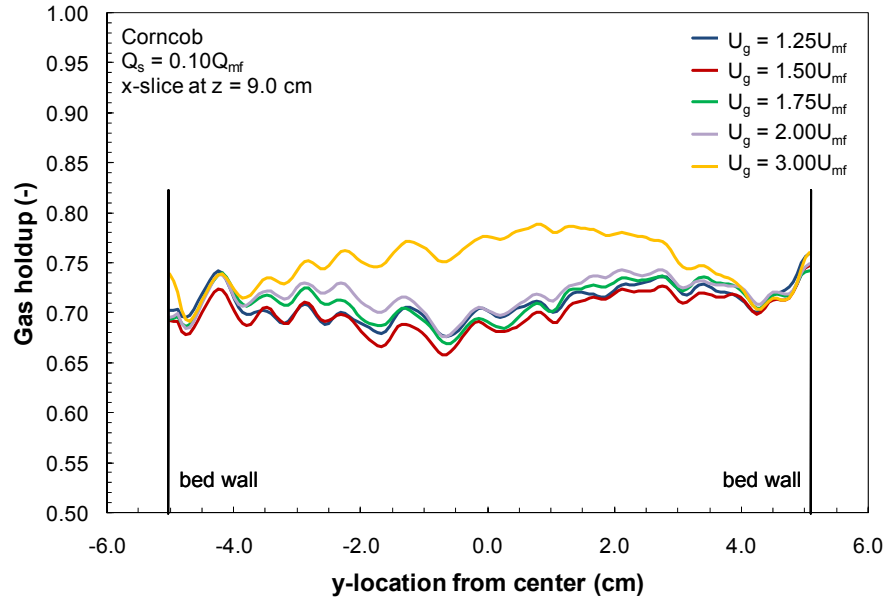


Figure C.51: X-slice gas holdup for corncob fluidization at $z = 9.0$ cm: $Q_s = 0.10Q_{mf}$, varying U_g .

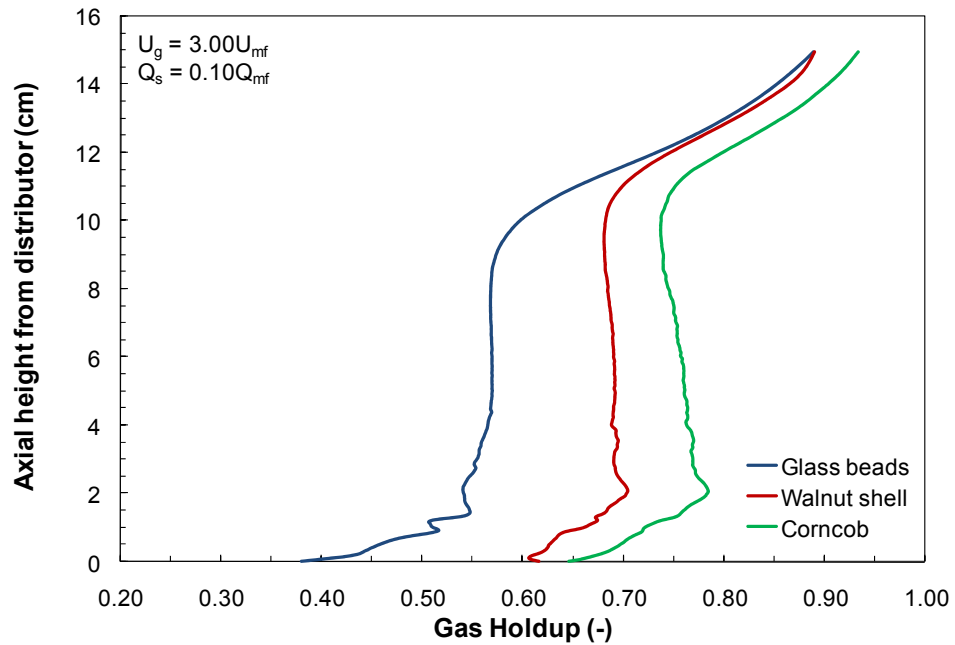


Figure C.52: Average gas holdup by height for all materials: $U_g = 3U_{mf}$, $Q_s = 0.10Q_{mf}$.

Appendix D: Particle Tracking Results

Appendix D contains additional particle tracking images and raw data to complement the results described in Chapter 4.

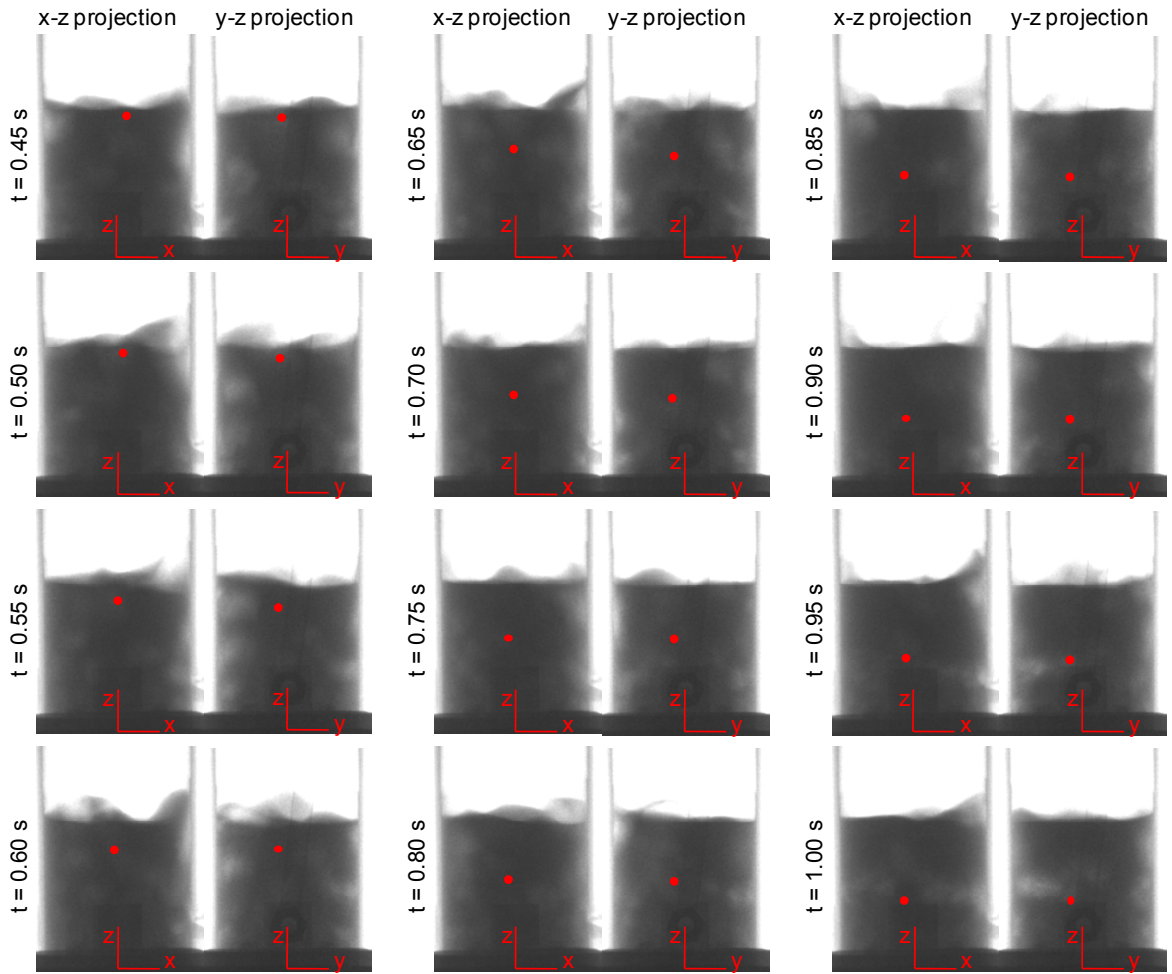


Figure D.1: Supplemental particle tracking images in glass bead bed from $t = 0.45$ to 1.00 s: $U_g = 1.5U_{mf}$, $Q_s = 0.05Q_{mf}$.

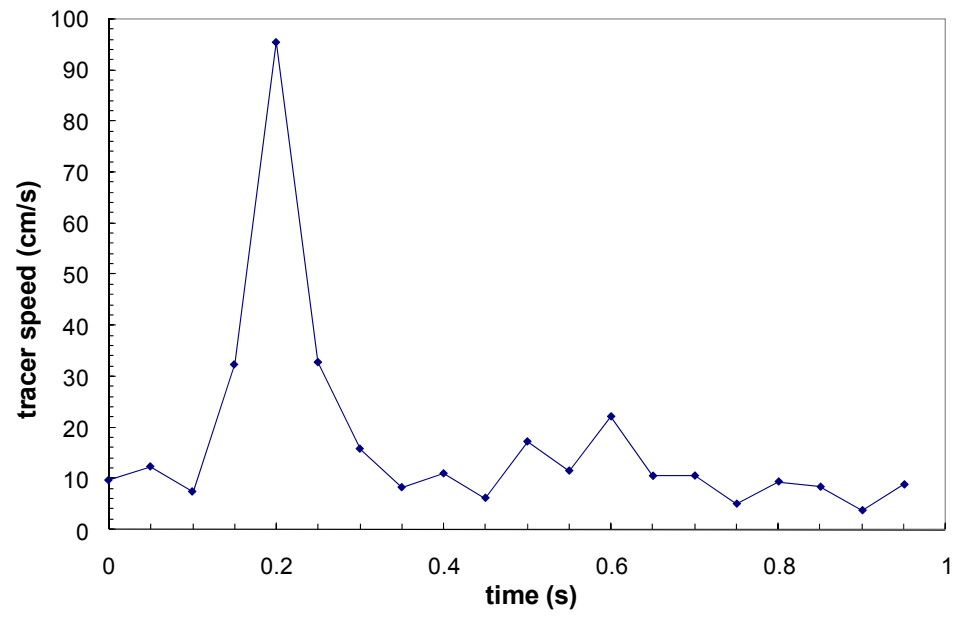


Figure D.2: Injected particle speed as a function of time in glass bead bed: $U_g = 1.5U_{mf}$ and $Q_s = 0.05Q_{mf}$.

Table D.1: Tracer particle locations at 0.05 s increments.

Pixel resolution	21.46	pixels/cm
Reference coordinates (pixels)		
x axis (x-z projection)	309	y axis (y-z projection) 316
z axis (x-z projection)	338	z axis (y-z projection) 350

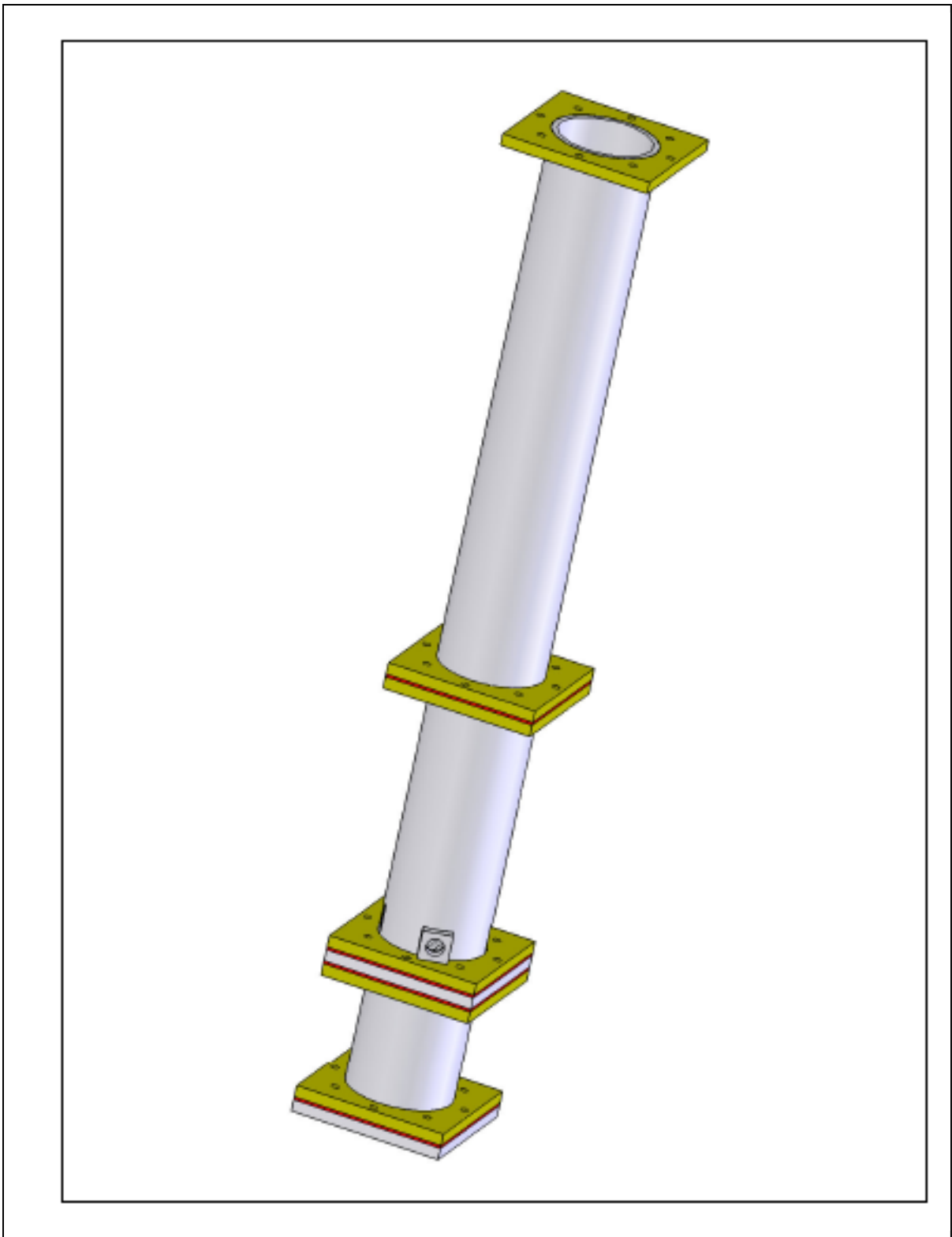
time (s)	x-location pixel	y-location pixel	z-location pixel	x-location cm	y-location cm	z-location cm
0.00	113	8	60	5.3	0.4	2.8
0.05	107	7	68	5.0	0.3	3.2
0.10	96	7	76	4.5	0.3	3.5
0.15	91	5	82	4.2	0.2	3.8
0.20	97	-26	96	4.5	-1.2	4.5
0.25	66	-11	193	3.1	-0.5	9.0
0.30	50	-6	224	2.3	-0.3	10.4
0.35	33	-5	223	1.5	-0.2	10.4
0.40	26	-4	217	1.2	-0.2	10.1
0.45	15	-6	213	0.7	-0.3	9.9
0.50	11	-9	209	0.5	-0.4	9.7
0.55	3	-12	192	0.1	-0.6	8.9
0.60	-2	-9	181	-0.1	-0.4	8.4
0.65	-2	-13	158	-0.1	-0.6	7.3
0.70	0	-15	147	0.0	-0.7	6.8
0.75	-7	-15	138	-0.3	-0.7	6.4
0.80	-7	-15	132	-0.3	-0.7	6.2
0.85	-10	-17	123	-0.5	-0.8	5.7
0.90	-9	-17	114	-0.4	-0.8	5.3
0.95	-9	-18	110	-0.4	-0.8	5.1
1.00	-10	-15	101	-0.5	-0.7	4.7

Table D.2: Tracer particle velocities at 0.05 s increments.

time (s)	x-velocity cm/s	y-velocity cm/s	z-velocity cm/s	tracer speed cm/s
0.00				
0.05	-5.6	-0.9	7.9	9.7
0.10	-10.3	0.0	7.0	12.4
0.15	-4.7	-1.9	5.6	7.5
0.20	5.6	-28.9	13.5	32.4
0.25	-28.9	14.0	89.9	95.5
0.30	-14.9	4.7	28.9	32.8
0.35	-15.8	0.9	-0.9	15.9
0.40	-6.5	0.9	-5.1	8.3
0.45	-10.3	-1.9	-3.7	11.1
0.50	-3.7	-2.8	-4.2	6.3
0.55	-7.5	-2.8	-15.4	17.3
0.60	-4.7	2.8	-10.3	11.6
0.65	0.0	-3.7	-21.9	22.2
0.70	1.9	-1.9	-10.3	10.6
0.75	-6.5	0.0	-8.4	10.6
0.80	0.0	0.0	-5.1	5.1
0.85	-2.8	-1.9	-8.9	9.5
0.90	0.9	0.0	-8.4	8.4
0.95	0.0	-0.9	-3.7	3.8
1.00	-0.9	2.8	-8.4	8.9

Appendix E: 10.2 cm Fluidized Bed Reactor Drawings

Appendix E presents the SolidWorks (2007) CAD drawings used to fabricate the 10.2 cm fluidized bed.

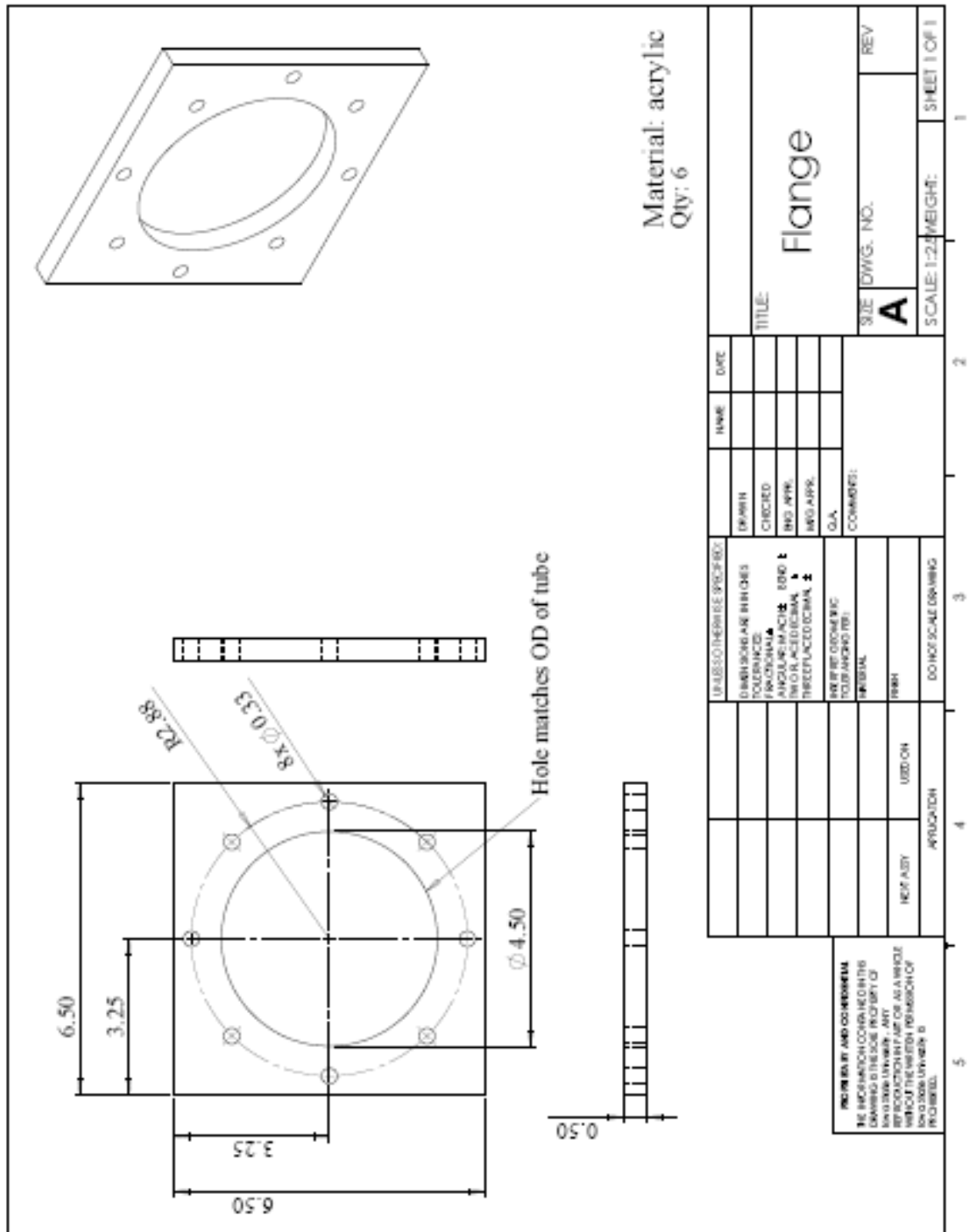


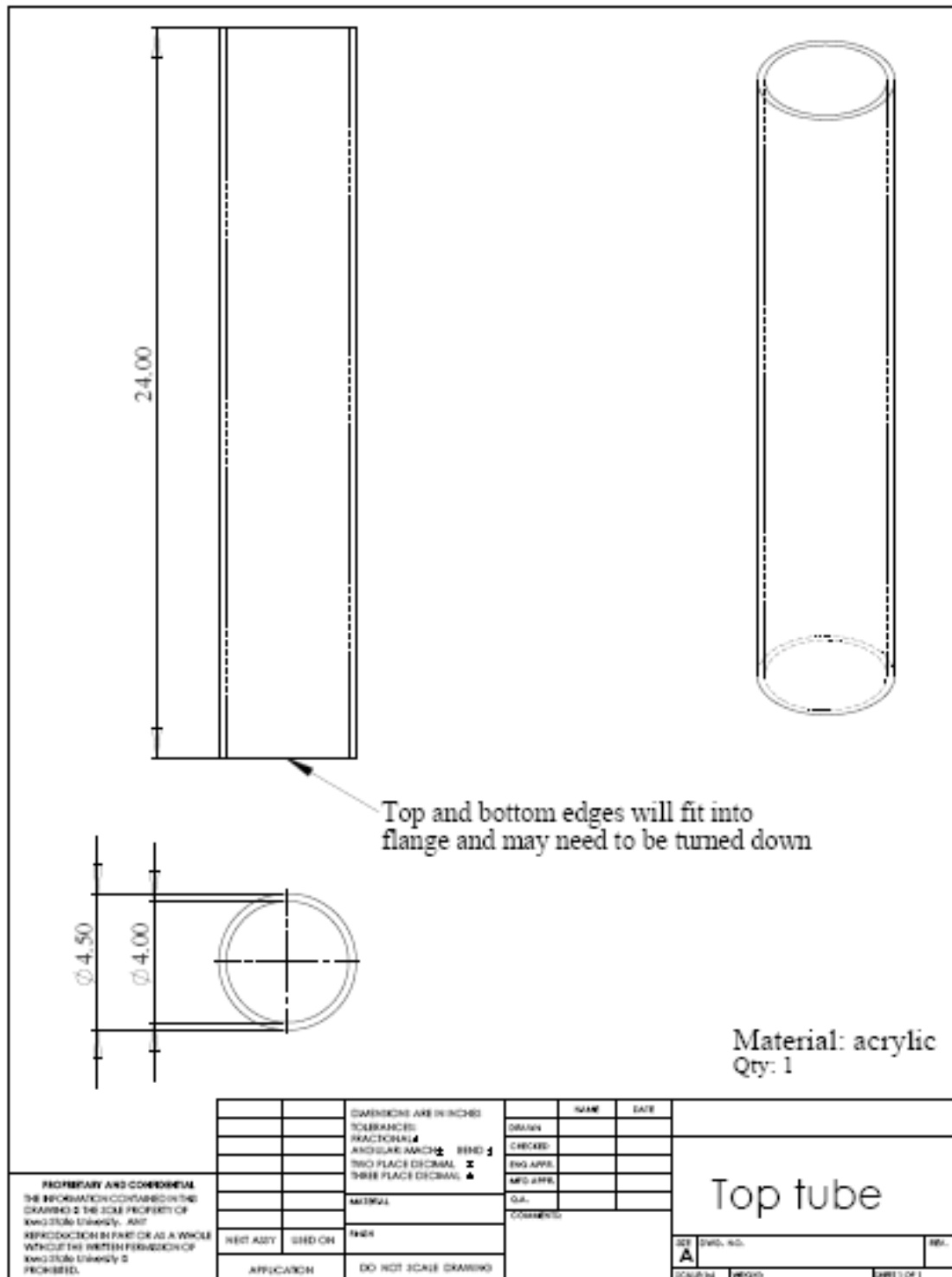
ITEM NO.	DESCRIPTION	QTY.
1	Plenum chamber assembly	1
2	Rubber gasket	4
3	Distributor plate	1
4	Reactor chamber assembly	1
5	Top chamber assembly	1
6	Bottom plenum plate	1

DIMENSIONS ARE IN INCHES TOLERANCES: FRACTIONS: \pm ANGULAR: \pm MIN TWO PLACE DECIMAL: \pm THREE PLACE DECIMAL: \pm		NAME	DATE
		DESIGN	
MATERIAL FINISH NEXT ASSY USED ON APPLICATION		CHECKED	
		ENG APPR.	
COMMENTS		Q.A.	
DO NOT SCALE DRAWING		Complete assembly	
		SET DWG. NO. A	
		COURSE	WORKSHEET

PROPRIETARY AND CONFIDENTIAL
 THE INFORMATION CONTAINED IN THIS
 DRAWING IS THE SOLE PROPERTY OF
 KNOX STATE UNIVERSITY. ANY
 REPRODUCTION IN PART OR AS A WHOLE
 WITHOUT THE WRITTEN PERMISSION OF
 KNOX STATE UNIVERSITY IS
 PROHIBITED.

SHEET 1 OF 1





Top and bottom flange should be parallel

Tube fits inside flange holes and flush with flanges' outside edges

ITEM NO.	DESCRIPTION	QTY.
1	Flange	2
2	Top column	1

1

2

1

PROPRIETARY AND CONFIDENTIAL
THE INFORMATION CONTAINED ON THIS DRAWING IS THE SOLE PROPERTY OF KNOX STATE UNIVERSITY. ANY REPRODUCTION IN PART OR AS A WHOLE WITHOUT THE WRITTEN PERMISSION OF KNOX STATE UNIVERSITY IS PROHIBITED.

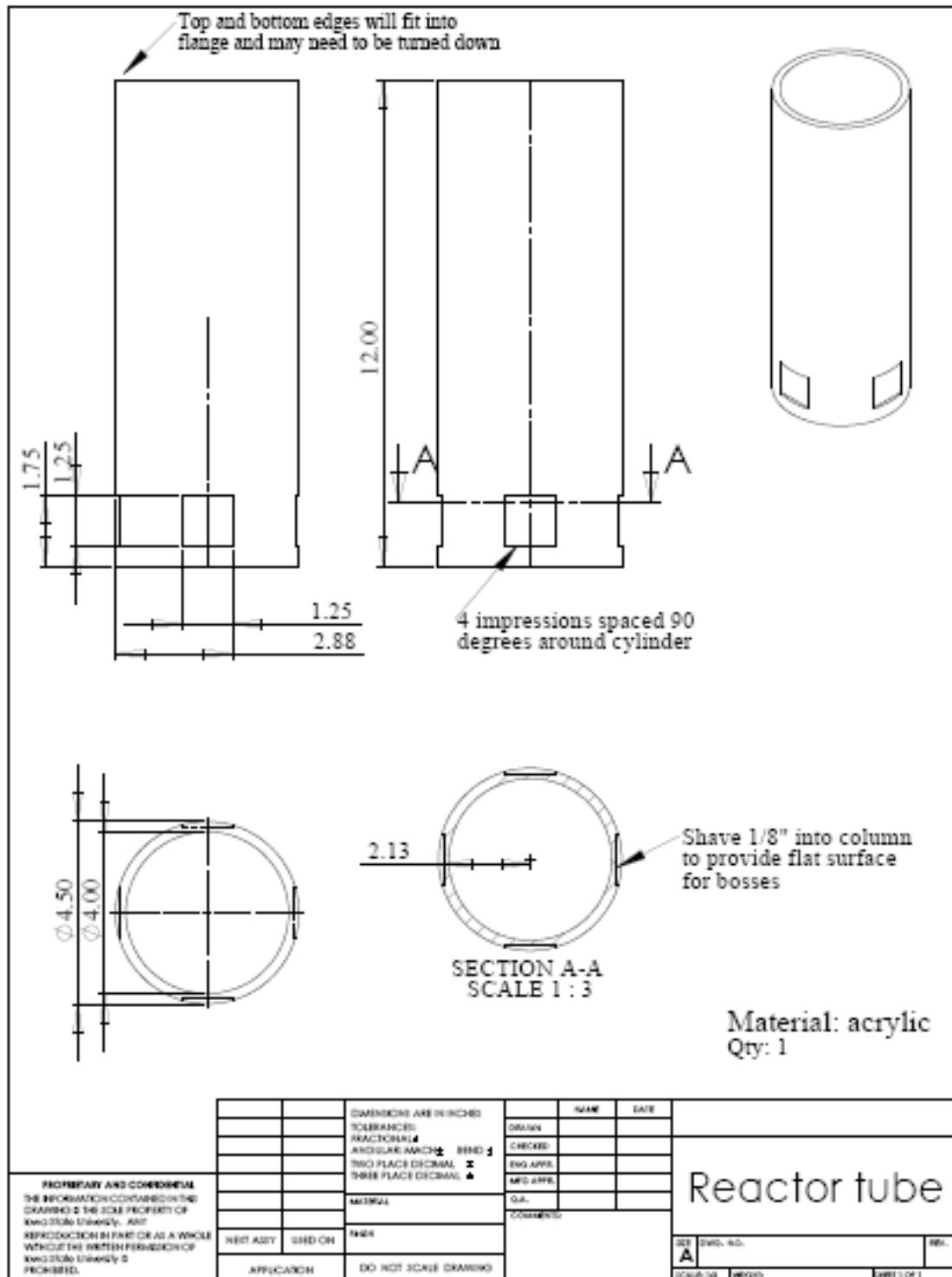
DIMENSIONS ARE IN INCHES		NAME	DATE
TOLERANCES:		DRAWN	
FRACTIONS		CHECKED	
ANGULAR MATCH	± .0001	ENG APPR.	
TWO PLACE DECIMAL	± .0001	MFG APPR.	
THREE PLACE DECIMAL	± .0001	QA	
MATERIAL		COMMENTS	
FINISH			
NEST ASBY	USED ON		
APPLICATION	DO NOT SCALE DRAWING		

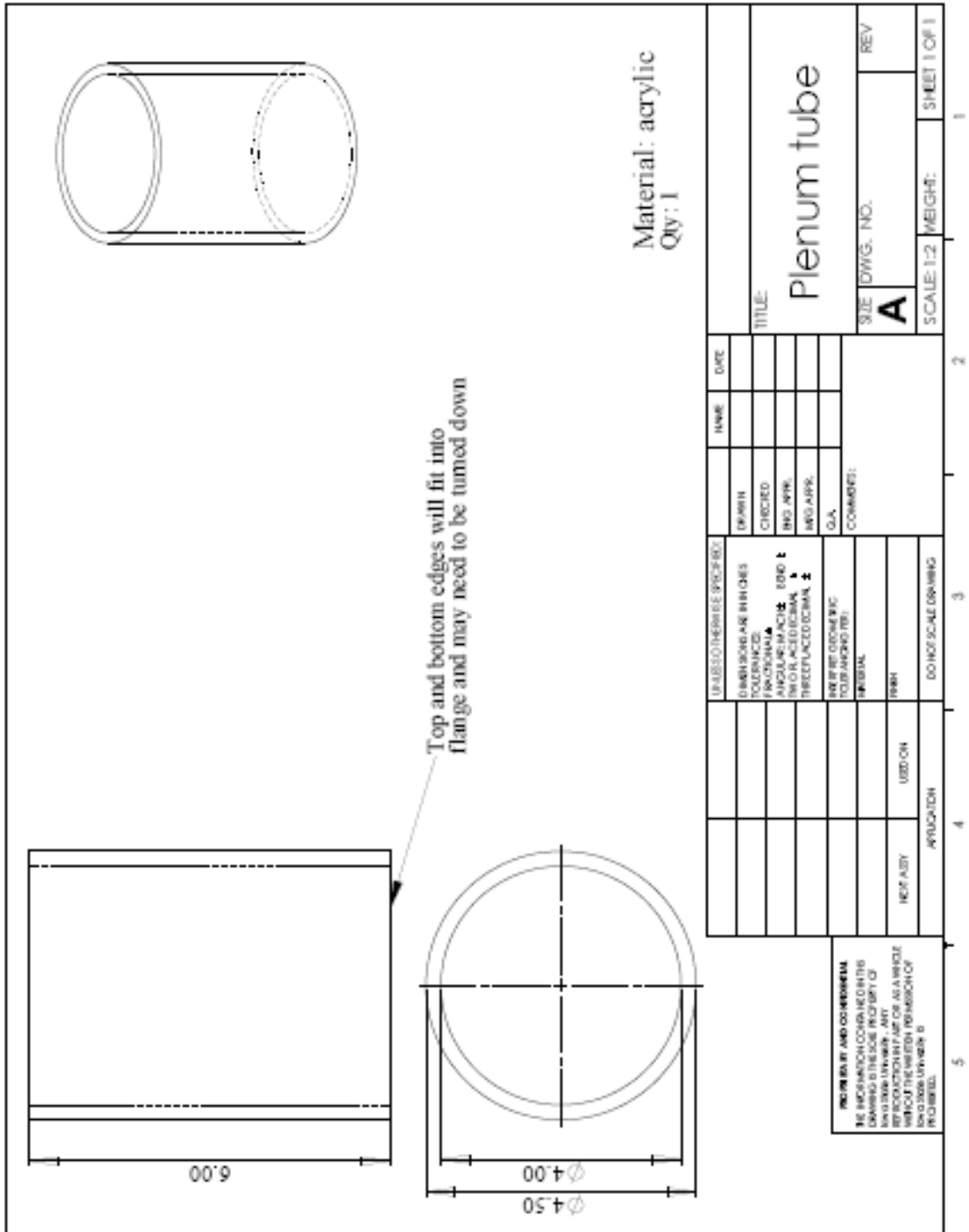
Top chamber

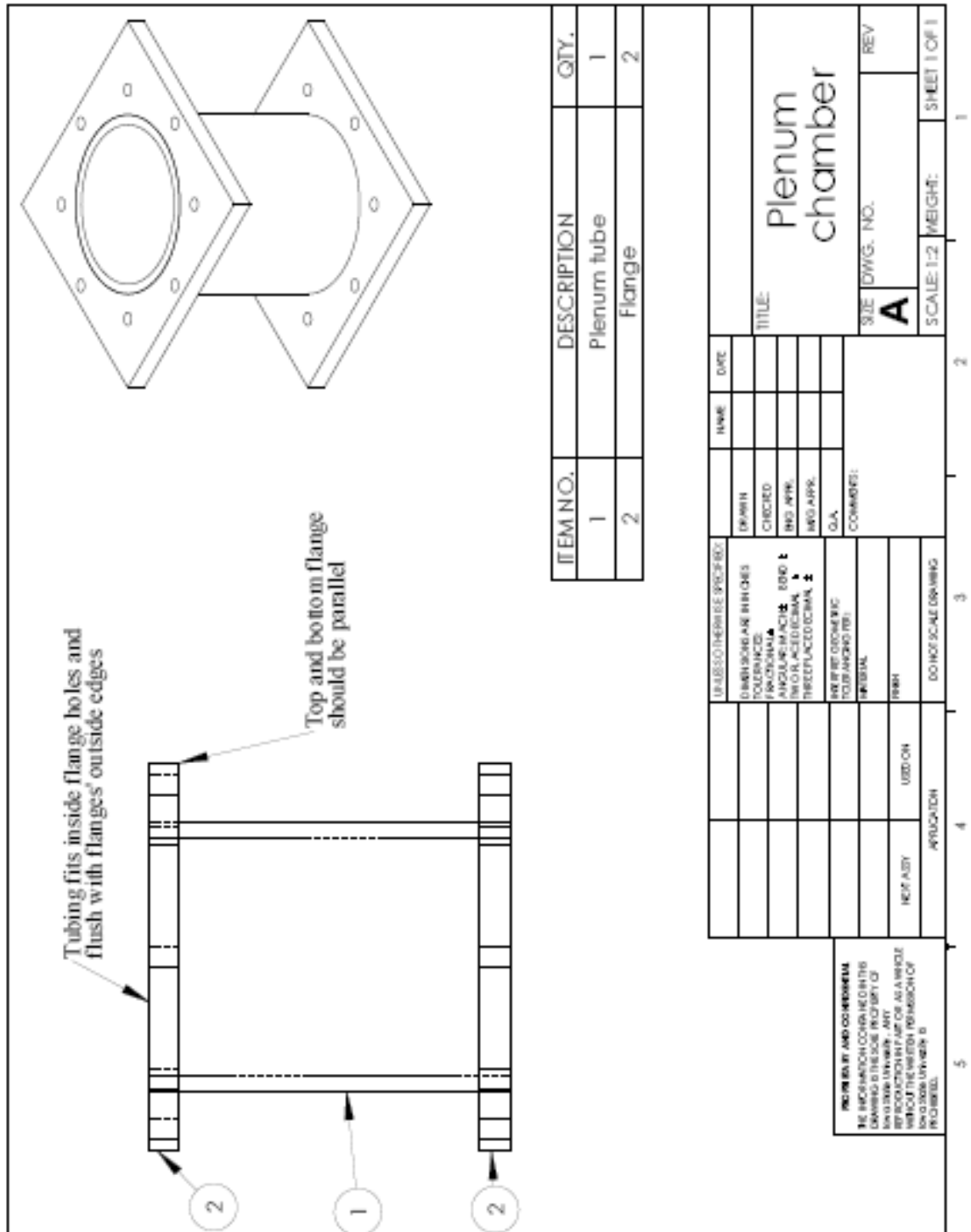
SET DWG. NO. REV.

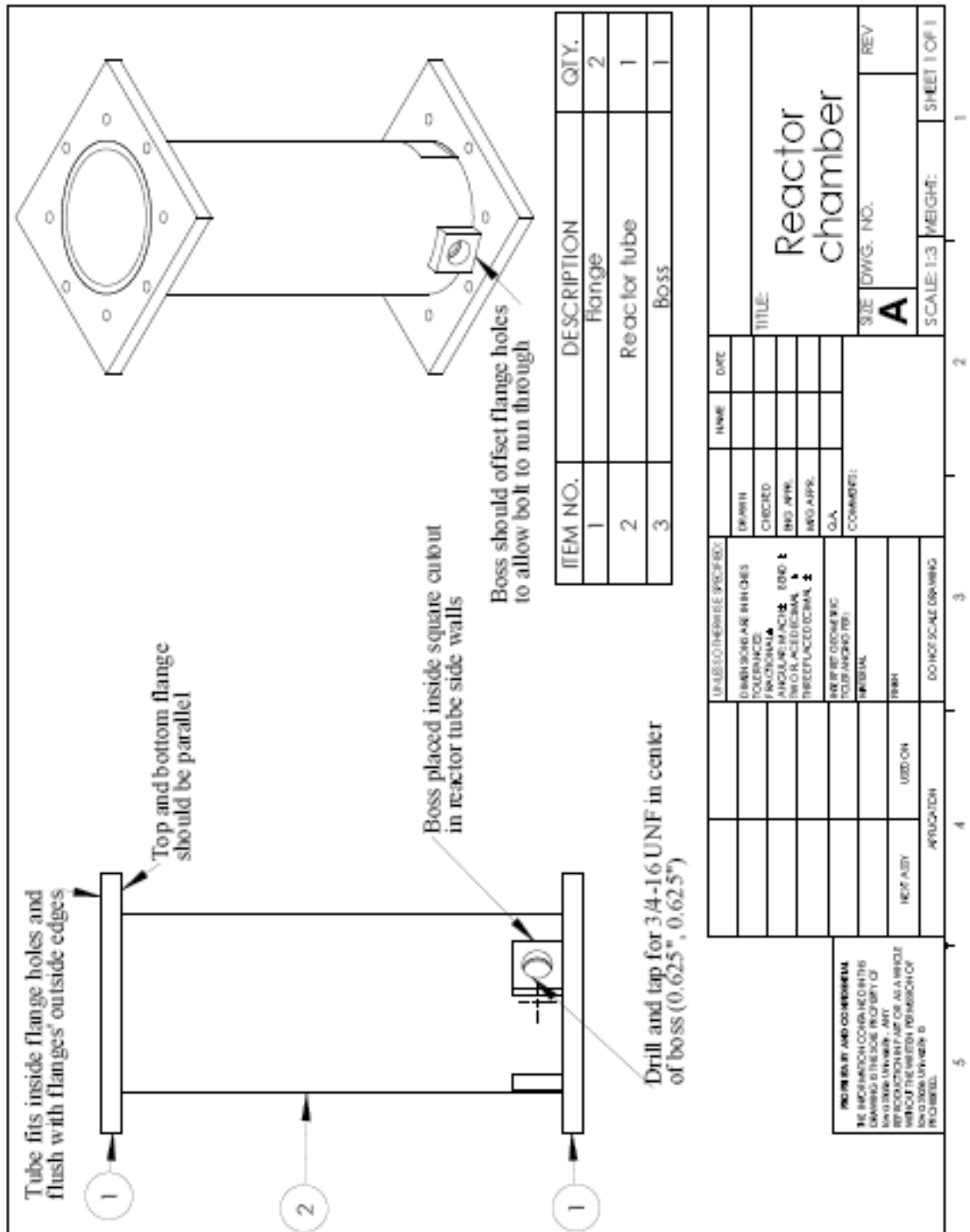
A

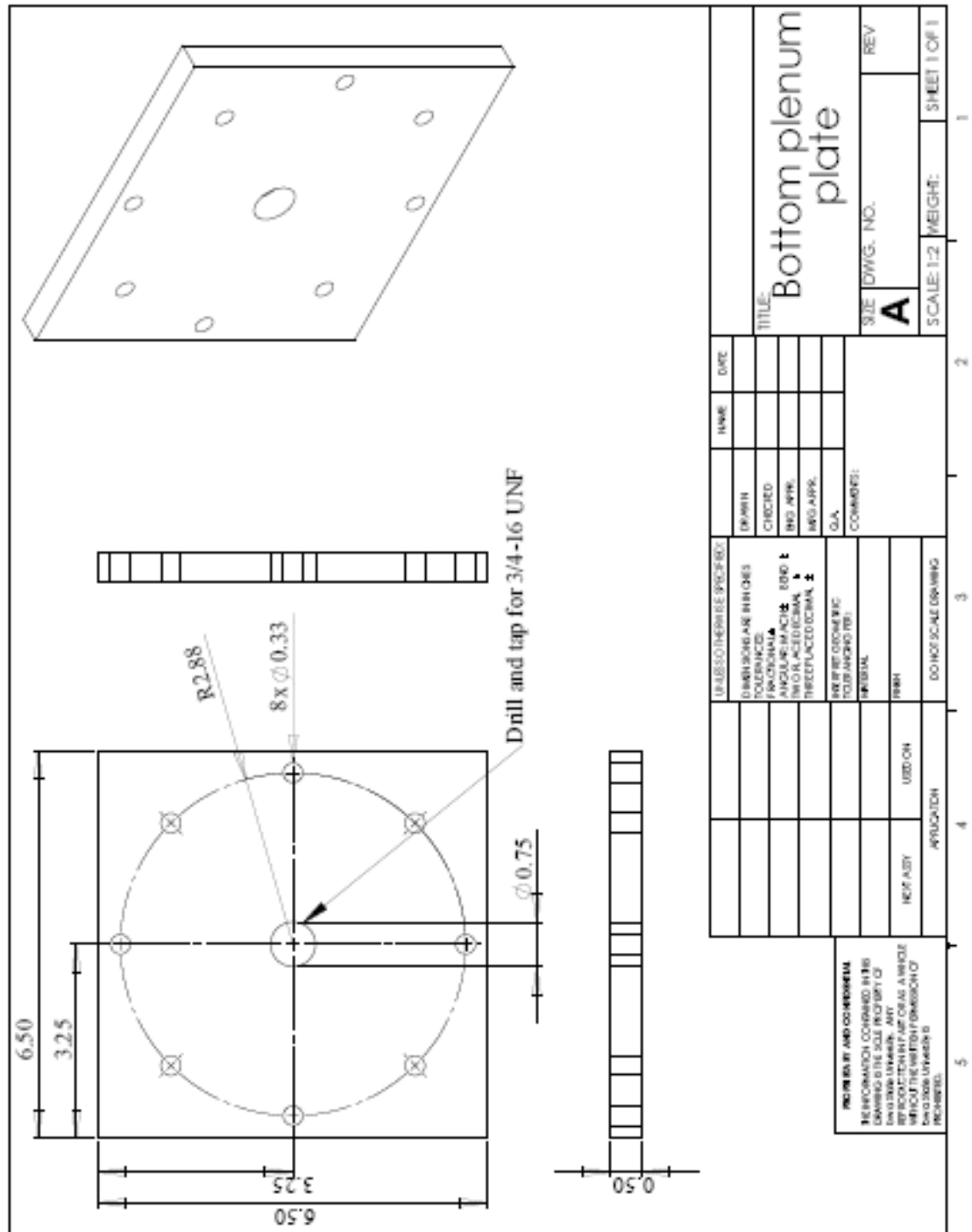
SCALE: 1/2" = 1'-0" SHEET 1 OF 1

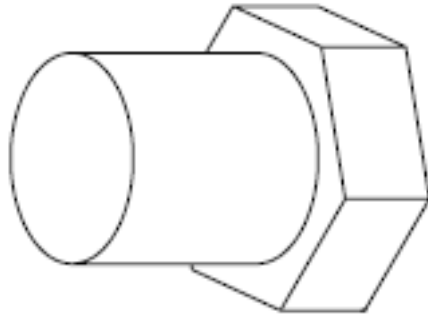




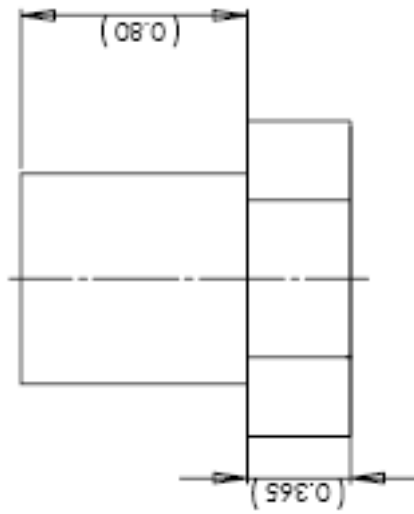




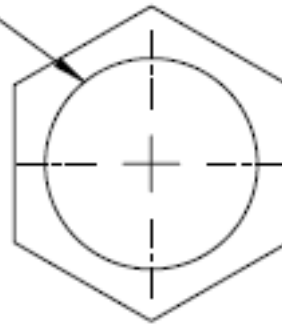




Quantity: 2
 Material: Nylon
 Tolerances: ± 0.05 "
 Nate Franke
 1121 Black Engr.



Tapped for 3/4"-16 threads



Bed chamber plug